Structural Characterization of a Transmembrane Protein by Solid-state NMR

-

A Biophysical and Functional Study of the ABC Transporter ArtMP-J

A Dissertation

Submitted in Partial Fulfilment of the Requirements for the Degree of

Doktor der Naturwissenschaften (Dr. rer. nat.)

to the Department of Biology, Chemistry, Pharmacy

of the Freie Universität Berlin

by

Anja Marion Voreck

Berlin, 2014

February 2010 - May 2014

Supervisor: Prof. Dr. Hartmut Oschkinat (Freie Universität Berlin)

Second examiner: Prof. Dr. Bernd Reif (Technische Universität München)

Date of defense: November 24, 2014

For Linda

(since this made me miss your fifth birthday)

Acknowledgements

Table of Content

1 List of abbrevations

AMPPNP/AMPCP	non-hydrolyzable ATP analogs
ArtMP	Shortened form for the ArtM$_2$P$_2$ dimer, used in descriptions for NMR experimets, capital letters indicate which subdomain was triple-labeled (ArtMP, ArtmP, ArtMp)
aTc	Anhydrotetracylin
AUC	Analytical ultracentrifugation
bp	Base pairs
CH	Coupling helix
CP	Cross polarization
CSP	Chemical shift perturbation
DNA	Deoxyribonucleic acid
HCDF	High cell density fermentation
IMP	Integral membrane protein
INEPT	Insentive nuclei enhanced by polarization transfer
IPTG	Isoprophyl-β-D-thiogalactopyranoside
ITC	Isothermal titration calorimetry
K_A	Association constant
K_D	Dissociation constant
kDa	Kilo Dalton
MAS ssNMR	Magic-angle-spinning solid-state NMR
MP	Membrane protein
NBD	Nucleotide binding domain
NBS	Nucleotide binding site
OD$_{600}$	Optical density at 600 nm
PCR	Polymerase Chain Reaction
PDB	Protein Data Bank
rpm	Rounds per minute
SDS-PAGE	SDS Polyacrylamide Gelelectrophoresis
SEC	Size exclusion chromatography
SBP	Substrate binding protein
TM	Transmembrane (helices, proteins etc.)
v/v	Volume per volume
w/v	Weight per volume

2 Introduction

2.1 Structural investigation of integral membrane proteins

2.1.1 Approaches for the biophysical characterization of proteins in lipid environments

Membrane proteins (MP) play vital roles in numerous cellular processes including energy generation, tissue integrity and signal transduction. They mediate nutrient uptake and protection against pathogens and toxic compounds. The ATP synthase uses the mitochondrial proton gradient to synthesize the universal energy storage molecule ATP[1]. Tight-junction proteins like claudins are essential for mediation and stability of cell-cell contacts in epithelial tissue while transmembrane (TM) receptors and channels are specified signal transducers involved in cell homeostasis and response to extracellular stimuli[2,3]. This includes the B- and T-cell receptors that are central to the adaptive immune system while the Toll-like receptors (as part of the innate immune response) provide a first line of defense against viral and bacterial infections[4]. Passive and active TM transporters e.g. mediate uptake of sugars, amino acids and vitamins, are involved in lipid metabolism and confer protection against toxic compounds by actively removing them from the cytosol[5-7]. The diversity of biological functions makes TM proteins account for about 60 % of approved drug targets underlining the medical relevance of this protein class[8,9]. However, the detailed mode of action is not known for many of these drugs due to the challenges faced upon structural investigation of TM proteins, which include limitations in expression yields, protein stability and activity in non-native environments[6].

In May 2014 about 2000 unique entries for membrane protein structures were deposited in the Protein Data Bank (pdb)[10]. This represents only about 2 % of all pdb entries and directly reflects the difficulties of structural studies on proteins that are naturally surrounded by a complex lipid environment. Structure and function of TM proteins crucially depends on this lipid environment which in turn varies with organism, cell type and growth phase[11-13]. Considering that close to 30 % of the human proteome consists of α-helical TM proteins with various pathophysiological implications[14], there is an urge to constantly develop and improve bioinformatical and biophysical techniques for atomic level information on these difficult-to-access targets[15,16].

The investigation membrane proteins often starts with analysis of their secondary structure using bioinformatical tools, that predict the number of TM helices as well as their rough orientation and topology judging from the amino acid (aa) sequence of the protein. A variety of prediction tools based on different algorithms is available online[17-19]. In the past decade, standard methods in biophysics strongly developed towards investigation of membrane proteins, including investigation of oligomerization states by <u>a</u>nalytical <u>u</u>ltra<u>c</u>entrifugation (AUC)[20,21] or ligand-binding studies for various lipid-embedded receptors and transporters using <u>s</u>urface <u>p</u>lasmon <u>r</u>esonance (SPR)[22]. Other studies used <u>i</u>sothermal <u>t</u>itration <u>c</u>alorimetry (ITC) to monitor ligand binding to different TM proteins (reviewed in

Draczkowski, 2014[23]) and to analyze the lipid reconstitution behavior of the potassium channel KcsA[24]. Microscale thermophoresis (MST) — a relatively new tool that needs minimum amounts of protein — was already successfully applied to observe and quantify protein-ligand interactions for a human G-protein coupled receptors (GPCRs)[25].

For structural investigation, cryo-electron microscopy (cryo-EM) has been increasingly applied to obtain density maps for large TM protein assemblies that were used to fit subdomain structures solved by NMR or X-ray. Next to others, various viral TM complexes were studied this way including the envelope protein of the human immune deficiency virus (HIV)[26]. Recently, serial femtosecond crystallography (SFX) using an x-ray free laser (XFEL) proved especially useful for structure determination on very small crystals while causing substantially reduced irradiation damage compared to standard X-ray crystallography[27]. Combined with lipidic cubic phase crystallization (LPC), where the membrane protein is embedded in a monolein layer that can be combined with other lipids, this method has great potential for structure determination of TM proteins.

Despite these recent successes, crystalline preparations often suffer from crystal-crystal contacts[28]. This may induce artificial conformations or protein-protein interfaces that are hard to distinguish from natural assemblies. Moreover, protein function is influenced by pH and salt concentration so that the natural conformation of certain protein regions (e.g. the sidechain configuration in an active center) might differ from the one under conditions that enabled crystallization. Although many detergents have been especially useful for crystallization of TM proteins[29,30], Cross & Zhou state that these molecules have largely different concentrations for self-assembly when compared to lipids[31]. While lipids start to form bilayers at nanomolar concentrations, the critical micellar concentration of detergents is often in the millimolar range. This may lead to unnatural incorporation of detergent molecules into membrane protein structures as seen for the M2 transmembrane domain (pdb code: 3BKD). The lateral pressure naturally enforced by the lipid bilayer on integral membrane proteins is central for correct protein folding and cannot be mimicked correctly in detergent micelles or 3D crystalline environments[31]. Further, protein function is also largely influenced by the presence of the correct or near native membrane lipids, which for example will modify protein-protein interactions and enzyme activity[32]. Table 1 summarizes a small number of recent publications (including some reviews) on innovative biophysical and structural studies of TM proteins.

Table 1: Biophysical methods with recent developments in membrane protein research

Objectives	Examples for targets	Methods	Recent references
Oligomerization state	EmrE, glycophorin A, erythropoietin receptor GPCR	Analytical ultracentrifugation (AUC) Atomic force microscopy (AFM)	Fleming *et al.*, 2008[20] Zhao *et al.*, 2013[21] Shi *et al.*, 2009[33]
Ligand binding	GPCRs, ABC transporters GPCRs, channels, transporters GPCR	Surface plasmon resonance (SPR) Isothermal titration calorimetry (ITC) Microscale thermophoresis (MST)	Patching, 2014[22] Draczkowski *et al.*, 2014[23] Corin *et al.*, 2011[34]
Membrane insertion	Potassium channel KcsA	Isothermal titration calorimetry (ITC)	Jahnke *et al*, 2014[24]
Topology/structure determination	GPCRs,enzymes, TM pores KcsA, M2 channel, GPCRs, YadA autotransporter GPCR viral TM proteins	Lipidic cubic phase crystallization (LCP) Magic-angle-spinning (MAS) solid-state NMR Oriented-sample (OS) solid-state NMR Cryo electron microscopy	Cherezov, 2011[35] Hong *et al.*, 2012[36] Shahid *et al.*, 2012[37] Opella, 2013[38] Zhou *et al.*, 2014[26]
Functional investigation	Cytochrome c oxidase, ion exchangers, amino acid transporters	Electrophysiology	Grewer *et al.*, 2013[39]
Membrane mimetics and detergent alternatives	Rhodopsins, cytochrome P450 β-barrel TM proteins, rhodopsins, GPCRs	Nanodiscs Amphipols	Inagaki *et al.*, 2013[40] Popot *et al.*, 2011[41]

In many fields, there is a strong effort to mimic the membrane bilayer using modern detergents or synthetic lipids like DOPC (1,2-dioleoyl-sn-glycero-3-phosphatidylcholine) and DMPC (1,2-dimyristoyl-sn-glycero-3-phospho-choline). In X-ray, especially using LCP, this has led to over 2000 membrane protein structures (pdb, May 2014), including many GPCRs, enzymes and porins[42].

When investigating structure-function relationships of membrane proteins (MPs), the ideal experimental conditions would be working with the native membrane of the protein in the optimal case also including the full variety of proteins naturally incorporated in that membrane. This, of course, is not possible for most structural studies like X-ray and electron crystallography where isolated and homogeneous preparations of the protein of interest are required.

2.1.2   Complexity of biomembranes

Figure 1 illustrates several examples for integral and peripheral MPs that in reality comprise up to 70 % of the biomembrane[13]. Peripheral MPs can anchor to the lipid bilayer via a short hydrophobic helix or by a lipid-modification of an N-terminal or C-terminal cysteine. The types of IMPs are diverse, ranging from monotopic MPs (that only span one leaflet of the bilayer) and bitopic (spanning both leaflets) to multispan proteins[43]. The latter group includes various pores, channels, receptors and transporters, most of them comprised of α-helical bundles (e.g. rhodopsins and GPCRs) or β-barrels (like the outer membrane pores, OMPs). These folds are strongly dictated by the lipid environment, which, in contrast to soluble proteins, involves solvent inhomogeneity, gradients of the pH, pressure and dielectric constant as well as a largely different chemical environment for bonding networks[43].
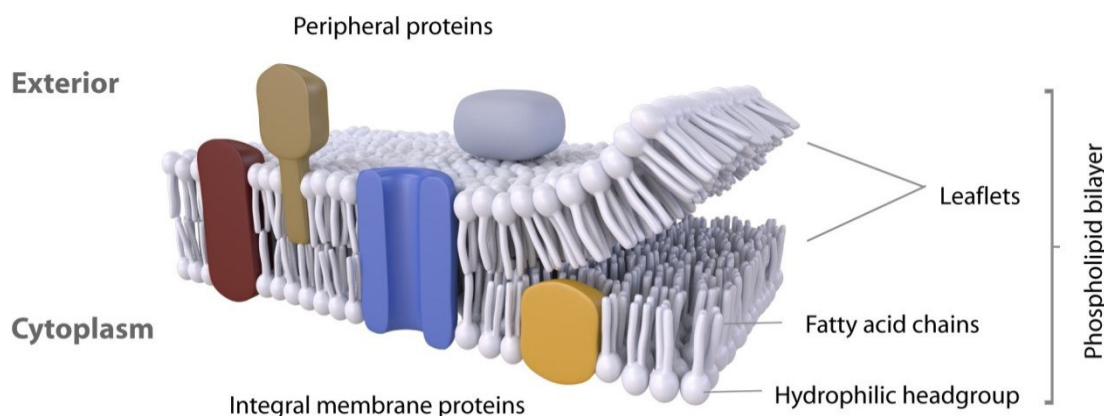
Figure 1: Schematic representation of a biomembrane composed of two lipid leaflets and different integral membrane proteins. Examples for peripheral and membrane-anchored proteins are also given. Eukaryotic membrane proteins often carry posttranslational glycosylations that are omitted in this representation. The figure was created by Dr. B. van Rossum, FMP, Berlin.

Next to the variety of MPs, biological membranes contain various classes of polar (phospho-, sphingo- and glycolipids) and non-polar (e.g. sterols) lipids. These molecules differ in their combinations of head groups and fatty acid chains (Figure 2) and even lipids of the same type still vary in length and saturation state of their acyl chains. Gram-negative bacteria like *E. coli* have phosphatidylethanolamine (PE) as the most abundant component (up to 80 % of the lipid fraction) next to smaller amounts of phosphatidylglycerol (PG) and cardiolipin (CL) while membranes from gram-positive organisms like *B. subtilis* additionally include diglycosyl diacylglycerols[44-46]. Eukaryotic membranes are fundamentally more complex. They are primarily comprised of phosphatidylcholin (PC) but in addition they also contain PE as well as small amounts of phosphatidylserine (PS), phosphatidylinositol (PI) and phosphatidic acid (PA)[47]. Incorporation of sterols (e.g. cholesterol) provides additional stability and regulates membrane fluidity over a wide range of temperatures. The composition of the membrane

bilayer is often asymmetric, showing different lipid configurations at the inner and the outer leaflet[6,47]. Numerous molecular dynamics (MD) projects were set out to model complex lipid bilayers in order to understand their dynamic behavior[48]
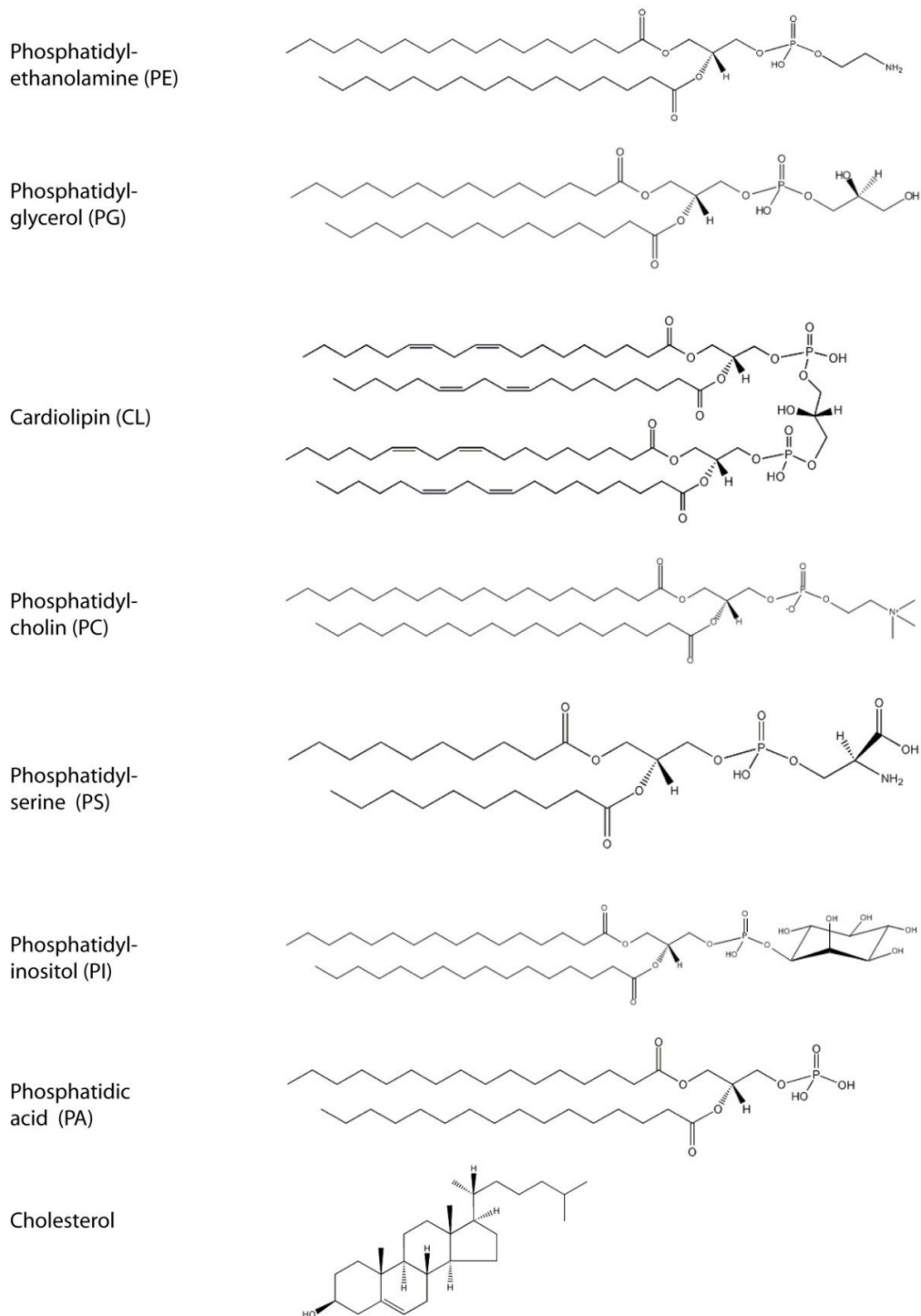
Figure 2: Examples for common lipids in bacterial and mammalian membranes highlighting the variety of head groups. The fatty acids chains of each lipid type can vary in length and saturation state which is important to regulate thickness and stability of the bilayer. Structures were downloaded from the LIPID MAPS Structure Database[49]..

2.2   MAS solid-state NMR for protein structure determination in native environments

One complication faced when investigating membrane proteins by X-ray or electron crystallography is largely resolved in solid-state nuclear magnetic resonance (ssNMR), as crystalline packing is not required[50]. In ssNMR, the resolution is also not limed by the size of the target protein because the fast molecular tumbling (in solution NMR) is simulated by spinning the sample at the so-called magic angle (54.74°, with respect to the external magnetic field). This leads to averaging of anisotropic interactions also within larger molecules that would tumble very slowly in solution.

2.2.1   NMR theory

2.2.1.1   NMR active nuclei and their interaction types

NMR active isotopes possess a magnetic moment (μ), associated with a nuclear spin quantum number of I ≠ 0. ^{1}H, ^{13}C, ^{15}N, ^{31}P and ^{19}F (all I = ½) are the most frequently used spin types in biomolecular NMR (Table 2). However, deuterium (I = 1), which additionally possesses a quadrupolar moment, is now increasingly used to study dynamics of biosolids[51-53].

The phenomenon of nuclear magnetic resonance relies on the 'Zeeman' interaction of an external magnetic field B_0 with the inherent magnetic moment of a nucleus and was demonstrated by the groups of Purcell and Bloch in the 1940s[54-57]. The nuclear magnetic moment is defined by

$$\mu = \gamma I \hspace{4cm} \text{Eq. 1,}$$

where γ is the gyromagnetic ratio that is characteristic to each nucleus. By definition, in NMR experiments the external magnetic field B_0 is aligned along the z-axis and the energies of the nuclear spin states are given by

$$E = -\gamma I_Z B_0 = \mu B_0 \hspace{4cm} \text{Eq. 2.}$$

I_z can accommodate $(2I + 1)$ values referred to as the 'Zeeman' levels (Figure 3). These different quantum states are of equal energy in the absence of a magnetic field but split into levels of different energy when an external magnetic field B_0 is applied.
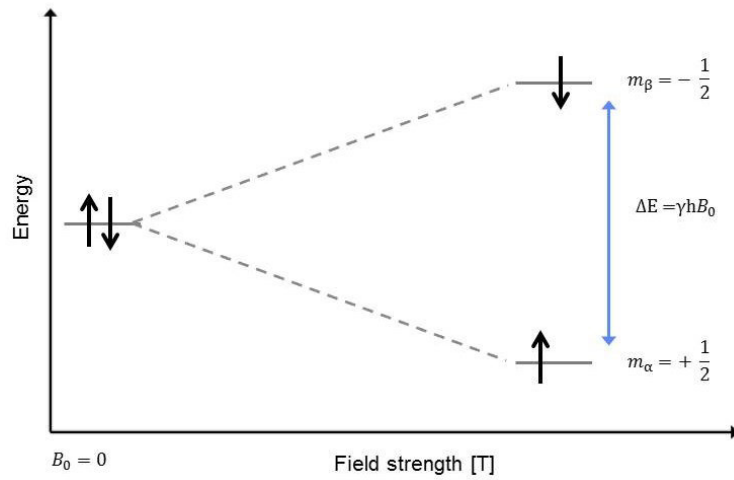
Figure 3: Schematic representation of the Zeeman levels in the B$_0$ field. The larger the B$_0$ field, the bigger the energy difference ΔE between the m$_\alpha$ and m$_\beta$ states.

For spin I = ½ nuclei, two levels (m$_\alpha$ = + ½ and m$_\beta$ = - ½) occur that are differently populated at equilibrium as determined by the Boltzmann distribution (Eq. 3). Here, N represents the populations in the α and β state, k is the Boltzmann constant and T the temperature.

$$\frac{N_\beta}{N_\alpha} = e^{\frac{-\Delta E}{kT}}$$
Eq. 3

If the magnetic energy (μB$_0$) of a spin is lower than its thermal energy (kT), the spin polarization P will be ineffective and small

$$P = \tan\frac{\mu B_0}{kT}$$
Eq. 4.

The energy needed to induce a transition between two different states is given by

$$\Delta E = \frac{h\gamma B_0}{2\pi}$$
Eq. 5,

where h is Planck's constant.
In the B$_0$ field the magnetic moment precesses around the z-axis with a frequency, given by

$$\omega_0 = -\gamma B_0$$
Eq. 6.

Thus, the Lamor frequency ω_0 of a nucleus depends on its gyromagnetic ratio and the strength of the applied magnetic field. For example the Lamor frequency of protons at 21.2 T is at 900 MHz. With $\frac{\omega_0}{2\pi}$ we obtain

$$\nu_0 = \frac{-\gamma B_0}{2\pi}$$
Eq. 7.

Table 2: NMR active nuclei in biosolids[58]

Nucleus	Spin I	γ $[\text{T s}]^{-1}$	Gyromagnetic ratio $\gamma / 2\pi$ [MHz/T]	Natural Abundance [%]
^{1}H	½	2.675×10^8	42.574	99.98
^{2}H	1	4.107×10^7	6.536	0.02
^{13}C	½	6.728×10^7	10.708	1.10
^{14}N	1	1.934×10^7	3.078	99.63
^{15}N	½	-2.713×10^7	-4.318	0.37
^{31}P	½	1.084×10^8	17.232	100
^{19}F	½	2.518×10^8	40.075	100

The Boltzmann distribution can be combined with the Lamor frequency v_0 as shown in equation (Eq. 8). Thus, nuclei with high gyromagnetic ratios will provide highest sensitivity in NMR experiments.

$$\frac{N_\beta}{N_\alpha} = e^{\frac{-\Delta E}{kT}} = e^{\frac{-h v_0}{kT}}$$

Eq. 8

Interaction types

If more than one type of NMR active spin is present, these spins will influence each other. The strongest interaction between different spin pools I and S are homonuclear (e.g. ^{13}C-^{13}C) and heteronuclear (^{1}H-^{13}C) dipolar couplings. These result from interactions of the local magnetic fields of the two spin systems. The dipolar coupling depends on the distance between I and S as well as on the magnetic permeability constant μ_0. The dipolar coupling constant is defined by

$$v_D = -\frac{\mu_0}{4\pi} \cdot \frac{\gamma_I \gamma_S \hbar}{r_{IS}^3} \qquad in \ [\frac{rad}{s}]$$

Eq. 9,

where $\hbar$ is Planck's constant h divided by 2π.

Consequently, dipolar couplings are very powerful indicator dependent on the three-dimensional environment of a given nucleus. With the use of specifically designed NMR pulse sequences, they enable measurements of distance restraints and are a major source of information for calculation of molecular structures. Nevertheless, due to their strength dipolar couplings also hamper resolution and in many NMR experiments they have to be overcome by specific radio frequency (RF) decoupling schemes. While in solution NMR dipolar couplings are largely averaged by the intrinsic molecular tumbling, Magic-angle spinning solid-state NMR (MAS ssNMR) uses fast rotation to average these anisotropic interactions.

The scalar *J-coupling* results from spin interactions of different nuclei via shared electron pairs. It is rather small but an important analysis parameter in solution NMR of small molecules. In ssNMR, J-couplings have been used for spectral editing[59] and are increasingly exploited for solution NMR like assignment experiments[60,61].

Any interaction that modifies the electronic environment of a nucleus will influence its exact nutation frequency or *chemical shift*. This includes covalent and ionic bonds, H-bridges, van-der-Walls interactions, solvent effects, pH and many more. The chemical shift is defined in respect to a reference substance, which for ^{1}H and ^{13}C in solution NMR is usually tetramethylsilan (TMS) or the less pH sensitive 4,4-dimethyl-4-silapentane-1-sulfonic acid (DSS).

$$\delta = 10^6 \, \frac{\nu - \nu_{Reference}}{\nu_{Reference}} \, [ppm] \qquad \text{Eq. 10}$$

This definition is independent of the magnetic field strength. The *primary chemical shift* is an intrinsic characteristic for a chemical group, resulting from the chemical structure of a molecule (i.e. from nearby electronegative groups like oxygen or aromatic bonding in a ring). For instance, C_α nuclei in a protein resonate between 45 and 65 ppm while CO groups show signals from 170 to 190 ppm[62]. On top of the primary chemical shift, the three-dimensional environment of a group results in the *secondary chemical shift*. This can be used to distinguish folded versus unfolded regions in proteins and define secondary structure elements[63,64].

Additionally, spins with I=1 possess a quadrupolar moment eQ. Here, the *quadrupolar coupling* leads to interaction of the quadrupolar moment with small electric field gradients that result from asymmetrically distributed electrons around the nucleus. The most frequently used spin 1 nucleus is deuterium, which has a very large quadrupolar coupling constant. The typical interaction types observed by NMR are listed in Table 3.

Table 3: Possible interactions of NMR active nuclei and linewidth[65]

Interaction type	Origin	Linewidth
Zeeman interaction	External B_0 field	$10^6 - 10^9$
Dipolar coupling	Other spins (coupling through space)	$10 - 10^5$
J-coupling	Other spins (coupling through bonds)	$0 - 10^4$
Chemical shift	Small internal magnetic fields, induced by electrons	$10 - 10^5$
Quadrupolar coupling	Quadrupolar moment	$0 - 10^9$

2.2.1.2   *Experimental background*

NMR experiments exploit the ability to interact with mixtures of NMR spins (e.g. a protein sample) via applied radiofrequency pulses. As a simple example, a pulse perpendicular to the B_0 field (RF pulse in B_1) rotates the spins from the z-axis into the XY plane. When the frequency of the RF pulse equals the Lamor frequency of the nucleus of interest, the effects on the spin precession add up and modify the angle between the magnetic moment and the precession axes. The precessing spins induce a current in the surrounding RF coil, which can be measured as a FID (Free Induction Decay) and converted from the time to the frequency domain by Fourier transformation[66]. The longer the FID continues, the sharper the signal in the spectrum will be.

In absence of an RF pulse the excited spins relax back to equilibrium from the M_{XY} plane into the direction of the B_0 axis. Two main processes define this relaxation behavior: the longitudinal spin-lattice (T_1) and the transverse spin-spin (T_2) relaxation.

T_1 describes the time for recovery of the M_Z component and is influenced by the surrounding spin lattice structure, as the spins spread their energy within this lattice upon relaxation. As the M_z magnetization is the initial source of polarization for an NMR experiment, the T_1 time governs how quickly experimental pulses can be applied after each other. Thus it defines the maximum possible repetition rate of an NMR experiment, meaning that short T_1 times enable faster signal acquisition.

T_2 defines the decay of the M_{XY} component (loss of coherence), which can be equal to T_1 for small molecules in solution. For larger molecules and proteins, T_2 is shorter than the T_1 recovery. The T_2 time is affected by changes in the apparent magnetic environment of a spin. These can result from field inhomogeneity of the NMR magnet or field inhomogeneity induced by homo- and heteronuclear interactions (couplings) between different spins. From the half-maximal line width $\Delta v_{1/2}$ of an NMR signal, a combined T_2^* time can be calculated, which has contributions both from T_2(field inhomogeneity resulting from spin-spin interactions) and T_2(field inhomogeneity of B_0):

$$\frac{1}{T_2^*} = \frac{1}{T_{2(coupling)}} + \frac{1}{T_{(B_0 inhom)}} \qquad\qquad \text{Eq. 11.}$$

Together, these components lead to loss of phase coherence of the excited spins. The B_0 field inhomogeneity has a stronger impact on T_2 on high-γ compared to low-γ nuclei but can be compensated by induction of additional small magnets (*shimming*). In solution, the remaining T_2 is mainly determined by the molecular correlation time τ_c that describes the interval a molecule needs for rotation of one radian. The larger the molecule, the longer τ_c will be, as visualized by a figure from the openly accessible NMR website by H.J. Reich at the University of Wisconsin (Figure 4)[67-69].
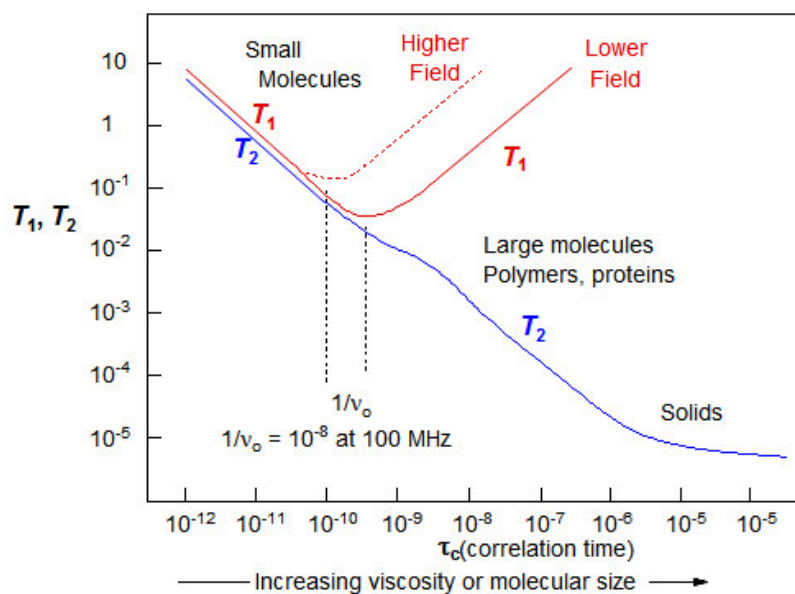
Figure 4: The behavior of T_1 and T_2 as a function of correlation time. τ is the molecular correlation time. The figure was taken from the publically available NMR website by H.J. Reich[67].

Another way to express this is with the use of relaxation rates:

$$R_2 = \frac{1}{T_2} \; [Hz] \qquad\qquad \text{Eq. 12}$$

$$R_2^* = R_2 + R_{2(B_0 inhom)} \qquad\qquad \text{Eq. 13}$$

As field inhomogeneities of modern NMR magnets have become as low as 1 Hz, the minimum $\Delta\nu_{1/2}$ of an NMR signal is governed by $T_{2\,(coupling)}$ [58].

For a Laurentzian signal lineshape, the homogeneous linewidth related to the spin-coupling can be calculated from:

$$\Delta\nu_{1/2} = \frac{R_2}{\pi} \qquad\qquad \text{Eq. 14}$$

Table 4: Relation of molecular weight and NMR line width[68]

Molecular weight (Da)	Typical T_2	Minimum $\Delta\nu_{1/2}$ (Hz)
100	1.3 s	0.13
1,000	200 ms	0.80
10,000	50ms	3.2
100,000	5 ms	32

2.2.2   Selected methods for high-resolution ssNMR

In principle, detection of high-γ nuclei like protons is beneficial for NMR experiments, due to higher initial polarization and thus greater sensitivity. On the other hand, larger dipolar coupling leads to anisotropies that heavily affect spectral resolution and therefore require more complex decoupling efforts. ^{15}N and ^{13}C are of low natural abundance and have to be enriched artificially for NMR experiments, whereas ^{1}H is the dominant isotope of hydrogen (99.98 %). While ^{1}H-^{13}C couplings are on the order ~20-60 kHz, homonuclear ^{1}H-^{1}H coupling can be extremely strong (>100 kHz).

Magic Angle Spinning (MAS) NMR

In solution NMR, fast molecular tumbling leads to efficient averaging of anisotropic interactions. In the solid state, the molecules lack free rotation and physical spinning (*Magic angle spinning*) of the sample is required to average anisotropic interactions and reduce the resulting line broadening. As can be seen from Eq. 15, the Hamiltonian for interactions by dipolar coupling depends on the spinning angle with respect to the B_0 field.

$$H_D = -d(3cos^2\Theta - 1)\, I_Z S_Z \qquad\qquad \text{Eq. 15}$$

$$3cos^2(\Theta) - 1 = 0 \qquad \text{when } \Theta = 54.74° \qquad \text{Eq. 16}$$

Thus, at an angle of Θ = 54.74° (*magic angle* Θ) with a spinning rate equal or higher than the dipolar linewidth, the dipolar coupling and the chemical shift anisotropy term are averaged out.
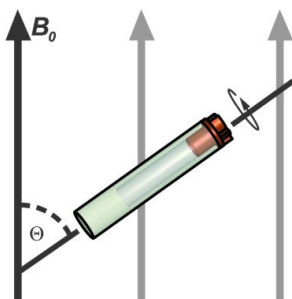
Figure 5: Schematic illustration of a solid-state NMR rotor spinning at the magic angle θ with respect to the B$_0$ field (figure prepared in collaboration with Dr. M. Hiller, 2014).

MAS ssNMR with high power decoupling is able to overcome heteronuclear dipolar interactions of heavier nuclei with protons (e.g. ^{1}H-^{13}C). With the recent developments in NMR hardware like probe heads that are capable of spinning frequencies up to 100 kHz, low power proton decoupling (e.g. Waltz16) is often sufficient and helps to reduce radio frequency induced sample heating[70,71]. However,

to fully overcome the homonuclear dipolar coupling of protons, MAS frequencies of several hundreds of kHz would be necessary.

Isotopic dilution, proton detection and multidimensionality

As the strength of the dipolar coupling declines with the distance between the coupled spins (see eq. 1.9), another approach to reduce its spectroscopic impact is *isotopic dilution*, achieved by mixing the desired nuclei with less strongly coupled isotopes (i.e. $^{13}C/^{12}C$ or $^{1}H/^{2}H$). For protons, this is achieved by expression of proteins in deuterated media, in combination with the use of specifically protonated carbon precursors. To obtain defined protonation/deuteration (H/D) ratios, backexchange of protons at exchangeable sites may follow during the subsequent purification steps. For many years solid-state NMR experiments have mostly been based on detection of ^{13}C and ^{15}N. While with fully protonated proteins, MAS spinning rates of several hundred kHz would be necessary to mitigate the line broadening caused by ^{1}H dipolar couplings, the use of perdeuterated proteins has enabled *proton detection* in two- and three-dimensional solid-state NMR experiments also at moderate spinning rates as low as 13 and 14 kHz, respectively[60,72]. Sensitivity could be increased by a factor of 14 compared to experiments employing carbon detection. Akbey *et al.* investigated the optimal H/D ratio at exchangeable sites (mainly amide protons) and found a ratio around 30:70 % to give optimal signal-to-noise (S/N) for the model protein α-spectrin Src-homology 3 (SH3) at 20 kHz MAS[73]. The introduction of protons as a third independent detection dimension now greatly facilitates resonance assignments in solid-state NMR as it helps to resolve the signal overlap often observed in standard ^{13}C-detected MAS 2 and 3D spectra.

Proton-detected assignment experiments

Since direct excitation of low-γ nuclei like ^{13}C and ^{15}N can be inefficient because of their low spin polarization and long T_1 times, crosspolarization (CP) from high-γ nuclei has become a general principle in many solid-state NMR pulse sequences. During the Hartmann-Hahn match condition (Eq. 17) the excitation of one nucleus can be efficiently transferred to a second nucleus. By further using optimized magnetization transfers like the adiabatic ^{RESPIRATION}CP, the CP efficiency can be improved substantially[74].

$$\gamma_H B_1(H) = \gamma_C B_1(C)$$
<div align="right">Eq. 17</div>

While CP-derived pulse sequences deliver through-space correlations, through-bond correlations have recently been accessed via solution NMR-like ^{1}H-detected experiments exploiting INEPT (<u>I</u>nsensitive <u>N</u>uclei <u>E</u>nhanced by <u>P</u>olarization <u>T</u>ransfer) transfers[60]: 3D experiments (hCaNH, hCaCbNH and hCoNH) were used to correlate solely covalently bonded atoms for assignment of SH3. This was followed by another series of proton-detected correlation experiments introduced by Zhou *et al.* which

also provides unambiguous correlations to connect exclusively either intra- or interresidue carbons (Figure 6)[61]. All these experiments now offer an invaluable alternative to ^{13}C-detected PDSD, DARR and 3D NCACX or NCOCX experiments which have been successfully used for many systems but often suffer from poor sensitivity and resolution.
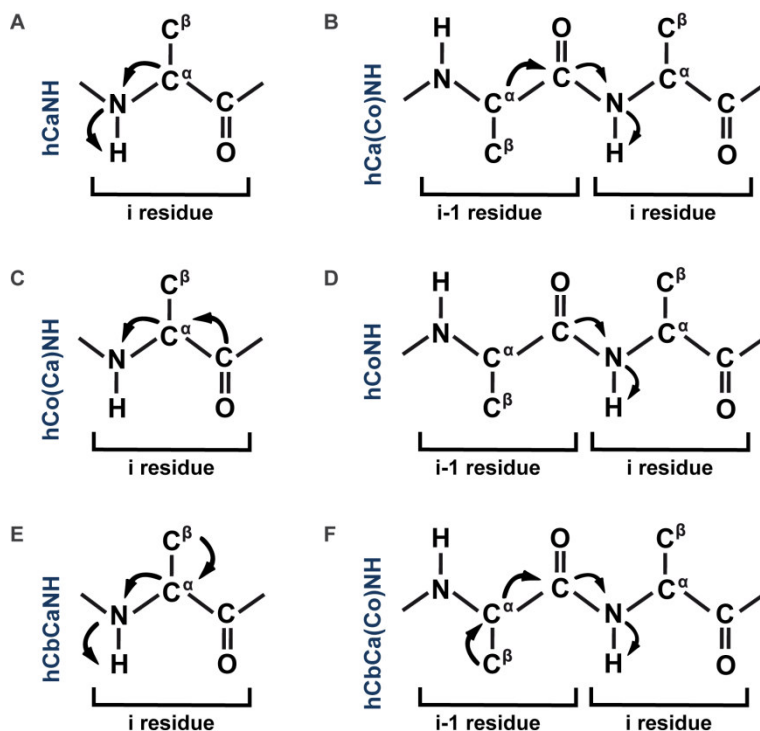
Figure 6: Triple-resonance experiments for backbone assignments in solid-state NMR. The first CP step from protons to the initial carbon is not shown. Experiments **A**, **C** and **E** result in intramolecular assignments while **B**, **D** and **F** provide interresidue connectivities (figure adapted from Zhou et al. (2012)[61]).

Deuterium crosspolarization

In the context of extensive protein deuteration, another novel approach for excitation of low γ-nuclei in biopolymers was developed using excitation transfer from the quadrupolar deuterium nucleus[75,76]. This method requires MAS NMR probe heads with an additional independent deuterium channel or a nitrogen channel that can be tuned to the deuterium frequency. High-resolution [2]H-^{13}C correlation spectra with assignments have been obtained on SH3, ubiquitin and the membrane protein OmpG[53,75,77].

2.2.3   MAS ssNMR of biomolecules in native environments

The size and complexity of biomolecules studied by oriented-sample NMR and MAS ssNMR, has increased tremendously. Starting with small peptides in the late 1990ies, structures for the SH3 domain, chaperones like alphaB crystallin, fibrillar systems like HET-s and amyloid β (Aβ) up to large molecular assemblies like the type III secretion needle have now been published[78-82]. While fibrillar systems, that are hard to assess with other structural methods, were one of the main targets of ssNMR, the field of interest now expands towards membrane proteins in lipid bilayers and large multiprotein complexes[83-85]. In March 2014, of the 76 structures in the pdb that were solved by, or with large contributions from, solid-state NMR, 10 structures describe fibrillar systems, while 17 structures are of α-helical membrane proteins including channels, GPCRs and other heptahelical receptors[86-88]. Interestingly, the ssNMR structure of Anabena sensory rhodopsin (ASR) solved in model lipids showed a trimeric organization that was similar to bacteriorhodopsin but distinct from the dimeric crystal structure of ASR[88]. The structure of the transmembrane domain of the trimeric beta-barrel autotransporter YadA was solved from experiments taken of a single microcrystalline NMR sample. This structure led to the proposal of a refined model for the cell adhesion mechanism by Yersinia enterocolitica, a widespread gram-negative enterobacterium responsible for severe enteritis and diarrhea in mammals and humans[37]. A summary of recent solid-state NMR structures is given in Figure 7.

Generally, for membrane proteins it becomes evident that the lipid environment affects the structures themselves as well as their oligomeric arrangements[88]. When comparing the structural organization of the M2 proton channel studied by X-ray, solution and ssNMR in different environments involving diverse membrane mimetics and varying pH, it is obvious that the differences seen are often related to the experimental set-ups[89,90]. Thus, care has to be taken when interpreting these results in the sense of biological functions or even mechanisms. Here, ssNMR offers a great opportunity to tackle membrane proteins at a close to native level.
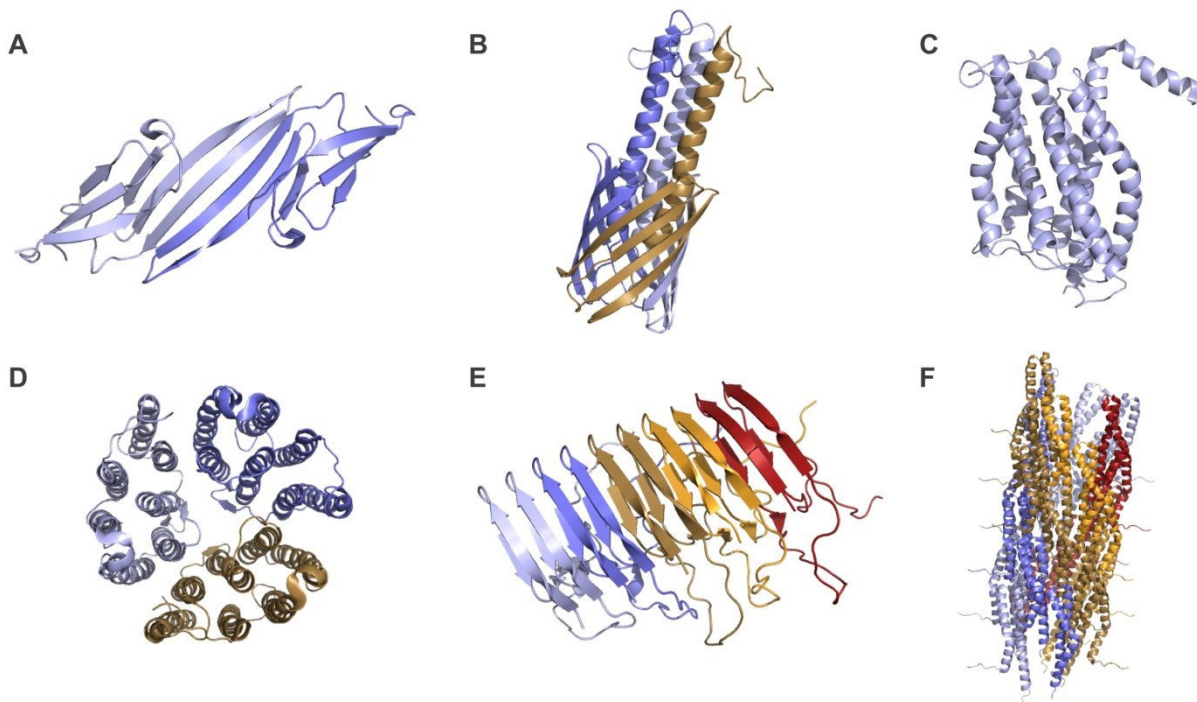
Figure 7: Examples for larger proteins and complexes solved by or with contributions from solid-state NMR. A dimer of the eye lense chaperone alphaB crystallin (2KLR, 2010) **B** trimeric YadA autotransporter of Yersinia enterocolitica (2LME, 2012) **C** heptahelical CXCR1 receptor (2LNL, 2012) **D** trimeric form of the Anabena sensory rhodopsin ASR (2M3G, 2013) **E** HET-s fibril (2LBU, 2011) **F** Type III secretion needle (2LPZ, 2012)

2.2.4 Expression and labeling of transmembrane proteins for NMR studies

Although with higher MAS frequencies and smaller rotor sizes in ssNMR, the required amount of protein has decreased, the hunt for the ideal expression set-up is still a tough one. Many variables need to be optimized including the expression construct, the vector, the expression host and the purification scheme to preserve protein activity. Cost-efficient isotopically labeling is an additional challenge, as expression rates and protein stability might decrease substantially.

Expression hosts

E. coli still is the expression host of choice and frequently is satisfactory for TM proteins of bacterial origin. *E. coli* strains are well tunable in terms of enzyme and tRNA composition, provide easy but sophisticated genetic manipulation tools and can be cultivated in scalable fermenters[91]. This upscaling in turn provides easy measures for comparing effects of pH, inducer concentration, oxygen supply and temperature on protein expression levels. An alternative gram-positive organism successfully used for membrane protein expression is *L. lactis*, which is able to grow under anaerobic high-cell density conditions and provides a tightly controlled induction system[92]. Other proteins require eukaryotic organisms like *S. cerevisea* (Baker's yeast) and *P. pastoris* as expression hosts, as these provide a more sophisticated folding machinery and the possibility of posttranslational modifications (PTM) like glycosylation[93]. Sf9 insect cells and mammalian cell lines like CHO and HEK293 have also been used for expression of labeled membrane proteins, but often suffer from very low protein yield[94,95]. As media requirements for these organisms are rather complex, protein samples prepared this way can be extremely expensive. An alternative, especially for proteins that show toxicity effects during expression, is cell-free expression using, for example, extracts of wheat germs[96].

The optimal DNA construct

The expression construct needs to include all necessary domain borders for proper folding and subsequent stability of the protein. Additionally, cleavable purification tags like MBP (maltose-binding protein) and GST (glutathione S-transferase) can be used, that might also serve to increase the solubility in some cases[97]. A smart strategy to ensure proper folding is the use of a GFP tag that is only fluorescent in the correctly folded state[98,99]. If yields are high enough to be detected from the culture medium in a multiwell-plate reader with a corresponding filter, this can greatly simplify screening for optimal expression conditions. In case of strongly different codon usage between source and target organism, codon optimization of the target gene can also help to raise expression yields.

Vectors for expression in prokaryotes

Amongst the most common expression vectors is the pET vector system which exists in a large variety of combinations of different antibiotic resistance genes, solubility and affinity tags. This system relies on the strong IPTG inducible T7 promotor ensuring a rapid start of target protein synthesis. Especially for membrane proteins, fast expression sometimes causes problems, as folding and membrane insertion cannot be realized correctly for the large amounts of recombinantly expressed protein. This often results in enrichment of partially unfolded protein deposited in inclusion bodies. Using a weaker promotor, e.g. the T5 promotor, or decreasing the expression temperature can help to circumvent these problems.

   A combination of an expression vector carrying the modified target gene in a ACA-free form and a plasmid providing an RNase, which specifically cleaves ACA-containing RNA of the host, has recently been successfully used for production of different membrane proteins[100-102]. This condensed Single Protein Production (cSPP) approach enables concentration of the expression cultures by up to 1/40 while the target protein yield stays constant (Figure 8).
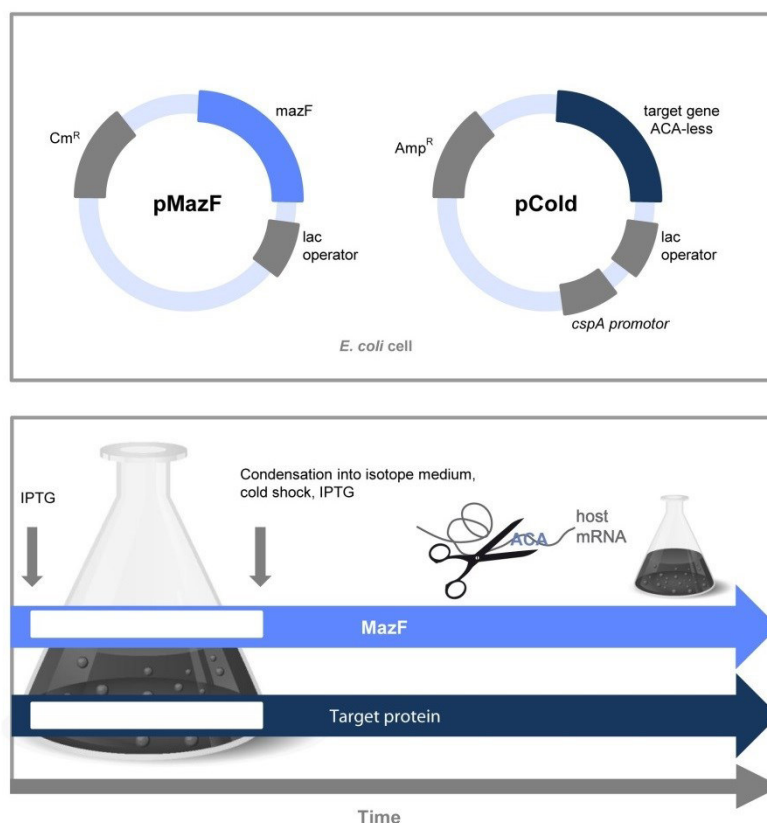
Figure 8: Condensed Single Protein Production using the pMazF and pCold vectors. Expression of the RNase MazF is induced by addition of IPTG before concentration of the precultures into a reduced volume of minimal medium containing the carbon and nitrogen sources for labeling of the target protein. While MazF cleaves intrinsic host RNA and leads to a quasi-dormancy of the cell, the engineered ACA-free mRNA of the target protein gets enriched which enables significantly increased expression yields for the target protein.

Membrane protein purification

Membrane protein isolation and purification is more expensive and time-consuming compared to soluble proteins. After separation of the membrane fraction by gradual centrifugation, TM proteins can be extracted with a variety of non-ionic or zwitter-ionic detergents. All of these have different critical micellar concentrations which is important for subsequent preparation steps like detergent exchange or removal. Also solubilization capacities and effect on protein function will vary and should be screened to obtain highest yields of functional protein. After solubilization, in most cases affinity chromatography followed by gel filtration is performed for maximum purity.

Protein labeling with NMR active isotopes

Of course, the abovementioned considerations are important for expression of membrane proteins in general. Labeling with NMR active isotopes is mainly a financial aspect and expression optimization is a perquisite for cost-effective structural studies. Unfortunately, protein yields are often affected especially when labeling with deuterated carbon precursors and D_2O. For uniformly labeled proteins, the use of deuterated glucose as sole carbon source in expression cultures based on D_2O sometimes reduces protein yield to 1/5 or lower compared to unlabeled set-ups. This can also be a side effect of 2-^{13}C- or 1,3-^{13}C-glycerol labeling, which reduces the number of labeled ^{13}C atoms in the protein and thus leads to increased resolution in NMR spectra[78]. Specific labeling of amino acid types is also possible, when scrambling (spreading of isotopes to other amino acids with related biochemical pathways) is sufficiently prohibited by blocking the specific biosynthetic pathways. A scheme known as *ILV* (isoleucine/leucine/valine) labeling has become extremely valuable for of determination of distance restrains for structural investigations[103].

2.3   ABC transporters - small machines with big impact

2.3.1   Physiological roles of ABC transporters

ATP-binding cassette (ABC) transporters are TM proteins with diverse physiological and pathophysiological roles found in all three kingdoms of life. They couple hydrolysis of ATP to the transport of a single specific ligand or in some cases even a variety of structurally different substrates across cellular membranes[104]. Depending on the direction of transport, ABC transporters are classified as export and import systems and further categorized into eight subgroups according to their cellular functions (ABC-A to ABC-H).

Numerous ABC transporters share vital roles in healthy tissue, keeping intracellular concentrations of toxic compounds to a minimum, thus maintaining e.g. the blood-brain and the placental barrier[105,106]. They are also involved in membrane buildup and lipid transport. Defects in ABCA1 lead to Tangier disease while mutations in ABCA4 cause Stargardt macular degeneration of the retina[107]. The TAP1/2 antigen peptide transporter is part of the adaptive immune system and shuttles peptide fragments into the endoplasmic reticulum for presentation on MHC I complexes and subsequent activation of cytotoxic CD8+ T-lymphocytes[108]. In patients with bare lymphocyte syndrome 1 (BLS1), the TAP allele exhibits a point mutation causing a pre-mature stop in translation. The resulting nonfunctional complex has been associated with chronic alteration and infections of the upper respiratory tract[109]. In virus infections and tumor cells, TAP is specifically blocked by viral proteins or downregulated in expression profiles, in both cases leading to an immune escape mechanism of the diseased cell[110-112]. ABC proteins of the ABC-E & and ABC-F family lack the transport domain and are involved in DNA repair and diverse cellular house-keeping functions[113].

Due to their essential physiological functions, ABC transporters also account for many pharmacological difficulties. In endemic parasites like *Leishmania* and *Schistosoma*, ABC exporters are frequently responsible for failure of anti-infective treatments[114]. In humans, the exporters P-glycoprotein (ABCB1), multi-drug resistance protein 1 (MDR1, ABCC1) and breast-cancer resistance protein (BCRP, ABCG2) have been linked to ineffective chemotherapy for various cancers, as they remove xenobiotic drugs from the cytoplasm[105]. In bacteria and yeast, the export systems SP2073/75 from *Streptococcus pneumoniae* and Cdr1p from *Candida albicans* have also been associated with drug resistance which may lead to severe infections especially in immunocompromised patients[115-117].

ABC importers, in contrast to exporters, are unique to prokaryotes and plants and perform uptake of nutrients like sugars, amino acids, ions and vitamins[118,119]. Because of their essential functions in cell homeostasis, many importers are crucial for bacterial virulence and have thus been suggested as potential targets for new treatments and vaccines[120-122].

2.3.2   ABC transporter modularization

The core structure of ABC transporters is formed by a translocation pore comprised of a homo- or heterodimer of transmembrane domains (TMDs) and an energizing unit formed by two nucleotide-binding domains (NBDs). Import systems additionally interact with an extracellular substrate-binding protein (SBP) which captures the substrate from the environment and delivers it to the transmembrane region of the transporter[118]. The subdomains occur both as single polypeptide chains (e.g. Maltose transporter from *E. coli*) and in fused forms where both TMDs or NBDs are linked as in the iron-chelate transporter FhuBC-D and the ribose transporter RbsAC-B, respectively (Figure 9)[123]. In half-transporters like BmrA and LmrA, one TMD is fused to its corresponding NBD whereas in full-transporters like P-glycoprotein all subunits are part of a single polypeptide chain. ABC transporters NBDs may also include regulatory domains or interact with additional inhibitory proteins leading to a complex and tight regulation of substrate transport and ATP consumption[124-126]. The related bacterial ECF (energy-coupling factor) transporters also contain two ATP-binding cassettes and one TMD interacting with a transmembrane substrate-capture protein (S-component) that makes the ECF-type transporters function independently of an additional SBP[127]. Although grouped into the same class of primary active transporters, large differences in the subdomain structures of ABC transporters exist, as discussed in the following section.
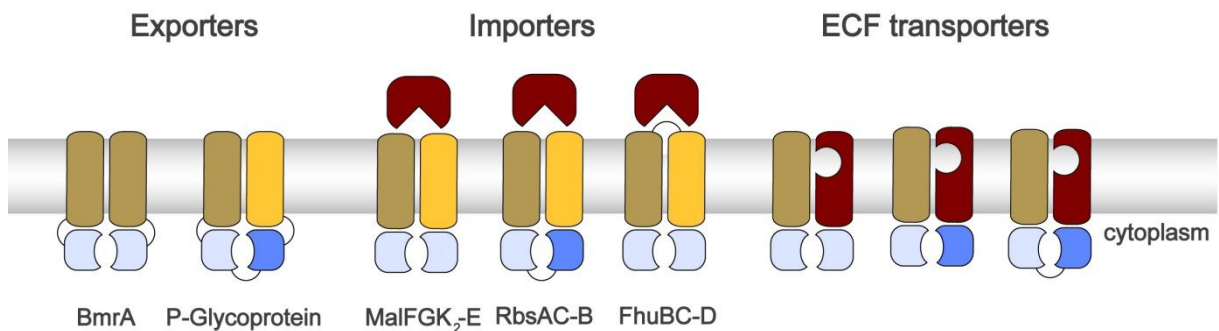
Figure 9: Domain arrangement in ABC exporters, importers and the related ECF transporters. Homo- and heterodimers of NBDs (light and dark blue) and TMDs (brown and yellow) specifically assemble to functional ABC transporters. The single domains can be linked covalently as shown for the half transporter BmrA, the full transporter P-Glycoprotein, the RbsAC-B importer and some ECF transporters. Importers rely on an extracellular SBP (red) while in case of ECF transporters one TMD assembles with an S-component to capture and translocate substrates.

2.3.2.1   *Substrate binding proteins in bacteria and archaea*

Since their discovery in the 1960ies[128], studies on SBPs (also referred to as solute receptors) from bacteria and archaea have yielded detailed structural and biochemical data about binding modes and affinities. Some SBPs are highly specific for their substrates as observed for the cysteine receptor Ng0214 and the cystin receptor Ng0372[122], whereas others like LivJ (*E.coli*; L-leucine, L-isoleucine, L-valine), ModA (*E. coli/ A. fulgidus*; molybdate, tungsten) and MalE (*E. coli*; oligosaccharides) bind a variety of related structures with different affinities (Figure 10)[129]. While in gram-positive bacteria such as *B. subtilis* and in archaea, SBPs are lipid-anchored to the cytoplasmic membrane by an N-terminal lipid moiety or a small lipophilic helix[130-134], they exist as soluble proteins in the periplasm of gram-negative bacteria such as *E. coli*.
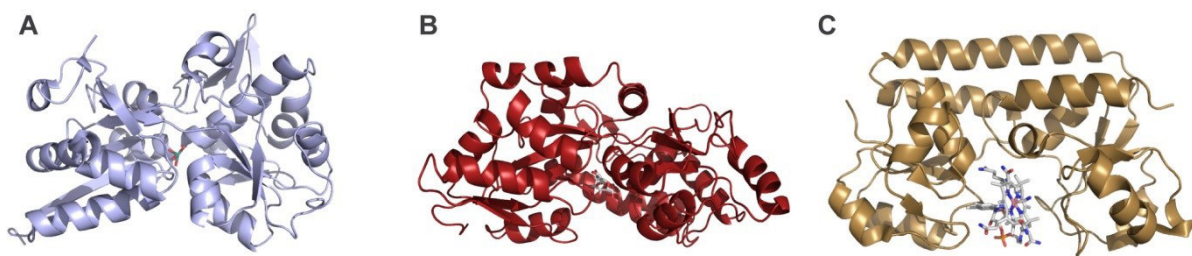
Figure 10: SBPs of different bacterial origin and specifities for small and larger molecules. **A** ModA from *Archaeoglobus fulgidus* with molybdate (cluster F/II, 2ONR) **B** MalE from *E. coli* with maltose, cluster (B/I, 1ANF) **C** BtuF from *E. coli* with vitamin B12 (cluster A/III, 1N4A)

In some cases, one or more copies of the SBP are covalently linked to the transmembrane domains of the transporter[135]. Over 120 unique structures of SBPs that greatly vary in aa sequence and size, have been solved to high resolution which in 2010 led to an extensive reclassification of SBPs into six main clusters (A-F) considering the details of the 3D structures[129]. Nevertheless, these proteins still exhibit three common features that include the existence of i) two globular domains (N- and C-lobe) linked by a groove region, which ii) bind the ligand in an engulfed way by iii) a large 'hinge-bending' motion. The underlying process is often referred to as a venus fly-trap mechanism as the substrate is captured by an open conformation of the protein that subsequently condenses to a tightly closed structure with the ligand occluded in the interior (Figure 11)[136-138].
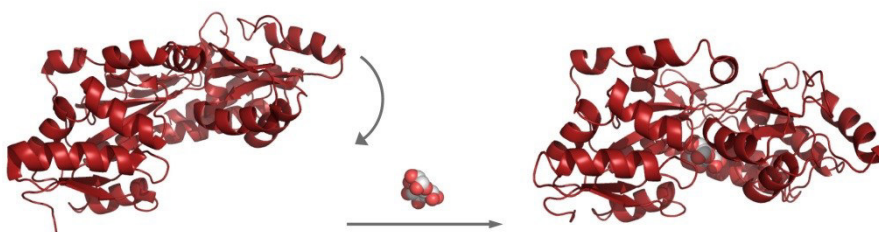
Figure 11: Example for the fly-trap mechanism for substrate binding by SBPs. Ligand-free MalE (1OMP) forms a condensed structure upon binding of maltose or related sugars (1ANF).

2.3.2.2 *Nucleotide-binding domains - the energizing units of ABC transporters*

In contrast to the SBPs, the NBDs harboring the ATP-binding cassette exhibit fairly high amino acid sequence homology (about 30 %) and their DNA sequences belong to the most conserved classes in bacteria, eukarya and archaea[139]. Lobe I of the bilobal NBD consists of a catalytic core domain similar to RecA-ATPases which is composed of six β-strands and two α-helices. The second lobe comprises a small α-helical subdomain (3-4 helices) which is unique to ABC transporters. The common features necessary for hydrolysis of ATP are the Walker A (GxxGxGKS/T) and B (ΦΦΦDE) motifs (x: any amino acid Φ: aliphatic amino acid) located in the catalytic core domain and the ABC signature motif (LSGGQ), which is part of the small α-helical domain[140]. For ATP hydrolysis, two NBDs dimerize in a head-to-tail fashion, sandwiching two ATP molecules at the interface between the Walker A motif of one and the ABC signature of the other NBD[141-144]. Figure 12 shows the dimeric and monomeric NBD MalK of the *E. coli* maltose transporter indicating the orientation of typical ABC transporter motifs.
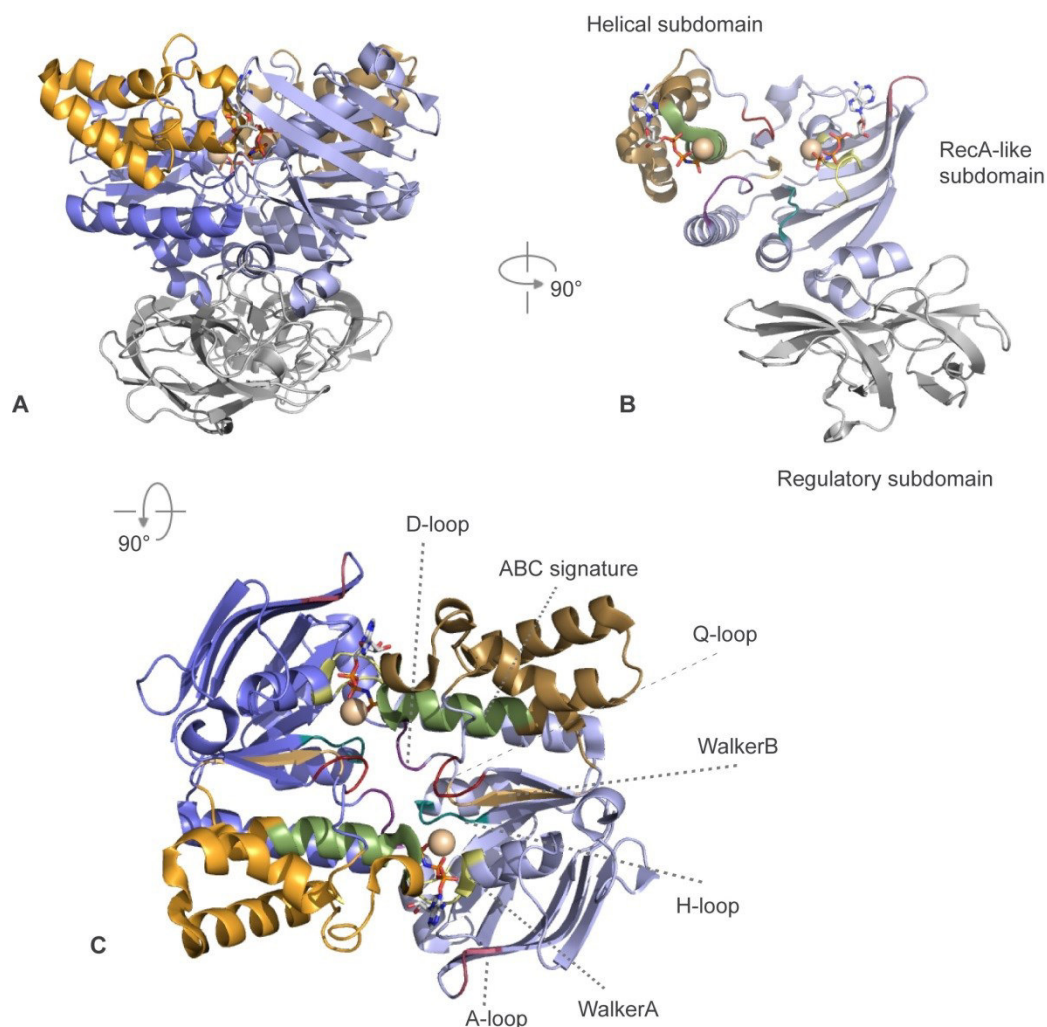
Figure 12: NBD dimer of MalK in the full Maltose transporter structure (3RLF). A MalK dimer with the ATP analog AMPPNP/Mg^{2+} **B** MalK monomer with subdomains indicated **C** NBD dimer arrangement in MalK2FG-E as seen from the transmission interface to the TMDs (the regulatory domain was omitted for better visibility of the relevant motifs).

Additional features in the RecA subdomain have been identified that either take part in the hydrolysis mechanism itself or support nucleotide binding and catalysis by providing extensive bonding networks. A conserved aromatic residue (tyrosine or phenylalanine) in a loop region (A-loop, for aromatic) assists in positioning the nucleotide in the binding pocket for hydrolysis by π-stacking against the adenine-ring of ATP[145]. The Walker A motif (also called P-loop for phosphate-binding loop) binds both directly and indirectly – by the coordination of a Mg^{2+} ion – to the β- and γ-phosphates (mainly accomplished by the invariant K residue)[140,146]. The Walker B motif has direct catalytic impact. Its C-terminal aspartate is hydrogen-bonded to the Mg^{2+} while the neighboring highly conserved glutamate acts as a general base as recently observed in crystal structures from Oldham *et al.*[140,146-149]. The N-terminal glutamine of the Q-loop, a stretch of about eight amino acids bridging the catalytic to the small α -helical subdomain, was also shown to interact with the Mg^{2+} ion directing a positive charge towards the γ-phosphate of the nucleotide[146,150]. In P-glycoprotein, mutation of this conserved glutamine resulted in reduction of the basal ATPase activity and led to the conclusion that the Q-loop may play an important role in interdomain-communication with the TMDs[149-151]. During the hydrolysis cycle, the Q-loop is suggested to move in and out of the binding pocket upon ATP binding and release of ADP and P$_i$. This would result in a concerted movement of the small α -helical domain leading to a more tightly packed conformation within the NBD monomer in the ATP-bound state. The ABC signature in the α-helical subdomain seems necessary for completion of the active site, also directing a positive charge towards the γ-phosphate[146,150]. Here, especially the serine sidechain and the second glycine proved relevant for ATP hydrolysis[152,153]. Ye *et al.* suggested that this motif could resemble the arginine finger found in RecA ATPases[154]. The D-loop, named after a conserved aspartate in the SALD consensus sequence, might also represent a structural correlate to a conserved switch region found in other ATPases like G proteins and myosin[150]. Since the D-loop and the Walker B motif are separated by only two amino acids, their 3D geometries which change in the presence of nucleotide will strongly influence each other. In the intact hydrolysis-competent NBD dimer, the D-loops of two monomers are in direct contact and have thus been proposed to be involved in inter-monomer communication between the two catalytic centers[155]. A 'linchpin' role has further been suggested for a loop region harboring a conserved histidine that interacts with the D-loop and the γ-phosphate of the nucleotide (H-loop)[146,150,156]. This histidine residue also proved essential for transport activity in several multi drug resistance proteins including MDR3 (ABCB4)[157].

Many ABC import systems are tightly controlled and harbor additional regulatory domains at the C-termini of their NBDs, as found for the maltose and the methionine transporters of *E. coli* and the

molybdate transporter of *M. acetovorans*[125,158-160]. At high intracellular concentration, the substrate binds to these C2 regulatory domains of the NBDs, locking the transporter in a hydrolysis-incompetent state, inhibiting the transport cycle and limiting wasteful ATP consumption (transinhibition)[124,125,160].

The functional connection to the TMDs of the transporter is accomplished by a transmission interface, a groove region between the RecA-like and small α-helical subdomain in each NBD, which embeds a conserved helix present in the TMDs of all ABC transporters and commonly referred to as the coupling helix (CH)[161]. The Q-loop of the NBD seems to be involved in interactions with the CH in both importers and exporters. Additionally, in bacterial exporters like Sav1866, an interaction motif including the sequence TEVGERV (X-loop) was identified in the NBD whereas in importers residues from two helices of the α-helical subdomain are part of the transmission interface[5,142,143].

2.3.2.3 *Transmembrane domains*

Although the TMDs are highly divergent in terms of sequence, substrate recognition, and structural arrangements of their transmembrane helices (TMH) they exhibit one common feature that ensures interaction with the corresponding NBD: a short α-helix that reaches into a groove formed between the RecA-like and small α-helical subdomains of the NBD monomer[161]. This coupling helix is universally found in import and export systems (CH2), although it is more conserved in terms of structure than in amino acid sequence. Still, in importers a common motif including the residues EAA was identified by Mourez *et al.*[162]. In exporters, a second coupling helix in the TMD (termed CH1) directly binds to regions involved in nucleotide binding in the adjacent NBD[142]. This helix was further suggested to possess a solvent shielding function for the nucleotide and the LSGGQ motif in exporters, but its functional role is still debated[150].

The TM portion of ABC transporters is composed of a homo- or heterodimer of two TMDs building a bundle of ten to twenty TMH in total. Depending on the number of TMH in their core region, importers are grouped into the smaller type I (five to eight TMH per TMD) and the larger type II importers (up to 10 TMH per TMD). Most structurally characterized exporters of bacterial and mammalian origin as well as the TAP1/2 transporter possess six TMH per TMD. In the larger type II importers like BtuCD, the two transmembrane domains build two separate densely packed blocks[150]. In small type I transporters and in exporters the TMHs divide into two wing-like shapes that can contain helices from both TMDs. While in the MetNI importer each TMD exhibits five TMH that form separate bundles, in the maltose and the molybdate transporters there is a sixth helix crossing over to the opposite TMD, holding the bundle together[143]. An important feature of exporters is the length of their TMHs which extend far into the cytoplasm, as seen for the TMH 2-5 of the MsbA exporter. These helices build the so-called intracytoplasmic loops (ICL), possibly involved in substrate recognition. Additionally, in exporters like Sav1866 (2HYD) and P-Glycoprotein (4M1M) domain swapping is observed, as two TMH of one TMD come together with four helices of the other, building two separate wings. These twisted conformations in exporters enable each TMD to interact with both the opposite NBD

via CH1 and the adjacent NBD via CH2. An overview of crystal structures for ABC transporters of different subgroups and at different states in the transport cycle is given in Figure 13.
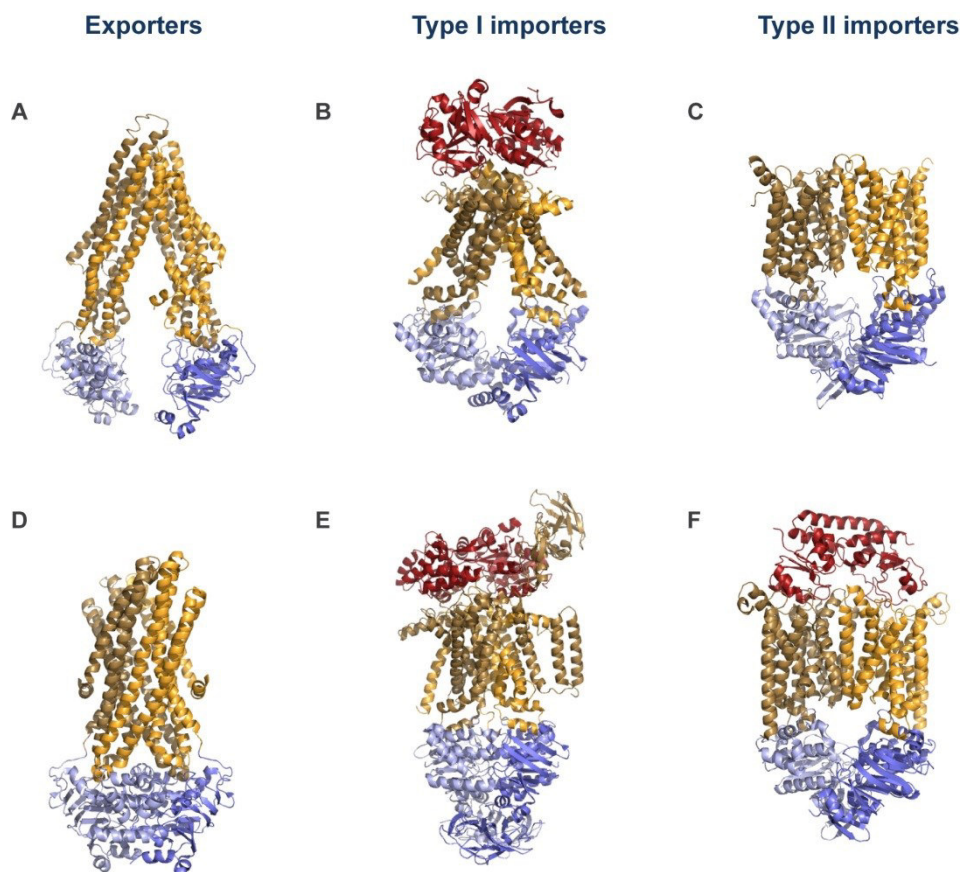
Figure 13: Examples for crystal structures of ABC exporters and importers in different states of the transport cycle. The TMDs are shown in orange and sand, while NBDs are in light and darker blue and the SBP is colored in red. The upper row of structures shows transporters in a conformation that is open towards the cytosol while the second row depicts examples for closed or intermediate states. In the type II importers the helices of the TMDs build two separate blocks. **A** P-glycoprotein from *Mus musculus* (4M1M) **B** ModBC-A from *Archaeoglobus fulgidus* (2ONK) **C** HI1470 from *Haemophilus influenza* (2NQ2) **D** Sav1866 from *Staphylococcus aureus* (2HYD) **E** MalFGK$_2$-E from *E. coli* (2R6G) **F** BtuCD-F from *E. coli* (2QI9)

2.3.3   Models for the translocation mechanism of ABC transporters

Most of the elements necessary for catalysis and interdomain communication are conserved in sequence and/or structure amongst importers and exporters. The '**ATP switch' model** described by Higgins & Linton combines data from both ABC transporter classes, although it seems more descriptive of exporters[163]. In the inward-facing conformation, the nucleotide-free NBDs rest in an 'open dimer' state with the TMDs exposing a high-affinity binding site to the cytoplasm. Binding of the allocrite then triggers conformational changes in the TMDs that transmit to the ATP-binding site resulting in

tight binding of two ATPs and closure of the NBD dimer. This in turn leads to conversion of the transporter to the outward-facing state and turns the allocrite binding site to low affinity releasing the substrate (ATP switch). Consecutive hydrolysis of ATP at the NBDs results in opening of the dimer and release of ADP and P_i, resetting the transporter to the inward-facing conformation.
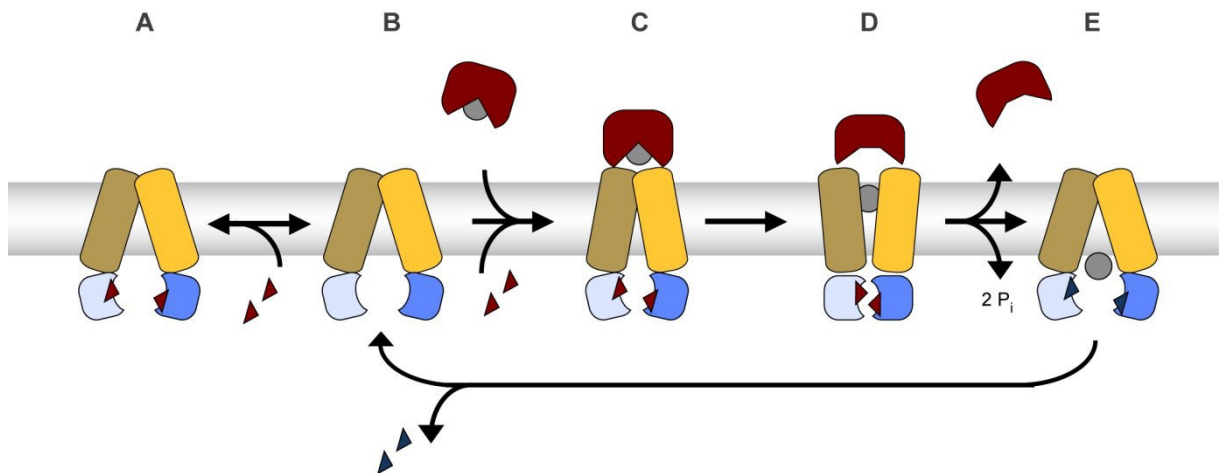
Figure 14: The Alternating Access model as described for the maltose transporter from *E. coli*. ATP (red triangles) can bind to the open conformation of the transporter (A/B). In presence of substrate-loaded SBP ATP binding leads to formation of a pre-translocation complex (C). In the translocation state (D), the NBD dimer is tightly closed around the nucleotides while the TMDs open towards the periplasm and enable release of the substrate from the SBP into the channel of the transporter. Upon hydrolysis of ATP and dissociation of ADP (blue triangles) and P_i the transporter returns to the inward-open conformation (E).

Hollenstein *et al.* also suggested a general mechanism for both transporter subfamilies that is based on Jardetzky's model for membrane pumps published in 1966 (Figure 14)[161,164]. In their **'Alternating Access' model** the transporter rests in an inward-facing ground state, with the NBDs held in an open dimer conformation that is not hydrolysis-competent. Binding of ATP and substrate (exporters) or substrate-loaded SBP (importers) induces a conformational shift of the TMDs from inward- to outward-facing which in turn leads to closure of the NBD dimer and correct positioning of the catalytic motifs around the ATP-binding site. Upon ATP hydrolysis and release of ADP and Pi the NBDs dissociate, resetting the transporter to the inward-facing ground-state. It is further stated that ATP and not the transported substrate is responsible for accessibility of the transporter to the cytoplasm or extracellular space.

But how is ATP hydrolysis precisely linked to shuffling between inward- and outward-facing conformations of ABC transporters? In the **'Processive Clamp' model**, both ATP molecules at the NBD dimer interface are hydrolyzed sequentially to enable full dissociation of the dimer (Figure 15A)[158,165-167]. Although the alternating access model with a processive clamp mechanism is in agreement with X-

ray structures of isolated NBDs and full transporters, it cannot explain all observations from biochemical and biophysical studies. These gaps are partially resolved in the **'Alternating (catalytic) Sites'** **model** put forward by Senior and colleagues, which also has an NBD dimer with two tightly bound ATP molecules as a central state (Figure 15B)[168-172]. Nevertheless, here only one ATP-binding site performs hydrolysis, leading to opening of the dimer at this site and exchange of the hydrolysis products for ATP. After reclosure of the dimer, ATP-hydrolysis takes place at the second, previously unaffected NBS. This again leads to opening of the NBD dimer at this site and exchange of ADP and P_i for ATP. This model is supported by vanadate trapping experiments where vanadate mimics the hydrolysis product P_i and is used in combination with ATP (or the hydrolysis product ADP) to lock the transporter in a NBD-closed transition state. Here, only one nucleotide per NBD dimer could be detected which might hint at a dimer state where one NBD is partially open and allows release of the nucleotide. Although the alternating sites model seems to explain various biochemical and structural results, it is hard to imagine how NBD movements would be coupled to the concerted motions of the TMDs for substrate transport.
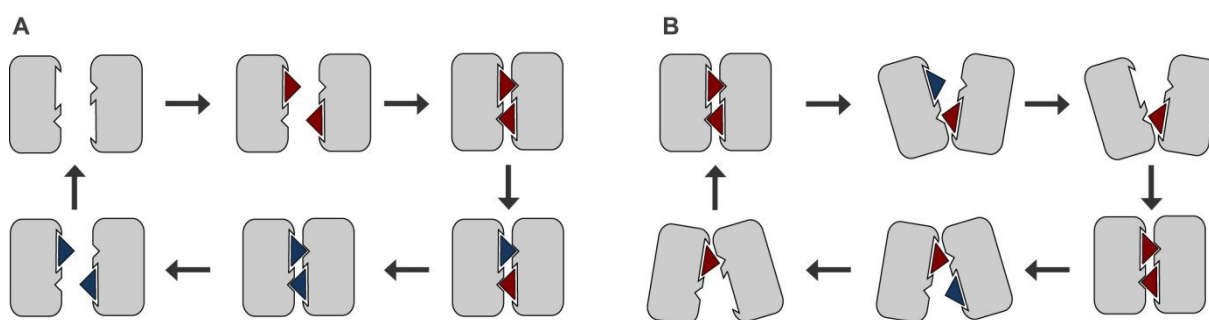
Figure 15: Two opposing models for coupling ATP hydrolysis to opening and closing of the transporter. Conformation of the NBD dimer in the **A** Processive Clamp and the **B** Alternating Sites model (figure based on Van der Does, 2004[167])

Jones and George proposed the related **'Constant Contact' model** and argue that many studies performed in non-native environments might not represent true physiological conditions, referring to crystal structures and EPR data for MsbA but also to the maltose transporter[173]. They state that many of these data could also be explained by a model where complete dissociation of the NBD never occurs. In recent molecular dynamics simulations comparing three different MalFGK$_2$-E states in a DMPC (dimysristoylphosphatidylcholine) lipid environment, dimer dissociation at only one nucleotide binding site was observed in the post-hydrolysis state which had two ADP molecules bound[174]. Nevertheless, it remains unclear if this asymmetry has a functional role or might be the result of limited simulation times. The question of functional asymmetry is still very relevant considering the nature of the NBD dimer which may exist as homodimer with two identical, hydrolysis-competent sites but also as a heterodimer with one impaired catalytic site.

2.3.4 The *E. coli* maltose transporter as a model system for ABC type I function?

Numerous recent crystal structures together with EPR and cross-linking data, point towards the alternate access model as the common mechanism for type I ABC importers[5,118,175-177]. Most of these conclusions come from experiments performed on the maltose transporter system of *E. coli* and have surely been influenced by crystal structures published by Oldham and Chen between 2003 and 2013[126,143,146,158,176-179]. These structures provide snapshots of the catalytic cycle, including an open nucleotide-free state without the SBP MalE as well as the full MalFGK$_2$-E in the ground and transition state (Figure 16). In these structures, the ATP-bound ground state and the transition state – in which ATP is hydrolyzed and the substrate enters the membrane channel – look surprisingly similar. This revived the discussion whether release of the hydrolysis product P$_i$ is in fact what triggers the conformational reset of the transporter from outward- to inward-facing[146,148]. A stereo representation comparing the different maltose transporter structures is given in the appendix (Figure 60).
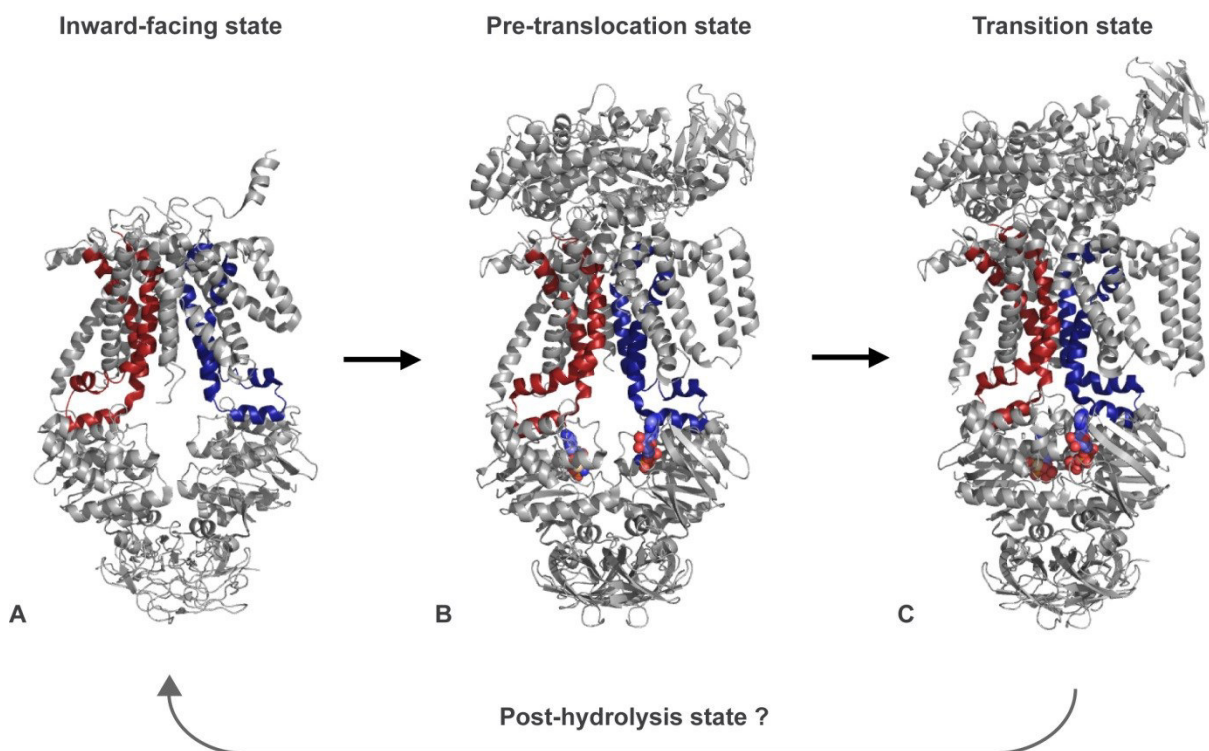
Figure 16: Different states of the maltose transporter during substrate translocation. **A** Open, nucleotide-free state of the transporter (3FH6) **B** Pre-translocation state with AMPPNP/Mg2+ bound to the NBDs (3PUZ). Opening of MalE was prevented by an engineered cysteine bridge. **C** Structure of the transition state with ADP and VO4 (3PUV). This structure is extremely similar to the 3RLF structure, which has AMPPPNP bound and no cysteine bridge in MalE. The structure of a potential post-hydrolysis state is still missing.

Recent findings challenge this established model for ABC type I transporters. While in EPR experiments and in the aforementioned crystal structures ATP and maltose-loaded SBP (maltose binding protein, MBP) had to be present to create an outward-facing state[175,178], Bao *et al.* reported that ATP alone was sufficient to trigger this conformational switch[180]. It was also suggested that the stimulation of ATPase activity in presence of substrate-loaded SBP as reported by numerous authors may not result from a shift of the transporter state equilibrium to the outward-facing state. It was claimed that the role of the SBP might rather lie in an allosteric auto-regulation mechanism[181]. Bao *et al.* further reported high-affinity binding of open SBP to the outward-facing state of the transporter in the presence of AMPPNP (a non-hydrolyzable ATP analog), while at saturating maltose concentrations they observed dissociation of the SBP from the complex[181]. In 2013, Böhm *et al.* found that the apo-, ADP- and ATP-bound states of the maltose transporter can all bind to open and closed MBP, but only in the presence of ATP is the transport of the substrate accomplished. Binding to open, unliganded MBP resulted in an ineffective cycle without substrate shuttling[182]. Open MBP is able to bind to the transporter and stimulate ATPase activity as also observed by Gould *et al.*[183]. In a different study, the authors further concluded that ATPase stimulation was not dependent on the nature of the substrate, but rather coupled to specific interactions of the complex with the open form of the MBP[184]. A possible explanation for binding of unliganded, presumably open SBP to its cognate transporter is presented in a recent MD study of the histidine binding protein HisJ[185]. The authors found that HisJ undergoes large conformational motions in its substrate-free state, also sampling the closed conformation that is then able to dock to the TMD.

Interestingly, there is controversy also for exporters as to whether ATP is generally sufficient to stabilize an outward-facing state. While for Sav1866 and MsbA, binding of non-hydrolyzable analogs was sufficient to establish a stable outward-facing conformation that could even be crystallized[186,187], Shintre *et al.* recently reported several inward-facing structures that had AMPPNP or AMPPCP bound to the NBDs[188]. Taken together, these data indicate a certain plasticity of ABC transporters that has not yet been considered in most studies.

2.3.5 Challenges of studying ABC transporter function

While the alternating access model seems very intuitive and largely fits the available structural data, it cannot account for all recent biochemical findings and MD simulations performed in lipid environments. This illustrates that static crystal structures, although of great value for elucidating the overall arrangement of larger protein complexes, might not be sufficient to explain complex functional mechanisms including the regulatory steps along the catalytic cycle of ABC transporters.

Complicating this further is the fact that many studies were performed in very different environments: detergent, model membranes or native-like lipids. The correct lipid environment is crucial for function of various IMPs and also specifically for the maltose transporter[32,189,190]. The ABC type II transporters BtuCD and HI1470/71 were crystallized in the absence of nucleotides in both inward- and outward-facing states[135,150]. Thus, it is likely that the lipid bilayer and the composition play a crucial role in maintaining a functional, nucleotide-dependent equilibrium state of the transporter. Although LCP crystallization by has been successful for several receptors and channels[191-196], almost all ABC transporter structures were solved in a lipid-free environment. Additionally, the conditions necessary to obtain well-defracting membrane protein crystals are often far off from physiologial conditions in terms of pH and salt concentrations.

For large protein machineries that do not crystallize easily it is common to make use of their modular nature and dissassemble the complexes into subdomains. For ABC transporters this 'divide-and-conquer'strategy has mainly been used for intensive study of the NBDs, although it becomes more and more evident that conclusions drawn from studies of isolated domains may not always hold true for the full complexes[197]. In the absence of the restricting coupling helices and the nucleotide, the NBDs are very flexible and can adopt potentially unnatural conformations that might partially be responsible for ATPase activity observed for several isolated NBDs. The measured hydrolyis rates are consequently uncoupled from the membrane transport function of the transporter and should be interpreted carefully in this regard.

Investigation of pseudo-functional states of ABC transporters further often requires mutation of key residues necessary for hydrolysis. These hydrolysis-incompetent mutants can be used as ground state mimics, that bind nucleotide but do not perform hydrolsis. Another possibility to trap intermediate states of transporters is to work with ATP analogs that are less prone to hydrolysis. Although both mutations and the use of non-physiological analogs might not alter the overall arrangement of the transporter, the precise conformation of active site residues as well as the location of the nucleotide itself could be inaccurate and possibly lead to wrong conclusions about the detailed hydrolysis mechanism[146].

2.4   Structural and functional characterization of a wild-type ABC transporter in the native lipid environment using ssNMR

2.4.1   The amino acid importer ArtMP-J

The amino acid transporter ArtMP-J from the thermophilic *Geobacillus stearothermophilus* was chosen to investigate the functional effects of nucleotide binding to an unmutated ABC type I importer in the native lipid environment. ArtMP-J was first described in 2005 as one of the smallest ABC transporters known to date[198] and is an ideal system to study ABC transporter function by NMR as it shows remarkable thermostability, can be produced in *E. coli* and reassembled from the single subdomains[199].

The complex is composed of a homodimeric transmembrane core of two ArtM subunits that are non-covalently bound to two NBDs called ArtP (Figure 17A). The processed form of the SBP ArtJ (28 kDa) carries a lipid-modification at the N-terminal cysteine as membrane anchor. An anchor-free version of ArtJ was shown to bind different basic amino acids like lysine and histidine, but the highest binding affinity was found for arginine[200]. Various crystal structures of substrate-loaded ArtJ lacking its lipid modification have been solved (Figure 17B)[200]. Mutagenesis studies on ArtM and ArtJ provide hints towards potential interfaces of the different subdomains and identify several residues involved in hydrolysis and transport[200,201].
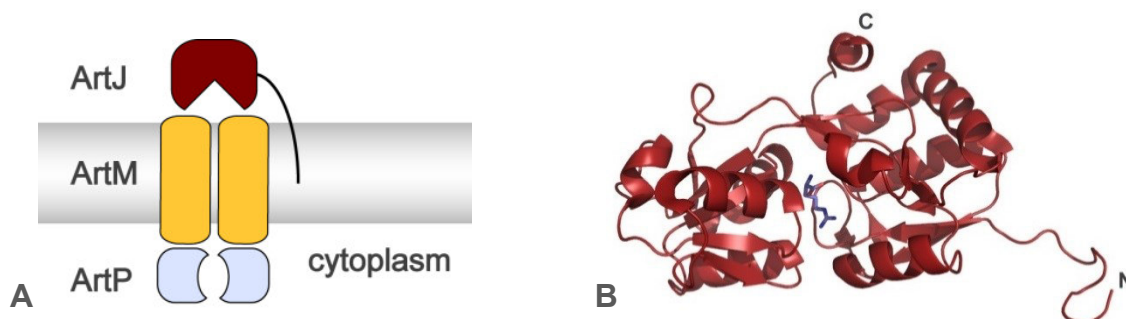
Figure 17: The amino acid importer ArtMP-J. **A** Domain organization of ArtMP-J **B** Crystal structure (2Q2A) of the ArtJ with bound arginine. N- and C-termini are indicated.

ArtP lacks the regulatory domain that is often observed in other small molecule transporters but exhibits all of the common motifs necessary for ATP hydrolysis (Figure 18 and Figure 19). Its amino acid sequence is most similar to the NBDs of the arginine and the glutamate transporter from *E. coli* as well as to an arginine transporter from *Bacillus subtilis*[198]. The sequence similarity to NBDs with known 3D structure is depicted in (Figure 18).

```
                 β1                        β2        TT   β3     TT    α1                  β4      T
ArtP       1         10                20              30              40            50              60

ArtP      MIDVHQLKKSF..GSLEV..LKGINVHIREGEVVVICPSCSGKSTFLRCLNLLEDFDEGEIIID
MetN      MIKLSNITKVFHQGTRTIQALNNVSLHVPAGQIYGVIGASGAGKSTLIRCVNLLERPTEGSVLVD
Mj0796    MIKLKNVTKTYKMGEEIIYALKNVNLNIKEGEFVSIMGPSGSGKSTMLNIIGCLDKPTEGEVYID
ModC      .IEIESLSRKW..KNFSLD...NLSLKVESGEYFVILGPTGAGKTLFLELIAGFHVPDSGRILLD
MalK      SVQLQNVTKAW..GEVVVS..KDINLDIHEGEVVVGPSGSGKSTLLRMIAGLETITSGDLFIG
HylB      DITFRNIRFRYKPDSPVI..LDNINLSIKQGEVIGIVGRSGSGKSTLTKLIQRFYIPENGQVLID
MsbA      DVEFRNVTFTYPGRDVPA..LRNINLKIPAGKTVALVGRSGSGKSTIASLITRFYDIDEGEILMD
              A-loop                                    WalkerA

               β5  TT      α2       β6          TT   α3               α4
ArtP       T          70              80              90         100        110        120

ArtP      GI.NLKAKDTNLNKVRE.EVGMVFQRFNLFPHMTVLNNITLAPM.KVR.KWPREKAEAKAMELLD
MetN      GQELTTLSESELTKARR.QIGMIFQHFNLLSSRTVFGNVALPLELDNT...PKDEVKRRVTELLS
Mj0796    NIKTNDLDDDELTKIRRDKIGFVFQQFNLIPLLTALENVELPLIFKYRGAMSGEERRKRALECLK
ModC      GK.....DVTDLSPEKH.DIAFVYQNYSLFPHMNVKKNLEFGMRM......KKIKDPKRVLDTAR
MalK      EK.....RMNDTPPAER.GVGMVFQSYALYPHLSVAENMSFGLKLAGA...KKEVINQRVNQVAE
HylB      G...HDLALADPNWLRR.QVGVVLQDNVLLNR.SIIDNISL........ANPGM.SVEKVIYAAK
MsbA      G...HDLREYTLASLRN.QVALVSQNVHLFND.TVANNIAY........ARTEQYSREQIEEAAR
                                         Q-loop

                       η1    η2        α5              β7          α6
ArtP                        130        140        150              160        170

ArtP      KV...........GLKDKAHAYPDSLSGGQAQRVAIARALAMEPKIMLFDEPTSALDPEMVGEVL
MetN      LV...........GDKHDSYPSNLSGGQKQRVAIARALANNPPIILADQPTGALDSKTGEKIM
Mj0796    MA.......ELEERF...ANHKPNQLSGGQQQRVAIARALANNPPIILADQPTGALDSKTGEKIM
ModC      DL...........KIEHLLDRNPLTLSGGEQQRVALARALVTNPKILLLDEPLSALDPRTQENAR
MalK      VL...........QLAHLLDRKPKALSGGQRQRVAIGRTLVAEPSVFLLDEPLSNLDAALRVQMR
HylB      LAGAHDFISELREGYNTIVGEQGAGLSGGQRQRIAIARALVNNPKILIFDEATSALDYESEHVIM
MsbA      MAYAMDFINKMDNGLDTVIGENGVLLSGGQRQRIAIARALLRDSPILILDEATSALDTESERAIQ
                             ABC signature           WalkerB   D-loop

                    β8     α7      β9     TT  β10    α8       α9
ArtP           180        190        200        210        220        230        240

ArtP      SVMKQLANE.GMTMVVVTHEMGFAREVGDRVLFMDGCYIIEEGKPEDLFDRPQHERTKAFLSKVF
MetN      ELLKDINRRLGLTILLITHEMDVVKRICDCVAVISNGELIEQDTVSEVFSHPKTPLAQKFIQSTL
Mj0796    QLLKKLNEEDGKTVVVVTHDINVARF.GERIIYKDGEVEREEKLRGFDDR...........
ModC      EMLSVLHKKNKLTVLHITHDQTEARIMADRIAVVMDCKLIQVGKPEEIFEKPVEGRVASFVGFE.
MalK      IEISRLHKRLGRTMIYVTHDQVEAMTLADKIVVLDAGRVAQVGKPLELYHYPADRFVAGFIGSPK
HylB      RNMHKICK...GRTVIIIAHRLSTVKN.ADRIIVMEKGKIVEQGKHKELLSEPESLYSYLYQLQSD
MsbA      AALDELQK..NRTSLVIAHRLSTIEK.ADEIVVVEDGCVIVERGTHNDLL.EHRGVYAQLHKMQFG
                    H-loop
```

Figure 18: Multiple sequence alignment for ArtP and NBDs of other bacterial transporters with known 3D structure. Secondary structures and important motifs are indicated. For all other NBDs, only that part of the sequence aligning with ArtP is shown, N- and C-terminal extensions including regulatory domains in other transporters were omitted. The numbering relates to the amino acid sequence of ArtP. Alignment and figure were created using Clustal Omega and ESPript 3.0, respectively.

Crystal structures of isolated ArtP (27 kDa) with different nucleotide analogs are available in the pdb (e.g. 3C41). Nevertheless, these structures do not appear to reflect the native interface of the NBD dimer in the intact ArtMP-J complex (Figure 19B) and also showed asymmetries that seem non-natural when compared to the full complex in lipidic environment investigated by solid-state NMR[202]. Although no experimental structural information is available for ArtM, from secondary structure predictions the 24 kDa TMD monomer is expected to comprise only five TMH and seemingly lacks the crossing helix that in other type I importers like MalFGK$_2$-E and ModBC-A spans over to the second TMD monomer. Similar to other importers, ArtM also exhibits the EAA motif involved in coupling to

its specific NBD. Weidlich *et al.* also recently speculated about a potential substrate binding site in the transmembrane region that might be analogous to the location in the MalFGK$_2$-E transporter[203].
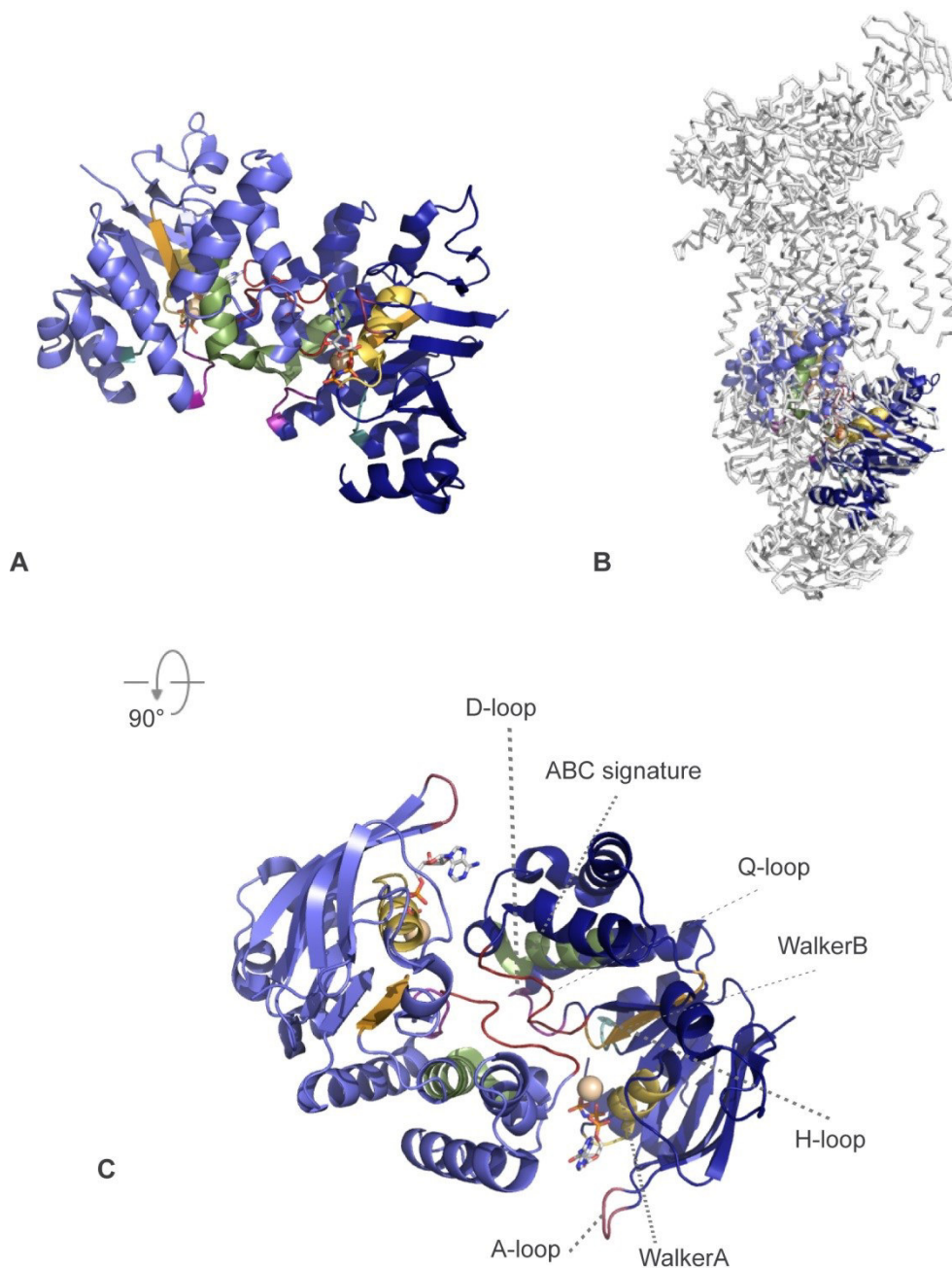
Figure 19: Dimeric ArtP as observed in the 3C41 crystal structure. **A** Side-view of the ArtP dimer in 3C41 **B** The overlay of the ArtP dimer (3C41) and the Maltose transporter (3RLF) indicates the misorientation of the ArtP monomers relative to each other. **C** The top-view of the ArtP dimer with relevant motifs indicated clearly differs from the NBD arrangement observed for the MalK dimer in the full maltose transporter complex (see Figure 12 for comparison).

2.4.2   Project outline

ABC transporters are multi-component transmembrane proteins that couple the energy derived from ATP hydrolysis to translocation of substrates across cellular membranes. This project aims at understanding the mechanism of ABC transporter function in the native lipid environment investigating the arginine importer ArtMP-J of *Geobacillus stearothermophilus* as an example.

The modular nature of ArtMP-J enables separate expression of all subunits with subsequent in-vitro assembly and reconstitution of the complex into a lipid environment without large effects on the ATPase activity of the complex[199]. An initial ssNMR study of ArtMP already showed that the conformation of ArtP was different in 3D crystals of the soluble domain compared to 2D crystalline preparations of the full transporter in native lipids[202].

These results were exploited in the course of this PhD project for a comprehensive biophysical study of nucleotide binding to the transporter using analytical ultracentrifugation, isothermal titration calorimetry and NMR. For this purpose, protein expression yields had to be optimized for the soluble domains ArtP and ArtJ. Since expression for the TMD ArtM is substantially reduced when expressed in absence of ArtP, a very cost-efficient protocol needed to be established and optimized that would ultimately allow for production of ^{2}H^{15}N^{13}C-labeled ArtM.

Residues involved in nucleotide-binding and signal transmission to the TMDs should be identified in initial solution NMR experiments with ArtP alone, whereas ^{1}H detected MAS ssNMR should be used as the major tool to monitor nucleotide-dependent changes in the ArtMP complex when embedded in the native lipid environment.

A suite of ^{1}H-detected ssNMR assignment experiments should be used for assignment of ArtMP to generate the basis for structure determination of the full complex in the native environment. As no structural data for the full ArtMP complex was available, a simple homology model needed to be established to interpret initial results from ssNMR studies in a structural perspective.

3   Material and Methods

3.1   Material

3.1.1   Bacterial strains

E. coli strains

BL21 (DE3)	F$^-$, *omp*T, *hsd*S$_B$(r$_B$-, m$_B$-), *dcm*, *gal*, λ(DE3)
BL21 Rosetta™ 2 (DE3) pLysS	F$^-$, *omp*T, *hsd*S$_B$(r$_B$-, m$_B$-), *dcm*, *gal*, λ(DE3) pRARE (Cm^R) pLysS (Cm^R)
DH5α™	F$^-$, φ80d*lacZ*ΔM15, Δ(*lacZYA-argF*)U169, *deoR*, *recA*1, *endA*1, *hsdR*17(rk$^-$, mk$^+$), *phoA*, *supE*44, λ$^-$, *thi*-1, *gyrA*96, *relA*1

Geobacillus stearothermophilus

DSM 13240	wild-type

3.1.2   Primers and plasmids

All oligodeoxynucleotides for sequencing, mutagenesis and cloning were constructed with the *Geneious* software and obtained from BioTez, Berlin in HPLC-controlled quality.

Table 5: Primers used in this work

Primer name	Sequence (5'-3')	Objective
AV6_for	CATGCTGTTTGACGCGCCGACATCAGCGC	Quick Change Mutagenesis of artP leading to E162A
AV7_rev	GCGCTGATGTCGGCGCGTCAAACAGCATG	Quick Change Mutagenesis of artP leading to E162A
AV8_fw	CTATTGGAATTCATGGATTTTCGCTTTGATATT	Cloning of artM from pColdIV into pASK-IBA3plus including EcoRI restriction site
AV9_rev	CGCGCCATGGTTATTATTACTGGGTGCTATATTTA	Cloning of artM from pColdIV into pASK-IBA3plus including NcoI restriction site

The plasmids pRF2 and pSS1 were a gift from Prof. Dr. Erwin Schneider, Humboldt Universität zu Berlin and already available in our lab. pMaz and pColdIV were obtained with the SPP system from Takara Bio. pASK-IBA3plus was obtained from IBA GmbH, Göttingen, Germany.

Table 6: Plasmids used in this work

Plasmid	Vector	Specification	Tag	Target gene	Reference
pVL4-P1	pET46	IPTG inducible T7 promotor Amp^R	N-terminal 6xHis-tag	*artP* from *G. stearohermophilus*	Lange *et al.*, 2010[202]
pRF2	pQE60	IPTG inducible T5 promotor Amp^R	C-terminal 6x His-tag	*artMP* from G.*stearothermophilus* (contains C96A in the *artM* gene resulting in F32L)	Fleischer *et al.*, 2005[198]
pSS1	pET15b	IPTG inducible T7 promotor Amp^R	N-terminal 6x His-tag	*artJ* from *G. stearothermophilus*	Vahedi-Faridi *et al.*, 2008[200]
pQE60-artM	pQE60	IPTG inducible T5 promotor Amp^R		*artM* from G.*stearothermophilus* (contains C96A in the *artM* gene resulting in F32L)	Kunert, 2011[199]
pColdIV-artM	pColdIV	IPTG *inducible cspA* promoter Amp^R	-	*artM* from *G. stearothermophilus*	Takara Bio This work
pASK-IBA-3plus-artM	pASK-IBA-3plus	aTc inducible T7 promotor AmpR	-	*artM* from G.*stearothermophilus*	This work
pRF2_E162A	pQE60 (pRF2)	IPTG inducible T7 promotor Amp^R	C-terminal 6x His-tag	*artMP* from G.*stearothermophilus* (contains C96A in the *artM* gene resulting in F32L and a mutation in *artP* leading to E162A)	This work
pVL4-P1 _E162A	pET46 (pVL4-P1)	IPTG inducible T5 promotor, Amp^R	N-terminal 6xHis-tag	*artP* from G.*stearothermophilus* (contains a mutation in the *artP* leading to E162A)	This work

3.1.3   Enzymes, standards and kits

Benzonase	Novagen/ Merck KGaA, Darmstadt, Germany
Fast Digest DnpI	ThermoFisher Scientific, Waltham, USA
KOD Hot Start Polymerase	Novagen/ Merck KGaA, Darmstadt, Germany
T4 Ligase	Novagen/ Merck KGaA, Darmstadt, Germany
Lysozyme	Carl Roth GmbH + Co. KG, Karlsruhe, Germany
Restriction enzymes (EcoRI, NcoI)	MBI Fermentas, St. Leon-Roth, Germany
Gene Ruler™ 1kb ladder	MBI Fermentas, St. Leon-Roth, Germany
Quick load™ 100 bp DNA ladder	New England BioLabs GmbH, Frankfurt am Main, Germany
Unstained Protein MW Marker	Fisher Scientific - Germany GmbH, Schwerte, Germany
Ammonium Test	Merck KGaA, Darmstadt, Germany
Glucose Test	Merck KGaA, Darmstadt, Germany
DNA Gel Extraction Kit	Merck KGaA, Darmstadt, Germany
NucleoSpin® Plasmid	Machery-Nagel GmbH & Co. KG, Düren, Germany

3.1.4   Chemicals

All standard and bulk chemicals including ingredients for media, buffers substances, salts, unlabeled amino acids and glycerol were obtained from:

> Carl Roth GmbH + Co. KG, Karlsruhe, Germany
>
> AppliChem GmbH, Darmstadt, Germany
>
> Sigma-Aldrich Chemie GmbH, Taufkirchen, Germany

Agarose	SERVA Electrophoresis GmbH, Heidelberg, Germany
Ammonium molybdate tetrahydrate	Sigma-Aldrich Chemie GmbH, Taufkirchen, Germany
Anhydrotetracyclin (aTc)	IBA GmbH, Göttingen, Germany
Ammonium persulfate (APS)	Carl Roth GmbH + Co. KG, Karlsruhe, Germany
Ascorbic acid	Carl Roth GmbH + Co. KG, Karlsruhe, Germany
Biotin	Carl Roth GmbH + Co. KG, Karlsruhe, Germany
cOmplete EDTA-free	Roche Diagnostics, Mannheim, Germany
Carbenicillin	Carl Roth GmbH + Co. KG, Karlsruhe, Germany
Isoprophyl-β-D-thiogalactopyranoside (IPTG)	AppliChem GmbH, Darmstadt, Germany
β-Mercaptoethanol	Carl Roth GmbH + Co. KG, Karlsruhe, Germany
Di-sodium hydrogen arsenate	Fluka Chemie GmbH, Buchs, Switzerland
Sodium citrate	Fluka Chemie GmbH, Buchs, Switzerland
Sodium dodecyl sulfate (SDS)	Sigma-Aldrich Chemie GmbH, Taufkirchen, Germany
TEMED	Carl Roth GmbH + Co. KG, Karlsruhe, Germany
Thiamin-HCl	AppliChem GmbH, Darmstadt, Germany

Rotiphorese® Gel	Carl Roth GmbH + Co. KG, Karlsruhe, Germany
Uranyl acetate	Sigma-Aldrich Chemie GmbH, Taufkirchen, Germany

Special chemicals

Detergents:	GLYCON Biochemicals GmbH, Luckenwalde, Germany

n-Octyl-β-D-glucopyranoside (OG)

n-Decyl-β-maltoside (DM)

n-Dodecyl-β-maltoside   (DDM)

Nucleotides:	Sigma-Aldrich Chemie GmbH, Taufkirchen, Germany

Adenosin 5'-diphosphate sodium salt (≥ 95 %) (ADP)

Adenosin 5'-triphosphate disodium salt (≥ 99 %) (ATP)

Adenosin 5' (β,γ)-imidotriphosphate lithium salt (≥ 93 %) (AMPPNP)

β,γ -Methylenadenosin 5'-triphosphate disodium salt (≥ 95 %) (AMPPCP)

Isotopes:

D_2O, ^{13}C-glucose, d^7-^{13}C-glucose, $^{15}NH^4Cl$,

1,3-^{13}C-glycerol, 2-^{13}C-glycerol, $NaH^{13}CO_3$	Euroisotop, Saint-Aubin Cedex, France
	Cambridge Isotopes, Andover, USA
	Sigma-Aldrich/ISOTEC, München, Germany

3.1.5   Media, antibiotics and buffer solutions

All rich media and ingredients for H_2O-based M9 media were autoclaved while solutions for deuterated M9 media were filter sterilized. Except for culture media, all solutions were prepared with MilliQ® water. Culture plates were stored at 4°C.

3.1.5.1   *Media for cultivation of E. coli*

Antibiotics/Inducers:

Carbenicillin (Carb)	60 µg/mL final concentration
Chloramphenicol (Cam):	34 µg/mL final concentration
Isopropyl β-D-thioglactopyranosie (IPTG)	0.5 mM final concentration
Anhydrotetracylin (aTc)	3-15 µg/mL

LB medium (Miller, 1972[204])

NaCl	1 % w/v
Peptone	1 % w/v
Yeast extract	0.5 % w/v

supplemented with 1.5 % agar-agar for selection plates.

32Y medium (Sambrook et al., 1989[205])

NaCl	0.58 % w/v
Peptone	0.8 % w/v
Yeast extract	3.2 % w/v

supplemented with 0.05 % glucose, 0.5 % glycerol and 0.2 % lactose

when used as autoinduction medium[206].

M9 minimal medium

Minimal medium was based on the listed components (autoclaved or filter sterilized) that were added to auto-claved H_2O in the mentioned order. For deuterated M9 media, trace elements were lyophilized and resuspended in D_2O.

Na_2HPO_4	51 mM
KH_2PO_4	15 mM
NaCl	8.5 mM
$MgSO_4$	1 mM
$CaCl_2$	0.3 mM
Thiamin-HCl	4.4 µM
Biotin	6.1 µM
EDTA	0.1 mM
$FeSO_4$	33 µM
$ZnCl_2$	3.7 µM
$CuSO_4$	0,6 µM

Additional trace elements were added as recommended by Studier, 2005[206]:

$FeCl_3$	50 µM
$MnCl_2$	10 µM
$ZnSO_4$	10 µM
$CoCl_2$	2 µM
$CuCl_2$	2 µM
$NiCl_2$	2 µM
Na_2MoO_4	2 µM
$NaSeO_3$	2 µM
H_3BO_3	2 µM

For isotope free precultures, 0.05 % glucose and 0.01 % NH_4Cl were used as N- and C-sources and for the cSPP method, 0.2 % CAA (casamino acids) were additionally added.

Triple-labeled protein was produced with 0.05 % d7-13C-glucose and 0.01 % $^{15}NH_4Cl$ (0.02 % in case of the cSPP system). Glycerol labeling was achieved with 1,3-^{13}C-glycerol/$NaHCO_3$ and 2-^{13}C-glycerol/ $NaH^{13}CO_3$.

M9 plates for cSPP

1.5 % agar-agar was autoclaved in H_2O and all listed M9 ingredients were added in the mentioned order when the agarose solution had cooled sufficiently.

3.1.5.2   Frequently used buffers

<u>Electrophoresis buffers</u>

1x TAE buffer (agarose gel electrophoresis)

Tris-acetate	40 mM
EDTA	2 mM

10x loading buffer for agarose gel electrophoresis

Bromphenol blue	1 mg/ml
Xylencyanol	1 mg/ml
Glycerol	50 % v/v

1x SDS running buffer

Tris	50 mM
Glycine	190 mM
SDS	1 g/l

with no further adjustment of pH.

5x SDS loading buffer

Tris/HCl pH 8,0	250 mM
SDS	7,5 % w/v
Glycerin	25 % v/v
Bromphenol blue	0,25 mg/ml
2-Mercaptoethanol	12,5 % v/v
	(for reducing loading buffers)

Fixing/Staining solution

Acetic acid	10 % v/v
Ethanol	40 % v/v
Coomassie Brilliant blue R-250	0.25 % w/v

Destaining solution
like staining solution, but without Coomassie Brilliant blue R-250

Buffers for protein preparation and proteinchemical works

Standard buffer

Tris/HCl pH 8.0	50 mM
Glycerol	4.3 % (w/v)
for purification of ArtMP or ArtM:	+ 0.4 % DM

Cell disruption buffer

Standard buffer +

Complete (EDTA-free)	1 tablet/ 20 ml cell suspension

supplemented with lysozyme and benzonase.

Buffer for Ni^{2+} affinity chromatography

Standard buffer +

Imidazole	5 / 250 mM (wash / elution)

For preparation of ssNMR samples with partial proton back exchange, the desired proton:deuterium ratio was adjusted accordingly by use of D_2O instead of H_2O.

Buffer for gelfiltration

Standard buffer

for purification of ArtMP:	+ 0.4 % DM

For preparation of ssNMR samples with partial proton back exchange, the desired proton:deuterium ratio was adjusted accordingly by use of D_2O instead of H_2O.

Lipid reconstitution buffers

Reco buffer 1

Tris pH 8.0	20 mM
NaCl	300 mM
$MgCl_2$	10 mM
Glycerol	4.3 %
NaN_3	0.01 %

Reco buffer 2

HEPES pH 6.8	20 mM
NaCl	25 mM
$MgCl_2$	10 mM
Glycerol	1.7 %
NaN_3	0.01 %

For preparation of ssNMR samples with partial proton back exchange, the desired proton:deuterium ratio was adjusted accordingly by use of D_2O instead of H_2O.

3.1.6 Consumables

Seriological pipettes	VWR International GmbH, Dresden, Germany
Reaction tubes (0.2, 1.7, 2.0, 15, 50 ml)	Sarstedt AG & Co., Nürnbrecht, Germany
Bio-Beads® SM-2 Adsorbents	Bio-Rad Laboratories GmbH, München, Germany
Dialysis tubing	SpectrumLabs, Frankfurt, Germany
Rotilabo® syringe filters (0.22 and 0.45 μM)	Carl Roth GmbH + Co. KG, Karlsruhe, Germany
Amicon Centrifugal Filter Units (10,000 and 30,000 MWCO)	Merck KGaA, Darmstadt, Germany
Ultrafiltration membranes (10,000 and 30,000 MWCO)	Merck Millipore, Billerica, USA
Costar 3474 Ultra low attachment 96 well plates (flat bottom)	Corning Incorporated, USA
Electron microscopy grids (grid size 400 mesh × 62 μm pitch)	Sigma-Aldrich Chemie GmbH, Taufkirchen, Germany

3.2 General equipment and special instrumentation

Protein purification equipment

FPLC system	Pharmacia Biochem/ GE Healthcare Europe GmbH, Freiburg Germany
Chelating sepharose	GE Healthcare Europe GmbH, Freiburg Germany
Superdex 75 (320 ml)	GE Healthcare Europe GmbH, Freiburg Germany

Electrophoresis equipment

Mighty Small SE250 electrophoresis chamber	Hoefer, San Fransisco, USA
GNA 100 / EPS 200	Pharmacia Biochem/ GE Healthcare Europe GmbH, Freiburg Germany

Shakers/stirrers

Innova 4000 Incubator Shaker	New Brunswick Scientific Co., Inc., Edison, USA
Innova 4230 Incubator Shaker	New Brunswick Scientific Co., Inc., Edison, USA
Multitron Standard	Infors GmbH, Einsbach, Germany
Solution mixer / rotary wheel	neoLab, Heidelberg, Germany
Thermomixer 5436	Eppendorf, Hamburg, Germany

Centrifuges

    Avanti J®   Beckman Coulter, Krefeld, Germany

        with rotors Beckman JA-25.50,

        and F10RCI -6x500y Fiber*Lite*®   Piramoon, USA

    Optima LE-80K Ultracentrifuge   Beckman Coulter, Krefeld, Germany

        with rotors 45 Ti, 70.1 Ti

    Optima TLX Ultraentrifuge (table-top)   Beckman Coulter, Krefeld, Germany

        with rotor TLA 45

    Allegra X-22R Centrifuge   Beckman Coulter, Krefeld, Germany

    Allegra 21R Centrifuge   Beckman Coulter, Krefeld, Germany

    Centrifuge 5417R   Eppendorf, Hamburg, Germany

    Centrifuge 5415C (rotor filling)   Eppendorf, Hamburg, Germany

AUC equipment

    Optima XL-I analytical Ultracentrifuge   Beckman Coulter, Krefeld, Germany

        equipped with UV absorbance and interference optics

        with two-sector titan and six-sector Epon cells

Spectrophotometers

    Smartspec™ 3000   Bio-Rad Laboratories, München, Germany

    Nanodrop™ 2000c with   ThermoFisher Scientific, Waltham, USA

        ND 2000 software

    Safire Microplate Reader   Tecan, Crailsheim, Deutschland

Other instruments

    Mastercycler epgradient S (for PCR)   Eppendorf, Hamburg, Germany

    Ultra Yield Flasks™ for expression   Thomson instrument company, Oceanside, USA

    Biological safety cabinet class   BDK GmbH, Sonnenbuehl-Genkingen, Germany

    Homogenizer DIAX 900   Heidolph, Schwabach, Germany

    EmulsiFlex-C3   Avestin Europe GmbH, Mannheim, Germany

    RK52Sonorex ultrasound waterbath   Bandelin electronic GmbH & Co. KG, Berlin, Germany

    Microcal™ ITC200 with   GE Healthcare Life Sciences, Berlin, Germany

        with Origin software

    fedbatch-pro® High cell density fermentation   Dasgip GmbH, Jülich, Germany

    EM902A TEM   Carl Zeiss, Jena, Germany

<u>NMR spectrometers</u>

All experiments were performed on spectrometers by Bruker Corporation, Billerica, USA.

Solution NMR

AV600 (14.1 T)   **Nucleotide binding studies with ArtP**

Solid-state NMR spectrometers and probes

AV600 (14.1 T)   with a wide-bore 4-channel probe (H/D/C/N), 3.2 mm rotor

diameter, variable temperature **(Quadruple resonance experiments)**

AV700 (16.4 T)   with a wide-bore standard 3-channel probe head (H/C/N) with

additional ^{2}H coil, 3.2 mm rotor diameter, variable temperature

(Inept-/ CP-based 2D HN correlations correlations at 20 kHz MAS, first 3Ds

on ArtMP at 20 kHz MAS)

AV800 (18.8 T)   with a wide-bore standard 3-channel probe head (H/C/N), 3.2 mm rotor

diameter, variable temperature **(2D CC correlation of ArtM)**

AV900 (21.2 T)   with a narrow-bore fast-MAS 4-channel probe (H/D/C/N), 1.9 mm rotor

diameter, variable temperature and field gradient

(3D correlations of ArtmP at 40 kHz, CP-based 2D HN correlation of ArtMp

at 37 kHz)

3.3   Molecular biological methods

3.3.1   Transformation of *E. coli* with plasmid DNA

Competent *E. coli* cells were obtained with the classical $CaCl_2$ method[207]. Cells were stored at -80 °C until further usage. For transformation, 100 µl of cell suspension was mixed with 1 µl of plasmid DNA (~100 ng/µL) or 5 µl of a ligation mix and incubated on ice for 10 min. The sample was heated to 42 °C for 45 sec, mixed with 1 ml LB medium and incubated for at 37 °C and 200 rpm for 1 h. 100 µl of this suspension was then spread on LB agar plates containing 60 µg/ml carbenicillin and/or 34 µg/ml chloramphenicol. Plates were incubated overnight at 37 °C

3.3.2   Cultivation of *E. coli* strains

Single colonies of *E. coli* were obtained by streaking bacteria on LB-agar plates and incubation at 37 °C overnight. Selection for plasmid uptake was performed by addition of corresponding antibiotics to the culture medium. Culture plates were stored at 4 °C and used for inoculation of liquid cultures for a maximum of two weeks.

Liquid cultures were prepared with LB medium, supplemented with carbenicillin (60 µg/mL) or/and (34 µg/mL). Up to a volume of 100 mL, cultures were inoculated directly with one bacterial colony from a culture plate. Larger volumes were inoculated in a ratio of 1:100 with an overnight culture. Cultures were incubated at 37 °C and 160 rpm.

For the cSPP system, all steps were carried out on minimal medium.

3.3.3   Isolation of plasmid DNA from *E. coli*

Isolation of plasmid DNA from 5 and 10 ml *E. coli* DH5α cultures was performed with the Nucleo-Spin® Plasmid according to the user manual. Typically 20 to 50 µl of MilliQ® water were used for elution of bound plasmid DNA. The plasmid DNA was stored at -20 °C and used for sequencing and transformation of *E. coli* cells.

3.3.4   Analytical and preparative gel electrophoresis of DNA

For analytical gel electrophoresis 50 ml of a 1.5 % w/v suspension of agarose in TAE-buffer was prepared and homogenized by heating in a microwave. Safe dyes were used to visualize the DNA. 10 µl (30 µl for preparative gels) of the DNA solution were mixed with the corresponding volume of 10x loading buffer were used per pocket. Electrophoresis was performed for about 60 min at 100 V. DNA fragments were visualized under UV light using a Gel Doc™ XR+ system from Bio-Rad.

3.3.5   *In vitro* modification of DNA

3.3.5.1   *Polymerase chain reaction (PCR)*

PCR was carried out to subclone *artM* from pColdIV-artM into pASK-IBA3plus using AV8_for and AV9_rev. The following parameters were used:

step 1	95 °C 2 min	(Initialization step)
step 2, repeated 25 times		
	95 °C 20 sec	(Denaturation)
	58 °C 10 sec	(Annealing)
	70 °C 12 sec	(Extension)
step 3	72 °C 2 min	(Final elongation)
step 4	4 °C ∞	(Final hold)

3.3.5.2   *Mutagenesis*

Mutagenesis of the catalytic glutamate E162 to alanine in the *artP* gene in pRF2 and pVL4-P1 was carried out with the primers AV6_for and AV7_rev. The mutagenesis PCR was performed with KOD hot start polymerase and the following parameters:

step 1	95 °C 30 sec	(Initialisation step)
step 2, repeated 14 times		
	95 °C 30 sec	(Denaturation)
	58 °C 1 min	(Annealing)
	60 °C 6 min	(Extension)
step 3	4 °C ∞	(Final hold)

Dnpl1 was used to digest the methylated template DNA, before the reaction mix was used for transformation of E. coli DH5α cells. Positive clones were verified by sequencing of isolated plasmids.

3.3.5.3   *Cleavage of double-stranded DNA with restriction endonucleases*

For restriction enzyme digest of plasmids and PCR fragments, the DNA was cleaved using restriction endonucleases by MBI Fermentas. The enzymatic reaction was performed according to the vendor manual. For cleavage of DNA with several enzymes at the same temperature, the buffer providing optimal conditions for all enzymes was chosen. Sample mixtures were prepared in a volume of 20 to 60 µl containing a maximum of 1 µl of each restriction enzyme.

3.3.5.4   Purification of DNA constructs

Purification of DNA constructs from agarose gels, after digestion with restriction enzymes or amplification by PCR was carried out with the DNA Gel Extraction Kit (Merck) according to the user manual. 30 to 50 µl MilliQ® water were applied as typical elution volume.

3.3.5.5   Ligation of DNA fragments

Purified DNA fragments, which were previously cleaved with the according restriction enzymes, were ligated with T4 DNA ligase. A sample volume of 20 µl containing 2µl cut plasmid DNA, 14 µl cut insert DNA, 2 µl 10x buffer (300 mM Tris/HCl pH 7.8, 100 mM $MgCl_2$, 100 mM DTT, 10 mM ATP; Promega), and 2 µl T4 DNA ligase was prepared and incubated at room temperature for 16 h. 5 µl of this ligation mix were then used for transformation of $CaCl_2$ competent *E. coli* DH5α cells.

3.3.6   Sequencing of DNA constructs

Newly constructed plasmids were sequenced to verify correct ligation. Sequencing was carried out at STRATEC Molecular GmbH (Berlin, Germany). Results were analyzed with the openly accessible *TRANSLATE* tool (ExPASy) and compared to the target sequence with *ALIGN* (Genestream).

3.4   Expression and purification of recombinant proteins

3.4.1   Small-scale expression tests

For screening of optimal expression strains and conditions (temperature, inducer concentrations etc.), small-scale expression tests in 3 ml volumes were carried out for ArtP, ArtMP, ArtJ and ArtM (expressed from the respective vectors listed under 3.1.2). Standardly, cultures grown on rich medium were induced at OD_{600} of 0.6 while cultures on minimal medium were induced at 1.0. Uninduced samples were taken at this time point and used as negative controls in SDS Page analysis.

3.4.2   Large scale production of recombinant proteins in *E. coli* BL21

3.4.2.1   Unlabeled and isotopically labeled expression of His₆-ArtP and His₆-ArtJ

For biophysical characterization including the nucleotide binding and dimerization behavior, expression of **ArtP** from pVL4-1 in *E. coli* BL21 DE3 cells was essentially performed as in Kunert, 2011[199]. Yields of singly- and doubly-labeled protein were optimized by taking advantage of a medium condensation method, in which the precultures were grown in LB medium at 37 °C and 160 rpm until the cells reached an OD_{600} of 0.6. They culture was then concentrated two-fold into M9 medium containing the desired isotopes ($^{15}NH_4Cl$, ^{13}C-glucose, 1,3-^{13}C-glycerol, 2-^{13}C-glycerol and their combinations, respectively). After an adaption period of 30 min, 0.5 mM IPTG was added for induction of target protein expression at 30 °C for up to 20 h. For production of triple labeled protein, the preculture was grown on M9 minimal medium instead of LB before concentration into expression

medium containing 100 % D_2O, 4 g/L. D_7-^{13}C-glucose and 1 g/L NH_4Cl. Expression was carried out until all glucose was used up, which was checked with a Glucose concentration test (Merck).

For cell disruption, the bio wet mass (bwm) was resuspended in cell disruption buffer (10 mL/1 g bwm) to homogeneity using the DIAX-900 mixer. Cells were then broken with the EmuliFlex-C3 homogenizer according to the user instructions. The soluble protein fraction was obtained with the supernatant after a 30 min centrifugation step at 22.000 rpm at 4 °C using the Avanti J® centrifuge equipped with a JA-25.50rotor. The solution was filtersterilized before application to a purification column.

Protein purification was carried out at room temperature on a Pharmacia FPLC system equipped with an 80 ml Ni^{2+}-sepharose column using 10 and 250 mM imidazole for washing and elution of the target protein. The imidazole was removed during concentration of the elution fractions by buffer exchange. When proteins were used for activity assays, solution NMR, AUC or ITC experiments, subsequent gel filtration using a Superdex75 column (320 ml) was performed at 8 °C.

Expression and purification of **ArtJ** was analogous, using pSS1 and *E. coli* BL21 (DE3) Rosetta2 pLysS as expression strain.

Concentrated protein solutions (in standard buffer) were flash-frozen in liquid N_2 and stored at -80 °C until further use.

3.4.2.2 *Unlabeled and isotopically labeled ArtMP-His$_6$*

For ITC experiments and activity assays, **unlabeled, co-expressed ArtMP** was produced from pRF2 in *E. coli* BL21 (DE3) as described in Kunert, 2011[199]. Yield from 1 L LB medium induced with 0.5 mM IPTG was 30 mg ArtMP, which could be increased further in 32Y autoinduction medium (45 mg ArtMP from 1L). Cell disruption was essentially performed as described for ArtP, with the exception that the centrifugation step was carried out at 5000 x g. The membrane fraction subsequently was washed with standard buffer in several ultracentrifugation steps (1 x 100.000 x g, 4°C, 1 h; 2 x (100.000 x g, 4°C, 30 min)) to remove impurities like peripheral membrane proteins. Membrane protein solubilization was achieved with 1 % w/v DDM at 8 °C for 1h. Before further purification, the membranes were pelleted by ultracentrifugation and the supernatant was diluted 1:1 with standard buffer to reduce the concentration of DDM to 0.5 % w/v. Affinity chromatography was performed as described for ArtP on an FPLC system, using standard-buffer supplemented with 0.4 % DM for exchange of detergent.

For co-expressed, **triple-labeled ArtMP**, the precultures were grown in H_2O-based M9 minimal medium until OD_{600} of 0.6. For isotopic labeling, the cells were collected by centrifugation and suspended in M9 medium containing 100 % D_2O, 5 g / L D_7-^{13}C-glucose and 1 g/L $^{15}NH_4Cl$ as sole carbon and nitrogen sources. After an adaption period of 30 min, 0.5 mM IPTG was added for induction of target protein expression at 30 °C. Expression was carried out until all glucose was used up (~20h). Cell disruption and membrane solubilization was performed as described above with standard buffer

(+0.4 % DM) at a D/H ratio of 70/30 %. Affinity chromatography of labeled ArtMP was carried with the same buffer using gravity columns with Co^{2+} sepharose resin. Afterwards, imidazole was removed with PD-10 desalting columns.

Concentrated protein solutions (in standard buffer with 0.4 % DM) were flash-frozen in liquid N_2 and stored at -80 °C until further use.

3.4.2.3   *Unlabeled and isotopically labeled ArtM*

For **unlabeled ArtM** protein expression and isolation of the membrane fraction was performed as described for unlabeled ArtMP (3.4.2.2).

For production of **labeled ArtM** using the "condensed Single Protein Production" method described by Mao, 2009[208], the *artM* gene was first codon-optimized for expression in *E. coli* and all ACA sequences were exchanged to alternative codons without changing the primary amino acid sequence. The gene was synthesized and subcloned into the pColdIV expression vector by GENEART without a purification tag, as the previously established purification strategy together with his-tagged ArtP should be preserved. *E. coli* BL21 (DE3) cells were transformed with pColdIV-artM and the pMazF plasmid, harboring the RNAse for destruction of ACA-containing host RNA. Agar plates made from H_2O-based M9 minimal medium with 60 µg/mL carbenicillin and 34 µg/mL chloramphenicol were used for section of positive clones. Growth of colonies was significantly slower compared to transformations performed with *E. coli* BL21 (DE3) and other plasmids using LB plates (up to 60h at 37°C compared to 12 h). This can probably be attributed to growth on minimal medium with two antibiotics as selection markers. The expression of MazF, which could theoretically destroy host RNA necessary for growth and cell division, should be suppressed in lactose free minimal medium.

For protein expression, small overnight cultures (100 ml) were inoculated with fresh clones obtained from transformation and used for inoculation of large precultures (8 x 1L in 2L Ultra Yield flasks) on the next day. In the first expression trials, these large precultures were grown until OD_{600} of 0.5 in M9 medium, when expression of MazF was induced by addition of 1 mM IPTG for 3 hours. While this should lead to cell arrest and stop host protein production, the *artM* gene should only be turned on efficiently when the *cspA* promotor is additionally activated by cold shock. For this, the cultures were kept in an ice-bath for 30 min before culture condensation was performed into 1/20 of the initial volume of isotopically enriched M9 expression medium based on D_2O (with 5 g/L D_7-^{13}C-glucose and 2 g/L $^{15}NH_4C$ and 1 mM IPTG). Expression was carried out at 15 °C until all glucose and ammonium chloride was used up. Although ArtM was successfully produced in this initial set-up, protein yield was not sufficient.

Protein yield should be increased by use of larger preculture volumes. As it was not possible to handle more than 8 L of volume at once, an alternative was to grow precultures to higher cell densities before culture condensation and target protein expression. To additionally circumvent the problem of co-

induction of the target gene with induction *mazF* by IPTG, the *artM* gene was cloned into the pASK-IBA3plus vector harboring an aTc inducible promotor that is tightly regulated and tunable by concentration of the inducer. The use of the pASK-IBA3plus-artM as expression plasmid also abolished the need for coldshock treatment and enabled efficient expression at 30 °C, which had already proven optimal in previous expression trials for ArtM. To estimate the optimal aTc concentration for induction, concentrations between 3 and 15 µg/ml were tested (estimated from the pCold(tet) and pASK manual). Thus, in an optimized protocol using 20x culture condensation, 8 L of preculture (8 x 1L in 2L HY flasks) were grown overnight to cell densities of around 2.3 OD_{600}. MazF production was then induced by 1 mM IPTG for one hour, before the cells were collected by centrifugation at 3000 xg (at 20 °C) and resuspended in 400 ml (2 x 200 ml in glass flasks) isotopically enriched M9 expression medium (also containing 1 mM IPTG). After 30 min, expression of ArtM was induced with 15 µg/ml aTc and carried out at 30 °C until all glucose was used up.

Isolation and solubilization of the membrane fraction was then performed as described for ArtMP using standard buffer based on 100 % H_2O for maximum proton backexchange at labile sites.

3.4.2.4   *Co-purification of ArtM with His$_6$-ArtP*

For purification of affinity-tag free ArtM, the solubilized membrane fraction was mixed with 20 mg pure His$_6$-ArtP and the final DDM concentration was adjusted to 0.5 % w/v by addition of detergent-free standard buffer. For assembly of the complex, the mixture was incubated at room temperature for 1 h under gently mixing. The solution was then used for Ni^{2+}-affinity chromatography and excess ArtP was subsequently separated from assembled ArtM-P by gel filtration with buffer of the desired D/H ratio. The flow rate was 0.5 mL/min and 2 mL elution fractions were collected after a void volume of 80 ml.

3.4.3   **SDS polyacrylamide gel electrophoresis (SDS-PAGE)**

Protein samples were analyzed by discontinuous SDS-PAGE using resolving gels with 15 % polyacrylamide. The electrophoretic mobility of proteins negatively charged by adsorption of SDS molecules is determined by the molecular sieve effect of the polyacrylamide gel. Roughly, the migration speed of the proteins is reciprocally proportional to the logarithm of their molecular weight.

Gels were prepared with the following recipe:

Resolving gel

15 % Rotiphorese® Gel

370 mM Tris-HCl, pH 8.8

0.05 % SDS

0.07 % APS

+ TEMED (to start polymerization)

Stacking gel

5 % Rotiphorese® Gel

80 mM Tris, pH6.8

0.1 % SDS

0.05 % APS

+ TEMED (to start polymerization)

20 µl of protein sample were mixed with 5 µl of 5x loading buffer and 10 µl of this mix were applied per gel pocket. Electrophoresis was performed at 200 V until the MW marker had reached the bottom of the gel. The gel was separated from the chamber and the glass plates and incubated in staining solution for 1 h before changing into destaining solution. Pictures of the electrophoresis gels were taken with a Gel iC imager by INTAS Science Imaging Instruments GmbH.

3.4.4   Concentration of protein samples

Proteins were concentrated with Amicon Centrifugal Filter Units (Merck), which were equilibrated with MilliQ® water or the corresponding buffer before use. Concentrating was performed at 4000 rpm with Allegra centrifuges (Beckman) at 4 °C. The protein solution was mixed carefully with a 200 µl pipette after each run to avoid protein aggregation. The flow-through was collected and used as blank in concentration measurements.

Concentration of larger volumes and exchange of buffer was carried out in concentration cells by Merck Millipore using 10,000 and 30,000 MWCO ultrafiltration membranes.

3.5   Preparation of lipids from G. stearothermophilus

G. stearothermophilus was essentially cultivated as described in Kunert, 2011[199] using the fedbatch-pro® (Dasgip) for high cell density fermentation (HCDF).

An overnight preculture (200 ml) was inoculated from a glycerol stock and cultivated in antibiotic-free rich medium (1.5 % w/v casein peptone, 0.5 % w/v soy peptone, 0.5 % w/v NaCl, pH 7.3) in a shaking flask at 160 rpm and 55 °C. This culture was used to inoculate a large preculture (1 L of rich medium), which was then grown to OD_{600} of 0.8-1 at 55 °C. The cells were collected by gentle cen-

trifugation (2500 xg, 20 °C, 15 min) and resuspended in 1 L of minimal medium prepared from the following components:

K_2HPO_4	29 mM
KH_2PO_4	37 mM
$MgSO_4$	1.7 mM
EDTA	0.1 mM
$FeSO_4$	33 µM
$ZnCl_2$	3.7 µM
$CuSO_4$	0.6 µM
$FeCl_3$	50 µM
$MnCl_2$	10 µM
$ZnSO_4$	10 µM
$CoCl_2,$ $CuCl_2$, $NiCl_2$, $NaMO_4$,	
$NaSeO_3$, H_3BO_3	2 µM each
Glucose	3 g/ L
NH_4Cl	1.25 g/ L

(pH was adjusted to 7.4 using NaOH;

medium composition adapted from Studier, 2005[206] and Al-Qodah, 2006[209])

The culture was distributed evenly into four 400 ml reactor cells tempered to 52 °C and 100 µl antifoam solution were added to each reactor. Cultivation was performed for around 20 hours and while keeping the pH at 7.4 (by NaOH) and monitoring of the oxygen consumption during cell growth. Oxygen supply was kept at 20 sl/min by automatically adjusting the speed of a magnetic stirrer (between 500 and 1000 rpm) in response to growth behavior. After decrease of the oxygen content to 50 % followed by an increase to 70 % (indicating that all C and N source was used up), the C/N-feed (250 g/L glucose, 62.5 g/L NH_4Cl, prepared in minimal medium, pH 7.4) was automatically started. During fermentation glucose and ammonium chloride concentrations were checked with test kits (Merck) while cell density was monitored photometrically at 600 nm. When all C and N sources were used up, cells were harvested by centrifugation (5000 xg, 4 °C) and stored at -20 °C. About 6.5 g cells were obtained from 250 ml culture.

10 - 20 mg of lipids were obtained from 1 g of cells following a protocol by Folch, *et al.* 1957[210]. The lipids were stored in chloroform at -20°C.

3.6 Reconstitution of ArtMP into native lipids

For preparation of ssNMR samples, the lipid reconstitution was carried out in a dialysis set-up as described in Lange, 2008[211] and Kunert, 2011[199]. To remove all traces of chloroform, the lipids were

dried in a glass vessel under a constant nitrogen stream. They were then dissolved in an ultrasound bath for 2 h in 50 mM Tris pH 8.0, 150 mM NaCl, 2 % n-octyl-β-D-glucopyranoside (OG), adjusting a final concentration of 5 mg lipid/ml. ArtMP (at 2 mg/ml in standard buffer with 0.4 % DM) was mixed with the OG-dissolved lipids in a lipid-to-protein ratio of 1:2 (w/w) and the mixture was transferred into dialysis tubing with a MWCO of 6-8 kDa.

The first sample of ArtMP was prepared as described in Kunert, 2011[199] using reco buffer 1 at a D/H ratio of 70/30 % (see 3.1.5). The dialysis volume was 1 L and 5 g of preincubated biobeads were added and exchanged every 3 days to remove all detergent and accelerate the lipid reconstitution of ArtMP. This process was monitored SDS-PAGE. For [1]H-detected experiments, proton exchange should be increased at slightly acidic buffer conditions, which is why the pH of the dialysis buffer was decreased to 6.7 for the last two days before the sample was harvested at 20.000 xg and 4 °C.

Sample 2 was prepared as described above, followed by an additional washing step with HEPES-based buffer (reco buffer 2 (see 3.1.5).

All other samples were prepared using reco buffer 1 (7-14 days) and 2 (4-7 days) as listed under 3.1.5. The final D/H ratio for ^{1}H-detected ssNMR experiments was 70/30 % at 20 kHz MAS and 40/60 % at 40 (and 37) kHz MAS. For nucleotide-containing preparations, 4 mM nucleotide were added to the reconstitution buffers.

The samples were dissolved in about 200 µl of reco buffer to avoid and storage at 4°C until further use. For ssNMR measurements, the liquid was removed by ultracentrifugation at 45.000 rpm and the protein-lipid sample was transferred into zirconia rotors (3.2 and 1.9 mm, obtained from Bruker).

3.7 Transmission electron microscopy (TEM)

Lipid-reconstituted ssNMR samples were screened for crystalline regions in collaboration with Dr. D. Lorenz at the FMP, Berlin. Diluted aliquots from reconstitution set-ups were transferred onto carbon-coated EM grids and negatively stained with 5 µl of 2 % uranyl acetate. Excess uranyl acetate was removed carefully with lint-free paper wipes before the grid was washed with 5 µL H_2O. Measurements were performed with an EM902A (Carl Zeiss) and a maximum acceleration voltage of 80 kV.

3.8 ATPase assay

The ATPase activity of detergent-solubilized ArtMP-J was determined in an assay that detects free inorganic phosphate (P_i) by a colorimetric reaction with ammonium molybdate, which can be quantified at 750 nm. This method was described for lens ATPases by Chifflet, et al., 1988[13] and was miniaturized and adapted for ABC transporters by Nikaido et al., 1997[212]. For ArtMP-J, the assay was performed as described in Kunert, 2011[199]. Briefly, samples of 120 µl contained 10 µg ArtMP (in standard buffer + 0.4 % DM), 50 µg ArtJ and 1 mM arginine in standard buffer. This translates to a 17-fold molar excess of ArtJ over $ArtM_2P_2$. The sample was preincubated at 55 °C for 1 min before the reac-

tion was started with addition of 3 mM ATP and 5 mM $MgCl_2$. Activity at 55 °C was assayed for four minutes taking 25 µl aliquots (at 1, 2, 3 and 4 min), which were mixed with 25 µl of 12 % SDS solution in a microwell plate to stop the enzymatic reaction. The colorimetric reaction was performed by addition of 50 µl of solution A (3 % ascorbate in 1N HCL; 0.5 % ammonium molybdate). After 5 min of incubation, the reaction was stopped by addition of 75 µl of solution B (2 % sodium citrate, 2 % sodium arsenate, 2 % acetic acid). Absorbance at 750 nm was measured after 20 min using a Safire microplate reader (Tecan). The amount of hydrolyzed ATP (which equals the amount of liberated P_i) was calculated from the concentration of free phosphate using Na_2HPO_4 as standard.

To exclude false positive results by Pi impurities in the reaction components (ArtMP, ArtJ, buffer, $MgCl_2$, ATP), all components as well as the basal activity of ArtMP were analyzed in control measurements.

3.9   Analytical ultracentrifugation

Sedimentation experiments were performed using a Beckman Optima XL-I analytical ultracentrifuge equipped with UV absorbance and interference (IF) optics (675 nm). Two-sector titan or six-sector Epon cells were utilized for SV and SE experiments, respectively. The sample and reference sectors of the cells were filled with protein solution and buffer in dialysis equilibrium.

Rotor speed was 45,000 rpm for SV experiments at 25°C. Data were acquired using interference absorbance detection at 695 nm, with radial increments of 0.01 cm and regular time intervals. Loading volume was 400 µL of 39 and 129 µM ArtP in standard buffer with $MgCl_2$.

SE experiments were performed with rotor speeds of 10,000, 14,000 and 18,000 rpm for 24 h each. Approach to equilibrium was followed by data acquisition every other hour. Loading volume was 100 µL of 25, 50, 50, 75, 100, 125, 150, 200, 250 and 300 µM ArtP or ArtP_162A in standard buffer supplemented with a 10-fold molar excess of $MgCl_2$ and nucleotide. Rotor temperature for all experiments was 20°C.

Data was evaluated using the software SEDFIT40 for SV experiments and, additionally, SEDPHAT41 for SE experiments essentially as described in as described by Schuck *et al.*, 2000 2004[213,214]. Buffer density and viscosity as well as partial specific volume of the protein were calculated using SEDNTERP.42[215].

Partial specific volume v-bar:	0.7448 ml
Buffer density ρ:	0.99823 g·cm^{-3}
Buffer viscosity η:	0.01002 N·s·m^{-2}
MW of ArtP:	27,890.5 Da

SE experiments were best fitted with a two-component system with the lower component (M1) set to the MW of monomeric ArtP while the second component M2 was a floating parameter separately fitted for each protein:nucleotide combination.

3.10 Isothermal titration calorimetry (ITC)

Binding of natural nucleotides and analogs was assayed in an ITC$_{200}$ (Microcal/GE Healthcare). ArtP and detergent-solubilized ArtMP were dialyzed against 1000x volume of standard buffer (+ 0.4 % DM in case of ArtMP). Stock solutions of nucleotides were prepared in 1M Tris pH 8.0, 4.3 % glycerol, which were used to prepare the injectant solutions by dilution with the dialysis buffer used for protein dialysis. The solutions were filter sterilized to avoid artefacts by lints or protein aggregates. All experiments were carried out at 30 °C by injecting nucleotide solution (300 to 1400 μM) into protein solution (70-110 μM) in the sample cell (201.9 μl volume). The rotation speed of the syringe was 1000 rpm for experiments with ArtP and 500 rpm for ArtMP (to avoid extensive foaming caused by the detergent). Reverse titrations were not possible as the protein concentrations could not be increased as would have been necessary for these experiments. In a standard experiment using constant volume titrations, 25 titrations of 1.5 μl nucleotide were injected into protein solution adjusting injection intervals so that full return of the signal to the base line was ensured. The very first titration was only 0.5 μl and was omitted in data analysis. Control experiments to analyze dilution effects of nucleotides where performed by titration nucleotide in the sample cell filled with standard buffer. Data was integrated with NITPIC[216] and baseline-corrected manually if necessary. Analysis and fitting to a 1:1 binding model was performed separately and globally (for experiments of the same protein/ligand combination) with SEDPHAT v10.58[217]. Figures were prepared with ORIGIN® and GUSSI 1.0.8d[218]. The parameters obtained from ITC experiments are depicted in Figure 20.
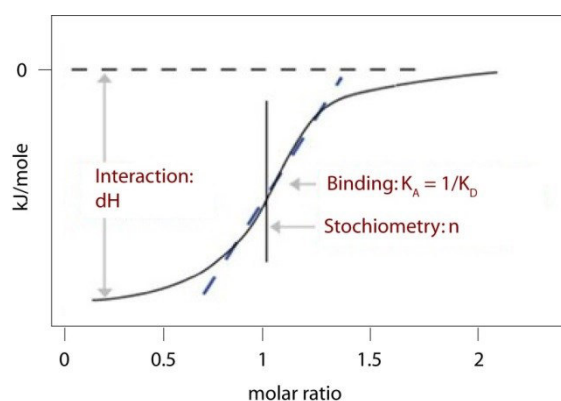
Figure 20: Extraction of interaction parameters from ITC isotherms The figure was adapted from http://www.huck.psu.edu/facilities/calorimetry-up/guides/itc).

To obtain thermograms that better spanned the plateau regions, experiments with increasing titration volumes (from 0.5-2.3 µl) were carried out. The difference in protein saturation with ligand is illustrated in Figure 21.As free [L_0] is not >> [P_0] in these experiments, the simplified approximation given by

$$\frac{[PL]}{[P_0]} = \frac{[L]}{K_D + [L]}$$

Eq. 18

cannot be used to estimate saturation. Instead, the saturation was calculated from the more general quadratic equation that is solely based on K_D, P_0 and L_0.

$$[PL]^2 - ([L_0] + [P_0] + K_D)[PL] + [P_0][L_0] = 0$$

Eq. 19

Of the two solutions, only one is reasonable:

$$[PL] = \frac{([L_0] + [P_0] + K_D) - \sqrt{([P_0] + [L_0] + [K_D])^2 - 4[P_0][L_0]}}{2}$$

Eq. 20

The ratio of protein/ligand complex can thus be calculated from:

$$\% \ saturation = \frac{[PL]}{[P_0]} \cdot 100$$
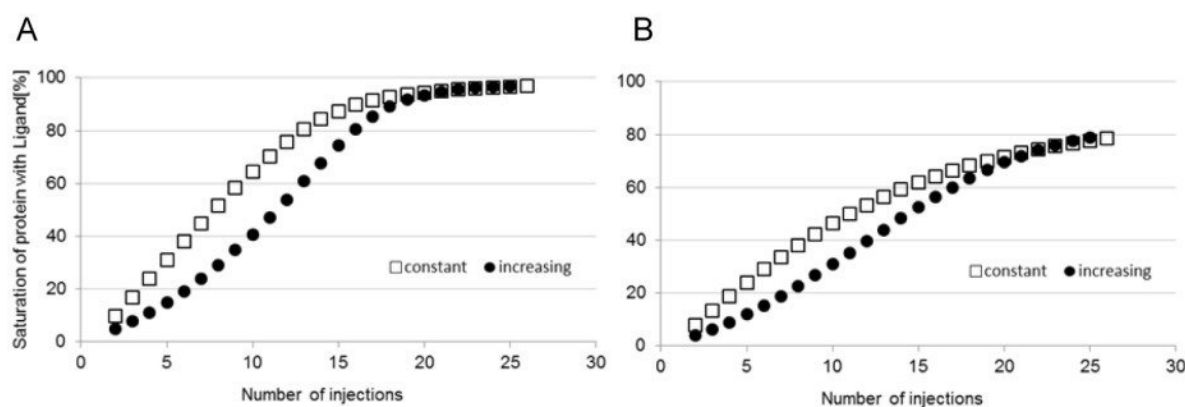
Eq. 21

Figure 21: Protein saturation with ligand in ITC experiments using constant and increasing volume injections. Examples were calculated with a protein concentration of 100 µM and a ligand concentration of 1000 µM. **A** Example for an interaction with a K_D of 2.5 µM **B** Example for an interaction with a K_D of 25 µM

3.11 Solution-state NMR

TROSY (Transverse Relaxation-Optimized Spectroscopy[219]) experiments for triple-labeled ArtP were performed in collaboration with B. Schlegel, FMP Berlin at 600 MHz and 300 K. Protein concentration was 100 µM in H_2O-based standard buffer. 5 mm NMR tubes (Norell®) were filled with 500 µl of sample and 10 % D_2O were added for deuterium lock. All samples were prepared separately using the same stock solutions for buffers and additives like $MgCl_2$.

For nucleotide binding experiments with ATP, the nucleotide was added directly before the measurement to avoid hydrolysis prior to the NMR experiment (resulting from a potential residual ATPase activity of ArtP or from autohydrolysis).

All spectra were set-up and processed in Topspin 3.1 (Bruker). Further analysis was carried out using CcpNMR Analysis (Vranken, the CCPN DATA MODEL, 2005) or Sparky 3.1. Figures were prepared with Adobe Illustrator.

3.12 MAS solid-state NMR

Analogous to solution NMR, all spectra were set-up and processed in Topspin 3.1 (Bruker). Further analysis was carried out using CcpNMR Analysis (Vranken, the CCPN DATA MODEL, 2005) or Sparky 3.1. Figures were prepared with Adobe Illustrator.

3.12.1 ^{1}H-detected MAS ssNMR

Initial experiments on ArtMP (sample 1, D/H 70 /30 %) comparing CP- and INEPT transfer steps in [1]H-detected HN-correlation experiments were carried out with Dr. M. Hiller, FMP Berlin. Spectra were recorded on at 700 MHz, 20 kHz MAS and 275 K with pulse sequences by Dr. Rasmus Linser[60,220]. The INEPT- and CP-based spectra were recorded with 512 and 160 scans/increment. Qsine window functions were used for processing of both dimensions.

The 2D and 3D versions of the hCaNH and dCaNH experiments for the ArtMP sample 2 (D/H 70/30 %) were recorded with Dr. A. Nieuwkoop at 700 MHz, 20 kHz MAS and 295 K. The 2D experiments were acquired for 15.8 and 15.5 h, while the 3D versions took 96 and 116 h. 2D and 3D spectra were processed with 60° and 80° shifted sine-bell functions in the ^{13}C and ^{15}N dimensions.

The 2D and 3D CP-based experiments of ArtMp (sample 5, D/H 40/60 %, 37 kHz MAS) and ArtmP (sample 3, D/H 40/60 %, 40 kHz MAS) as well as a set of 3D experiments (hCaNH, hCoNH, hCaCbNH) of ArtmP (sample 3, D/H 40/60 %, 40 kHz MAS) were recorded with Dr. A. Nieuwkoop at 295 K at 900 MHz. The 3D spectra at 40 kHz were averaged for about 7 days each.

3.12.2 ^{13}C-detected MAS ssNMR

The 2D CC correlated experiment (with 100 ms DARR mixing) for Art^{13}M^{15}P (sample 5, D/H 40/60 %) was recorded by Dr. A. Nieuwkoop at 800 MHz, 17777 Hz MAS and 275 K.

3.13   Evaluation and quantification of chemical shift changes

Amide protons are sensitive monitors for changes of the chemical environment of amino acid residues, which are reflected by changes in chemical shift. To evaluate effects from variation of buffer substances and pH but also to quantify effects resulting from presence of nucleotide, the chemical shift perturbation of peaks in solution NMR TROSY spectra and ^{1}H-detected INEPT-based ssNMR spectra of ArtP and ArtmP were calculated.

Williamson recently reviewed various ways to calculate the combined chemical shift perturbation (δ$_{comb}$), which all take into account that the peaks of glycines respond slightly differently to changes in the environment compared to all other residues[221]. It was concluded that Eucledian weighting according to

$$\delta_{comb} = \sqrt{\frac{1}{2}[\delta_H^2 + (\alpha \cdot \delta_N^2)]}$$ Eq. 22

with $\alpha_{gly} = 0.2$

and $\alpha_{other} = 0.14$

was most appropriate.

To evaluate the effects found in presence of nucleotide, the following threshold values were used:

no effect $0\ ppm \leq \delta_{comb} < 0.03\ ppm$

weak effect $0.03\ ppm \leq \delta_{comb} < 0.06\ ppm$

moderate effect $0.06\ ppm \leq \delta_{comb}$

Peaks were grouped into a fourth category (strong effects), if peak maxima could not be defined confidently because of a shift to crowded regions or extreme loss in intensity.

3.14 Protein structure illustration and simple modeling

Homology modeling for ArtM

For a simple model of the ArtM monomer, Phyre2 (<u>P</u>rotein <u>H</u>omology/analog<u>Y</u> <u>R</u>ecognition <u>E</u>ngineV 2.0) was used[222,223]. This server (http://www.sbg.bio.ic.ac.uk/phyre2/html/page.cgi?id=index) combines information from the SCOP (Structural Classification of Proteins) and PDB data bases. The amino acid sequences of deposited structures are scanned against a non-redundant sequence database. The correlated information about sequence and secondary structure is then stored in a so-called 'fold library'. For structure prediction, that is purely based on the amino acid sequence of the target protein, pairwise sequence alignments against the non-redundant sequence database using PSI-Blast are generated in multiple iterations. The phyre server then integrates three different programs (Psi-Pred, SSPro, JNet) for secondary structure prediction differentiating between α-helical, β-strand or coiled conformation. The sequence-specific results obtained by these tools are combined into a consensus prediction, which is subsequently cross-checked against the 'fold library' by a 'profile-profile' alignment algorithm. The highest scoring (best 10 %) alignments chosen to calculate full 3D models of the query protein. Missing loop regions are constructed with the help of a 'loop library' and sidechain orientations are corrected using a 'rotamer library'. The final model, obtained as a PDB file in combination with other information about alignments and secondary structure predidtion, can be evalutated with the 'Phyre Investigator' (in beta state).

Simple models for the ArtM$_2$P$_2$ complex

Very basic models of ArtM$_2$P$_2$ were created by superimposing isolated ArtM and ArtP subunits onto the corresponding domains in X-ray structures of the *E. coli* maltose transporter. The structures with PDB codes 3RLF, 3PUV and 3FH6 were used as templates to model open and closed states. For monomeric ArtP, the isolated chain A (including the Mg^{2+} and AMPPNP) of the 3C41 X-ray structure was used. No further energy minimization steps were performed.

This simple modeling as well as protein structure analysis and preparation of figures was carried out with PyMOL v1.5 (DeLano Scientific LLC, San Francisco, USA).

3.15 Online tools, data bases and software

Sequence and structure data was downloaded from the following data bases:

Protein Data Bank	http://www.rcsb.org/pdb
Protein Data Bank of Transmembrane Proteins	
(PDBTM)[10]	http://pdbtm.enzim.hu/
ExPASy Molecular Biology Server	http://www.expasy.ch
Uniprot Protein Knowledgebase	http://www.uniprot.org
LIPID MAPS Structure Database (LMSD)[49]	http://www.lipidmaps.org/data/structure/

For analysis of DNA and protein sequences the online tools *TRANSLATE* (ExPASy) and *ALIGN* (Genestream) were used. Primers were designed with *Geneious* (Biomatters Limited, USA). Sequence alignments were performed with *Clustal-Omega* and used for the creation of figures with the openly accessible *ESPript* tool[224]. Protein parameters like pI and molecular weight were calculated with *ProtParam*.

TRANSLATE	http://www.expasy.ch/tools/dna.html
ALIGN	http://xylian.igh.cnrs.fr/bin/align-guess.cgi
Clustal-Omega	http://www.ebi.ac.uk/Tools/msa/clustalo/
ESPript	http://espript.ibcp.fr/ESPript/ESPript
ProtParam	http://web.expasy.org/protparam/

4 Results

4.1 A simple model of ArtMP to guide NMR studies

A basic homology model of ArtMP was established to interpret the effects of nucleotide binding on a structural level and support the characterization of the ArtM/ArtP interface. The structure of monomeric ArtM was predicted using the Phyre algorithm as described in 0, which performs alignments of structural features derived from the amino acid input sequence in comparison to published structures in the PDB. The TMDs of the molybdate transporter from *Archaeoglobus fulgidus* and *Methanosarcina acetivorans* (2ONK[225] and 3D31[160]) as well as MalF from the *E. coli* maltose transporter (2R6G[143]) and MetI from the *E. coli* methionine transporter (3DHW[125]) were identified as possible structural templates for an ArtM model.
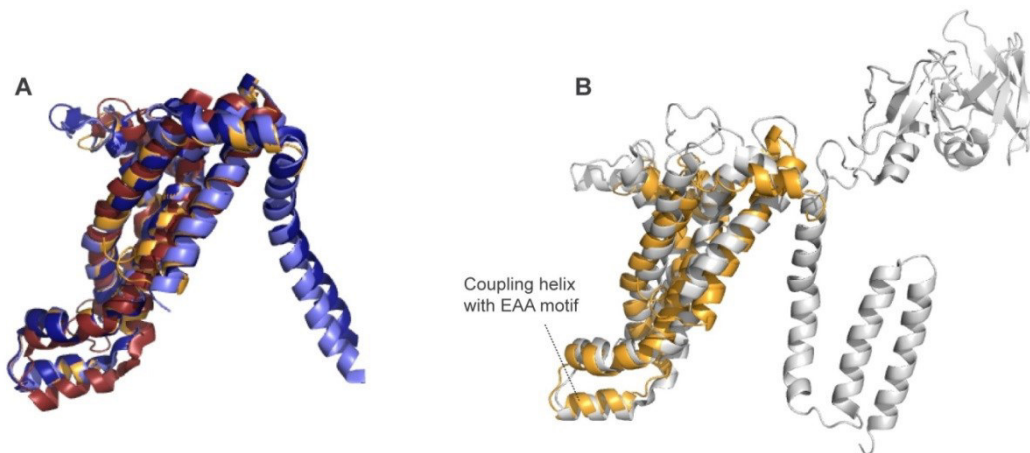

Figure 22: Overlays of the modeled ArtM monomer and structurally related TMDs of different (full-length) type I importer structures. **A** The monomeric model of ArtM is depicted in orange, while MetI (3DHW), AfModB (2ONK) and MaModB (3D31) are colored in dark red, light blue and dark blue, respectively. **B** The overlay of ArtM with MalF (grey, 2R6G) demonstrates the differences between the two domains, including 3 additional TMH in MalF as well as a large extracellular loop region that binds the SBP MalE. In this structure, MalK carried a mutation enabling stable crystallization of a closed state with ATP bound, while all other structures come from open conformations that were crystallized with ADP or in nucleotide-free environment. The location of the EAA motif is indicated.

While ArtM only has five TMH, all TMDs of the mentioned transporters excluding MetNI, possess an additional sixth helix which in all structures reaches over to the second TMD monomer. Notably except for ArtMP and AfModBC, all other transporters also contain a large regulatory domain attached to the NBD. Superpositioning of two independent ArtM monomers on the MalF and MalG subunits in the transition state structure of the *E. coli* maltose transporter (3RLF) led to a model for the closed ArtM dimer (Figure 23C).
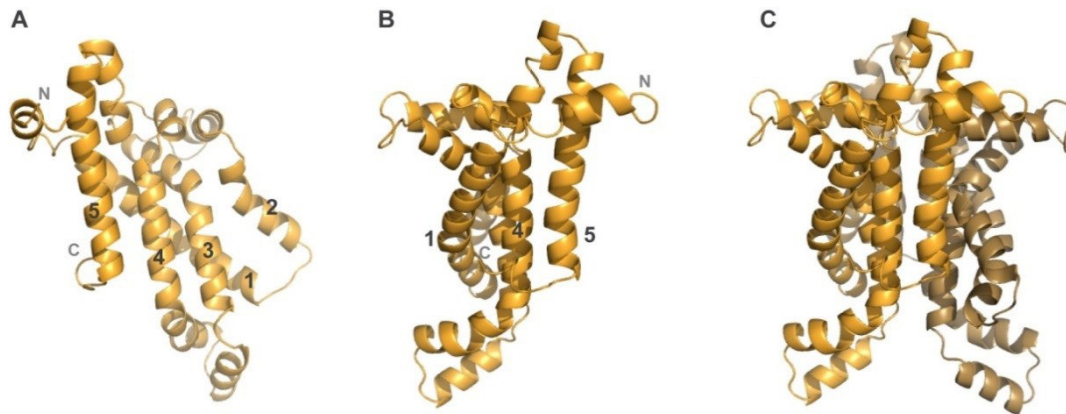

Figure 23: ArtM monomer and dimer arrangement. A The monomeric ArtM shown from inside the translocation channel. The TMH are numbered from the N- to C-terminus as indicated. The translocation channel is mainly formed by TMH 2-5 while helix 1 wraps around the other helices holding the bundle together. **B** Sideview of the ArtM monomer. **C** Dimeric arrangement of ArtM when plotted onto the TMDs in the 3RLF structure of the maltose transporter.

From the comparison of the dimeric ArtP crystal structure (3C41) and the arrangement of NBDs in crystal structures of other full-length transporters, it can be speculated that the dimer interface in 3C41 does not represent the native arrangement that ArtP would adopt in the ArtMP complex. Thus, for a full ArtMP model in an outward-facing state, two ArtM monomers (phyre model) and two isolated ArtP monomers (chain A from 3C41 including the Mg^{2+} ion and AMPPNP) were superimposed on the corresponding subunits of the 3RLF maltose transporter structure. The full model of ArtMP is depicted in comparison to the 3RLF structure in Figure 24.
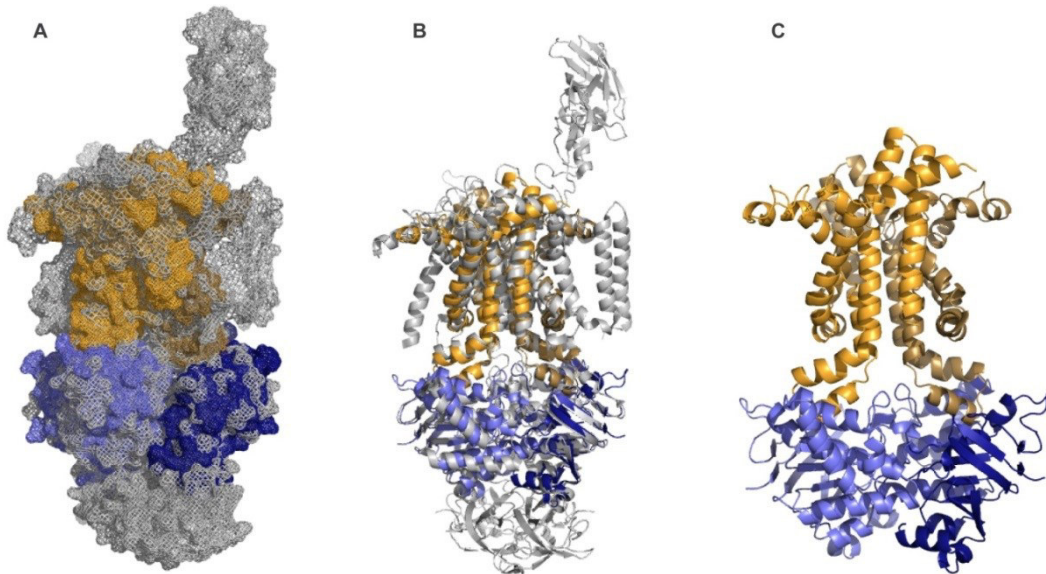
Figure 24: Homology model for ArtMP in closed configuration. **A** The ArtMP model shown in orange and sand for the TMDs and light and dark blue for the NBDs is aligned with the 3RLF structure of the maltose transporer shown in grey (MalE was omitted for better visibility). Both structures are shown in space filling mesh representation to indicate the size ratio of the transporters. **B** Overlay of the ArtMP model and the 3RLF structure in cartoon representation. **C** Final model of closed ArtMP assembled from the single subdomains.

A closer look at the ArtP-ArtP dimer interface in the ArtMP model shows that the D-loops of both monomers cross over (Figure 25A). In the dimeric 3C41 crystal structure of ArtP, the very flexible D-loop could have crystallized in a bulky conformation that might not be natural in the full structure of the complex. Thus, in the obtained ArtMP model the D-loops of both ArtP monomers are intertwined as a result of the simple rigid-body docking of the isolated subunits on the target structures (Figure 25A). To resolve the obvious artefacts of this very simple model, a collaboration for advanced homology modeling of ArtMP in a lipid environment has been established. Another difference that can be observed from the comparison of the ArtP crystal structure and the 3RLF maltose transporter structure is the orientation of the bound nucleotide (Figure 25B). The adenosine moiety shows opposite orientation and the phosphate groups (and the Mg^{2+} ion) stretch further inside the binding site. π-stacking of the A-loop and the bound nucleotide is achieved by tryptophan in MalK while ArtP uses phenylalanine (F11).
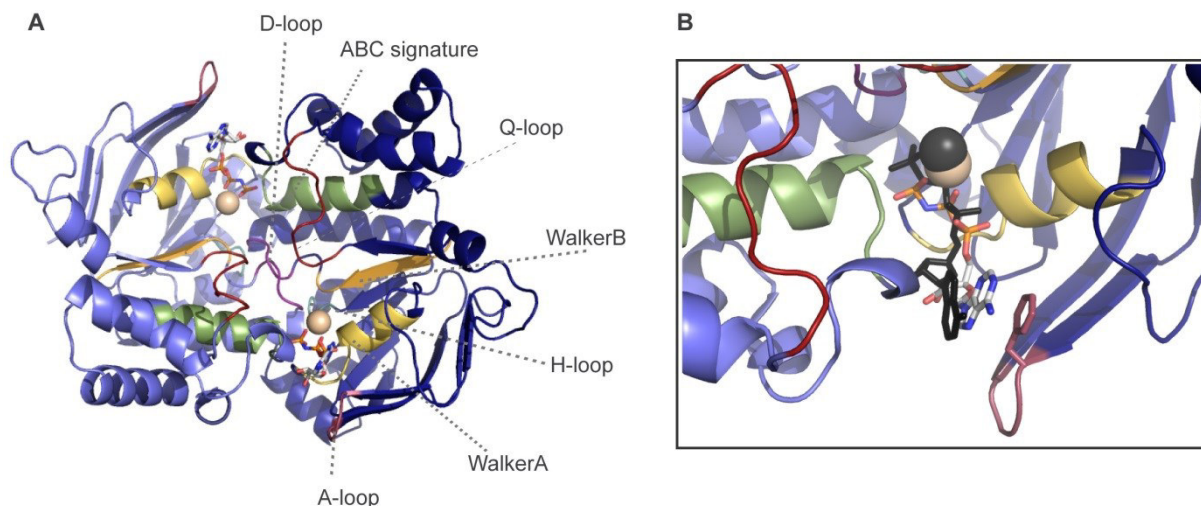
Figure 25: Top-view of the ArtP dimer in the obtained ArtMP model. A The ArtP arrangement clearly differs from the dimer observed in the 3C41 crystal structure (for comparison see Figure 19C). AMPPNP is in stick-configuration while the Mg^{2+} ion is shown as wheat-colored sphere. The flexible D-loops show a crossover in this artificial model. **B** Close-up view of a nucleotide binding site in the ArtMP model. To illustrate the different orientation of the nucleotide and the magnesium in the 3RLF structure of the MalFGK2-E transporter, these compounds are shown in dark grey for comparison. MalK has a tryptophan residue in the A-loop position where ArtP shows a phenylalanine (shown in the sticks-configuration).

4.2   Cost-efficient preparation of ssNMR samples

4.2.1   Optimized preparation of the soluble domains ArtP and ArtJ

For biophysical characterization including the nucleotide binding and dimerization behavior, expression of ArtP from pVL4 in BL21 DE3 cells was essentially performed as in Kunert, 2011[199]. Yields of isotopically-labeled protein were optimized by taking advantage of a medium condensation method described in 3.4.2.1. Using an FPLC system equipped with a Ni^{2+}-sepharose column, the yield of triple labeled protein was increased to over 110 mg/L culture compared to 80 mg protein/1L in previous studies[199]. This expression protocol could be readily adapted for production of ArtJ from pSS1 in *E. coli* BL21 DE3 Rossetta pLysS cells where yields were also improved considerably. Typical yields are summarized in Table 7.

Table 7: Protein yields for expression of ArtP in different labeling set-ups

	Yield after Ni-affinity chromatography		
Labeling Scheme	**mg/L culture**	**mg/g BWM**	**No. of experiments**
Unlabeled	266	-	1
^{15}**NH$_4$Cl**	208	27	1
^{15}**NH$_4$Cl, 1,3-^{13}C-Gly., Na$_2$^{13}CO$_3$**	204	38	1
^{15}**NH$_4$Cl, 2-^{13}C-Glyc., Na$_2$^{13}CO$_3$, D$_2$O**	228	41	1
D$_7$-^{13}C-glucose, ^{15}NH$_4$Cl, D$_2$O	116	23	1

Remarkably, yields for the separately expressed mutant ArtP_E162A remained almost constant compared to wild-type ArtP (expressed from pVL4-1), while yields dropped considerably when this mutant was expressed in combination with ArtM from pRF2_E162A (Figure 26).
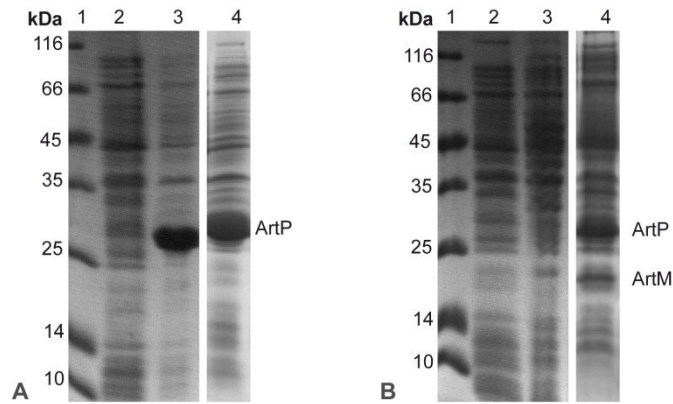

Figure 26: SDS Page analysis of expression tests for production of ArtP and ArtMP mutants and wild-type proteins. A 1-MW marker; 2-uninduced control; 3-induced ArtP_E162A (from pVL4-1_E162A); 4-induced ArtP wild-type **B** 1-MW marker; 2-uninduced control; 3-induced ArtMP_E162A (from pRF2_E162A) 4-induced ArtMP wild-type

4.2.2   Production of ArtMP for biophysical characterization

For ITC experiments and activity assays the transport complex ArtMP was coexpressed from pRF2 in BL21 DE cells as described by Kunert, 2011[199]. Yield from LB medium was about 30 mg ArtMP/L culture and could be increased further in 32Y autoinduction medium (45 mg ArtMP from 1L). A co-expressed, triple-labeled ArtMP sample was prepared to show that the assembly process from separately expressed subunits (see 3.4.2.2) does not alter the overall conformation of the ArtMP complex. Here, only 7 mg/L of triple labeled transport complex were obtained from minimal medium based on D_2O, D_7-^{13}C-glucose and $^{15}NH_4Cl$ as carbon and nitrogen sources. This translates to a decrease in protein yield of 85 % compared to expression of the unlabeled complex in rich medium.

4.2.3   Cost-efficient labeling of the TMD ArtM

Previous works showed that production and purification of the His-tagged TMD was not cost-efficient for preparation of ssNMR samples. Instead, the extremely tight binding between ArtM and ArtP could be used for purification purposes as already established by Kunert, 2011[199,202]. Following this protocol, untagged and unlabeled ArtM was produced from pBK06 in BL21 DE3 cells and co-purified by addition of his-tagged, isotopically labeled ArtP to the detergent-solubilized membrane fraction (as described in 3.4.2.3).

For preparation of ssNMR samples containing labeled ArtM with ArtP in an unlabeled or differently labeled state, the TMD had to be expressed from minimal medium. For coexpressed, isotopically enriched ArtMP, a substantial drop in yield per liter was observed (for comparison see 4.2.2). As even lower yields had to be expected for expression of ArtM with this method, costs for media would have been immense. Thus, a very cost-efficient alternative for production of labeled ArtM was established using the cSPP system (for details see 3.4.2.3). Initial expression trials were carried out from pColdIV-artM, carrying the codon-optimized, ACA-free *artM* gene, in which also the F32L mutation (present in pRF2 and pRF2 derivatives) was reversed to the wild-type phenylalanine. Although ArtM was successfully produced in this initial set-up, protein yields had to be optimized further.

As it was not possible to handle more than 8 L of preculture volume at once, an alternative was to grow precultures to higher cell densities before culture condensation and target protein expression. To additionally circumvent the problem of coinduction of the *mazF* and the target gene by IPTG, the artM gene was cloned into the pASK-IBA3plus vector harboring an aTc (anhydrotetracyclin) inducible promotor that is tightly regulated and tunable by concentration of the inducer. The use of the pASK-IBA3plus-artM as expression plasmid also abolished the need for coldshock treatment and enabled efficient expression at 30 °C, which had already proven optimal in previous expression trials for ArtM.
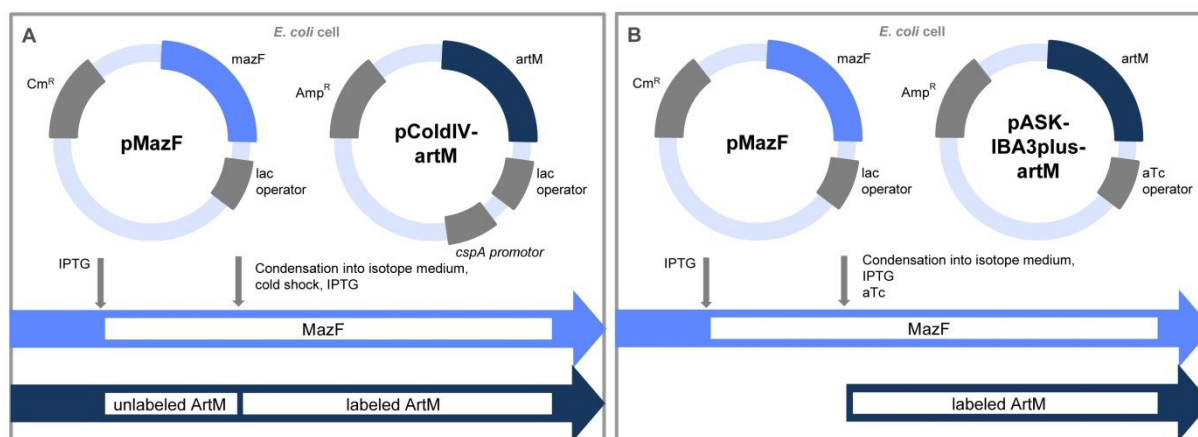
Figure 27: ArtM production with the cSPP method. A As the *artM* gene on pColdIV-artM is also induced by IPTG, a small fraction of unlabeled ArtM is produced in the conventional cSPP set-up. **B** Expression of ArtM from pASK-IBA3plus-artM is induced with aTc which avoids production of unlabeled ArtM.

During optimization of this new expression system, ArtM could be produced in the labeling schemes listed in Table 8. The yield of ArtM in mg / L expression culture was calculated from the final yield of ArtMP after copurification with ArtP.

Table 8: Protein yields for expression of ArtM in different labeling set-ups. .

Labeling Scheme	Plasmid combination	Final Yields				No. of experiments
		mg ArtMP/ L culture	mg ArtMP/ g BWM	mg ArtM/ L culture	mg ArtM/ g BWM	
Unlabeled	pBK06	35.0	1.5	16.1	0.7	1
$^{15}NH_4Cl$	pColdIV-artM/ pMazF	87.5	1.6	40.3	0.8	1
^{13}C-glucose	pColdIV-artM/ pMazF	37.5	0.6	17.2	0.3	3
D_7-^{13}C-glucose, $^{15}NH_4Cl$, D_2O	pColdIV-artM/ pMazF	17.0	0.3	7.8	0.1	5
$^{15}NH_4Cl$	pASK-IBA3plus-artM/ pMazF	58.1	0.6	26.7	0.3	1
D_7-^{13}C-glucose, $^{15}NH_4Cl$, D_2O	pASK-IBA3plus-artM/ pMazF	21.8	0.5	10.1	0.3	1

4.2.4   Preparation of solid-state NMR samples with differential labeling

For investigation of ArtMP in the natural environment, coexpressed ArtMP and reassembled ArtM-P were reconstituted into lipids isolated from *G. stearothermophilus* (as described in 3.6). Figure 28 summarizes different steps along the purification and reconstitution procedure for sample No. 5 (assembled from triple-labeled ArtM and deuterated ArtP). Excess ArtP was separated from ArtM-P by gel filtration.

The SDS-Page analysis summarizes the different steps of ssNMR sample preparation including the ArtM purification and the reconstitution process into lipids derived from *G. stearothermophilus*. In this way, next to other labeling schemes, production of triple labeled ArtM was achieved, which could be co-purified with deuterated ArtP and used for MAS ssNMR investigation. That labeling was successful and ArtM was well folded was confirmed in by ^{1}H-^{15}N CP and ^{13}C-^{13}C 2D correlation MAS ssNMR experiments (4.6.4 and 5.1). For the first time, this enabled a focus on the TDM of the transporter and will be of great relevance for analyzing the location of TMH in different nucleotide-bound states in future studies.
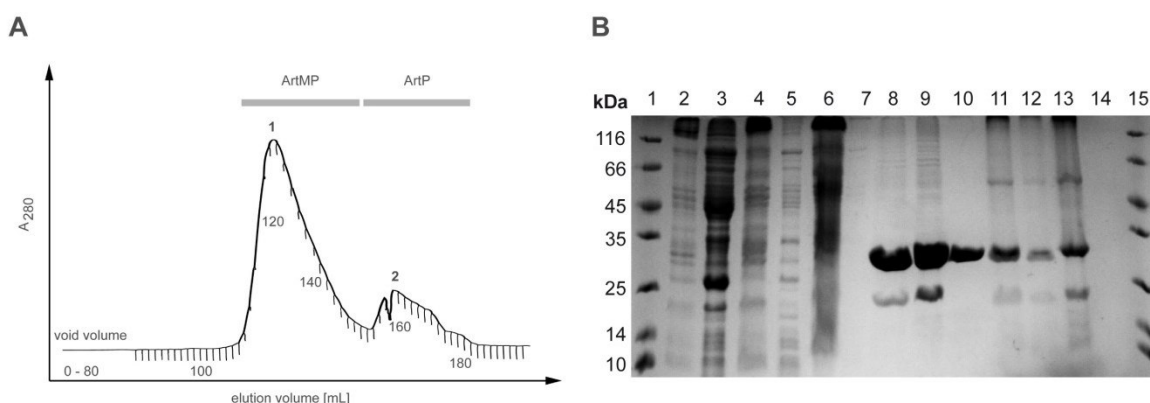

Figure 28: Preparation of the reassembled ArtM-P from single subunits for ssNMR investigation. The protein bands at 24 and 28 kDa correspond to ArtM and ArtP, respectively. **A** Gel filtration profile of reassembled ArtM-P. using a Superdex200 column at 0.5 ml/min. Void volume was 80 ml. The profile was recorded on a chart recorder and extracted graphically for this figure. **B** Preparation of ArtM$_{DCN}$P$_{D}$: membrane isolation (2-6), Ni^{2+} affinity chromatography (7), gel filtration for separation of assembled ArtMP from excess ArtP (9-10) and reconstitution in lipids (11-14). Lanes: 1-MW marker; 2-Membrane pellet of 1. UC step; 3-Supernatant (SN) of 1. UC step; 4-Membrane pellet of 2. UC step; 5-SN of 2. UC step; 6-DDM-solubized membrane fraction; 7-empty; 8-Concentrated elution fractions from Ni^{2+}-affinity chromatography after assembly of solubilized ArtM$_{DCN}$ and ArtP$_{D}$; 9-Concentrated SEC elution fractions for ArtM$_{DCN}$P$_{D}$ (Peak 1 in A);10-Concentrated SEC elution fractions for ArtP$_{D}$ (Peak 2 in A); 11-Pellet of lipid reconstitution of ArtM$_{DCN}$P$_{D}$ after 8 days in reco buffer 1; 12-SN of lipid reconstitution of ArtM$_{DCN}$P$_{D}$ after 8 days in reco buffer 1; 13-Pellet of lipid reconstitution of ArtM$_{DCN}$P$_{D}$ after additional seven days in reco buffer 2; 14-SN of lipid reconstitution of ArtM$_{DCN}$P$_{D}$ after additional seven days in reco buffer 2; 15-MW marker.

The first ssNMR sample of ArtMP (sample 1) was essentially prepared as described in Kunert, 2011[199] using reco buffer 1. Since strong sample heating especially in NMR experiments with high RF pulses was observed under these conditions, the sample was washed with reco buffer 2. This led to a significant increase in T_2 and permitted a first hCaNH experiment for initial assignment of ssNMR spectra.

For all subsequent samples, lipid reconstitution was carried out in reco buffer 1 for 7 to 14 days, as this condition was previously optimized by Kunert and Lange[199,202]. The dialysis bag with the ArtMP:lipid mixture was then transferred into reco buffer 2 for additional 4-7 days depending on the amount of sample. In total, 14 types of NMR samples were prepared in the course of this thesis (summarized in Table 9).

Table 9: SsNMR samples of ArtMP prepared during this project

No	Labeling	Final buffer	Additives	Questions	Measurements	Finished
1	DCN-ArtMP	Reco buffer 1 70 % D_2O	-	Conformation of full transporter	2D HN CP (20 kHz) 2D HN INEPT (20 kHz)	X x
2	DCN-ArtMP	Reco buffer 2 70 % D_2O	-	Conformation of full transporter, Assignments	2D CP (20 kHz) hCaNH (20 kHz)	x x x
3	DCN-ArtP / ArtM	Reco buffer 2 40 % D_2O	-	Assignments for ArtP in context of full transporter	2D HN CP (40 kHz) hCaNH (40 kHz) hCaCbNH (40 kHz) hCoNH (40 kHz) hCo(Ca)NH hCa(Co)NH	x x x x
4	DCN-ArtP / ArtM	Reco buffer 2 40 % D_2O	4 mM ADP	Effect of nucleotide	2D HN CP hCaNH (40 kHz)	
5	DCN-ArtM/ D-ArtP	Reco buffer 2 40 % D_2O	-	Conformation and assignments of ArtM in context of full transporter	2D HN CP (40 kHz) hCaNH (40 kHz) hCaCbNH (40 kHz) hCoNH (40 kHz) hCo(Ca)NH hCa(Co)NH	X

Table 9: SsNMR samples of ArtMP prepared during this project (continued)

No	Labeling	Final buffer	Additives	Questions	Measurements	Finished
6	1,3-^{13}C-^{15}N-ArtP / ArtM	Reco buffer 2	-	Effect of nucleotide, Facilitated assignment	2D HN CP 3D experiments	
7	1,3-^{13}C-^{15}N-ArtP / ArtM	Reco buffer 2	4 mM ADP	Effect of nucleotide, Facilitated assignment	2D HN CP 3D experiments	
8	1,3-^{13}C-^{15}N-ArtP / ArtM	Reco buffer 2	4mM AMPPCP	Effect of nucleotide, Facilitated assignment	2D HN CP 3D experiments	
9	D-2-^{13}C-^{15}N-ArtP / ArtM	Reco buffer 2 40 % D$_2$O	-	Effect of nucleotide, Facilitated assignment	2D HN CP 3D experiments	
10	D-2-^{13}C-^{15}N-ArtP / ArtM	Reco buffer 2 40 % D$_2$O	4 mM ADP	Effect of nucleotide, Facilitated assignment	2D HN CP 3D experiments	
11	D-2-^{13}C-^{15}N-ArtP / ArtM	Reco buffer 2 40 % D$_2$O	4 mM AMPPCP	Effect of nucleotide, Facilitated assignment	2D HN CP 3D experiments	
12	1,3-^{13}C-ArtP / ^{15}N-ArtM	Reco buffer 2	4 mM ADP	Characterization of the ArtM/P domain interface	REDOR	x
13	D-2-^{13}C-ArtP / ^{15}N-ArtM	Reco buffer 2	4 mM ADP	Characterization of the ArtM/P domain interface	REDOR	
14	^{15}N-ArtP / ^{13}C-ArtM	Reco buffer 2	4 mM ADP	Characterization of the ArtM/P domain interface, first ^{13}C resonances of ArtM, Lipid phase transition	REDOR DARR	x

4.3   Dimerization behavior of isolated ArtP - ArtP is a monomer in solution

Concentration- and nucleotide-dependent dimerization of isolated NBDs was suggested for several transporters including MJ0796 and HisP (NBD of the histidine transporter $HisQMP_2$)[212,226-228]. Although ArtP eluted as monomer (27.9 kDa calculated MW) from purification columns and showed a band corresponding to the monomeric form in SDS gels, nucleotide-induced dimerization had to be excluded, as this might produce heat effects in ITC experiments perturbing the calculation of binding constants while in solution NMR experiments, peak shifts could be wrongly interpreted as direct effects of nucleotide binding. Thus, as prerequisite for investigation of nucleotide binding to isolated ArtP by ITC and solution NMR, the oligomeric state of ArtP in absence and presence of nucleotides was analyzed by AUC in collaboration with Dr. Marcel Jurk. All runs were carried out in standard buffer supplemented with 3 mM $MgCl_2$ for SV and 10 mM in SE experiments.

ArtP homogeneity in absence of nucleotide was investigated at two concentrations (39 and 129 µM) in an initial sedimentation velocity experiment at 45,000 rpm and 25 °C. No impurities or aggregates were detected using the highly sensitive interference (IF) optical system. The main species for the two protein concentrations were found at 2.325 and 2.332 S (Figure 29). This corresponds to a MW of 28.4 and 29.1 kDa which fits well with the monomeric molecular weight of ArtP (27.9 kDa). For 129 µM ArtP, the c(S) distribution shows an indication of a very small fraction (< 5 %) of a higher molecular weight species as indicated by the small shoulder at higher S values.
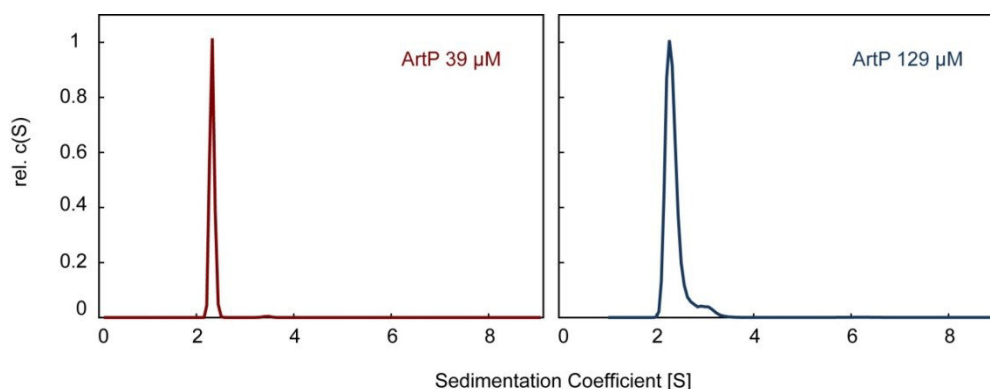

Figure 29: Relative c(S) distribution calculated from SV-data obtained for nucleotide-free ArtP. While at 39 µM a sharp peak at 2.325 S is detected, this peak is slightly broadened at 129 µM. This might indicate the starting formation of a higher molecular weight species.

Further SV experiments of ArtP in presence of a 10-fold molar excess of AMPPCP were also performed but UV absorbance had to be used in this (because of defective IF optics). Due to the overlap of the protein signal (detected at 290 nm) and the nucleotide absorption maximum at 259 nm, these experiments had to be fitted with two floating MW species. Nevertheless, also in this set-up (ArtP in combination with non-hydrolyzable AMPPCP) no hint for nucleotide-dependent dimerization was observed over a concentration range from 6-129 µM (data not shown). As it was not known if the ATP

analog AMPPCP is generally capable of inducing dimerization of isolated NBDs, the monomer:dimer equilibrium was additionally investigated with ATP as natural ligand in combination with wild-type ArtP and the hydrolysis-incompetent mutant ArtP_E162A. This was possible because neither ArtP nor ArtP_E162A showed effects corresponding to hydrolysis of ATP in ITC experiments indicating stability of ATP in these set-ups.

Sedimentation equilibrium (SE) experiments were performed at 20 °C and three speeds (10000, 14000, 18000 rpm) for 24 h each using a 9-step dilution series (300 to 25 µM) of ArtP in standard buffer. A 10-fold molar excess of nucleotide and $MgCl_2$ was chosen for all dilutions. The best fit (lowest rmsd between fit and experimental data) was achieved when using a two-component system and fixing the lower weight species (M1) to the MW of ArtP while fitting the data with a second species (M2) of unpredetermined MW. The resulting relative concentrations of M1 and M2 are plotted against the protein concentration in Figure 30. The data for 25 µM was omitted in this plot due to bad signal-to-noise ratio.
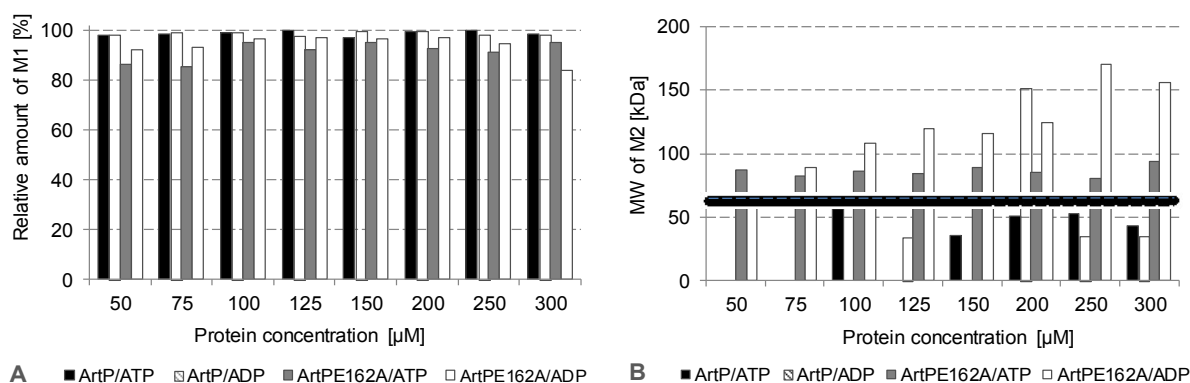

Figure 30: Results of SE experiments with ArtP and ArtP_E162 in combination with ATP or ADP. A protein concentration range of 50 - 300 µM was used with a 10-fold molar excess of $MgCl_2$ and nucleotide. **A** Relative amount of M1 (27.9 kDa) detected over the given concentration range. The lowest amount (83.9 %) of monomeric ArtP was found for 300 µM ArtP_E162E/ADP. **B** Calculated MW of M2 for each set-up. Missing bars indicate that a high molecular weight species (of over 1.5 MDa) was obtained from fitting M2 in these experiments, although this portion was extremely small (< 2 %).

Neither ADP nor ATP was able to induce dimer formation of ArtP in presence of 10 mM $MgCl_2$. Dimerization was also not observed for ArtP_E162A, although a larger portion of a higher weight species (M2) was present here. Nevertheless, this species did not correlate with the MW of dimeric ArtP but corresponded to higher molecular weight species that are more likely to reflect different forms of unspecific aggregates (ranging from 70 to 170 kDa). The higher molecular weight species M2 was invariable with concentration and did not increase significantly with higher concentrations. Furthermore, the same putative aggregation effect was observed for ArtP_E162A in both presence of ATP and ADP, indicating a mutein-specifc aggregation behavior rather than a specific and nucleotide de-

pendent oligomerization. Thus, ArtP regardless of the tested construct and condition is essentially monomeric at the protein concentrations used for further ITC and solution NMR experiments.

4.4 Nuleotide binding by ITC: natural and unnatural nucleotides show different affinities

For preparation of ssNMR samples of nucleotide-bound ArtMP, information about binding affinities is important to estimate the minimal nucleotide concentrations needed for protein saturation. Due to the broader lines in ssNMR spectra, nucleotide-dependent effects might easily be underestimated in ssNMR, when only a small portion of the transporter rests in a nucleotide-bound state.

Isothermal titration calorimetry (ITC) was used to study binding of ADP, ATP, AMPPNP and AMPPCP to the isolated ArtP domain and to detergent solubilized ArtMP at 30 °C. Concentrations of protein and nucleotide were checked photometrically using absorption maxima at 280 and 259 nm, respectively. All experiments were performed with protein solution in the sample cell and nucleotide solution as injectant. ITC injection peaks were picked with NITPIC and manually base-line corrected when necessary. Data fitting was performed with a 1:1 binding model using Sedphat v10.58 that allowed for a more sophisticated analysis of single parameters and global analysis of similar experiments. Nucleotide concentrations were verified by UV/Vis detection and are thus assumed to be accurate, while the active protein concentration was a fitting parameter. For some experiments, a substantial fraction of inactive protein was detected. During analysis, in some cases it was necessary to fix this fraction to zero for data fitting. This reduction of the active protein concentration has only a minor effect for calculation of K_D values (as K_A is calculated from the slope in the inflection point of the fitted isotherm) but leads to larger deviations in determination of the ΔH of the interaction. To obtain improved thermograms that better span the plateau regions for a more exact calculation of ΔH, experiments with increasing instead of fixed titration volumes were performed in some cases (especially for titrations with ArtMP (as described in section 3.9).
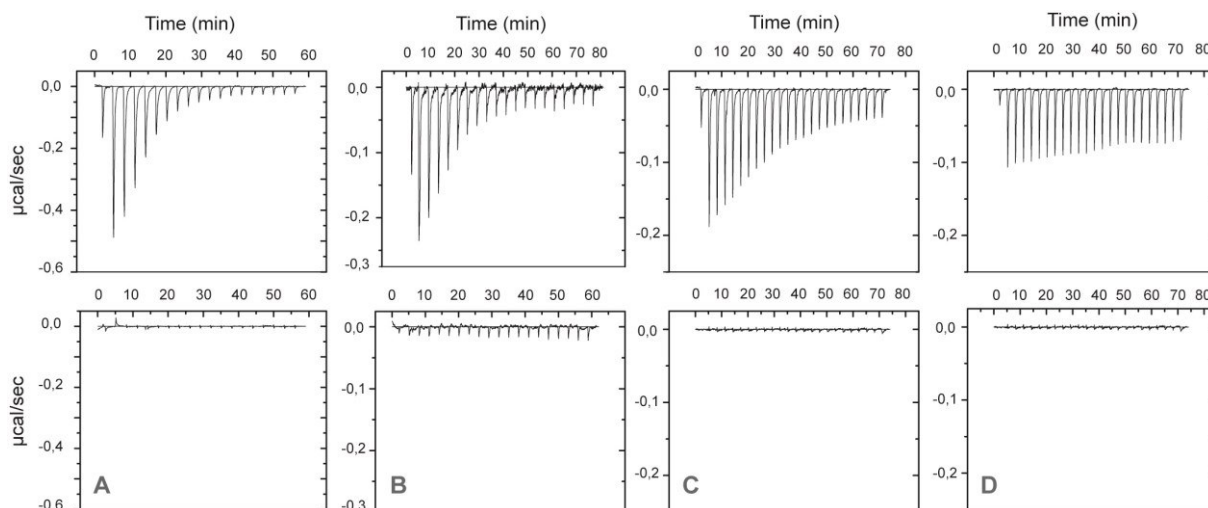
Figure 31: Examples for ITC thermograms obtained for soluble ArtP in presence of MgCl₂ with different nucleotides as injectants. A ADP (80 µM ArtP/800 µM nucleotide)/ B ATP (90/700) C AMPPNP (90/1019) D AMPPCP (90/968). The second row shows the corresponding controls titrating nucleotide solution in buffer.

Figure 31 summarizes examples for titrations of ArtP with different nucleotides in an experimental set-up using constant titration volumes. In control experiments, nucleotides showed only normal dilution effects when titrated in buffer. The amount of heat released upon binding was very different for the nucleotides. The determined dissociation constants were in the same range for the interaction of ArtP with ADP (7 µM) and ATP (6 µM). AMPPNP binding (47 µM) was lower by about a factor of 6 and AMPPCP binding (275 µM) was even weaker (Table 10). The titration of ArtP with ATP suggested a substantial fraction of inactive protein. Compared to all other titrations shown, this experiment was performed with a different batch of protein, which might account for this variation.
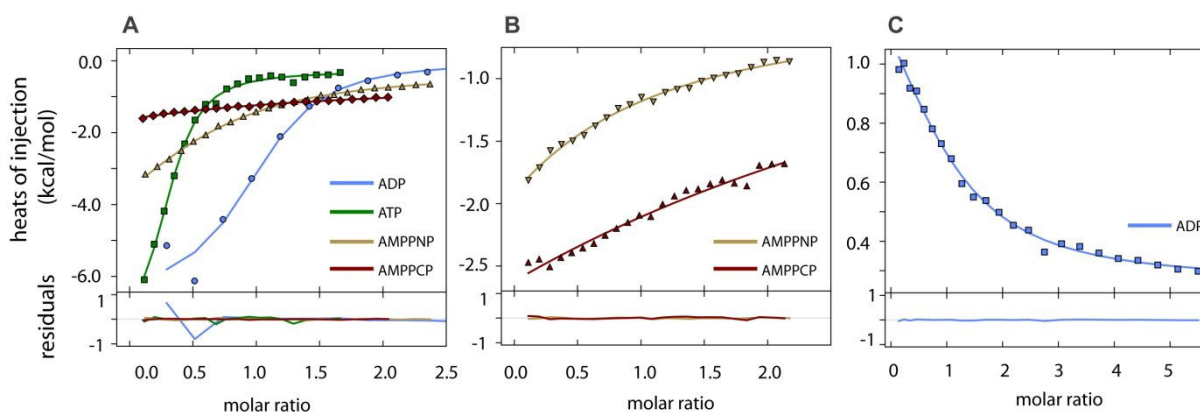

Figure 32: Examples for fitting curves obtained with Sedphat v10.58 for thermograms of A ArtP and B & C detergent-solubilized ArtMP with different nucleotides. ADP showed endothermic binding behavior with ArtMP but not with ArtP. The figure was created with GUSSI.

With detergent-solubilized ArtMP, ADP still showed strongest binding. Nevertheless, all interactions of ArtMP with nucleotides produced very small heat effects only allowed for a rough determination of K_D in these cases. Remarkably, binding of ADP to ArtMP resulted in endothermic effects while all nucleoside triphosphates led to exothermic binding behavior. For ArtP, binding effects for all nucleotides were exothermic. The results obtained from experiments with ArtP and ArtMP are summarized in Table 10.

An additional important observation was made during this ITC study. Hydrolysis of ATP or AMPPNP result in large exothermic heat releases that would easily be detected by ITC: Such effects were never observed for isolated ArtP over the time course of an ITC experiment (45-90 min). In comparison, hydrolysis activity was clearly detected when ATP was titrated into an ArtMP solution, but no corresponding heat effects were seen for ArtMP with AMPPNP. This indicates that the residual ATPase activity of isolated ArtP is negligible and that ATP and AMPPNP are stable under the buffer conditions used for these experiments.

Table 10: K_D values determined from ITC experiments with ArtP and ArtMP. 95 % confidence intervals for K_D are given in parentheses. Experiments for ArtP were performed with two different batches of protein indicated with § and $.

Protein	Ligand	Inc. protein fraction	dH (kcal/mole)	K_D (µM)
ArtP[§]	ATP	0.69	-7.7	**6** (4 - 10)
ArtP[$]	ADP	0.05	-6.5	**6** (3 - 14)
ArtP[$]	AMPPNP	0.408	-8.2	**47** (30 - 86)
ArtP[$]	AMPPCP	0 (fixed)	-3.7	**275** (64 - 1600)
ArtMP	ADP	0.34	0.6	**13** (7-25)
ArtMP	AMPPNP	0.06	-2.9	**69** (27 - 482)
ArtMP	AMPPCP	0 (fixed)	-4.6	**70** (23 - 869)

For a subset of protein/nucleotide combinations, global analysis was possible (Table 11). A trend emerged with the natural nucleotides ADP and ATP showing highest and very similar affinity. Binding of the ATP analogs AMPPNP and AMPPPCP was substantially weaker. This knowledge is important to estimate the saturation of ArtMP with nucleotides for preparation of ssNMR samples.

Table 11: K$_D$ values obtained for global analysis of multiple experiments. 95 % confidence intervals are given in parentheses. The abbreviation n.d. indicates that this value could not be determined.

Protein	Ligand	K$_D$ (µM)	No. of measurements
ArtP	ADP	**7** (4 - 12)	**4**
ArtP	ATP	**7** (2 - 31)	**4**
ArtMP	ADP	**9** (n.d.-106)	**4**
ArtMP	AMPPNP	**240** (62 - 418)	**2**
ArtMP	AMPPCP	**1100** (236 - n.d.)	**2**

4.5   Structural effects of nucleotide binding to ArtMP

4.5.1   Nucleotide binding to isolated ArtP

4.5.1.1   ArtP shows high sensitivity for buffer substance but is less affected by pH

For a structural interpretation nucleotide binding to triple labeled, isolated ArtP was assayed in TROSY experiments by solution NMR. In previous works HN resonances of ArtP were assigned in 200 mM phosphate buffer at pH 6.8 (by Dr. B. Kunert, A. Chowdhury, Dr. E. Ploskon-Arthur, see Figure 61). Nucleotide binding experiments should be carried out in Tris buffer at pH 8.0 to assure that the binding pocket is not blocked by phosphate and to minimize autohydrolysis of nucleotides as a potential result of slightly acidic pH.

In a first step, the previously obtained assignments of ArtP had to be transferred to spectra recorded in the buffer system to be used for nucleotide interaction studies. As many peaks were heavily affected by the changes in buffer, the assignment transfer was assisted by spectra recorded in Tris buffer at three different pH values (pH 6.8, 7.4 and 8.0). The combined chemical shift perturbation was calculated (as described in 3.13) was for all assigned peaks to investigate with regions in ArtP are most sensitive for solvent composition.

The change of the buffer substance showed stronger influence on peak positions than variation of pH. Switching from phosphate (pH 6.8) to Tris buffer (pH 6.8) affected surface residues all over the protein including uncharged residues like isoleucines, valines and alanines (Figure 33A). 13 peaks were absent in the Tris(pH6.8) spectrum while 21 peaks were either shifted too much or moved to crowded regions so that their peak maxima could not be assigned confidently. Thus these peaks were omitted in the subsequent analysis. The increase of pH from 6.8 to 8.0 led to signal loss for R45 and R110 and resulted in strong shifts for I63, I68, T70 and A234 that were also excluded from further analysis. Milder effects of pH change were seen for other charged residues including an aspartate (D61), glutamate (E36), arginine (R76), lysines (K9, K156) and histidine (H5) (Figure 33B).

With the described strategy 146 out of 186 original assignments could be transferred to the spectra obtained in Tris(pH 8.0). Nevertheless, large portions of the Walker A motif and the Q-loop as well as parts of the Walker B motif and the full H-loop remain unassigned and thus were not directly accessible for further interaction studies in this thesis.

Table 12: Summary of peaks and assignments for TROSY spectra of ArtP in different buffers. Potential side-chain peaks were also included. The spectrum in phosphate buffer is a standard HSQC.

Spectrum	No. of peaks	No. of assignments
Phosphate(pH6.8)	255	**186**
Tris(pH6.8)	191	**152**
Tris(pH7.4)	205	**148**
Tris(pH8.0)	210	**146**
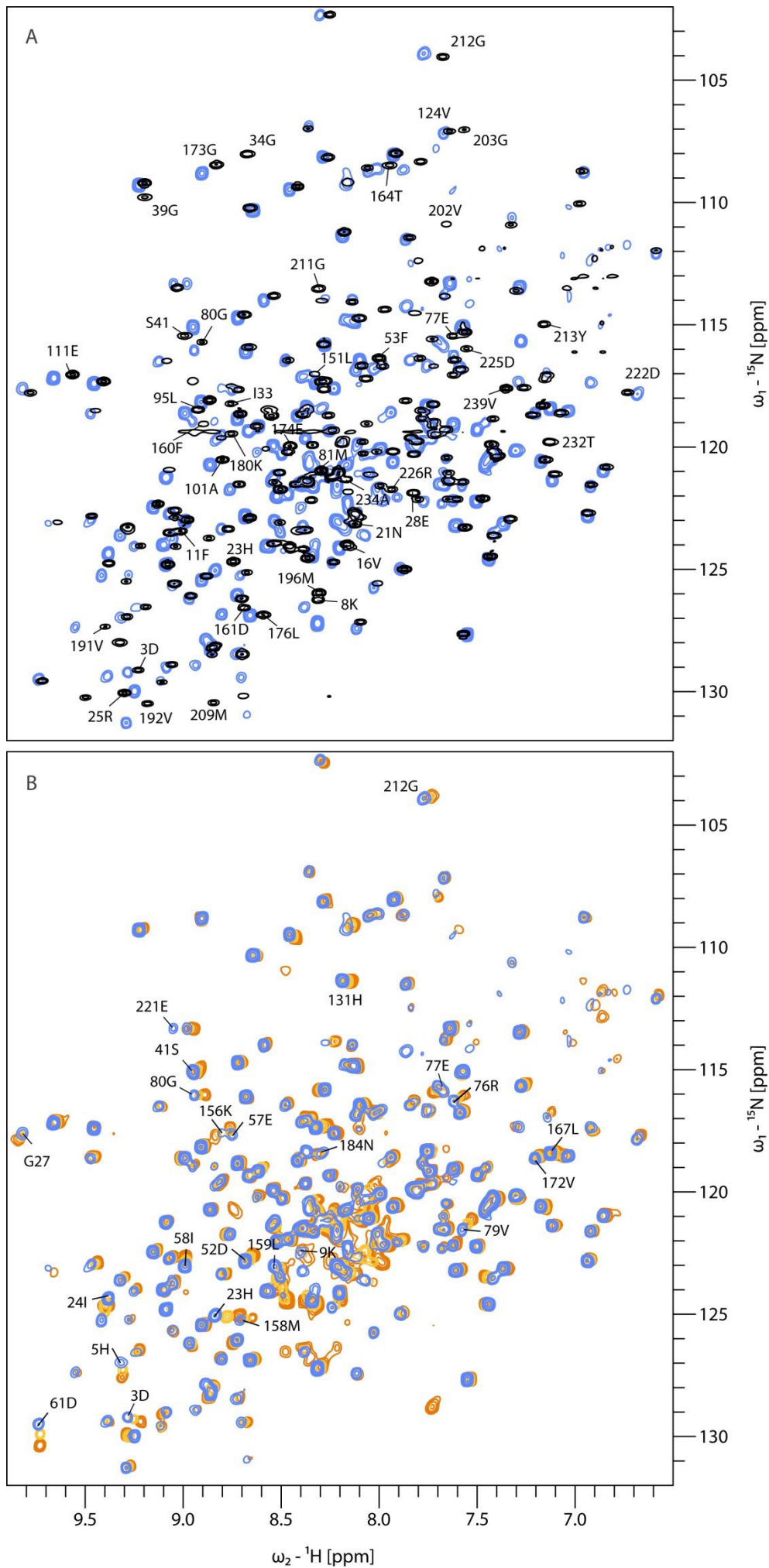
Figure 33: TROSY spectra of ArtP in different buffers. Examples for peaks that were most affected by the change of the buffer substance or pH are indicated. **A** HSQC of ArtP in 200 mM phosphate buffer (black) (provided by Dr. B. Kunert) on top of a TROSYspectrum of ArtP in Tris buffer (blue), both at pH 6.8. **B** Comparison of TROSY spectra for ArtP in Tris buffer at pH 6.8 (blue), 7.4 (yellow) and 8.0 (orange).

4.5.1.2 Mg^{2+} and nucleotide have distinct effects on soluble ArtP

Presence of Mg^{2+} affects not only the binding pocket, but also distant regions

From ITC experiments it could be concluded that the Mg^{2+} ion was essential for stable nucleotide binding, which is why binding of Mg^{2+} was first assayed separately. The presence of $MgCl_2$ led to disappearance of additional signals (e.g. E28, K68, T70, N184 and G186). These residues are all located in water accessible loops (Figure 34). Interestingly, many of the remaining residues affected by $MgCl_2$ align along the intramolecular interface of the small α-helical and the RecA-like subdomain or at the interface to ArtM. G80 and M81 for example are located at the start of the Q-loop and together with E77 and E78 come in close proximity to the coupling helix in the ArtMP model. L49 (in a loop region of ArtP next to the ArtM CH) only gives rise to a very weak peak in this experiment, but regains intensity in experiments with nucleotide present. Of the residues surrounding the Mg^{2+} ion in the nucleotide binding pocket, the catalytic E162 shows a significant shift with $MgCl_2$ while the peaks of D161 and S41 are only slightly altered.

Nucleotide effects

The effects of nucleotides were analyzed in two sets of experiments. In the first set, all samples contained equal amounts of nucleotide (0.2 mM/ 3 mM $MgCl_2$). If all nucleotides bind at the same sites with similar structural effects, the peak shifts should by strongest for the nucleotides, for which highest affinities were found in ITC experiments (ATP and ADP). In a second set of experiments, nucleotide concentrations resembling ~ 90 % saturation were used for each-set up (calculated according to 3.9) to investigate if AMPPNP and AMPPCP can substitute ATP causing the same structural effects at an identical saturation level.

Isolated ArtP does not distinguish between ATP and ADP

In the first set of experiments applying 0.2 mM nucleotide, the spectra of ArtP with ATP and ADP were almost identical, raising the question if ATP was already hydrolyzed. However, this is extremely unlikely as ATP was added directly before the measurement and residual ATPase activity of ArtP was extremely low (and not detected in ITC experiments with ArtP/ATP). Another possibility
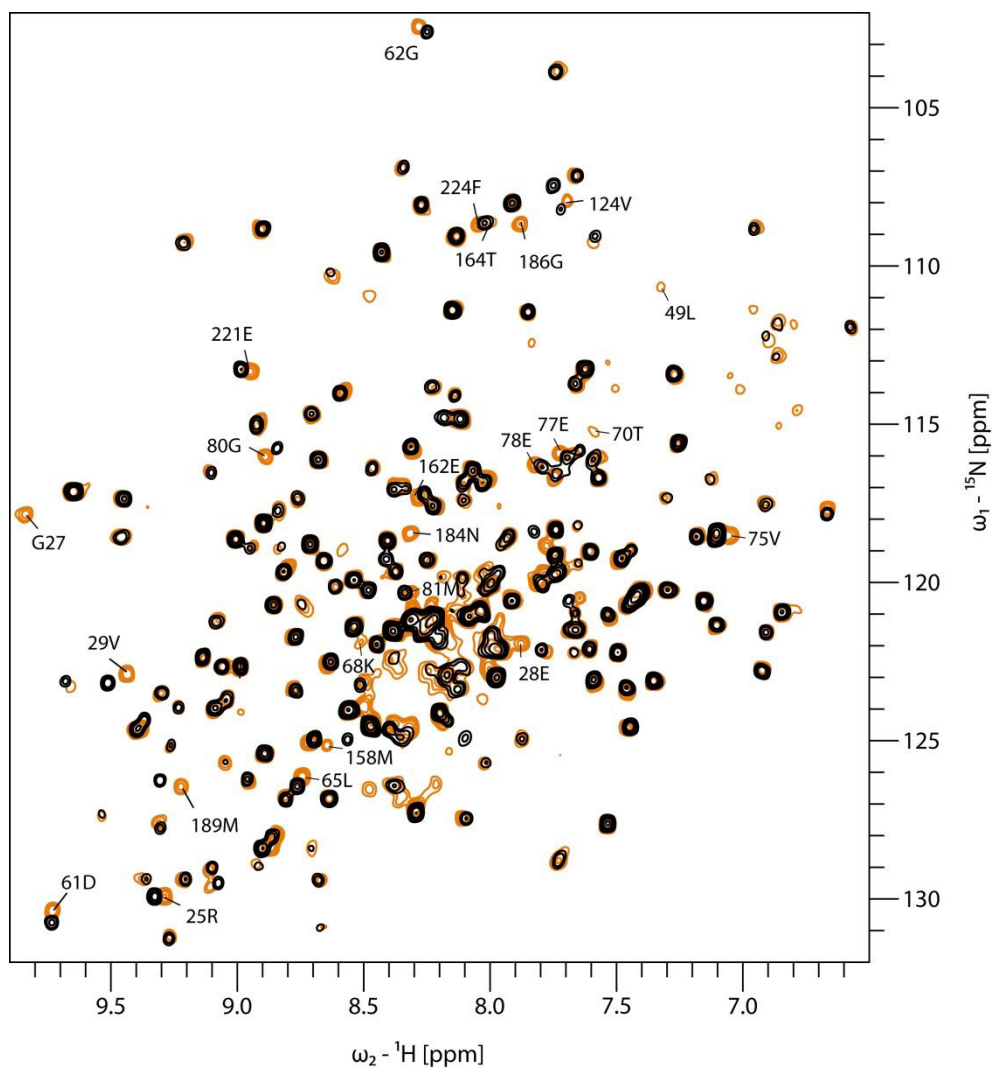
Figure 34: TROSY spectra of ArtP in presence (black) and absence of MgCl₂ (orange). The signals of G27, E28, K68, T70, N184 and G186 disappear upon addition of $MgCl_2$ while strong shifts and intensity changes are observed for the other residues indicated.

being that ATP in the stock solution had already fully hydrolyzed to ADP and P_i prior to the experiment, can also be excluded as this was checked by a colorimetric assay for detection of P_i (data not shown). Finally, that ADP was already an intrinsic impurity of the ATP powder obtained from Sigma-Aldrich is also unlikely as highest grade purity substances were used. Thus, it is more likely that ADP and ATP indeed have very similar effects on ArtP and that the differences between binding of nucleoside di- and triphosphates might be a result of the restricting presence of the TMDs in the full transporter.
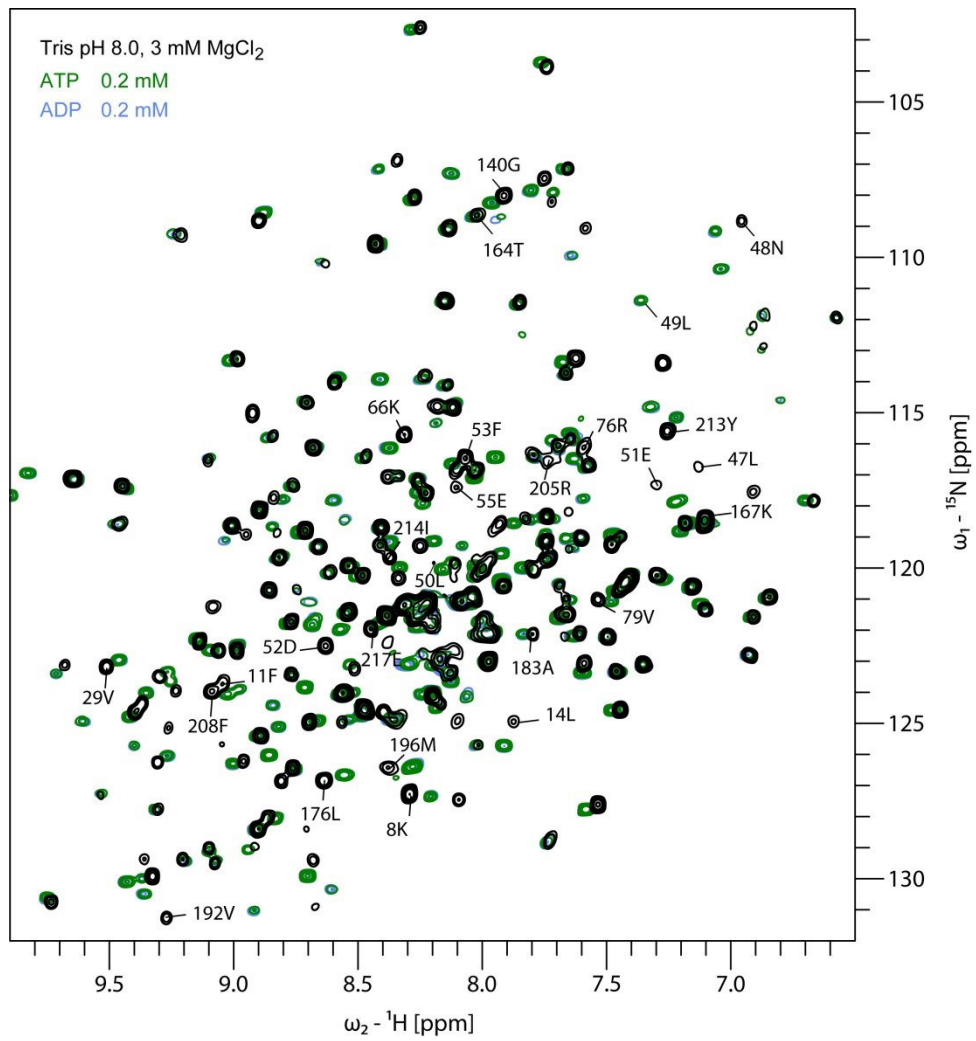
Figure 35: TROSY spectra of ArtP in Tris buffer at pH 8.0 in presence of MgCl₂ (black), MgCl₂/ATP (green) and MgCl₂/ADP (light blue). The ADP spectrum strongly resembles the ATP spectrum and is almost fully covered in this overlay.

Strength of peak shifts reflects dissociation constants found in ITC

As expected, AMPPNP and AMPPCP at concentrations of 0.2 mM generally affected the same residues as ATP and ADP did. However, most influenced peaks shifted in a concentration dependent manner, reflecting the K_D values found in ITC experiments (Figure 37). The dissociation constant of 6 µM for ATP and ADP translates to saturations of > 90 % in solution NMR experiments in presence of 0.2 mM nucleotide and indeed the strength of effects by ATP and ADP was almost identical (Figure 35). Analogous, for AMPPNP (K_D of 47 µM) and AMPPCP (K_D of 275 µM), saturations of about and 70 and 40 % should be reached in presence of 0.2 mM nucleotide. Indeed, the effect by AMPPNP was weaker than the one of ATP but stronger than the one observed for AMPPCP. This becomes obvious when for example comparing the peak positions of L14 (next to the A-loop) for the different spectra in Figure 36. This residue proved as a strong indicator of nucleotide binding and showed clear effects relating to the different ITC K_D values found for the four nucleotides.
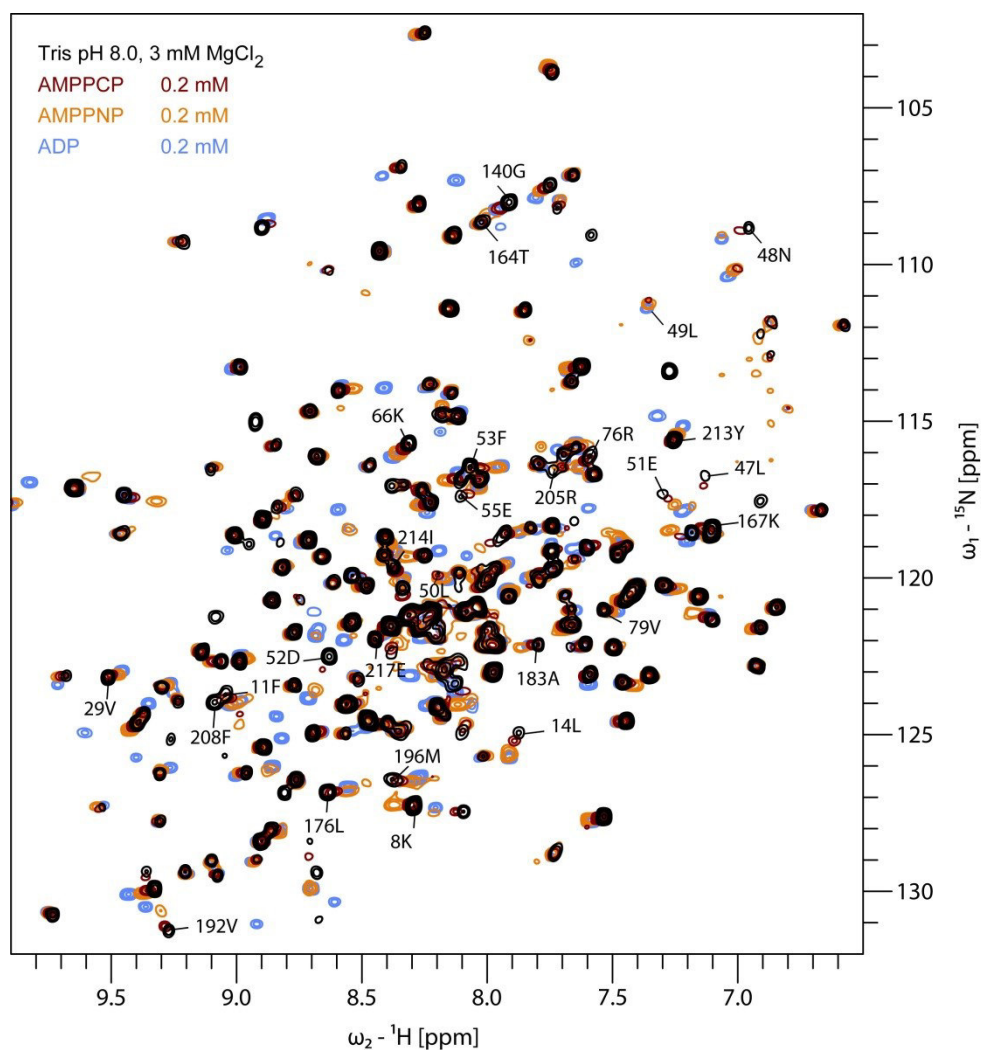
Figure 36: TROSY spectra of ArtP in Tris buffer at pH 8.0 containing 3 mM MgCl2 and 0.2 mM nucleotide. Residues that were most affected are labeled.

To clarify whether the observed differences between ADP/ATP and the two analogs are solely due to insufficient protein saturation, a second set of TROSY experiments using nucleotide concentrations that translate to ~ 90 % saturation of ArtP with nucleotide was carried out. Indeed, now for AMPPCP and AMPPNP stronger shifts of all affected residues were observed that resembled the ones for ATP e.g. in case of L14 and N48. Still, even at these high concentrations of nucleoside triphosphate analogs, the spectra did not fully overlay with the ArtP/ATP spectrum (Figure 37).
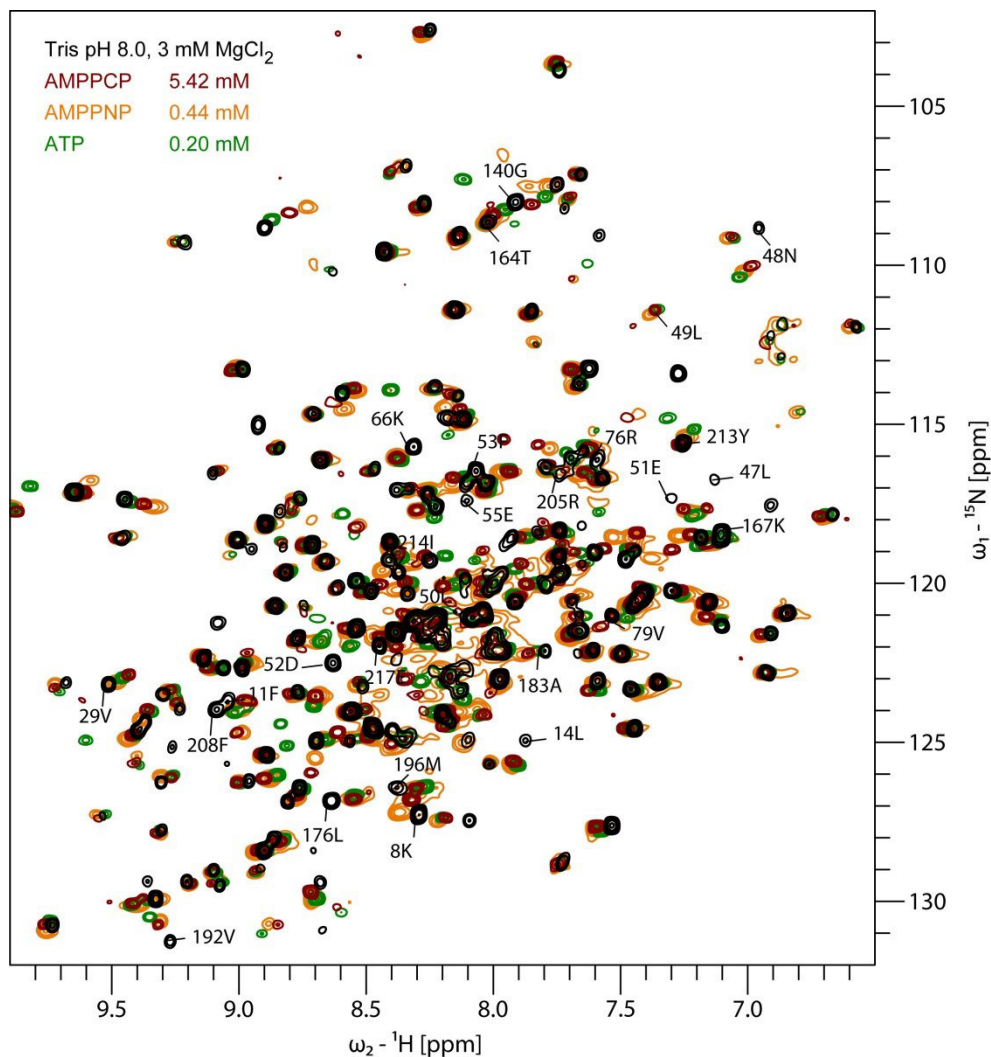
Figure 37: TROSY spectra of ArtP with nucleotide concentration resembling >90 % saturation of ArtP are compared. In the spectrum containing AMPPNP partial protein degradation was observed.

From close comparison of the combined CSPs, it became clear that the two analogs caused slightly different effects (compared to ATP) in motifs directly involved in nucleotide binding. An example is the Walker B motif that shows a strong response in presence of ATP but is less affected by the two analogs. This is not surprising as both analogs lack the third phosphoanhydride bond, which is strongly involved in hydrogen bonding networks to the nucleotide binding motifs. However, many of the affected regions distant from the actual binding site (like the Q-loop, regions N48-E55 and D204-G218) were influenced similarly by all nucleoside triphosphates. Thus, although the detailed geometry in the nucleotide binding site is different for ATP and the nonhydrolyzable analogs, the overall conformational effects are comparable, when sufficiently high concentrations (to account for the vastly different binding affinities) of the analogs are used.

Structural effects of nucleotide binding

Both, presence of ATP and ADP had very strong effects leading to loss of several signals (S10, 15E, S41, 84Q, 85R, 160F, 161D, 207L). For the peaks of K9, 51E, 82V and 226R a clear maximum could not be defined in these nucleotide containing experiments. Residues for which signals were lost completely or maxima could not be defined anymore, were grouped in the category of strongly affected residues. For the remaining 117 peaks with distinct maxima the combined CSP was calculated as described in 3.13. Results were then grouped into three categories, where 61 peaks showed no effect, 26 were slightly and 30 moderately affected by addition of ATP (or ADP). Figure 39 and Figure 40 in section 4.5.3 summarize these findings and give a full comparison to the effects found in solid-state NMR experiments.

The residues that were most affected by nucleotide binding are located in or near the common ABC transporter motifs that are proposed to interact with the nucleotide itself or to transmit the nucleotide state to the other subunits of the transporter. The residues in and around the A-loop (K8-E15) showed a clear indication of nucleotide binding. For the Walker A motif only the assignment for S41 could be transferred. However, this peak as well as residues of the Walker B motif and in the D-loop were clearly affected by the presence of ATP. The Q-loop is thought to act as a bridge between the α-helical and the catalytic domain, potentially transmitting the state of the bound nucleotide to the TMD. Several signals for residues of the Q-loop (V82, Q84, R85) disappeared with addition of ATP and adjacent residues also showed moderate effects. Residues flanking the H-loop (V192 and M196), which is proposed to interact with the γ-phosphate were also moderately influenced. Thus, also for the isolated NBD in solution, nucleotide binding is clearly accomplished by the common ABC transporter motifs that were proposed in mutagenesis studies and from their orientation in X-ray structures.

Interestingly, several regions that are rather distant from the nucleotide binding site also responded strongly to the presence of ATP. For instance, effects were observed for I24, R25 and V29 as well as for residues N48-E55 and D204-G218. Several residues N-terminal to the Q-loop were also affected.

Moreover, very weak interactions of the LSGGQ motif with nucleotides were also detected (G140, Q141, Q143, R144). As ArtP was not able to dimerize under the conditions used in AUC experiments (using a very similar buffer system and concentrations), it is likely that this also holds true for these solution-NMR studies and that in fact the effect of two separate nucleotide molecules interacting with one ArtP monomer was detected here. However, this interaction must be very weak in case of soluble ArtP as the ITC data was best fitted with a 1:1 binding model.

4.5.2 Lipid-embedded ArtMP shows similar effects for nucleoside di- and triphosphates

To determine the effect of ADP and AMPPCP on the lipid-embedded transporter, ^{1}H-detected MAS ssNMR INEPT spectra of ArtmP were previously recorded by Kunert and Hiller (20kHz, 700 MHz) and a limited set of isolated peaks was tentatively assigned by 2D overlay of the solution NMR HSQC spectrum used for the initial assignment with the solid-state NMR spectra[199]. These assignments were confirmed by triple resonance ssNMR (on the ArtMP sample 2) and 38 additional assignments could be transferred (for details see section 5.2.30). Out of these 45 assignments, 40 could be used for analysis of nucleotide binding to the transporter in lipid environment.

In experiments performed by Kunert (2011)[199], ArtmP was reconstituted into lipids in presence of 0.4 mM nucleotide and 10 mM MgCl$_2$. Here, ADP/Mg^{2+} and AMPPCP/Mg^{2+} showed very similar effects relative to a Mg^{2+}- and nucleotide-free control spectrum. It is important to note that binding of AMPPCP does not necessarily lead to conversion of the transporter from an inward- to an outward-facing state, especially since it is not known whether the majority of transporter molecules can be trapped in the outward-facing state at the nucleotide concentration used. Thus the observed effects are probably primarily caused by nucleotide binding and not by inter-state conversion of the transporter. Indeed, the residues in ArtmP that were most affected by nucleotide also showed strong responses in solution NMR experiments with ArtP, including N48 and L14 close to the A-loop. Indeed, substantial intensity changes were seen for G27, V29 and G212 and slight differences between the ADP and AMPPCP containing spectra were observed between 7.8 to 8.4 ppm ^{1}H and 123 to 125 ppm ^{15}N (Figure 38). However, due to the lack of peak assignments these cannot be related to regions in ArtP yet. The combined CSP for the 40 assigned peaks was calculated and the results are compared to data obtained in solution NMR studies with isolated ArtP in the next section.
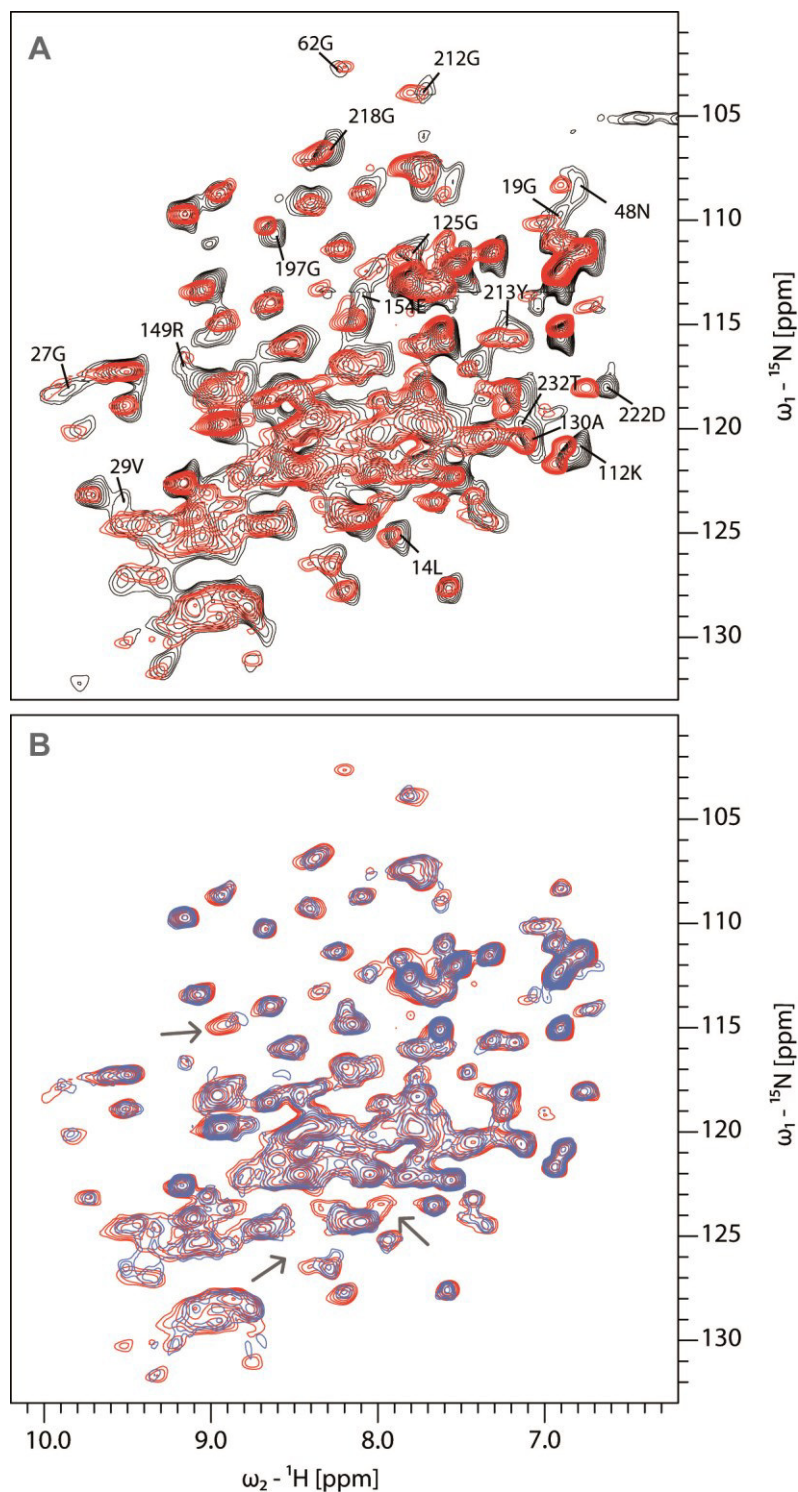
Figure 38: INEPT-based 2D HN correlation experiments of lipid-embedded ArtMP in presence and absence of nucleotides. **A** Comparison of ssNMR INEPT spectra of nucleotide-free (black) and AMPPCP-bound (red) ArtMP. Assigned peaks that showed strong changes in presence of nucleotide are labeled. **B** Comparison of ssNMR HSQC INEPT spectra of ADP- (blue) and AMPPCP-bound (red) ArtMP. The spectra show only minor differences (indicated with arrows).

4.5.3 Structural interpretation of nucleotide effects observed by NMR

For all assigned peaks, the chemical shift perturbation (CSP) in solution-NMR and ssNMR experiments was calculated as described in 3.13. Residues for which peak maxima could not be determined in the presence of nucleotide or for which intensities increased or decreased substantially were grouped in one category (strongly affected), while all other assigned residues were ranked in three groups referring to not affected (ΔCSP: 0-0.03 ppm), slightly affected (0.03-0.06 ppm) or moderately affected (>0.06 ppm) by presence of nucleotide. For comparison, the effects of ATP binding to ArtP and AMPPCP binding to ArtmP are summarized in the following figures.
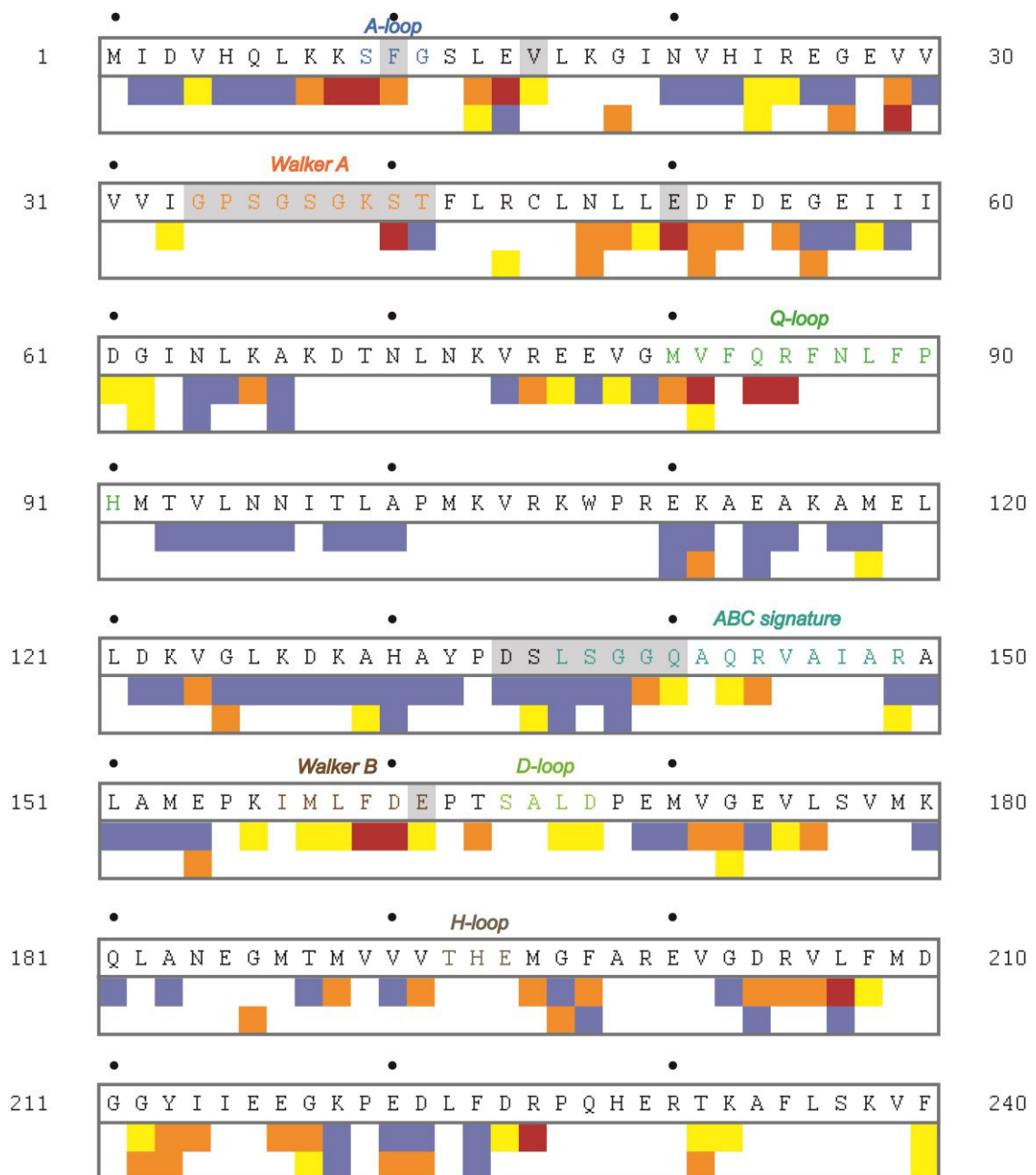
Figure 39: Amino acid sequence of ArtP with typical ABC transporter motifs indicated. Residues high-lighted by grey background are within 5 Å distance of the bound nucleotide in our model structure. The first row shows the ArtP sequence while the second row corresponds to the effects observed in solution NMR experiments (performed with ArtP and ATP). The third row shows the CSP for assigned peaks in solid-state NMR experiments with lipid-embedded ArtMP and AMPPCP (red: strong effect, orange: moderate effect, yellow: slight effect, blue: not affected by nucleotide binding).

From Figure 39 it becomes obvious that the presence of nucleotide had very similar effects on ArtP, in the isolated form and in the full transporter. Judging from the limited number of available assign-ments, the regions around the A-loop and the Walker B motif as well as the Q-loop were most affected in soluble ArtP. For ArtmP, AMPPCP binding was also clearly detected e.g. with the response by L14. As assignments for residues in the Walker A or B motif are still missing for the lipid-embedded trans-porter, no conclusion for these regions can be drawn yet. Surprisingly, R149 which is part of the ex-tended ABC signature motif (located in close proximity to the coupling helix of ArtM) was affected by nucleotide binding in ArtmP but not in isolated ArtP. Other parts of the α-helical subdomain in ArtmP also seemed to experience a stronger influence in presence of nucleotide compared to the effects for isolated ArtP.

In both experimental set-ups, several regions distant from the binding site were influenced by nu-cleotide. This includes H23-V29, L47-G56 and D204-R226. In other ABC transporters, V29 is mostly conserved in amino acid type and only exchanged only for other hydrophobic amino acids (e.g. substi-tuted for I, T, F, or Y). G56 shows full conservation in the sequences compared in Figure 18. Interest-ingly, this residue is only altered by nucleotide in ArtmP while no effect was seen for isolated ArtP. D204 is also conserved and only exchanged for a glutamate in case of Mj0796 while G212 shows full conservation. This indicates that these regions might have functional relevance although they are not directly involved in nucleotide binding or hydrolysis.

Figure 40 presents the findings from nucleotide binding studies by NMR in a structural perspective using the ArtMP homology model (see 4.1). From this representation it becomes clear that in soluble ArtP the presence of ATP also affects the Q-loop, while the largest part of the α-helical subdomain remained unaffected. The response of the Q-loop thus is specific to nucleotide binding and not related to changes in the α-helical subdomain.
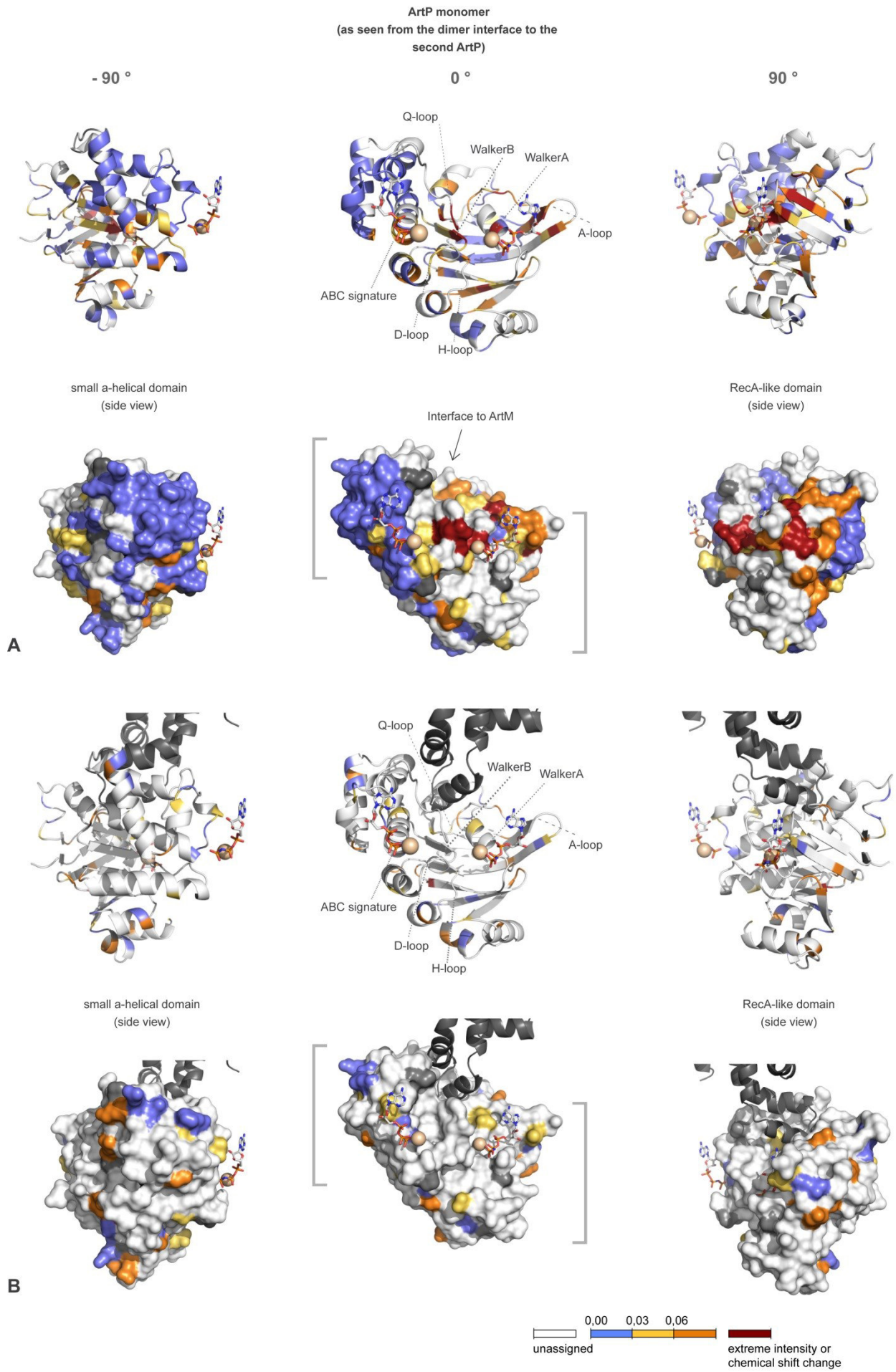
ArtP monomer
(as seen from the dimer interface to the
second ArtP)

- 90 °   **0 °**   **90 °**

Q-loop

WalkerB   WalkerA

A-loop

ABC signature

D-loop

H-loop

small a-helical domain
(side view)

Interface to ArtM

RecA-like domain
(side view)

A

Q-loop

WalkerB   WalkerA

A-loop

ABC signature

D-loop

H-loop

small a-helical domain
(side view)

RecA-like domain
(side view)

B

0,00   0,03   0,06

unassigned   extreme intensity or
chemical shift change

Figure 40: Structural interpretation of nucleotide effects. The typical ABC transporter motifs are indicated. ArtM is shown in dark gray. Prolines (colored in black) lack backbone amide protons and thus show no signal in HN correlated experiments. The color coding is analogous to Figure 39. **A** Effects observed in solution NMR with ATP plotted onto isolated ArtP. **B** Effects observed in ssNMR spectra with AMPPCP plotted onto ArtP within the homology model for the complex. ArtM is depicted in dark grey.

4.6 MAS ssNMR characterization and assignment of ArtMP

Although nucleotide binding was clearly detected in both the soluble NBD and the lipid-embedded ArtmP, a complete characterization and structural investigation of open and closed states will only be possible with full assignment of the lipid-embedded transporter. This will help to define the interface between ArtM and ArtP and improve knowledge about how the signal by nucleotide binding and hydrolysis is transmitted from the NBD to the TMD. The following section describes different ssNMR approaches taken to conformationally analyze and assign lipid-embedded ArtMP. These experiments demonstrate how ssNMR, in particular ^{1}H detected MAS ssNMR, can be applied to integral membrane proteins obtaining high-resolution spectra that can greatly accelerate the assignment process. This enables investigation with atomic resolution of otherwise inaccessible systems (like membrane proteins). All ssNMR spectra were obtained on non-crystalline protein-lipid samples in collaboration with Dr. M. Hiller (initial [1]H-detected experiments and CP/INEPT comparison), Dr. Ü. Akbey (Quadruple-resonance MAS ssNMR) and Dr. A. Nieuwkoop (Quadruple-resonance MAS ssNMR and [1]H-detected assignment experiments).

4.6.1 Conformational analysis of lipid-embedded ArtMP

The overall conformation of ArtP is not altered in ArtMP samples reassembled from subunits

Although the modular nature of ArtMP enables the focus on subdomains of the full transporter, it has to be ensured that the assembly process from single subunits does not alter the overall conformation of the transporter. For this, a conformational analysis using a co-expressed ArtMP (sample 1) and a reassembled ArtmP sample (spectra provided by Dr. B. Kunert) was carried out. INEPT-based 2D HN correlation spectra were obtained by MAS ssNMR on a 700 MHz spectrometer at 20 kHz MAS and 275 K. The side-by-side comparison in Figure 41 shows that the overall conformation in both preparations is homogeneous and that ArtP in the reassembled sample is extremely similar to ArtP when co-produced with the TMD. Although ArtM is labeled as well in sample 1 (black spectrum), very few peaks can directly be attributed to the TMD. This might have several reasons. First, it is likely that ArtM has dynamical properties distinct from ArtP, leading to increased relaxation and reduced transfer efficiencies. Moreover, ArtM is a fully α-helical protein containing many typical hydrophobic residues like alanine (21), isoleucine (22), leucine (29) and valine (14). As amide protons are a good indicator for secondary structure, this might also lead to strong overlap of the chemical shift for residues in helices. A third possibility that would lead to less intense signals for ArtM is insufficient proton back-exchange. As a H/D ratio of 30/70 % was found optimal in previous ^{1}H-detected MAS NMR studies on SH3 at 20 kHz MAS[73], this ratio was chosen for the purification and lipid reconstitution buffers for ArtMP. While in soluble ArtP, the entire surface is solvent-accessible during sample preparation, ArtM stays rather shielded (by detergent or lipids). As un- and refolding of ArtM is not possible, this

probably results in reduced re-incorporation of protons and loss of signals for residues in inaccessible regions. Taken together, it is likely that faster MAS frequencies in combination with more efficient back-protonation will increase signal intensity for ArtM.

The few peak shifts or intensity differences for ArtmP (blue spectrum, regions indicated with arrows) might result from residues in ArtP that are solvent-accessible during the assembly process for ArtmP but not in the co-expressed ArtMP preparation. In the ArtMP spectrum (black), the peak of ArtP F240 is either strongly shifted or absent: while the ArtP construct used in the ArtmP (blue) spectrum carries an N-terminal His-tag, this tag is C-terminal in the construct for coexpressed ArtMP (black). This might have increased the flexibility of the terminal F240 beyond the detection limit.
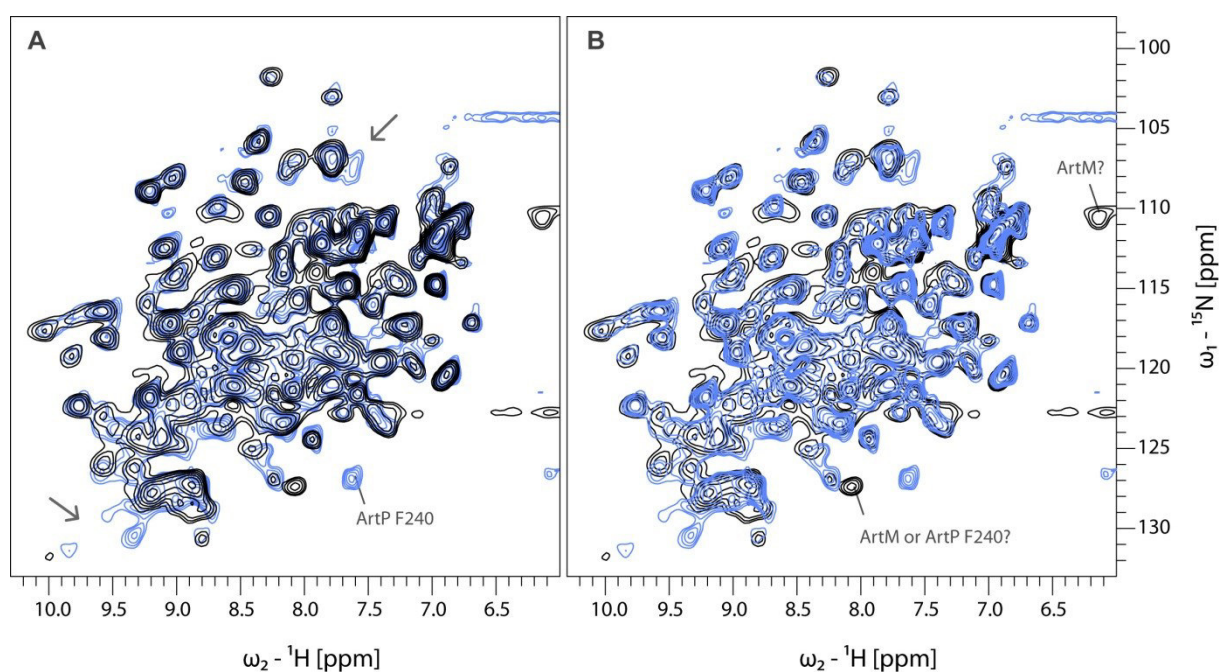
Figure 41: INEPT-based HN correlation spectra of ArtmP (blue) and ArtMP (black). Minor differences were detected in the indicated regions. Only very few peaks can be assigned to ArtM. Both spectra were recorded with 512 scans/increment at 275 K and 700 MHz with 20 kHz MAS. Qsine window functions were used for processing in the direct and indirect dimension.

4.6.2   CP-based experiments for detection of less mobile regions in ArtMP

[1]H-detected 2D HN correlation experiments were compared for ArtMP (sample 1) with one experiment using an INEPT and the other using a CP magnetization transfer for ^{1}H to [15]N (Figure 42). The INEPT spectrum showed a limited set of peaks that also seemed present in the CP experiment. In other systems, the INEPT transfer acted as non-decoupled T_2 filter leading to detection of mobile protein regions. Whether this is also true for ArtMP will be answered with more assignments at hand. Nevertheless, judging from the spectral density it seems like mainly ArtP is detected in both experiments. As discussed already, this might either be due to insufficient back-exchange of protons for the TMD or be related to a vastly different mobility of the TMD.
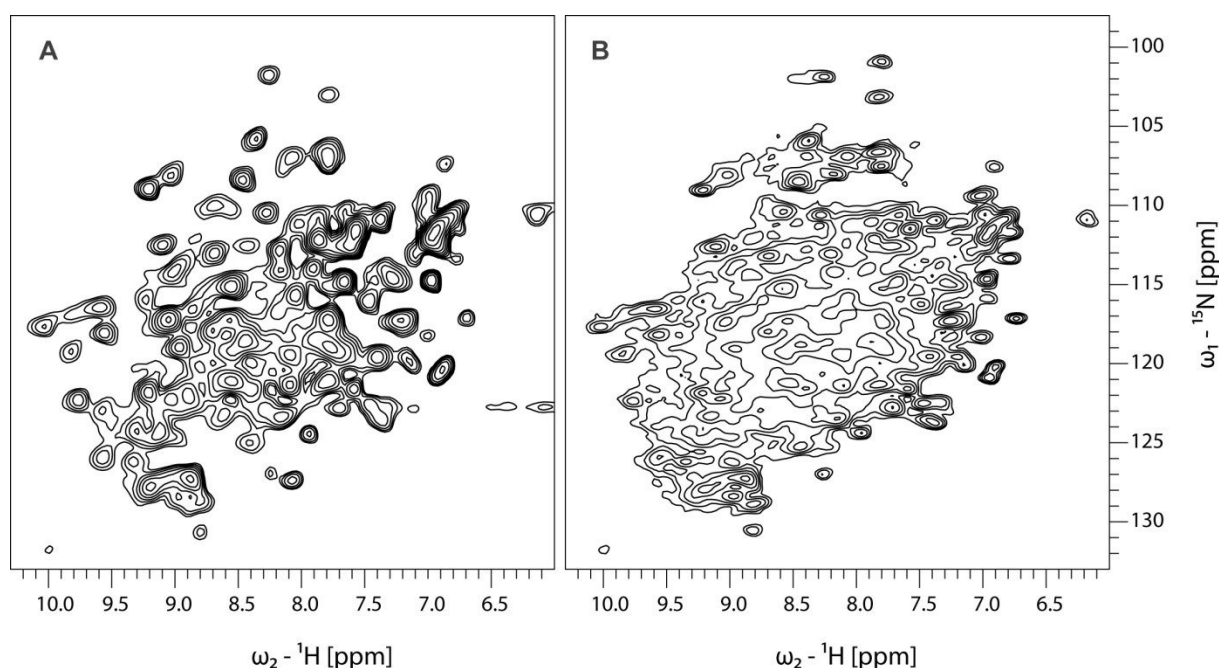
Figure 42: CP magnetization transfer from ^{1}H to ^{15}N detects additional regions compared to an INEPT-based transfer for ArtMP (sample 1). A INEPT- and **B** CP-based 2D HN correlation experiments, both recorded at 700 MHz and 20 kHz MAS and 275K. The INEPT spectrum was recorded with 512 scans/increment while the CP spectrum had 160 scans/increment. The subset of signals detected in the INEPT-based experiment is also present in the CP spectrum.

4.6.3   Deuterium excitation to investigate shielded regions in membrane proteins

Proton instead of carbon detection results in a huge gain in sensitivity. However, the proton dipolar couplings leads to line broadening that can be overcome by dilution of the proton network using extensive deuteration. Triple-labeled proteins are commonly produced from fully deuterated media with D_2O and deuterated carbon precursors. For a systematic backexchange of amide protons, subsequent un- and refolding of the protein in buffer with the desired H/D content would be necessary. However, this is not possible for all proteins (especially not for α-helical TMPs) and some regions in the interior will remain shielded from the surrounding exchange buffer during proton back-exchange. As the magnetization in the initial CP step is transferred from all neighboring protons (and not only from directly bonded ones) the residual proton content might not be sufficient for efficient CP transfer at these heavily deuterated sites.

Lalli *et al.* suggested a ^{13}C-detected alternative that instead of the standard ^1H-^{13}C CP employs an initial $^2H_{DQ}$-^{13}C transfer based on deuterium excitation[75]. 3D $^2H_{DQ}$-$^{13}C_{\alpha}$-$^{13}C_{\beta}$ experiments recorded for ubiquitin (20 % protons, 25 kHz) showed the potential for a ^2H dimension to assist in resolving ^{13}C signals as well as increasing the overall signal. Applying the same experiments to the membrane protein OmpG (30 % protons, 20 kHz), resulted in $^2H_{DQ}$ linewidths that were broader but still promising.

For coexpressed ArtMP, ^2H CP was combined with the more sensitive proton detection. Two- and 3D versions of an hCaNH experiment were compared to their counterparts starting from deuterium using ArtMP sample 2 (30 % protons at accessible sites) at 275 K and 20 kHz MAS. The pulse sequences are shown Figure 43.
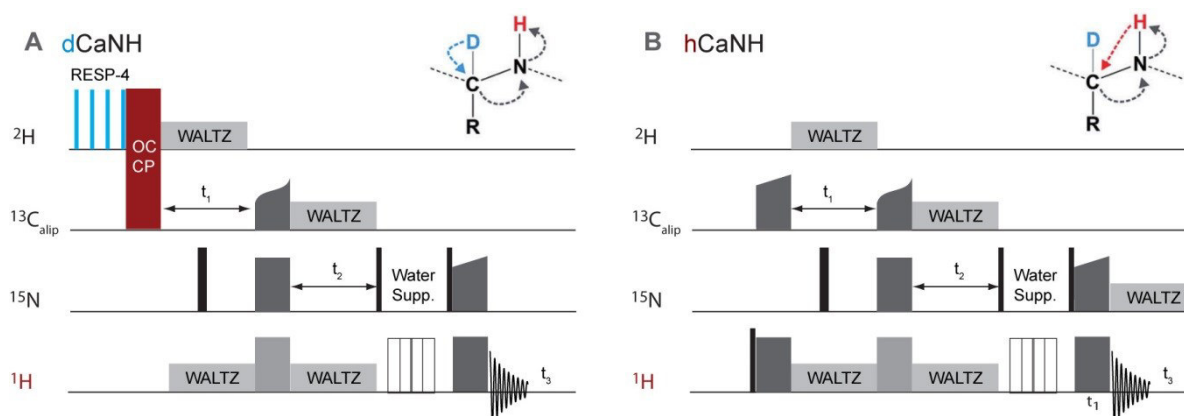
Figure 43: The pulse sequences used to record the dCaNH and hCaNH 2D and 3D MAS NMR experiments. (implemented by Dr. Ü. Akbey and Dr. A. Nieuwkoop).

The deuterium excited 2D experiment had about half of the S/N of the experiment starting with proton excitation (Figure 44A & B). Nonetheless, isolated cross peaks were well resolved in both experiments. To analyze whether specific regions of the protein were differently affected by the two excitation strategies, 3D versions of the above mentioned experiments were recorded. 92 and 185 cross-peaks were found in the 3D dCaNH and the hCaNH spectra. Peak positions were compared to solution NMR assignments obtained for monomeric ArtP. 28 and 94 peaks of the dCaNH and the hCaNH spectra respectively matched to assignments of ArtP and were spread over the entire protein sequence (indicating that no specifically shielded regions in ArtP were present). The non-correlating peaks thus either belong to ArtP residues with different conformation in the full ArtMP complex or residues from the membrane protein ArtM. For nearly 50 % of peaks in the hCaNH spectrum and 70 % of the peaks in the dCaNH no counterparts in the solution ArtP assignments were found implying that the dCaNH experiment is more efficient for residues likely belonging to ArtM. 2D planes of the 3D experiments are compared in Figure 44 C-F. The results of this study are published in Akbey, 2014[229].
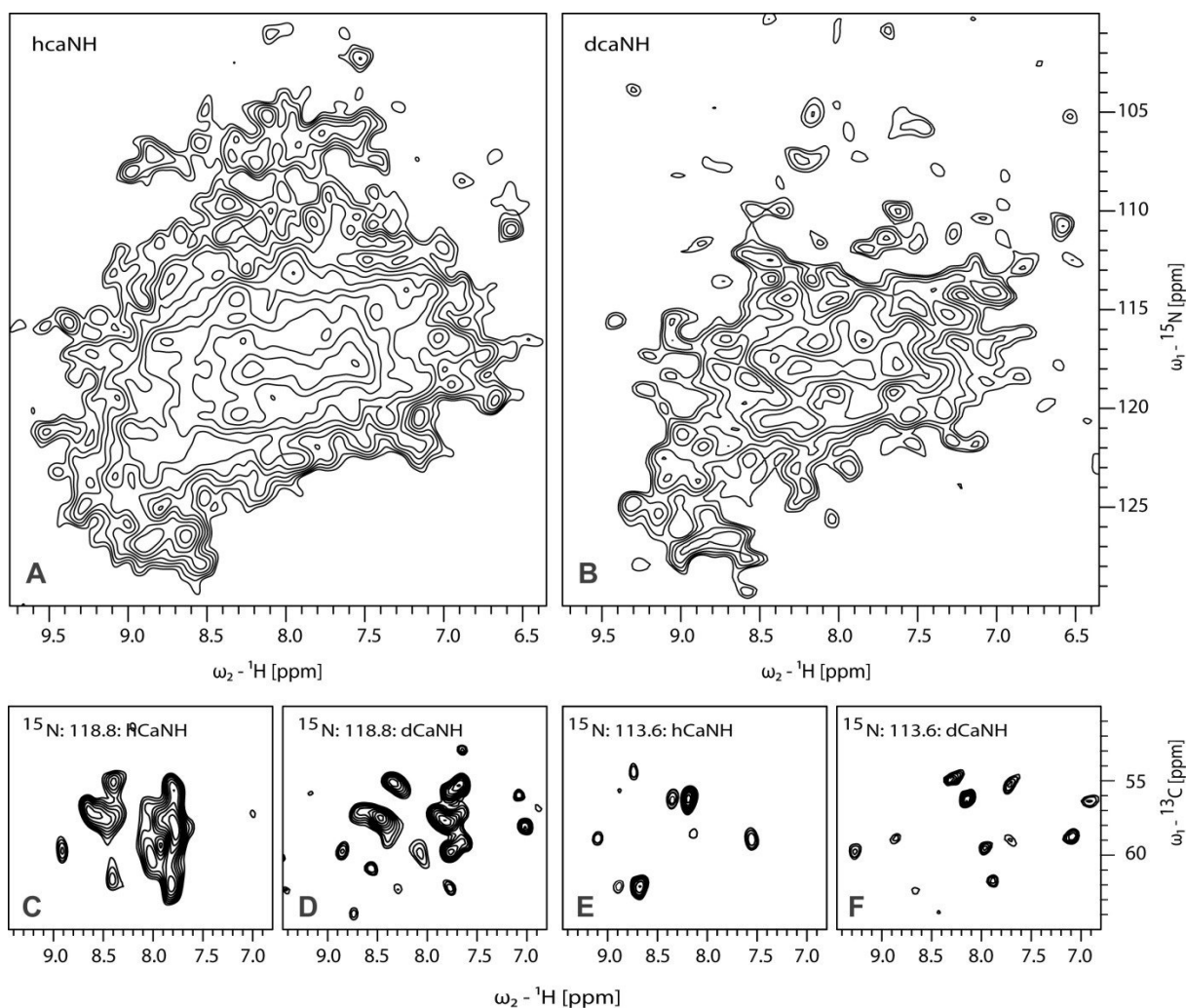
Figure 44: Deuterium vs. proton excitation in ¹H-detected 2D and 3D experiments for ArtMP. First row: Comparison of 2D hc$_\alpha$NH (A) and dc$_\alpha$NH (B) correlation experiments recorded on ArtMP (sample 2) at 275K and 600 MHz with 20 kHz MAS. Second row: Extracted planes from the 3D hC$_\alpha$NH (A) and dC$_\beta$NH (B) experiments recorded with the same parameters. The two excitation transfers clearly led to different peak patterns, indicating that different regions in ArtMP were preferentially excited.

4.6.4 Improved resolution for ArtP and ArtM at higher frequencies - necessity of fast spinning in ¹H-detected MAS NMR

At 20 kHz MAS, 3D experiments with more transfers than the hCaNH were not possible for ArtMP (sample 1 & 2). Also it seemed like large parts of ArtM was not detected in these experiments. For improved suppression of dipolar couplings, ¹H detected experiments were recorded at 40 kHz MAS on a 900 MHz spectrometer. For samples in which either the NBD or the TMD was triple-labeled (ArtmP/sample 3 and ArtMp/sample 5) 2D HN correlated spectra based on CP transfer could be obtained. These experiments yielded improved resolution especially for ¹⁵N linewidths of ArtP. For ArtM, for the first time, a resolved 2D HN correlated spectrum could be obtained (at 37 kHz MAS). The TMD is well folded but as expected due to the large α-helical content peaks cluster between 7 and 9.5 ppm ¹H and 115 to 125 ppm ¹⁵N. The transfer efficiencies were still better for ArtmP which could also be related to the fact that the triple-labeled ArtM (ArtMP, sample 5) is still surrounded by protonated lipids.
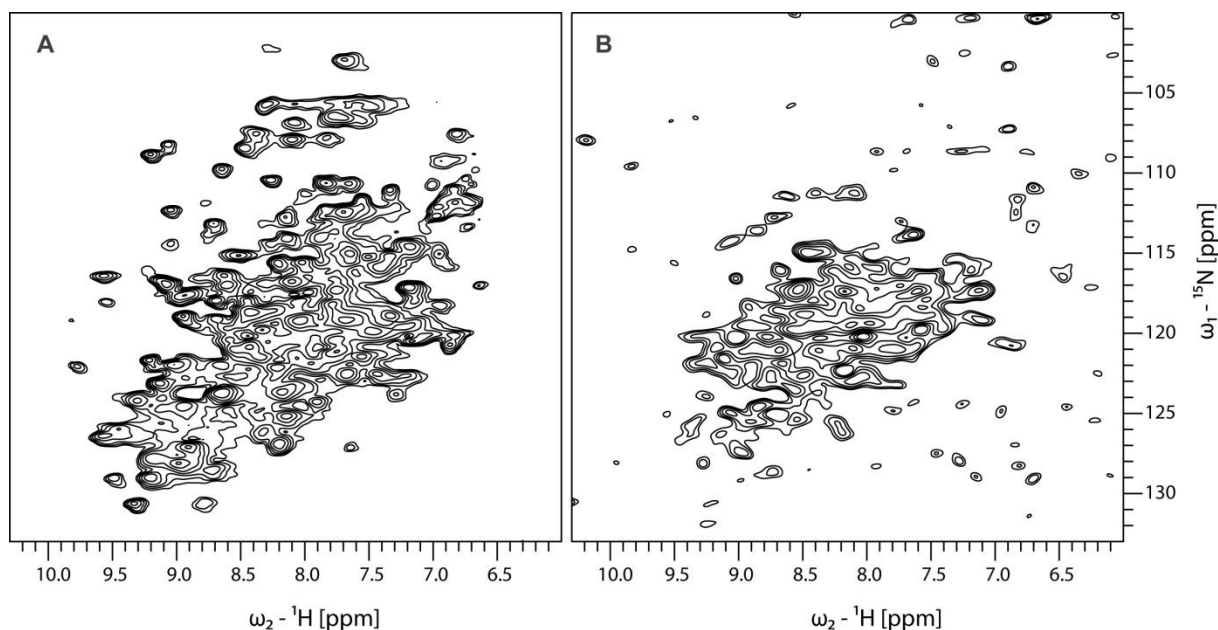
Figure 45: CP-based 2D NH correlated spectra of ArtmP and ArtMp with 60 % protons recorded at ~295 K at 900 MHz **A** 2D NH spectrum of ArtmP (sample 3) recorded at with 40 kHZ MAS for 15h **B** 2D NH spectrum of ArtMp (sample 5) recorded at 37 kHz for 16.5 h.

4.6.5 ¹H-detected 3D ssNMR enables assignment of ArtMP in lipids

In Kunert, 2011 seven peaks were tentatively assigned by overlay of a solution 2D HSQC spectrum of soluble ArtP and an INEPT-based ssNMR spectrum of ArtmP[199]. An optimized reconstitution buffer for ssNMR samples now allowed for improved ¹H decoupling and increased T_2 times, which enabled a first hCaNH experiment for ArtMP (sample 2) at 20 kHz MAS.
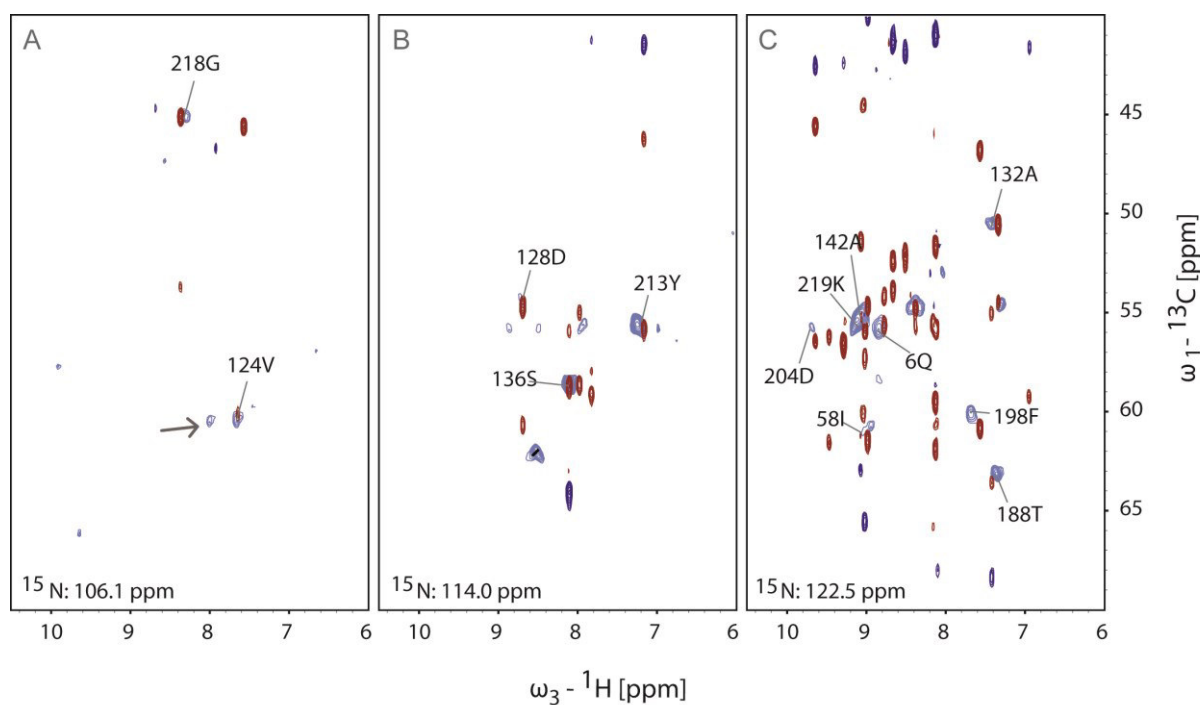

Figure 46: Overlay of a solution HNCaCb spectrum obtained for soluble ArtP (red: positive, dark blue: negative) and an ssNMR hCANH spectrum obtained for ArtMP (sample 2; light blue) at 20 kHz MAS. The solution spectrum is more crowded as peaks from the Cα and Cβ carbons of the i and i-1 residue are observed. Peak positions for Cα resonances of successfully transferred assignments are indicated. The peaks in the ssNMR hCaNH that do not correlate with solution peaks could reside from ArtM but are more likely to refer to regions in ArtP that were not detected in solution NMR experiments on the isolated domain.

From comparison with the corresponding solution NMR hCaCbNH spectrum, the initial seven assignments were confirmed and 38 additional transfers were possible. Out of these, 40 assignments could be used to evaluate the effects of nucleotide binding in 2D HN correlation spectra obtained by Kunert, (2011)[199] (section 4.5.2 and 4.5.3). The transferred assignments are summarized in Figure 47 showing the ArtmP INEPT spectrum that was used as the nucleotide-free control spectrum in 4.5.2.
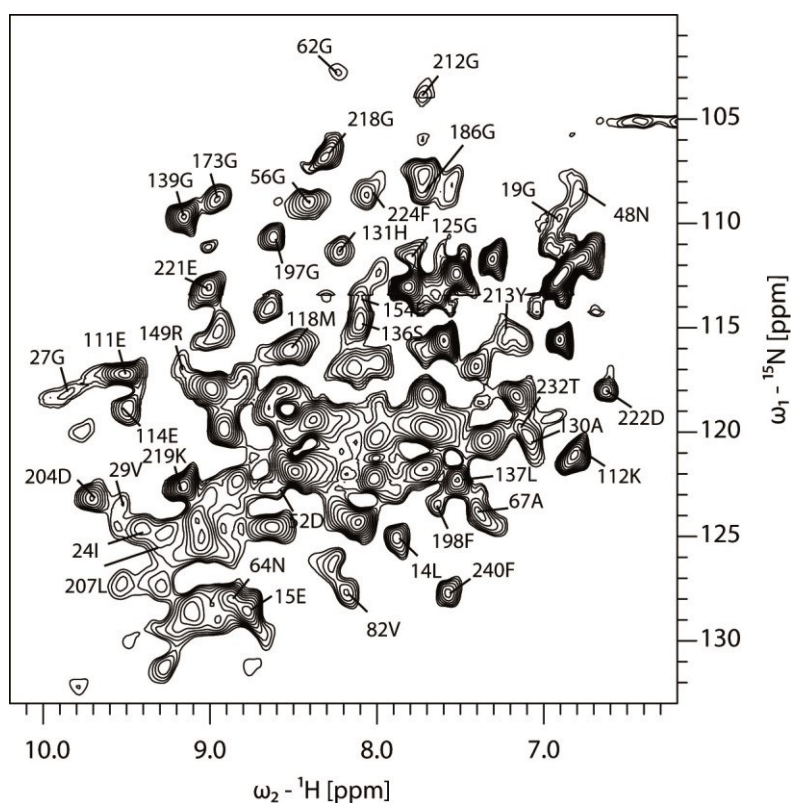
Figure 47: Assignment transfers obtained from the spectral overlay of the solution NMR hCaCbNH for isolated ArtP and the hCaNH of lipid-embedded ArtmP at 20 kHz MAS. Several additional C_α resonances were identified in the hCaNH (e.g. for 45R, 68K, 124V, 128D and 188T). These residues are located in congested regions of this INEPT-based 2D HN correlation for ArtmP (provided by Dr. B. Kunert) and were thus not labeled in this representation.

Spinning at 40 kHz MAS substantially improved the S/N and the resolution and thus far enabled acquisition of hCoNH, hCaNH and hCaCbNH spectra. 199 and 202 resolved peaks were obtained for the hCaNH and the hCoNH and the ^{15}N linewidth were considerably narrowed compared to the hCaNH spectrum at 20 kHz MAS (Figure 48 and Figure 49).
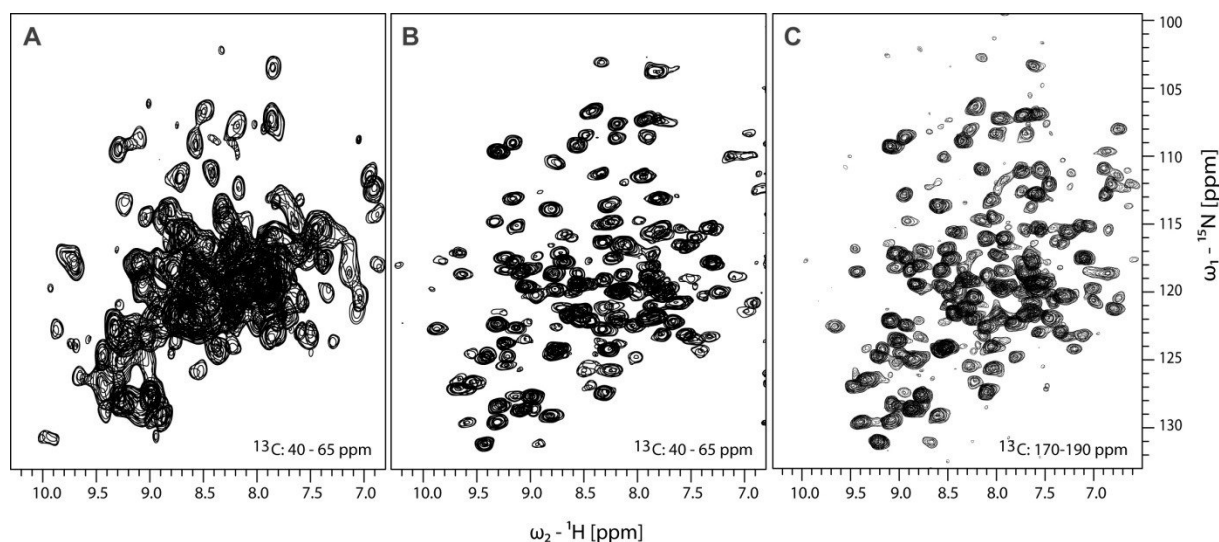
Figure 48: Full 2D projections of different 1H-detected 3D experiments for ArtMP (sample 2) and ArtmP (sample 3) at 20 and 40 kHz MAS. A Projection of the hCaNH of ArtMP recorded at 600 MHz and 275K with 20 kHz MAS. **B** Projection of the hCaNH of ArtmP recorded at 900 MHz and ~295K with 40 kHz MAS **C** Projection of the hCoNH of ArtmP recorded at 900 MHz and ~295K with 40 kHz MAS. The spectra at 40 kHz were recorded for about 7 days each.

The hCaNH and hCoNH spectra obtained at 40 kHz MAS showed about 200 peaks each. Counting the N-terminal His-tag, the ArtP construct has 254 residues, out of which ten are prolines that do not contain backbone amide protons. Thus, almost 80 % of expected peaks were detected in these two experiments. Considering that the N-terminus is probably too flexible to be detected, almost 87 % of theoretically possible peaks were seen. Completion of this ^{1}H detected assignment series will enable assignment of ArtP in the full, lipid-embedded transporter complex, which is the basis for structure determination by ssNMR. This allows a detailed, residue-specific investigation of conformational changes during the ABC transport cycle including the role of nucleotide binding and hydrolysis as well as closure and opening of the translocation channel.
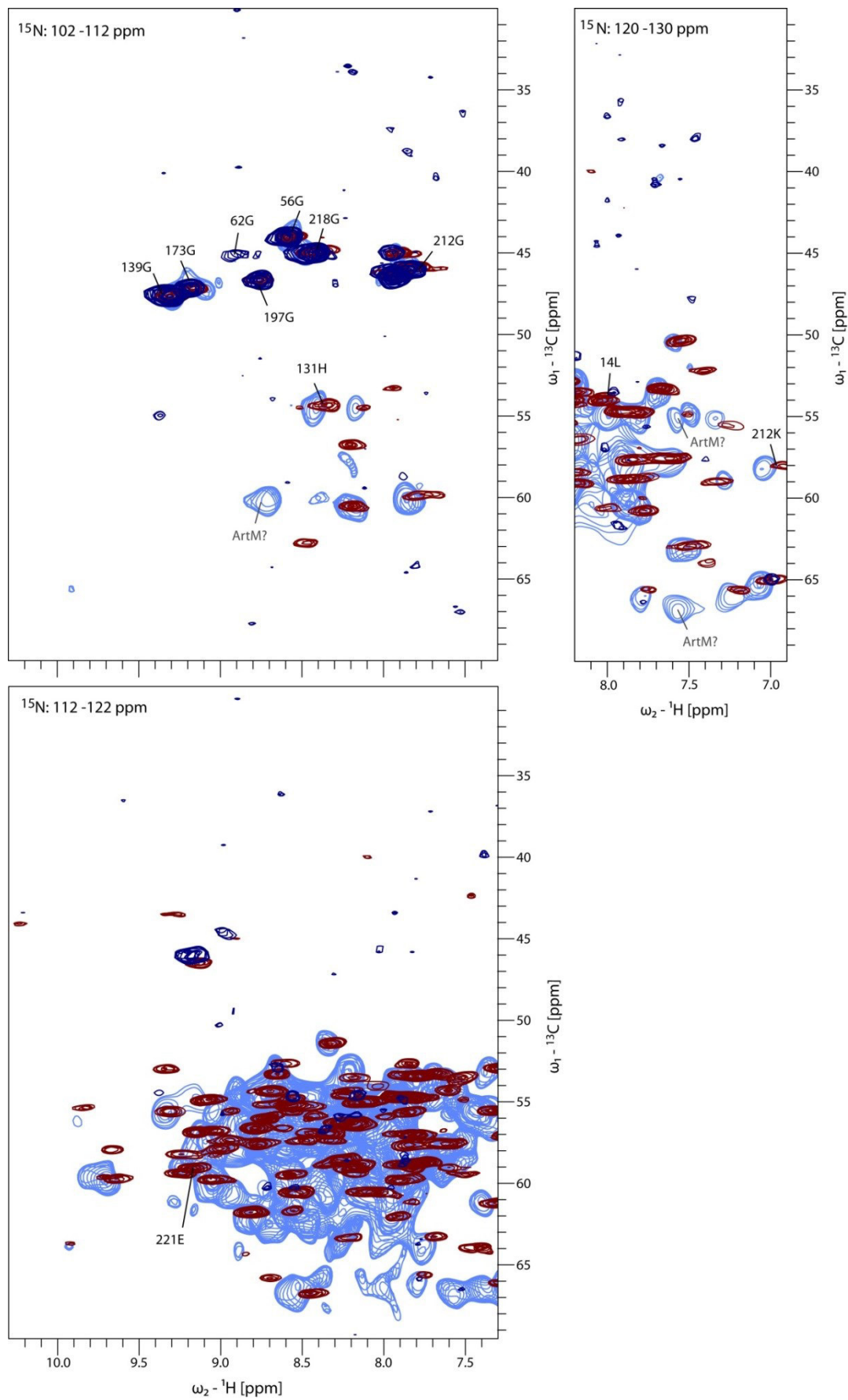
Figure 49: ^{15}N projections of hC$_α$NH and hC$_α$C$_β$NH spectra of ArtMP and ArtmP. Overlay of partial projections for the hCaNH of ArtMP at 20 kHz (light blue); the hCaNH of ArtmP at 40kHz (red) and the hCaCbNH of ArtmP at 40kHz (dark blue). C$_α$ resonances with ArtP assignments are labeled and potential peaks from ArtM are indicated.

5   Discussion

5.1   Cost-efficient production of transmembrane proteins by cSPP

For co-expressed, triple-labeled ArtMP, protein yields dropped by a factor of six compared to production in rich medium. Expression efficiency for isolated, unlabeled ArtM was generally even lower than for ArtMP, likely due to the missing stabilizing effect of ArtP. For ssNMR samples that focus on the TMD, the cSPP protocol was established and optimized for ArtM. In principle, the pMaz plasmid can be used in combination with any compatible vector containing the target gene, as long as it has a different selection marker and no ACA sequences in the transcribed regions including the untranslated regions (UTRs) at the 5'- and 3'-end of the target gene[100].

For production of ArtM, use of the pASK-IBA3plus-artM vector instead of the initial pColdIV-artM provided several improvements. First, induction can now be tightly controlled and expression leakage and co-expression by induction with IPTG is abolished[101]. This is extremely important considering the generally low amounts of labeled TMD in the ssNMR sample (with a lipid-to-ArtMP ratio of 0.5). Secondly, because of absence of the cspA promotor in pASK-IBA3plus-artM, the production rate should be improved as previously optimized expression temperatures for ArtM can now be used.

Schneider *et al.* recently published a similar expression system with independently inducible vectors based on pMazF and aTc-inducible derivatives of the pCold vector series[100,230]. In another study, yields with this cSPP system (pMazF/pCold(tet)) were compared to protein yields obtained with conventional pET(IPTG) vectors in condensed and uncondensed expression set-ups[101]. With 20-fold condensation, the total amount of isotope incorporation was similar for both trials while the fraction of unlabeled protein was about 25 % in the condensed set-up using the pET(IPTG) vector and basically absent (< 1%) for the pMaz/pCold(tet) set-up. This is likely to also hold true for the method established in this thesis project, which is equivalently based on the combination of pMazF with an aTc-inducible vector for target protein expression,

A drawback of the pMazF system is that all optimization steps including transformation, cultivation and expression have to be performed in M9 minimal medium. Even in LB medium supplemented with glucose as suggested by Grossmann *et al.*[231], growth of transformants was strongly impaired. The little amount of lactose present in the medium seems sufficient to induce mazF expression from the low-copy number pMaz vector, which in turn is enough to severely deregulate the host RNA pool, leading to impaired growth of *E. coli*. Also on minimal medium, the clones were less stable and standard small scale expression tests (as routinely performed for ArtP, ArtJ and ArtMP) were hard to carry. With the use of a tightly regulated promotor/operator system for mazF induction, this problem could probably be overcome.

The optimal aTc concentration for induction of target protein expression has to be scaled with the cell density and the condensation factor keeping the appropriate expression rate for the target protein

in mind. Thus far, induction with 3 and 15 µg/ml aTc was tested and expression seemed improved at higher aTc concentration.

For increased protein yields, precultures were condensed 20-fold at an OD_{600} of about 2.5 compared to the 40-fold condensation at an OD_{600} of 0.5 as performed in other studies[100,101,230]. This resulted in cell-densities in the isotope enriched cultures as high as an OD_{600} of 60 compared to maximum densities around 20 reported in the previously mentioned studies[100,101,230]. In all cSPP experiments for ArtM, these high cell densities remained stable indicating that the quasi-dormant state of the cells was efficiently reached and that oxygen supply was sufficient to maintain cell viability. On average, starting from eight liters of preculture that were condensed in 0.4 L of labeling medium, 36 g of *E. coli* bio wet mass were obtained.

This protocol was successfully applied for production of ^{15}N-, ^{13}C and ^{2}H^{15}N^{13}C-labeled ArtM. A CP-based HN correlation spectra of triple-labeled ArtM (assembled with deuterated ArtP and reconstituted in protonated lipids; sample 5) was recorded at 37 kHz MAS (Figure 45).This spectrum showed that ArtM is well folded and has high α-helical content as expected. In the 2D CC correlated DARR spectrum (recorded on ^{13}C-labeled ArtM, sample 14), the C_α/C_β peaks for alanines can be identified. The C_α/C_β signals for threonines and serines in α-helical conformation cluster on or close to the diagonal and are thus not observable as resolved peaks. The ArtM dimer seems to be in a symmetrical conformation as no indication for peak doubling was observed in these initial spectra.
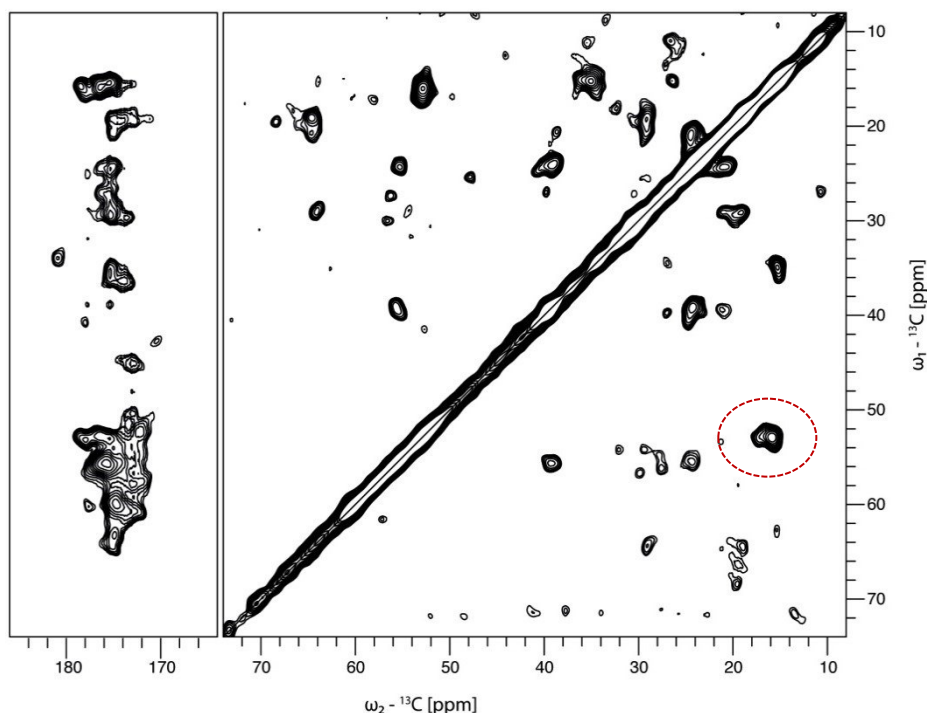

Figure 50: 2D CC correlation of ArtMp (sample 5) at 300 K. The spectrum was recorded at 800 MHz with 100 ms DARR mixing and ~ 18 kHz MAS.

The optimized cSPP for production of labeled ArtM considerably reduced the costs for isotopically enriched media (about 20-fold), while being only slightly more laborious than routine methods. This might even be pushed further using higher condensation factors and optimized inducer concentrations. Of course, this system can also be adapted for other hard-to-express targets including not only membrane but also toxic proteins.

5.2   Structural characterization of ArtMP by MAS ssNMR

5.2.1   Optimized ssNMR samples for multi-correlation NMR experiments

Improved yields for unlabeled ArtMP allowed for initial LCP crystallization trials using lipid preparations from *G. stearothermophilus*. In later set-ups, ArtJ was also included to trap a full complex of the transporter. First crystal hits were obtained in collaboration with Dr. Reginald McNulty (Luecke group, University of California, Irvine, USA) and an example is given in Figure 51.
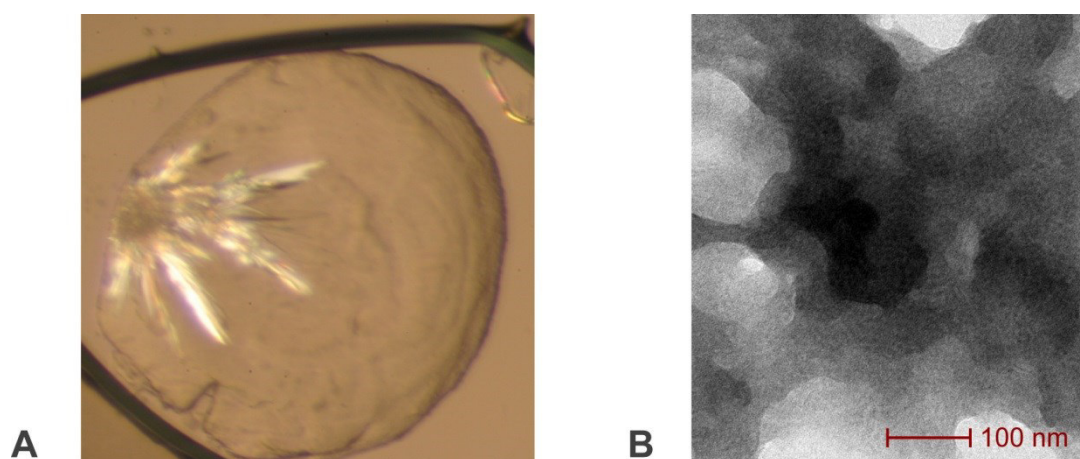
Figure 51: Crystallization trials for ArtMP. A Example of a first hit for ArtMP crystals by LCP crystallization **B** Electron microscopy picture of a ssNMR sample of ArtMP in lipids from *G. stearothermophilus* (sample 1)

2D crystallization of ArtMP in *G. stearothermophilus* lipids had already been achieved in previous studies carried out in collaboration with the group of Prof. A. Engel at Biozentrum Basel, Switzerland[211]. However, when these optimized crystallization conditions were applied for this project to ssNMR samples of triple-labeled protein, crystalline regions could not be identified. Rather, the samples contained densely packed sheets of lipid bilayers with ArtMP incorporated. Additionally, the high NaCl concentration in the optimized 2D crystallization protocol prohibited efficient transfer steps in multi-correlation experiments (ArtMP sample 1). As crystalline preparations in ssNMR are primarily used to obtain densely packed samples and thus high amount of labeled protein in MAS rotors, the 2D crystallization trials were not continued. Instead, the final lipid reconstitution buffer was optimized

by changing to the less conducting HEPES as buffering agent and lowering the NaCl concentration by a factor of 12. The glycerol concentration was also reduced from 4.3 to 1.7 %. These steps substantially decreased the dielectric of the sample, increasing T_2 times and allowing for multiple-step magnetization transfers in MAS experiments at 20 and 40 kHz.

5.2.2 Conformational characterization of ArtMP by MAS ssNMR

All MAS ssNMR spectra obtained for ArtMP, ArtmP and ArtMp showed homogenous protein conformations with no obvious indication of asymmetries (peak splittings etc.). Importantly for future studies, the reassembly of ArtMP from separately produced subunits did not alter the overall conformation of ArtP.

However, the cross polarization behavior of the two subunits is different and was less efficient for the TMD as can be judged from the very low intensity of ArtM peaks in spectra recorded at 20 kHz MAS. Both subdomains were fully deuterated during expression and a maximum of 30 % of the labile proton was back-exchanged. However, the protonated lipids surrounding the TMD could shorten the longitudinal ^{1}H T_2 time dramatically. This effect should be reduced by use of deuterated lipids. These were already successfully produced from *G. stearothermophilus* (by B. Kunert (2011)[199]) and their influence on ArtM will be investigated in the near future.

Regions of different dynamics — but on a slower timescale compared to ArtM — were also found in ArtP when comparing the 2D HN correlated spectra based on INEPT or CP magnetization transfer respectively. The residues observed in the first experiment are likely to reside in mobile regions with longer T_2 times for ^{1}H and ^{15}N while in regions with shorter T_2 times the magnetization relaxes too fast to be efficiently transferred. The CP experiment seemed to detect these additional regions. Linser *et al.* also observed that very mobile parts of microcrystalline SH3 were not detected in a CP- but only an INEPT-based 2D HN correlation experiment[232]. However, for a detailed analysis of regions of different mobility in ArtP, higher assignment coverage is necessary to allow site resolved T_2 relaxation experiments.

In the CP-based spectra, including all 3D correlation experiments obtained in this thesis, the final signal intensity is substantially influenced by the efficiency of the very first CP transfer from protons to carbon. The high level of deuteration necessary to reduce dipolar coupling by protons, also reduces the efficiency of this initial HC polarization transfer while detection of protons is still possible as long as an amide proton is present. The dCaNH experiment for ArtMP (sample 2) was based on an initial carbon (DC) CP step and mainly showed signals that had no corresponding peaks in a solution HSQC spectrum of ArtP. This indicates that many signals of the TMD were detected and that these are likely to correlate to regions of poor proton back-exchange. The HC CP is by definition a long-range transfer that strongly depends on the environment while the DC CP uses magnetization from the directly bonded deuterium. Due to the high concentration of deuterons in solvent-shielded parts the DC CP probably still leads to higher sensitivity for these regions, although the CP efficiency of deuterium is seven

times smaller compared to that of protons. Additionally, the shorter T_1 of deuterium compared to protons allows a higher experimental repetition rate and thus more scans per time unit, contributing to higher sensitivity.

Although deuterium NMR is challenging in terms of equipment and spectroscopy, it is extremely valuable for studying integral membrane proteins with solvent shielded regions. As an alternative, labeling approaches that do not rely on proton back-exchange can be used. The RAP (reduced adjoining protonation) method, for instance, combines deuterated ^{13}C-glucose with a certain amount of H_2O (5-25 %) in the expression medium[233]. This labeling scheme offers two additional possibilities: first, the introduced protons can be used to detect long-range contacts between aliphatic sites and secondly they allow relaxation measurements and extraction of order parameters to better describe side-chain dynamics. To more specifically introduce methyl protons, protonated carbon precursors can also be used during expression[103,234].

In addition to focusing on subdomains within the ArtMP transporter, the NBD-TMD interface should be characterized. This is not only important in terms of domain orientations but will also yield information about signal transduction when comparing different nucleotide bound states of the transporter. From the initial homology model for ArtMP, the interface of the two subunits can be predicted. To prove these speculations, differentially labeled ArtMP samples were prepared where the TMD and NBD were either ^{15}N or ^{13}C labeled (samples 12-14). Z-filtered TEDOR experiments were recently successful used for studying the quaternary arrangement in nanocrystalline protein preparations[235]. Similar experiments were recorded on samples with ^{15}N labeled ArtM and deuterated, sparsely 2-^{13}C labeled ArtP (sample 13). However, at 20 kHz MAS, no cross-peaks were observed after averaging for over 20 hours, which probably is due to the short ^{13}C and ^{15}N T_2 times of ArtM that led to insufficient coherence lifetime for the anyways rather insensitive transfer from the ^{15}N to the Ca of the other subunit. Deuteration of the TMD and the surrounding lipids, lower measurement temperatures and better decoupling at higher MAS frequencies should improve the transfer efficiencies and enable mapping of the ArtM-P interface.
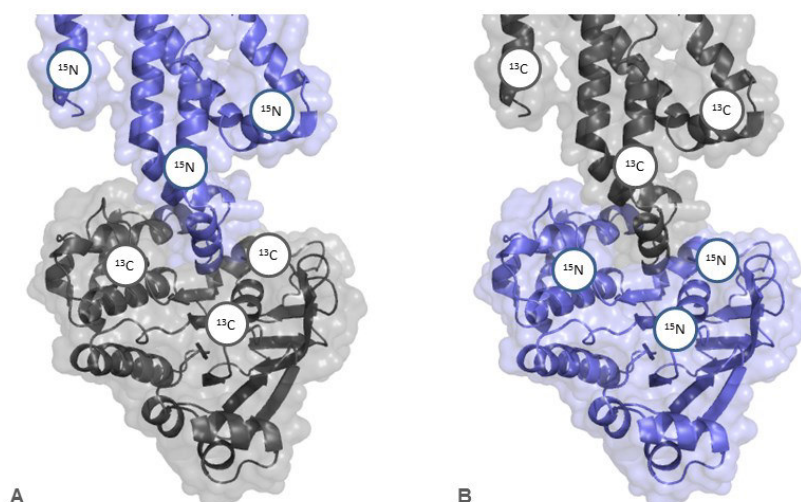
Figure 52: Differential labeling for characterization of the ArtM-P interface The CH tightly binds to a large grove region of ArtP and probably forms a stable salt-bridge to the NBD.

5.2.3   Assigning lipid-embedded ArtMP by ^{1}H detected ssNMR

Detection of protons enables 3D correlated experiments for ArtMP that would be extremely challenging to achieve with carbon detection, because of the immense amount of averaging time needed for sufficient S/N. These experiments not only contributed to assignments but also yielded information on regions of different mobility of the two subdomains. As one example, in the hCaNH spectrum of ArtMP (sample 2, 20 kHz MAS, Figure 46) several signals were identified that lacked a corresponding peak in the solution spectrum of ArtP. As these peaks are unlikely to arise from ArtM, they either belong to residues that have a different conformation in the full complex (especially possible for residues at the interface to ArtM) or to regions that were not detected in the solution experiment (like loops that are too mobile in the isolated domain). In total, 23 % of the residues belonging to the α-helical domain and 18 % of the RecA domain could already be assigned using the transfer strategy described in 4.6.5. Thus far, the identified residues are distributed over the entire ArtP sequence and none of the domains seems especially favored. About 80 % of the expected signals were obtained in the hCaNH, hCaCbNH and hCoNH experiments and the hCa(Co)NH and hCo(Ca)NH sequences will be acquired shortly to provide sequential connections. Completion of this assignment suite should soon enable almost full assignment coverage that builds the basis for structure determination of ArtP in context of the full transporter.

For assignment of the TMD, the hCbCaNH (and hCbCa(Co)NH) sequences by *Zhou et al.* will be especially useful, as C_β sensitivity can be optimized to avoid peak cancellation of C_α (positive) and C_β (negative) peaks. This might happen for the prominent α-helical residues, like threonines and serines, which have their C_α and C_β peaks in close neighborhood[61].

The pulse sequences used in this work were already of great use to assign resonances and solve structures of soluble proteins like GB1[236,237] but also for larger membrane protein complexes like DsbA/DsbB[238-241]. They yield either intra- or interresidue correlations, avoiding strong signal overlap that might become problematic with the set of ^{1}H detected assignment sequences commonly used in solution NMR and adapted for ssNMR by *Linser et al.*(especially when bigger proteins are investigated)[61,242].

The development of ^{1}H-detected ssNMR pulse sequences has picked up speed in the past years. The current signal enhancement of 3-5 (in theory up to 8) compared to carbon-detected experiments will drive this development further as biologically relevant systems often can only be obtained in an isotopically enriched form in small quantities and thus rely on sensitive detection. Combined with the increasing MAS frequencies this opens a door to tackle many previously inaccessible systems. Further

synergetic effects can additionally be expected by stronger integrating information from different methods of structural biology (like X-ray, SAXS, solution NMR and Cryo-EM), as successfully applied for the multimeric eyelense chaperon αB crystallin and the DsbA/DsbB complex[79,243].

5.3   Mechanistic implications from the ArtMP homology model

Quality of the model

Compared to other ABC transporters, the TMDs of type I importers are rather small domains comprising 5 (MetI) to 8 (MalF) TM-spanning helices. For prediction of the helix topology and the location of buried and exposed residues in ArtM, the RHYTHM server[18] was used. Five TMH were predicted with the N-terminus located at the extracellular and the C-terminus at the intracellular side (Figure 53). This topology is analogous to the *E. coli* methionine transporter MetNI. Both TMDs of the *E. coli* maltose transporter – the most frequently used model for type I transporters – include large periplasmic loops (especially the P2 loop of MalF) that tightly bind the SBP MalE and dock it to the TMD[244]. Such regions are absent in MetNI and *Af*ModBC-A (see Figure 7) and also for ArtM, none of the extracytoplasmic loops seems large enough to fulfill such a function.
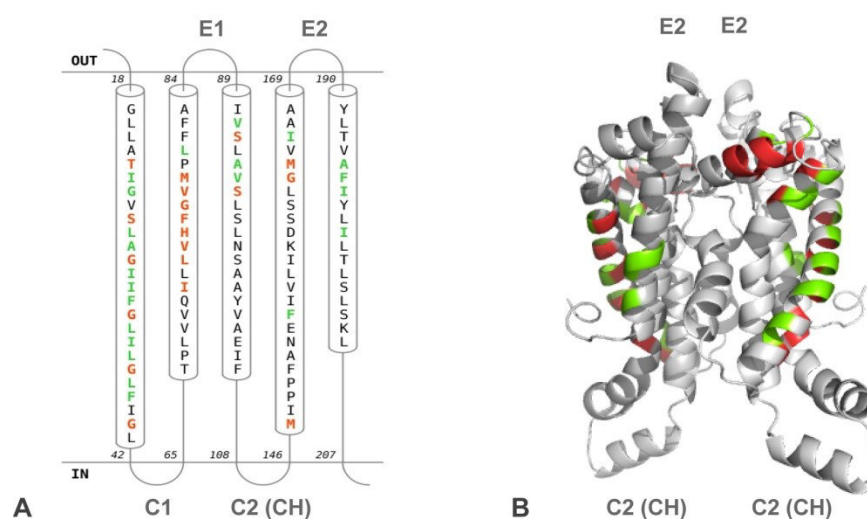
Figure 53: Topology and 3D model for ArtM. **A** The helix topology was predicted with the RHYTHM server using HMMTOP[245]. Predicted helix-helix contacts are labeled in red while possible helix-membrane contacts are highlighted in green. **B** Dimeric ArtM$_2$ assembled from the Phyre model for the ArtM monomer. The contacts predicted in **A** are labeled accordingly.

Phyre2[222] was used to create a 3D model for monomeric ArtM. 96 % of the ArtM sequence could be modeled (with two N- and seven C-terminal residues missing) at high confidence by the single highest scoring template. The confidence of the pairwise-template alignment (HHsearch) was especially good for the EAA motif and a set of conserved residues in the TM spanning helix.

The obtained model contains the five predicted TMH with the terminal helix probably ending fairly close to the membrane in the cytosol. With the 'Phyre2 investigator' (in beta test state) the quality of obtained model was analyzed in more detail (Figure 54). ProQ2[246] indicates that the prediction quality for the TM spanning helices and the coupling helix is better than for loops and no disordered regions are detected with the Disopred method. The Ramachandran analysis of the back bone yields that almost all residues have favorable conformations for *phi* and *psi* angles. For a very limited number of regions, clashes were reported when residues came in too close contact, which could be related to dissatisfactory side chain placement or incorrect backbone orientation. This is not surprising as the compactness of the molecule might be rather different in the membrane.
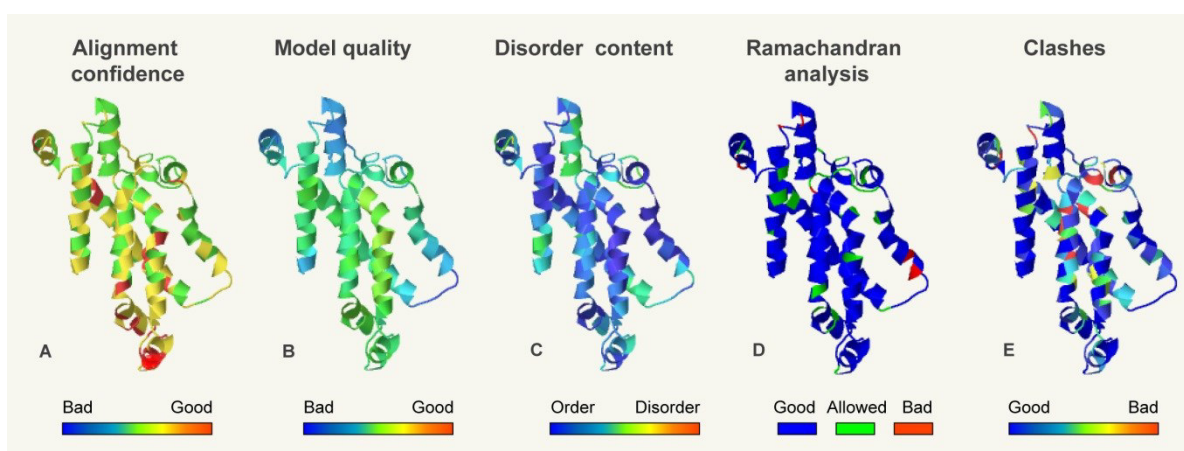
Figure 54: Quality evaluation of the ArtM model obtained using different tools in the Phyre2 investigator.

The ArtM/ArtP interface

For interpretation of NMR results, a very simple model of the outward-facing state for the full ArtMP complex was created as described in section 4.1 From this, it can speculated, that a salt bridge, which is also observed in X-ray structures of MalFGK$_2$-E, could be the reason for the extremely strong interaction of ArtM and ArtP that even enables co-purification of the two subunits (Figure 55).
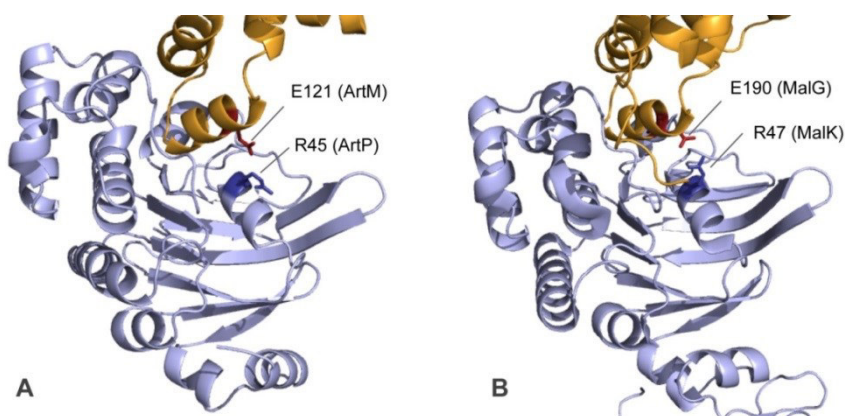
Figure 55: Potential residues involved in salt-bridge formation between the coupling helix and the corresponding NBD. A In the ArtMP model, E121 of the EAA motif in the TMD comes in close contact to R45 in ArtP. The side chain conformation of R45 is as in the 3C41 crystal structure of the TMD-stripped ArtP. **B** Residues forming a salt-bridge at the NBD-TMD interface in maltose transporter X-ray structure.

Substrate binding and interaction with ArtJ

During the course of this project, Weidlich *et al.* also published a model for ArtM that is similarly based on MetI as structural template. In this study, a potential substrate binding site in the channel was presented involving K159 (indicated in Figure 56A). NMR studies of ArtMP in different states during the transport cycle will help to understand if and how substrate is bound in the channel and at which step the substrate translocation is accomplished

Judging from the predicted helix topology and the 3D model of ArtM, the E2 loop likely harbors the interaction site for ArtJ (Figure 56B). Eckey *et al.* used a topology model obtained with the TMHMM prediction tool to create a series of mutations for residues located at the potential interface[247]. With the ArtMP model, the mutational effects observed in this study can be interpreted structurally. Mutations of K177, R185 and E188 to oppositely charged residues abolished ArtJ-dependent stimulation of ATPase activity while mutating E171 to a lysine had a stimulating effect (the location of these residues is given in Figure 56C). The authors were further able to crosslink cysteine mutants of ArtM(E182C) and ArtJ(N166C). In the ArtMP model, Y183-V186 are located at the very top of the E2 loop and it might be speculated that these residues establish the initial contact to ArtJ. Thus, mutation of the surrounding residues could very well disturb the conformation of this interaction site. However, a direct protein-protein interaction assay (i.e. ITC, SPR or NMR) would be necessary to differentiate between effects resulting from abrogated binding and defective activity.
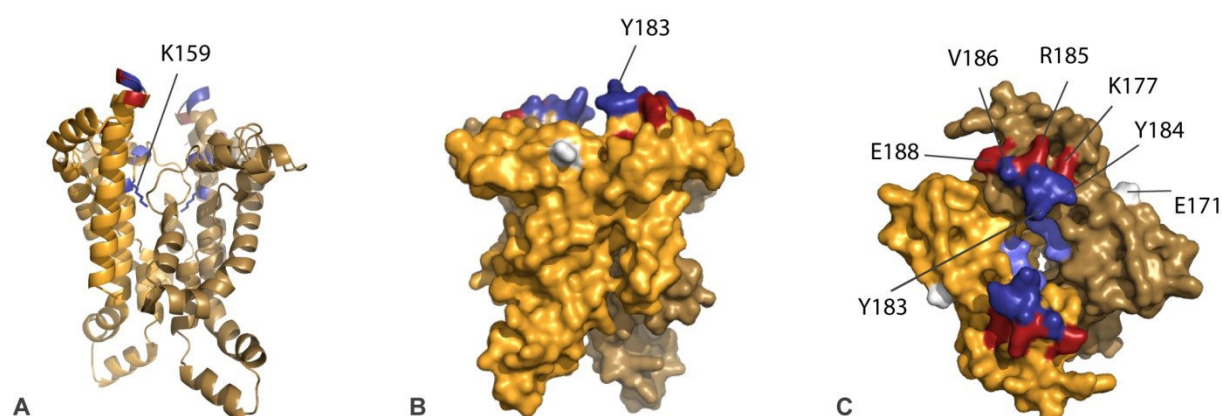

Figure 56: Location of a potential substrate binding and ArtJ interaction site in ArtM A Location of the substrate binding site proposed by Weidlich *et al.*. **B/C** Residues that are likely to interact with ArtJ are colored in blue, while the location of residues for which mutagenesis abolished ArtJ-dependent ATPase activity in Eckey *et al.* are colored in red. Mutation of E171 (white) had a stimulating effect in that study.

Comparison of inward- and outward-facing states of the ArtM$_2$ transmembrane channel

An inward-facing state of ArtMP was modeled using the 3FH6 structure of the maltose transporter, while for the outward-facing state the 3PUV structure was chosen as template. Figure 57 compares the two states for the ArtM$_2$ dimer in different orientations. In the top view of the outward-facing state, a potential entrance for the substrate is visible (lined by S161, S162 and W175) giving access to the substrate binding site mentioned by Weidlich *et al.*[203]. These residues come in close contact in the inward-facing model and lock the translocation pore to the outside. It has to be kept in mind that rigid body docking was used and no further energy minimization was carried out for these models. Additionally, the inside-open conformation seen in the 3FH6 structure of the maltose transporter lacking the lipid environment, is likely to show an unnatural degree of separation between the two TMDs. Still, the comparison of the two obtained models illustrates how sampling between the different conformations might look in ArtMP. Further, in the outward-facing state a very narrow solvent accessible channel spans the entire membrane pore. Similar channels were observed in recent MD simulations for the maltose transporter[248]. The authors claimed that these channels might explain why some transporters are leaky for water and small ions, while the substrate itself is transported by an alternating access mechanism.

In summary, these simple models help to interpret NMR data (regions of different mobility, shielded parts and nucleotide binding). They further provide a basis for the choice of residues suited for selective labeling or mutagenis. Amino-acid selective labeling might be valuable to focus on residues at the interface to ArtJ (e.g. tyrosines) or at the substrate entry site and the translocation pore. For ArtP, residues at the potential homo- and heterodimer interfaces could be investigated, improving our understanding of how interdomain communication is established and regulated in ArtMP-J.
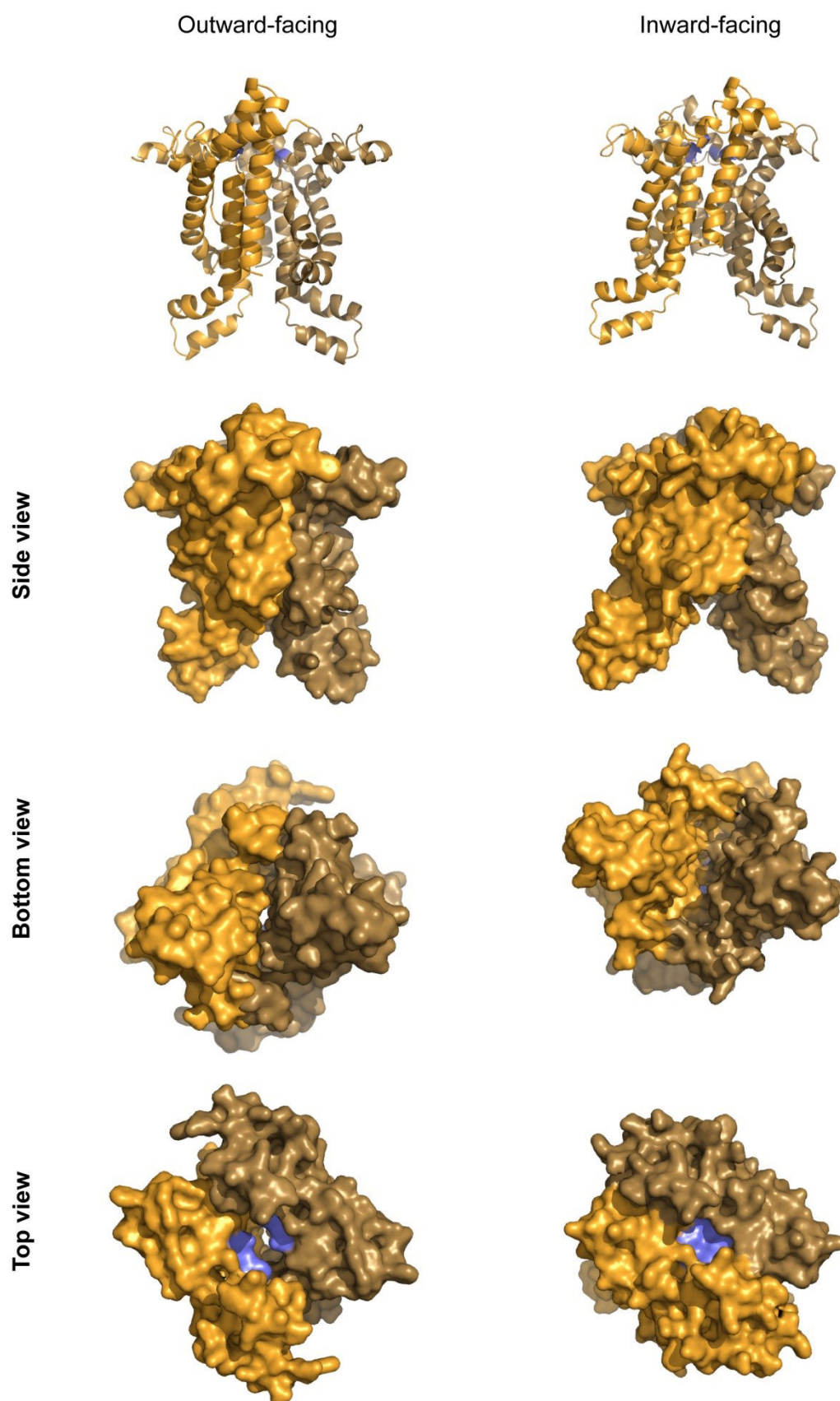
Figure 57: Models for an outward- and inward facing state for the ArtM dimer, obtained by rigid body docking of ArtM monomers onto the 3PUV and 3FH6 maltose transporter structures. The ArtM monomers are colored in yellow and sand. Residues at a potential entry channel (S161, S161 and W175) are colored in blue.

5.4   Functional investigation of ArtMP-J

5.4.1   Dimerization and nucleotide binding in comparison to other transporters

Dimerization behavior

The strength of nucleotide binding to isolated NBDs and full-length transporters has mostly been investigated in fluorescence studies using intrinsic tryptophan fluorescence combined with extensive mutagenesis to reduce the contributions from W residues distant from the nucleotide binding side[249,250]. Alternatively, the nucleotide ligand itself can be used in a derivatized form, making it suitable for detection[251]. Since wild-type ArtMP should be investigated while avoiding side-effects by derivatized nucleosides, ITC and NMR were chosen for characterization of nucleotide-binding to isolated ArtP and detergent-solubilized ArtMP.

For ArtP, to exclude side effects by random or nucleotide-dependent dimerization, the dimerization behavior of ArtP was investigated in AUC experiments in absence and presence of nucleotide. Under the conditions used (20-25 °C, standard buffer) none of the nucleotides including the non-hydrolyzable AMPPCP was able to induce dimerization. However, it should be noted that dimerization of ArtP generally seemed to be facilitated higher temperatures also for nucleotide-free ArtP (40 to 60 °C, data not shown). Nevertheless, from those experiments it cannot be judged if the dimerization was specific and happening at the same interfaces as in the full transporter. Considering, that the dimer interface observed in the 3C41 crystal of ArtP bound to AMPPNP is distinct from the interface in the ArtMP model, ArtP probably is able to dimerize in multiple conformations. Dimeric NBDs were for example observed in X-ray structures of isolated MalK, where the dimer was predominantly stabilized by the regulatory C-terminal domains and dimer closure was further promoted by presence of ATP[158]. For other isolated NBDs lacking these additional domains the affinity between monomers also seems rather weak (also in presence of ATP). In the MJ0796 and the GlcV transporters, mutation of the catalytic glutamates helped to stabilize an NBD dimer in presence of ATP [165,252]. To investigate whether such effects could also be observed for ArtP, the catalytic E162 was exchanged for an alanine. ITC experiments clearly indicated that nucleotide binding was not abrogated by the mutation (data not shown). However, also for this mutant no dimeric species was detected in presence of Mg^{2+}. Thus, the interactions at the NBD-NBD dimer interface are probably not strong enough to stabilize the ArtP dimer in solution. Nevertheless, high ion and nucleotide concentrations in combination with precipitants like PEG might induce dimer formation in crystallization set-ups leading to artificial arrangements that are not unlikely to occur in the full-length transporter.

Nucleotide binding

The AUC experiments showed that the ArtP was monomeric (in absence and presence of nucleotide) under the buffer conditions that were used in subsequent nucleotide binding studies. Thus, the observed effects have to be related to nucleotide binding on not to a dimerization event.

As ssNMR samples of ArtMP need to be stable for months to years, non-hydrolyzable ATP analogs have to be used to trap a closed transporter state. Only little data comparing binding of natural nucleotides and analogs has been published for ABC transporters. ITC was performed for isolated ArtP and detergent-solubilized ArtMP to obtain information on nucleotide dependent effects and the minimal nucleotide concentrations to induce observable effects in NMR spectra.

In ITC experiments, stable binding of nucleotides was only observed in presence of Mg^{2+}. Isolated ArtP bound ADP and ATP with identical dissociation constants (7 µM). This observation was also reported for the NBDs of the HylB (ATP/ADP 88/77 µM)[253] and MRP-1(118/139 µM)[254] transporters using tryptophan fluorescence. In an ITC study for GlcV, the K_D values found for ATP and ADP at 30 °C were also similar (in the nM range), while at 20 °C ADP bound about four times stronger than ATP[255]. In contrast, for P-glycoprotein K_D values around 400 µM for ATP and ADP were calculated from fluorescence data obtained using MIANS-labeled protein[256]. In the same study, these values improved by an order of magnitude (ATP/ADP 55/42 µM), when nucleotide derivatives with attached fluorophors were used, underlining the large effect that this kind of labeling can have on protein-ligand interactions. The given examples span a wide range of K_DS for the interaction of transporters with ATP/ADP starting from low nM to high µM This might partially be attributed to the different methods used in these studies. Moreover, these largely dissimilar values could indeed represent functional fine tuning for each transporter and be very specific for the corresponding function.

Compared to the natural nucleotides, binding of AMPPNP and AMPPCP was substantially weaker for both ArtP and ArtMP. In ITC studies with GlcV, binding of AMPPNP was also lower by over one order of magnitude compared to ATP (~ 50 µM for ATP and ~ 700 µM AMPPNP)[255]. Similar observations were made in fluorescence quenching studies for P-glycoprotein, where AMPPNP exhibited substantially reduced affinity compared to ATPgS and ATP[257].

Saturation of ArtMP with AMPPCP is a prerequisite for trapping a fully closed state of the lipid-embedded transporter. With K_DS in the high µM range, nucleotide concentrations of 10 to 100 mM should be applied to ensure that the majority of ArtMP molecules has nucleotide bound. Alternatively, ArtMP samples containing the mutation of the active glutamate could be used in combination with AMPPPNP (possibly also ATPgS or even ATP), although stability of nucleotide would have to be followed closely.

Nucleotide affinities will for sure depend on the environment and further binding studies should at best be performed in presence of lipids. Microscale thermophoresis could be optimal for analyzing these kinds of interactions with the additional advantage of being extremely protein-saving.

Structural effects by natural nucleotides and analogs

For ArtP and ArtMP, nucleotide-binding was further assayed on amino acid level applying solution and ssNMR. The range of binding affinities found for the different nucleotides in ITC, was clearly reflected in solution NMR with ArtP. At concentrations that resembled > 90 % saturation (calculated from the respective K_D values found in ITC), AMPPNP and AMPPCP were able to induce effects similar to ATP at distant sides while residues at the nucleotide binding site showed slight differences.

In the solid-state spectra of ArtmP in presence of 0.4 mM AMPPCP (obtained by Dr. B. Kunert) the concentration of the ATP-analog was probably not sufficient to trap a closed resting state of the transporter. Thus, the observed effects are likely to be purely related to nucleotide binding and not to large conformational rearrangements. This fits to the observation that ADP- and AMPPCP- bound ArtmP yielded very similar spectra that almost exclusively showed shifts for peaks, which were also affected in solution NMR experiments.

Care has to be taken, when interpreting results obtained with nucleotide analogs as recently seen for the K_{ATP} channel[258]. For long, it was concluded that ATP analogs failed to activate the channels because they could not be hydrolyzed. Reevaluation of the available data now suggests that binding of ATPγS to the NBDs is substantially weaker compared to ATP and that it can – when used at higher concentrations – indeed stimulate the channel. In contrast, AMPPNP and AMPPCP preferentially bind to the non-canonical and only to a small extent to the second NBD, which in turn prohibits NBD dimerization and switch of the channel to the outward-facing state.

For ArtMP, interpretation of nucleotide-dependent effects is clearly limited by the current assignment coverage for ArtP in standard buffer. For full assignment of ArtP in this buffer system, a set of 3D solution NMR spectra was already recorded (in collaboration with Dr. P. Schmieder and M. Beerbaum, FMP, Berlin) in the course of this thesis but could not be assigned yet for time reasons.

5.4.2 Signal transduction in ArtMP-J

For several transporters, asymmetric states in presence of nucleotide were reported in X-ray, tryptophan fluorescence quenching and EPR studies. For P-glycoprotein, an asymmetric state with one high affinity, occluded and a second low affinity, partially open nucleotide binding site was found in presence of ATPγS[259]. For lipid-embedded ArtMP, thus far no indication of asymmetry (like peak doublings in NMR spectra) was observed in absence and presence of 0.4 mM of nucleotide, indicating that both NB sites show identical conformations at these nucleotide concentrations.

For exporters, binding of analogs like AMPPNP was often not sufficient to induce an outward-facing state, indicating that the analog itself, while bound to one NBD via the Walker A motif, might not be capable of promoting the correct interaction with the ABC-signature of the opposite NBD, thus preventing closure of the transporter. Another possibility, independent from the bound nucleotide, is that a second stimulus (like drug-binding for P-glycoprotein) is generally necessary to fully induce the conformational switch to the outward-facing state. For importers like MalFGK$_2$, it was suggested that both, presence of ATP and the SBP are necessary for this transition[175]. At similar affinities, ATP-binding is favored over ADP considering that cellular ATP concentration is of about ten times higher than the one of ADP. Thus, at a cytosolic ATP concentration of around 10 mM, ArtMP is likely to rest in an ATP-bound state. Presence of substrate-loaded BP, but possibly also of substrate-free BP[183], would then induce progression to the pre-translocation state[146]. Subsequent ATP hydrolysis would further create a transition state, where the substrate is released from the SBP into the translocation channel.

Thus far, conformational switching between inward- (ADP-bound) and outward- (AMPPCP-bound) facing states was not observed for judging from the overall conformation of ArtP (in ArtmP) in HN correlated ssNMR experiments. Even if mainly rigid-body rotations of the different subunits would lead to closure of the NBD dimer in presence of AMPPCP[177], this would change the local chemical environment of residues at the dimer interface. These effects should be observed as intensity changes or peak shifts. Bao *et al.* recently found that ATP was sufficient to create an outward-facing state in the absence of MalE[180]. To check, if higher concentration of AMPPCP promote closure of the transporter, ssNMR ArtMP samples containing 4 mM (instead of 0.4 mM) AMPPCP were already prepared (samples 8 and 11). If existent, asymmetric states might also be detected in these samples.

For the maltose transporter, the role of the SBP has evolved from a mere capture and delivery function towards a necessary factor for the switch to the outward-facing state[175]. Recently, regulatory effects have also been reported for MalE[181]. Although grouped into the same importer class, MalFGK$_2$-E is very distinct from ArtMP-J in terms of structure. The TMDs MalF and MalG have additional helices compared to the minimum of five helices in ArtM. MalF additionally has a very large periplasmic loop (P2 loop) that binds to MalE and induces a semi-open state of the SBP[260]. Further, the MalK dimer is

quasi-crosslinked by the C-terminal regulatory domains. All of these structural differences might account for the intriguing stability observed for the maltose transporter in comparison to ArtMP-J.

A potential path for signal transduction to the TMD

Nucleotide binding was investigated for isolated ArtP by solution and in native lipids by ssNMR. This excludes potential artefacts resulting from crystal packing that could induce non-native conformations for functionally important loops, which could easily be mistaken for mechanistic effects.

As expected, all of the ABC transporter motifs involved in binding and hydrolysis were influenced by the presence of nucleotide in solution NMR experiments. The strongest indications for nucleotide binding were found in the A-loop but also for the Walker A (S41) and the Walker B motif (F159, D160). The Q loop is generally thought to be involved in signal transmission to the TMD and in most nucleotide-bound X-ray structures of other transporters it also strongly interacts with the γ-phosphate of the nucleotide. In isolated ArtP, this loop was substantially affected by both ATP and ADP. In structures for the maltose transporter, the carbonyl group of the Q-loop glutamine contacts the Mg^{2+} ion while the side-chain amide group of the same residue binds to the third phosphate of the nucleotide (Figure 58). Possibly the effects observed in solution NMR spectra result from tighter binding of Mg^{2+} in presence of nucleotide, no matter if ATP or ADP is present. However, presence of the γ-phosphate ATP might indeed lead to a slight reorientation of the side chain NH_2 group of Q84 in ArtP which could be involved in transmission of the signal to the neighboring ArtM CH. Unfortunately, in spectra of ArtP with ATP or ADP the peak for Q84 is not present (either broadened below the detection limit or shifted to a very different region in the spectrum), so that a definite statement about differentiation for di-and triphospho nucleotide by the Q-loop is not possible.
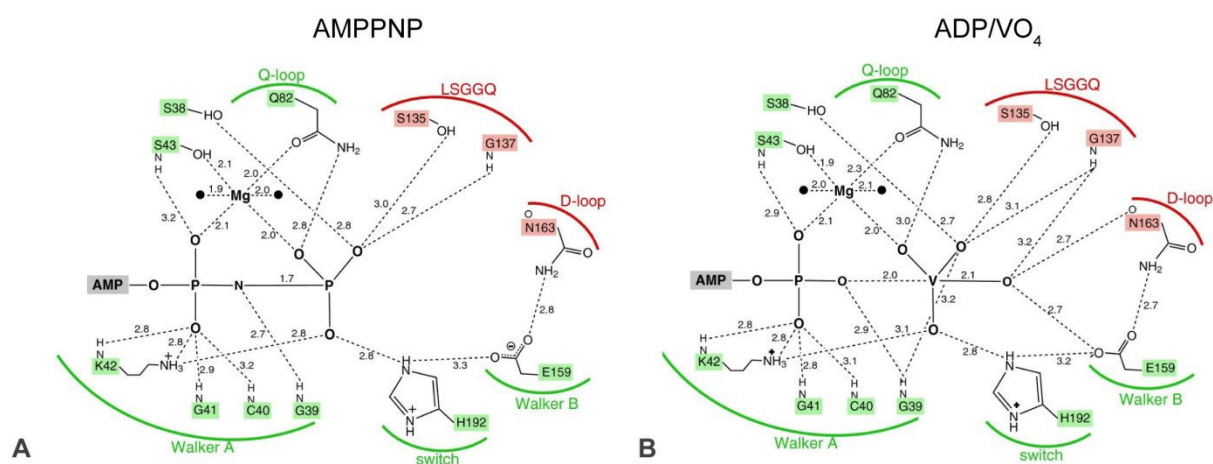
Figure 58: Conformation of the NBS of the maltose transporter in presence of AMPPNP (3RLF) and ADP/VO$_4$ (3PUV)[146]

Weak binding was also observed at the ABC signatures at nucleotide concentrations as low as 0.2 mM, although dimerization of the soluble domains can be excluded at the experimental conditions used. These binding effects were in essence seen for all of the tested nucleotides and were of similar strength for ADP and ATP which could imply that the ABC signature motif also shows similar affinity for both nucleotide types. This leads to the speculation that is not the presence of ADP that destabilizes the closed dimer interface after ATP hydrolysis, which fits to the postulation that in fact the release of the negatively charged phosphate group is responsible separation and progression to an inward-facing, post-hydrolysis state.

How the nucleotide-bound state is communicated from to NBD the TMD in ArtMP, might be guessed when closely examining the residues that were strongly affected in solution and solid-state NMR experiments. Many of these do not belong to (or only extend) the classical ABC motifs (see Figure 39). These residues were grouped according to their location in ArtP (Table 13).

Table 13: Additional regions affected in ArtP

Group	Residues
1	L14-V29
2	L47-E55
3	R75-G80
4	D204-G218

Figure 59 plots the location of these groups onto ArtP in the homology model for the complex. From this representation, it can be speculated that nucleotide binding to the A-loop could indeed strongly influence the close-by β-sheet, which is mainly composed of residues in group 1 and 4. Group 4 might simply adapt to the changed conformation of group 1 in presence of nucleotide and not perform an

explicit role in signal transduction. Group 2 comprises a large loop with several charged residues and a phenylalanine. R45, which is likely to form a salt bridge to the EAA glutamate in the CH of ArtM, is located N-terminal to this loop (see Figure 55). The residues in Group 3 are located N-terminal to the Q-loop and according to the homology model these residues could contact the "rear" part of the CH. The CH would thus be flanked by the underlying Q-loop and its N-terminal extension as well as by residues in the group 2 loop that basically flank the other side of the helix. This indicates that the nucleotide-bound state is transmitted to the TMD by a complex network of interactions involving several regions (L47-E55 and R75-G80) that are not directly involved in nucleotide binding or hydrolysis. The profound ssNMR investigation of the transporter will soon show, if these conclusions also hold true for the full ArtMP complex in the lipid environment.
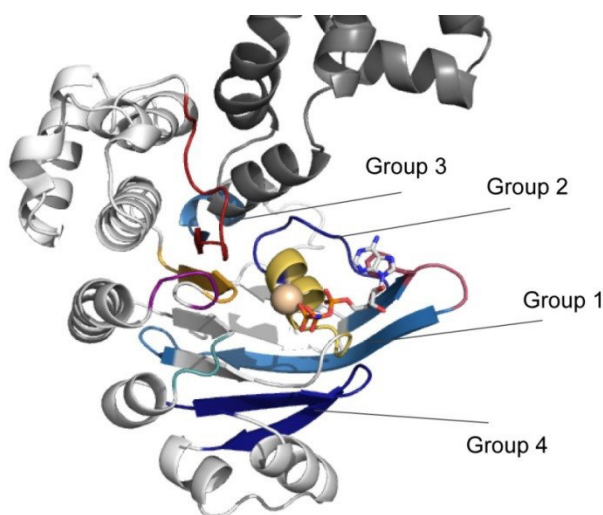
Figure 59: Distant regions in ArtP that were strongly affected by nucleotide binding (in addition to the typical ABC transporter motifs). The different groups are colored in blue. The Walker A and B motif are shown in yellow and orange. The A-loop is depicted in pink, while the Q-loop is colored in red, the D-loop in purple and the H-loop in cyan.

6   Outlook

The biophysical investigation of ArtMP already gave important insights into the effects of nucleotide binding to the transporter including possible ways of signal transduction. SsNMR studies in native lipids yielded information about regions of different dynamics in ArtMP and ^{1}H-detected 3D correlated ssNMR spectra paved the way for assignment and structure determination of the NBD in context of the full, lipid-embedded transporter. As isotopic enrichment is now also feasible for the TMD, the investigation of helix movements upon nucleotide binding and substrate translocation is possible in the future. Further, the interaction interfaces to ArtP and ArtJ will be mapped as a prerequisite for structure determination of the full ArtMP-J complex. When ArtJ binding to detergent-solubilized ArtMP was assayed by solution NMR, only minor intensity changes for several amide cross peaks could be detected and no hint for stable complex formation has been observed yet. This seems counterintuitive since the transporter was found to be active and showed about five-fold stimulation of the ATPase activity in presence of ArtJ and arginine. For MalFGK$_2$-E, it was speculated that both ATP and the substrate loaded SBP have to be present to create a stable outward-facing complex. Possibly, in solution, the interaction between ArtJ and ArtM is too transient to be observed with the experimental setup used in solution NMR. Thus, one of the future challenges for full structural characterization of ArtMP-J is the formation of a stable complex for ssNMR studies. Expression of ArtJ with its native lipid anchor is currently carried out in collaboration with Mahsheed Sohrabi (FMP, Berlin). Anchoring ArtJ to the lipid bilayer will reduce its degrees of freedom and increase the active concentration of ArtJ at the membrane. This might help to stabilize the interaction with lipid-embedded ArtMP and enable trapping of stable complexes in different states along the transport cycle.

7 Summary

ATP-binding cassette (ABC) transporters are ubiquitous multi-subunit transmembrane (TM) protein complexes. They play vital roles in physiological processes like nutrient uptake in prokaryotes, lipid metabolism and extrusion of toxic compounds. ABC transporters hamper chemotherapy of cancer and treatment of infectious diseases by actively removing drugs from the cytoplasm. Both, ABC import and export systems require the energy obtained from ATP hydrolysis within their nucleotide binding 'domains' (NBDs) to translocate their substrates across lipid bilayers. In contrast to exporters, ABC importers rely on an additional substrate binding protein (SBP) that captures substrate molecules and delivers them to the transmembrane domains (TMDs) of the transporter. X-ray structures of the *E. coli* maltose importer in different nucleotide-bound states and in a lipid-free environment have been published. On this basis, a transport cycle was proposed that includes an 'Alternating Access' mechanism describing the structural changes in ABC transporters upon substrate translocation. However, despite the many similarities, functional differences between the two transporter classes exist and the details of the translocation mechanism in native lipid environment are far from understood. In the frame of this thesis, structurally distinct states of the amino acid importer ArtMP-J from *Geobacillus stearothermophilus* were investigated in lipid bilayers using ADP and the non-hydrolyzable ATP-analog AMPPCP to capture the post-hydrolysis and transition states, respectively.

Magic angle spinning (MAS) solid-state NMR (ssNMR) was used as the primary tool to characterize lipid-embedded ArtMP. The occurrence of non-covalently linked subunits (ArtM and ArtP, two of each) in ArtMP-J facilitated their individual labeling within the functional complex. It was a major part of this thesis to develop the protocols for labeling of ArtP or ArtM in ArtMP and to subject the preparations to spectroscopic investigations.

To enable labeling of ArtM alone, protocols for heterologous expression and enrichment with NMR-active isotopes had to be optimized and highly cost-efficient ^{2}H,^{13}C,^{15}N labeling of the TMD was achieved by adapting the 'condensed Single Protein Production' protocol.

The thermodynamic parameters of nucleotide binding to ArtP and ArtMP were analyzed by isothermal titration calorimetry (ITC). Initial experiments with the soluble NBD ArtP alone yielded comparable affinities for ATP and ADP (6 μM), while the non-hydrolyzable analogs AMPPNP and AMPPCP bound by factors of 8 and 45 weaker. In the next step, the detergent-solubilized ArtMP complex was investigated. It showed strongest affinity for ADP (13 μM) while both AMPPNP and AMPPCP bound with K_Ds of around 70 μM. Interestingly, the interaction of ArtMP and ADP was endothermic, while all other nucleotides bound in an exothermic reaction.

Structural effects of nucleotide-binding to ArtP were initially analyzed by solution NMR. Binding of ATP and ADP led to identical chemical shift changes in agreement with the comparable K_Ds, suggesting very similar structural properties of the complexes. Next, ^{1}H-detected ssNMR spectroscopy was applied to further investigate nucleotide-dependent changes of the functional ArtMP complex in

lipid bilayers. As a requirement for this study, initial assignments for the subunit ArtP were obtained from combining the available solution NMR assignment with data from ^{1}H-detected 3D ssNMR experiments applied to the lipid-embedded transporter. The amide cross peaks of the assigned residues were used as sensitive monitors for ADP- and AMPPCP-induced conformational changes in ArtP within the ArtMP complex. Many of the observed chemical shift changes in the spectra of the full complex resembled the observations obtained by solution NMR on ArtP alone. Remarkably, the presence of nucleotide also affected signals from regions distant to the nucleotide binding site. Integrating data from both solution and ssNMR with a simple homology model of ArtMP enabled the proposal of a potential route for transmission of structural changes induced by nucleotide-binding towards the ArtP and ArtM interface.

Towards achieving full resonance assignments of ArtMP, ^{1}H detected experiments at 40 kHz MAS were performed. Several preparations were investigated, including samples containing either the NBD (ArtP) or the TMD (ArtM) in a triple-labeled form while the other subunit remained at natural abundance. In the respective basic triple-resonance experiments (hCaNH and hCoNH) 80 % of the expected peaks for ArtP were observed. Completion of this data set by experiments yielding correlations across amide bonds will soon enable full structural characterization of the transporter.

The produced samples were also used in projects aiming at the advancement of NMR technology, for example by including deuterium into quadruple-resonance NMR experiments. By combining deuterium excitation with proton detection additional cross peaks were obtained in 3D spectra as compared to triple-resonance experiments including only manipulation of proton, carbon and nitrogen spins. This implicated that ArtM contains solvent-shielded regions with insufficient reincorporation of protons at labile sites. These regions are challenging to investigate using pulse sequences that start with an initial ^{1}H to ^{13}C cross polarization (CP) transfer. For integral membrane proteins that cannot be fully un- and refolded to guarantee sufficient proton back-exchange, this new method offers a valuable alternative for structural investigations (published in Akbey *et al.*, 2014).

This structural study on ArtMP-J exemplifies how ^{1}H-detected fast spinning ssNMR can be applied to complex multi-component systems for investigation of biological function. It represents the first application of this technique to the detection of ligand binding, by monitoring conformational changes upon nucleotide binding to ArtMP within its native lipid environment.

8 Zusammenfassung

ATP-binding cassette (ABC)- Transporter sind ubiquitäre Transmembranproteine, die sich aus mehreren Komponenten zusammensetzen. Sie spielen entscheidende Rollen in physiologischen Prozessen wie der Nährstoffaufnahme in Prokaryoten, im Lipid-Metabolismus und der Ausschleusung toxischer Substanzen. ABC-Transporter erschweren die Chemotherapie von Krebs und die Behandlung infektiöser Krankheiten, indem sie pharmakologisch aktive Moleküle aktiv aus dem Zytoplasma entfernen. Sowohl ABC-Import- als auch -Export-Systeme nutzen die Energie der Hydrolyse von ATP zwischen ihren Nukleotidbindedomänen (NBDs) zur Translokation ihrer Substrate über Lipiddoppelschichten. Im Gegensatz zu Exportern, sind ABC-Importer auf ein zusätzliches Substratbindeprotein (SBP) angewiesen, welches Substratmoleküle einfängt und den Transmembrandomänen zuführt. Röntgenkristallstrukturen des Maltose-Importers aus *E. coli* in unterschiedlichen nukleotid-gebundenen Zuständen und in lipid-freier Umgebung wurden bereits publiziert. Auf dieser Basis wurde ein Transportzyklus postuliert, der einen sogenannten „Alternating Access"-Mechanismus für die Beschreibung der strukturellen Änderungen in ABC-Transportern während der Substratranslokation zugrunde legt. Trotz der vielen Gemeinsamkeiten existieren funktionale Unterschiede zwischen den beiden Transporter-Klassen und Details zum Translokationsmechanismus in nativer Lipidumgebung sind kaum verstanden. Im Rahmen dieser Arbeit, wurden verschiedene strukturelle Zustände des Aminosäure-Importers ArtMP-J aus *Geobacillus stearothermophilus* in Lipiddoppelschichten untersucht, indem ADP sowie das nicht-hydrolysierbare ATP-Analogon AMPPCP für die Präparation des post-hydrolytischen sowie des Übergangszustandes verwendet wurden.

Magic angle spinning (MAS)-Festkörper-NMR-Spektroskopie wurde als primäre Methode zur Charakterisierung des lipid-umschlossenen ArtMP verwendet. Der Aufbau aus nicht-kovalent gebundenen Untereinheiten (jeweils zweimal ArtM und ArtP) in ArtMP-J erleichtert deren individuelle Markierung mit NMR-aktiven Isotopen (Labeling) innerhalb des funktionalen Komplexes. Ein Großteil der vorliegenden Arbeit bestand in der Entwicklung von Labeling-Protokollen für ArtP, ArtM und ArtMP sowie der spektroskopischen Untersuchung der präparierten Komplexe. Für die Isotopenmarkierung des isolierten ArtM mussten Protokolle zur heterologen Expression sowie zur Anreicherung mit NMR-aktiven Isotopen optimiert werden. Eine höchst kosteneffiziente Markierung der TMD mit den Isotopen ^{2}H,^{13}C und ^{15}N konnte durch Adaptierung der 'condensed Single Protein Production'-Methode erzielt werden.

Die thermodynamischen Parameter der Nucleotidbinding an ArtP und ArtMP wurden mittels Isothermaler Titrationskalorimetrie (ITC) analysiert. Initiale Experimente mit der isolierten NBD ArtP lieferten vergleichbare Affinitäten für ATP und ADP (6 μM), während die nicht-hydrolysierbaren Analoga AMPPNP und AMPPCP um Faktoren von 8 bzw. 45 schwächer gebunden wurden. Im nächsten Schritt wurde der detergenzgelöste ArtMP-Komplex untersucht. Die Affinität für ADP lag bei 13 μM, wohingegen sowohl AMPPNP als auch AMPPCP mit K_Ds von etwa 70 μM gebunden wurden.

Interessanterweise verlief die Interaktion von ArtMP und ADP endotherm, während alle anderen Nukleotide exotherme Bindungsreaktionen zeigten.

Strukturelle Veränderungen in ArtP hervorgerufen durch Nukleotidbindung wurden zunächst mittels Lösungs-NMR-Spektroskopie analysiert. Die Bindung von ATP und ADP führte zu identischer Beeinflussung der Chemischen Verschiebungen, im Einklang mit den vergleichbaren K_D-Werten und suggeriert damit ähnliche strukturelle Eigenschaften der Komplexe. ^{1}H-detektierter Festkörper-NMR-Spektroskopie wurde verwendet um nukleotideabhängige Effekte innerhalb des funktionalen ArtMP-Komplexes in Lipidumgebung zu untersuchen.

Als Voraussetzung für diese Analyse wurden initiale Signalzuordnungen für die ArtP-Untereinheit aus Kombination einer verfügbaren Lösungs-NMR-Zuordnung für ArtP mit [1]H-detektierten dreidimensionalen Festkörper-NMR-Experimenten für den lipidumschlossenen Transporter erhalten. Die Kreuzsignale für Amidprotonen der zugeordneten Aminosäurereste konnten als sensitive Monitore für ADP- und AMPPCP-induzierte konformationelle Änderungen von ArtP innerhalb des ArtMP-Komplexes verwendet werden. Viele der beobachteten Effekte auf die Chemischen Verschiebungen in den Spektren des vollständigen Komplexes ähnelten den Beobachtungen in Lösungs-NMR-Experimenten mit isoliertem ArtP. Bemerkenswerterweise wurden auch Signale für Regionen abseits der Nukleotidbindetasche durch Anwesenheit von Nukleotid beeinflusst. Die Integration von Daten aus Lösungs- und Festkörperexperimenten sowie eines einfachen Homologiemodells für ArtMP, ermöglicht Rückschlüsse auf eine potentielle Route zur Weitergabe nukleotidbedingter struktureller Veränderungen in Richtung der Interaktionsfläche zwischen ArtP und ArtM.

Im Hinblick auf eine vollständige Resonanzzuordnung für ArtMP wurden [1]H-detektierte Experimente bei einer MAS-Frequenz von 40 kHz durchgeführt. Mehrere Präparationen wurden untersucht, darunter Proben die entweder die NBD (ArtP) oder die TMD (ArtM) in dreifach-markierter Form enthielten, während die andere Domäne mit Isotopen in natürlicher Häufigkeit vorlag. In den entsprechenden grundlegenden Dreifachresonanz-Experimenten (hCaNH und hCoNH) wurden über 80 % der erwarteten Signale für ArtP detektiert. Weitere Experimente, welche Korrelationen über Amidbindungen liefern, komplettieren diesen Assignment-Satz und ermöglichen die vollständige strukturelle Charakterisierung des Transporters.

Die hergestellten Proben wurden in zusätzlichen Projekten zur Weiterentwicklung der NMR-Technologie verwendet, wobei beispielsweise Deuterium in Quadruple-Resonance-Experimente einbezogen wurde. Durch Kombination von Deuteriumanregung mit der Detektion von Protonen wurden zusätzliche Kreuzsignale in 3D-Experimenten erhalten, welche in Dreifachresonanzexperimenten, die ausschließlich auf Manipulation von Protonen, Kohlenstoff und Stickstoff basierten, nicht auftraten. Dies lässt vermuten, dass ArtM abgeschirmte Regionen enthält, die unzureichenden Protonenrücktausch an labilen Gruppen aufweisen. Diese Regionen sind mit Pulssequenzen, die mit einem initialen Kreuzpolarisationstransfer von ^{1}H auf ^{13}C beginnen, schwer zu untersuchen. Für integrale Membranproteine, die nicht vollständig ent- und zurückgefaltet werden können um ausreichenden Protonen-

rücktausch zu gewähren, bietet diese neue Methode eine wertvolle Alternative für strukturelle Untersuchungen (publiziert in Akbey *et al.*, 2014).

Die vorgestellte strukturelle Untersuchung von ArtMP-J kann als Beispiel für die Anwendung [1]Hdetektierter fast-spinning ssNMR-Spektroskopie zur die Untersuchung biologischer Funktionen für komplexe Multikomponentensysteme angesehen werden. Diese Arbeit repräsentiert die erste Umsetzung dieser Technik zur Detektion von Ligandenbindung, d.h. der Verfolgung konformationeller Veränderungen infolge der Nukleotidbindung an lipidumschlossenes ArtMP.

9   Bibliography

1.   Okuno, D., Iino, R. & Noji, H. Rotation and structure of FoF1-ATP synthase. *J Biochem* **149**, 655-64 (2011).
2.   Van Itallie, C.M. & Anderson, J.M. Claudin interactions in and out of the tight junction. *Tissue Barriers* **1**, e25247 (2013).
3.   Krauss, G. *Biochemistry of Signal Transduction and Regulation*, (Wiley, 2006).
4.   Murphy, K.P., Travers, P., Walport, M. & Janeway, C. *Janeway's immunobiology*, (Garland Science, 2008).
5.   Davidson, A.L., Dassa, E., Orelle, C. & Chen, J. Structure, function, and evolution of bacterial ATP-binding cassette systems. *Microbiol Mol Biol Rev* **72**, 317-64, table of contents (2008).
6.   Tarling, E.J., de Aguiar Vallim, T.Q. & Edwards, P.A. Role of ABC transporters in lipid transport and human disease. *Trends Endocrinol Metab* **24**, 342-50 (2013).
7.   Alberts, B. *Molecular biology of the cell*, (Garland Science, New York, 2008).
8.   Yildirim, M.A., Goh, K.I., Cusick, M.E., Barabasi, A.L. & Vidal, M. Drug-target network. *Nat Biotechnol* **25**, 1119-26 (2007).
9.   Salom, D. & Palczewski, K. Structural Biology of Membrane Proteins in *Production of Membrane Proteins: Strategies for Expression and Isolation* (ed. Robinson, A.S.) (Wiley-VCH Verlag GmbH & Co. KGaA, 2011).
10.   Tusnady, G.E., Dosztanyi, Z. & Simon, I. Transmembrane proteins in the Protein Data Bank: identification and classification. *Bioinformatics* **20**, 2964-72 (2004).
11.   Lee, A.G. Biological membranes: the importance of molecular detail. *Trends Biochem Sci* **36**, 493-500 (2011).
12.   Morein, S., Andersson, A., Rilfors, L. & Lindblom, G. Wild-type Escherichia coli cells regulate the membrane lipid composition in a "window" between gel and non-lamellar structures. *J Biol Chem* **271**, 6801-9 (1996).
13.   Han, X. & Gross, R.W. Shotgun lipidomics: electrospray ionization mass spectrometric analysis and quantitation of cellular lipidomes directly from crude extracts of biological samples. *Mass Spectrom Rev* **24**, 367-412 (2005).
14.   Almen, M.S., Nordstrom, K.J., Fredriksson, R. & Schioth, H.B. Mapping the human membrane proteome: a majority of the human membrane proteins can be classified according to function and evolutionary origin. *BMC Biol* **7**, 50 (2009).
15.   Pebay-Peyroula, E. *Biophysical Analysis of Membrane Proteins: Investigating Structure and Function*, (Wiley, 2008).
16.   Babcock, J.J. & Li, M. Deorphanizing the human transmembrane genome: A landscape of uncharacterized membrane proteins. *Acta Pharmacol Sin* **35**, 11-23 (2014).
17.   Moller, S., Croning, M.D. & Apweiler, R. Evaluation of methods for the prediction of membrane spanning regions. *Bioinformatics* **17**, 646-53 (2001).
18.   Rose, A., Lorenzen, S., Goede, A., Gruening, B. & Hildebrand, P.W. RHYTHM--a server to predict the orientation of transmembrane helices in channels and membrane-coils. *Nucleic Acids Res* **37**, W575-80 (2009).
19.   Nugent, T. & Jones, D.T. Membrane protein structural bioinformatics. *Journal of Structural Biology* **179**, 327-337 (2012).
20.   Fleming, K.G. Determination of membrane protein molecular weight using sedimentation equilibrium analytical ultracentrifugation. *Curr Protoc Protein Sci* **Chapter 7**, Unit 7 12 1-7 12 13 (2008).

21. Zhao, H., Brautigam, C.A., Ghirlando, R. & Schuck, P. Overview of Current Methods in Sedimentation Velocity and Sedimentation Equilibrium Analytical Ultracentrifugation. in *Current Protocols in Protein Science* (John Wiley & Sons, Inc., 2001).

22. Patching, S.G. Surface plasmon resonance spectroscopy for characterisation of membrane protein–ligand interactions and its potential for drug discovery. *Biochimica et Biophysica Acta (BBA) - Biomembranes* **1838**, 43-55 (2014).

23. Draczkowski, P., Matosiuk, D. & Jozwiak, K. Isothermal titration calorimetry in membrane protein research. *Journal of Pharmaceutical and Biomedical Analysis* **87**, 313-325 (2014).

24. Jahnke, N. et al. Real-time monitoring of membrane-protein reconstitution by isothermal titration calorimetry. *Anal Chem* **86**, 920-7 (2014).

25. Corin, K. et al. Structure and function analyses of the purified GPCR human vomeronasal type 1 receptor 1. *Sci Rep* **1**, 172 (2011).

26. Zhou, Z.H. Structures of viral membrane proteins by high-resolution cryoEM. *Curr Opin Virol* **5C**, 111-119 (2014).

27. Boutet, S. et al. High-Resolution Protein Structure Determination by Serial Femtosecond Crystallography. *Science* **337**, 362-364 (2012).

28. Kobe, B. et al. Crystallography and protein-protein interactions: biological interfaces and crystal contacts. *Biochem Soc Trans* **36**, 1438-41 (2008).

29. Newstead, S., Hobbs, J., Jordan, D., Carpenter, E.P. & Iwata, S. Insights into outer membrane protein crystallization. *Mol Membr Biol* **25**, 631-8 (2008).

30. Newstead, S., Ferrandon, S. & Iwata, S. Rationalizing alpha-helical membrane protein crystallization. *Protein Sci* **17**, 466-72 (2008).

31. Zhou, H.X. & Cross, T.A. Influences of membrane mimetic environments on membrane protein structures. *Annu Rev Biophys* **42**, 361-92 (2013).

32. Bao, H., Dalal, K., Wang, V., Rouiller, I. & Duong, F. The maltose ABC transporter: action of membrane lipids on the transporter stability, coupling and ATPase activity. *Biochim Biophys Acta* **1828**, 1723-30 (2013).

33. Shi, C., Paige, M.F., Maley, J. & Loewen, M.C. In vitro characterization of ligand-induced oligomerization of the S. cerevisiae G-protein coupled receptor, Ste2p. *Biochim Biophys Acta* **1790**, 1-7 (2009).

34. Corin, K. et al. A robust and rapid method of producing soluble, stable, and functional G-protein coupled receptors. *PLoS One* **6**, e23036 (2011).

35. Cherezov, V. Lipidic cubic phase technologies for membrane protein structural studies. *Current Opinion in Structural Biology* **21**, 559-566 (2011).

36. Hong, M., Zhang, Y. & Hu, F. Membrane Protein Structure and Dynamics from NMR Spectroscopy. *Annual Review of Physical Chemistry* **63**, 1-24 (2012).

37. Shahid, S.A. et al. Membrane-protein structure determination by solid-state NMR spectroscopy of microcrystals. *Nat Methods* **9**, 1212-7 (2012).

38. Opella, S.J. Structure determination of membrane proteins in their native phospholipid bilayer environment by rotationally aligned solid-state NMR spectroscopy. *Acc Chem Res* **46**, 2145-53 (2013).

39. Grewer, C., Gameiro, A., Mager, T. & Fendler, K. Electrophysiological characterization of membrane transport proteins. *Annu Rev Biophys* **42**, 95-120 (2013).

40. Inagaki, S., Ghirlando, R. & Grisshammer, R. Biophysical characterization of membrane proteins in nanodiscs. *Methods* **59**, 287-300 (2013).

41. Popot, J.L. et al. Amphipols from A to Z. *Annu Rev Biophys* **40**, 379-408 (2011).

42. Cherezov, V. Lipidic cubic phase technologies for membrane protein structural studies. *Curr Opin Struct Biol* **21**, 559-66 (2011).

43. Luckey, M. *Membrane Structural Biology: With Biochemical and Biophysical Foundations*, (Cambridge University Press, 2014).
44. Gidden, J., Denson, J., Liyanage, R., Ivey, D.M. & Lay, J.O. Lipid Compositions in Escherichia coli and Bacillus subtilis During Growth as Determined by MALDI-TOF and TOF/TOF Mass Spectrometry. *Int J Mass Spectrom* **283**, 178-184 (2009).
45. Garrett, T.A., O'Neill, A.C. & Hopson, M.L. Quantification of cardiolipin molecular species in Escherichia coli lipid extracts using liquid chromatography/electrospray ionization mass spectrometry. *Rapid Commun Mass Spectrom* **26**, 2267-74 (2012).
46. Tatituri, R.V., Brenner, M.B., Turk, J. & Hsu, F.F. Structural elucidation of diglycosyl diacylglycerol and monoglycosyl diacylglycerol from Streptococcus pneumoniae by multiple-stage linear ion-trap mass spectrometry with electrospray ionization. *J Mass Spectrom* **47**, 115-23 (2012).
47. van Meer, G., Voelker, D.R. & Feigenson, G.W. Membrane lipids: where they are and how they behave. *Nat Rev Mol Cell Biol* **9**, 112-24 (2008).
48. Pyrkova, D.V. et al. Dynamic clustering of lipids in hydrated two-component membranes: results of computer modeling and putative biological impact. *J Biomol Struct Dyn* **31**, 87-95 (2013).
49. Sud, M. et al. LMSD: LIPID MAPS structure database. *Nucleic Acids Res* **35**, D527-32 (2007).
50. Gardiennet, C. et al. A sedimented sample of a 59 kDa dodecameric helicase yields high-resolution solid-state NMR spectra. *Angew Chem Int Ed Engl* **51**, 7855-8 (2012).
51. Jayanthi, S., Frydman, V. & Vega, S. Dynamic Deuterium Magic Angle Spinning NMR of a Molecule Grafted at the Inner Surface of a Mesoporous Material. *J Phys Chem B* (2012).
52. Bjerring, M., Paaske, B., Oschkinat, H., Akbey, U. & Nielsen, N.C. Rapid solid-state NMR of deuterated proteins by interleaved cross-polarization from (1)H and (2)H nuclei. *J Magn Reson* **214**, 324-8 (2012).
53. Akbey, U., Rossum, B.J. & Oschkinat, H. Practical aspects of high-sensitivity multidimensional (1)(3)C MAS NMR spectroscopy of perdeuterated proteins. *J Magn Reson* **217**, 77-85 (2012).
54. Zeeman, P. The effect of magnetisation on the nature of light emitted by a substance. *Nature* **55**(1897).
55. Purcell, E.M., Torrey, H.C. & Pound, R.V. Resonance Absorption by Nuclear Magnetic Moments in a Solid. *Physical Review* **69**, 37-38 (1946).
56. Bloch, F., Hansen, W.W. & Packard, M. Nuclear Induction. *Physical Review* **69**, 127-127 (1946).
57. Bloch, F. Nuclear Induction. *Physical Review* **70**, 460-474 (1946).
58. Cavanagh, J., Fairbrother, W.J., Palmer, A.G., Skelton, N.J. & Rance, M. *Protein NMR Spectroscopy: Principles and Practice*, (Elsevier Science, 2010).
59. Sakellariou, D., Lesage, A. & Emsley, L. Spectral editing in solid-state NMR using scalar multiple quantum filters. *J Magn Reson* **151**, 40-7 (2001).
60. Linser, R., Fink, U. & Reif, B. Proton-detected scalar coupling based assignment strategies in MAS solid-state NMR spectroscopy applied to perdeuterated proteins. *J Magn Reson* **193**, 89-93 (2008).
61. Zhou, D.H. et al. Solid-state NMR analysis of membrane proteins and protein aggregates by proton detected spectroscopy. *J Biomol NMR* **54**, 291-305 (2012).
62. Ulrich, E.L. et al. BioMagResBank. *Nucleic Acids Res* **36**, D402-8 (2008).
63. Fritzsching, K.J., Yang, Y., Schmidt-Rohr, K. & Hong, M. Practical use of chemical shift databases for protein solid-state NMR: 2D chemical shift maps and amino-acid assignment with secondary-structure information. *J Biomol NMR* **56**, 155-67 (2013).

64. Redfield, C. Using nuclear magnetic resonance spectroscopy to study molten globule states of proteins. *Methods* **34**, 121-32 (2004).

65. Fyfe, C.A. *Solid State NMR for Chemists*, (C.F.C. Press, 1983).

66. Ernst, R.R. & Anderson, W.A. Application of Fourier Transform Spectroscopy to Magnetic Resonance. *Rev. Sci. Instr.* **37**(1966).

67. Reich, H.J. 8.1 Relaxation in NMR Spectroscopy. (2014). http://www.chem.wisc.edu/areas/reich/nmr/08-tech-01-relax.htm, 07 May 2014

68. Jacobsen, N.E. *NMR Spectroscopy Explained: Simplified Theory, Applications and Examples for Organic Chemistry and Structural Biology*, (Wiley, 2007).

69. Bloembergen, N., Purcell, E.M. & Pound, R.V. Relaxation Effects in Nuclear Magnetic Resonance Absorption. *Physical Review* **73**, 679-712 (1948).

70. Demers, J.P., Chevelkov, V. & Lange, A. Progress in correlation spectroscopy at ultra-fast magic-angle spinning: basic building blocks and complex experiments for the study of protein structure and dynamics. *Solid State Nucl Magn Reson* **40**, 101-13 (2011).

71. Doherty, T. & Hong, M. High-resolution solid-state NMR of anisotropically mobile molecules under very low-power (1)H decoupling and moderate magic-angle spinning. *J Magn Reson* **199**, 225-32 (2009).

72. Chevelkov, V., Rehbein, K., Diehl, A. & Reif, B. Ultrahigh resolution in proton solid-state NMR spectroscopy at high levels of deuteration. *Angew Chem Int Ed Engl* **45**, 3878-81 (2006).

73. Akbey, U. et al. Optimum levels of exchangeable protons in perdeuterated proteins for proton detection in MAS solid-state NMR spectroscopy. *J Biomol NMR* **46**, 67-73 (2010).

74. Nielsen, A.B., Jain, S., Ernst, M., Meier, B.H. & Nielsen, N.C. Adiabatic Rotor-Echo-Short-Pulse-Irradiation mediated cross-polarization. *J Magn Reson* **237**, 147-51 (2013).

75. Lalli, D. et al. Three-dimensional deuterium-carbon correlation experiments for high-resolution solid-state MAS NMR spectroscopy of large proteins. *J Biomol NMR* **51**, 477-85 (2011).

76. Akbey, U., Camponeschi, F., van Rossum, B.J. & Oschkinat, H. Triple resonance cross-polarization for more sensitive 13C MAS NMR spectroscopy of deuterated proteins. *Chemphyschem* **12**, 2092-6 (2011).

77. Akbey, U., Oschkinat, H. & van Rossum, B.J. Double-nucleus enhanced recoupling for efficient 13C MAS NMR correlation spectroscopy of perdeuterated proteins. *J Am Chem Soc* **131**, 17054-5 (2009).

78. Castellani, F. et al. Structure of a protein determined by solid-state magic-angle-spinning NMR spectroscopy. *Nature* **420**, 98-102 (2002).

79. Jehle, S. et al. Solid-state NMR and SAXS studies provide a structural basis for the activation of alphaB-crystallin oligomers. *Nat Struct Mol Biol* **17**, 1037-42 (2010).

80. Van Melckebeke, H. et al. Atomic-resolution three-dimensional structure of HET-s(218-289) amyloid fibrils by solid-state NMR spectroscopy. *J Am Chem Soc* **132**, 13765-75 (2010).

81. Parthasarathy, S., Yoo, B., McElheny, D., Tay, W. & Ishii, Y. Capturing a Reactive State of Amyloid Aggregates: NMR-based Characterization of Cu-ion Bound Alzheimer's Amyloid beta Fibrils in a Redox Cycle. *J Biol Chem* (2014).

82. Loquet, A. et al. Atomic model of the type III secretion system needle. *Nature* **486**, 276-9 (2012).

83. Franks, W.T., Linden, A.H., Kunert, B., van Rossum, B.J. & Oschkinat, H. Solid-state magic-angle spinning NMR of membrane proteins and protein-ligand interactions. *Eur J Cell Biol* **91**, 340-8 (2012).

84. Comellas, G. & Rienstra, C.M. Protein structure determination by magic-angle spinning solid-state NMR, and insights into the formation, structure, and stability of amyloid fibrils. *Annu Rev Biophys* **42**, 515-36 (2013).

85. Goldbourt, A. Biomolecular magic-angle spinning solid-state NMR: recent methods and applications. *Curr Opin Biotechnol* **24**, 705-15 (2013).

86. Sharma, M. et al. Insight into the mechanism of the influenza A proton channel from a structure in a lipid bilayer. *Science* **330**, 509-12 (2010).

87. Park, S.H. et al. Structure of the chemokine receptor CXCR1 in phospholipid bilayers. *Nature* **491**, 779-83 (2012).

88. Wang, S. et al. Solid-state NMR spectroscopy structure determination of a lipid-embedded heptahelical membrane protein. *Nat Methods* **10**, 1007-12 (2013).

89. Hong, M. & DeGrado, W.F. Structural basis for proton conduction and inhibition by the influenza M2 protein. *Protein Sci* **21**, 1620-33 (2012).

90. Zhou, H.X. & Cross, T.A. Modeling the membrane environment has implications for membrane protein structure and function: influenza A M2 protein. *Protein Sci* **22**, 381-94 (2013).

91. Freigassner, M., Pichler, H. & Glieder, A. Tuning microbial hosts for membrane protein production. *Microb Cell Fact* **8**, 69 (2009).

92. Kunji, E.R., Slotboom, D.J. & Poolman, B. Lactococcus lactis as host for overproduction of functional membrane proteins. *Biochim Biophys Acta* **1610**, 97-108 (2003).

93. Verardi, R., Traaseth, N.J., Masterson, L.R., Vostrikov, V.V. & Veglia, G. Isotope labeling for solution and solid-state NMR spectroscopy of membrane proteins. *Adv Exp Med Biol* **992**, 35-62 (2012).

94. Gossert, A.D. et al. A simple protocol for amino acid type selective isotope labeling in insect cells with improved yields and high reproducibility. *J Biomol NMR* **51**, 449-56 (2011).

95. Werner, K., Richter, C., Klein-Seetharaman, J. & Schwalbe, H. Isotope labeling of mammalian GPCRs in HEK293 cells and characterization of the C-terminus of bovine rhodopsin by high resolution liquid NMR spectroscopy. *J Biomol NMR* **40**, 49-53 (2008).

96. Noirot, C. et al. Wheat-germ cell-free production of prion proteins for solid-state NMR structural studies. *N Biotechnol* **28**, 232-8 (2011).

97. Waugh, D.S. Making the most of affinity tags. *Trends Biotechnol* **23**, 316-20 (2005).

98. Waldo, G.S., Standish, B.M., Berendzen, J. & Terwilliger, T.C. Rapid protein-folding assay using green fluorescent protein. *Nat Biotechnol* **17**, 691-5 (1999).

99. Drew, D. et al. GFP-based optimization scheme for the overexpression and purification of eukaryotic membrane proteins in Saccharomyces cerevisiae. *Nat Protoc* **3**, 784-98 (2008).

100. Suzuki, M., Mao, L. & Inouye, M. Single protein production (SPP) system in Escherichia coli. *Nat Protoc* **2**, 1802-10 (2007).

101. Schneider, W.M. et al. Efficient condensed-phase production of perdeuterated soluble and membrane proteins. *J Struct Funct Genomics* **11**, 143-54 (2010).

102. Mao, L. et al. The E. coli single protein production system for production and structural analysis of membrane proteins. *J Struct Funct Genomics* **11**, 81-4 (2010).

103.   Goto, N.K., Gardner, K.H., Mueller, G.A., Willis, R.C. & Kay, L.E. A robust and cost-effective method for the production of Val, Leu, Ile (delta 1) methyl-protonated 15N-, 13C-, 2H-labeled proteins. *J Biomol NMR* **13**, 369-74 (1999).

104.   Rees, D.C., Johnson, E. & Lewinson, O. ABC transporters: the power to change. *Nat Rev Mol Cell Biol* **10**, 218-27 (2009).

105.   Sharom, F.J. ABC multidrug transporters: structure, function and role in chemoresistance. *Pharmacogenomics* **9**, 105-27 (2008).

106.   Ceckova-Novotna, M., Pavek, P. & Staud, F. P-glycoprotein in the placenta: expression, localization, regulation and function. *Reprod Toxicol* **22**, 400-10 (2006).

107.   Quazi, F. & Molday, R.S. Lipid transport by mammalian ABC proteins. *Essays Biochem* **50**, 265-90 (2011).

108.   Abele, R. & Tampe, R. The TAP translocation machinery in adaptive immunity and viral escape mechanisms. *Essays Biochem* **50**, 249-64 (2011).

109.   Zimmer, J. et al. Clinical and immunological aspects of HLA class I deficiency. *QJM* **98**, 719-27 (2005).

110.   Ahn, K. et al. Molecular mechanism and species specificity of TAP inhibition by herpes simplex virus ICP47. *EMBO J* **15**, 3247-55 (1996).

111.   Tomazin, R. et al. Stable binding of the herpes simplex virus ICP47 protein to the peptide binding site of TAP. *EMBO J* **15**, 3256-66 (1996).

112.   Kageshita, T., Hirai, S., Ono, T., Hicklin, D.J. & Ferrone, S. Down-regulation of HLA class I antigen-processing molecules in malignant melanoma: association with disease progression. *Am J Pathol* **154**, 745-54 (1999).

113.   Dassa, E. Natural history of ABC systems: not only transporters. *Essays Biochem* **50**, 19-42 (2011).

114.   Leprohon, P., Legare, D. & Ouellette, M. ABC transporters involved in drug resistance in human parasites. *Essays Biochem* **50**, 121-44 (2011).

115.   Lubelski, J., Konings, W.N. & Driessen, A.J. Distribution and physiology of ABC-type transporters contributing to multidrug resistance in bacteria. *Microbiol Mol Biol Rev* **71**, 463-76 (2007).

116.   Prasad, R., Sharma, M. & Rawal, M.K. Functionally Relevant Residues of Cdr1p: A Multidrug ABC Transporter of Human Pathogenic Candida albicans. *J Amino Acids* **2011**, 531412 (2011).

117.   Prasad, R. & Goffeau, A. Yeast ATP-binding cassette transporters conferring multidrug resistance. *Annu Rev Microbiol* **66**, 39-63 (2012).

118.   Davidson, A.L. & Chen, J. ATP-binding cassette transporters in bacteria. *Annu Rev Biochem* **73**, 241-68 (2004).

119.   Kubes, M. et al. The Arabidopsis concentration-dependent influx/efflux transporter ABCB4 regulates cellular auxin levels in the root epidermis. *Plant J* **69**, 640-54 (2012).

120.   Lewis, V.G., Ween, M.P. & McDevitt, C.A. The role of ATP-binding cassette transporters in bacterial pathogenicity. *Protoplasma* **249**, 919-42 (2012).

121.   Garmory, H.S. & Titball, R.W. ATP-binding cassette transporters are targets for the development of antibacterial vaccines and therapies. *Infect Immun* **72**, 6757-63 (2004).

122.   Bulut, H. et al. Crystal structures of two solute receptors for L-cystine and L-cysteine, respectively, of the human pathogen Neisseria gonorrhoeae. *J Mol Biol* **415**, 560-72 (2012).

123.   Higgins, C.F. ABC transporters: physiology, structure and mechanism--an overview. *Res Microbiol* **152**, 205-10 (2001).

124.   Johnson, E., Nguyen, P.T., Yeates, T.O. & Rees, D.C. Inward facing conformations of the MetNI methionine ABC transporter: Implications for the mechanism of transinhibition. *Protein Sci* **21**, 84-96 (2012).

125.   Kadaba, N.S., Kaiser, J.T., Johnson, E., Lee, A. & Rees, D.C. The high-affinity E. coli methionine ABC transporter: structure and allosteric regulation. *Science* **321**, 250-3 (2008).

126.   Chen, S., Oldham, M.L., Davidson, A.L. & Chen, J. Carbon catabolite repression of the maltose transporter revealed by X-ray crystallography. *Nature* **499**, 364-8 (2013).

127.   Eitinger, T., Rodionov, D.A., Grote, M. & Schneider, E. Canonical and ECF-type ATP-binding cassette importers in prokaryotes: diversity in modular organization and cellular functions. *FEMS Microbiol Rev* **35**, 3-67 (2011).

128.   Neu, H.C. & Heppel, L.A. The release of enzymes from Escherichia coli by osmotic shock and during the formation of spheroplasts. *J Biol Chem* **240**, 3685-92 (1965).

129.   Berntsson, R.P., Smits, S.H., Schmitt, L., Slotboom, D.J. & Poolman, B. A structural classification of substrate-binding proteins. *FEBS Lett* **584**, 2606-17 (2010).

130.   Elferink, M.G., Albers, S.V., Konings, W.N. & Driessen, A.J. Sugar transport in Sulfolobus solfataricus is mediated by two families of binding protein-dependent ABC transporters. *Mol Microbiol* **39**, 1494-503 (2001).

131.   Sutcliffe, I.C. & Russell, R.R. Lipoproteins of gram-positive bacteria. *J Bacteriol* **177**, 1123-8 (1995).

132.   Lee, S.J., Bohm, A., Krug, M. & Boos, W. The ABC of binding-protein-dependent transport in Archaea. *Trends Microbiol* **15**, 389-97 (2007).

133.   Gilson, E. et al. Evidence for high affinity binding-protein dependent transport systems in gram-positive bacteria and in Mycoplasma. *EMBO J* **7**, 3971-4 (1988).

134.   Kempf, B., Gade, J. & Bremer, E. Lipoprotein from the osmoregulated ABC transport system OpuA of Bacillus subtilis: purification of the glycine betaine binding protein and characterization of a functional lipidless mutant. *J Bacteriol* **179**, 6213-20 (1997).

135.   Pinkett, H.W., Lee, A.T., Lum, P., Locher, K.P. & Rees, D.C. An inward-facing conformation of a putative metal-chelate-type ABC transporter. *Science* **315**, 373-7 (2007).

136.   Mao, B., Pear, M.R., McCammon, J.A. & Quiocho, F.A. Hinge-bending in L-arabinose-binding protein. The "Venus's-flytrap" model. *J Biol Chem* **257**, 1131-3 (1982).

137.   Quiocho, F.A. & Ledvina, P.S. Atomic structure and specificity of bacterial periplasmic receptors for active transport and chemotaxis: variation of common themes. *Mol Microbiol* **20**, 17-25 (1996).

138.   Sharff, A.J., Rodseth, L.E., Spurlino, J.C. & Quiocho, F.A. Crystallographic evidence of a large ligand-induced hinge-twist motion between the two domains of the maltodextrin binding protein involved in active transport and chemotaxis. *Biochemistry* **31**, 10657-63 (1992).

139.   Isenbarger, T.A. et al. The most conserved genome segments for life detection on Earth and other planets. *Orig Life Evol Biosph* **38**, 517-33 (2008).

140.   Walker, J.E., Saraste, M., Runswick, M.J. & Gay, N.J. Distantly related sequences in the alpha- and beta-subunits of ATP synthase, myosin, kinases and other ATP-requiring enzymes and a common nucleotide binding fold. *EMBO J* **1**, 945-51 (1982).

141.   Karpowich, N. et al. Crystal structures of the MJ1267 ATP binding cassette reveal an induced-fit effect at the ATPase active site of an ABC transporter. *Structure* **9**, 571-86 (2001).

142. Dawson, R.J. & Locher, K.P. Structure of the multidrug ABC transporter Sav1866 from Staphylococcus aureus in complex with AMP-PNP. *FEBS Lett* **581**, 935-8 (2007).

143. Oldham, M.L., Khare, D., Quiocho, F.A., Davidson, A.L. & Chen, J. Crystal structure of a catalytic intermediate of the maltose transporter. *Nature* **450**, 515-21 (2007).

144. Korkhov, V.M., Mireku, S.A. & Locher, K.P. Structure of AMP-PNP-bound vitamin B12 transporter BtuCD-F. *Nature* **490**, 367-72 (2012).

145. Ambudkar, S.V., Kim, I.W., Xia, D. & Sauna, Z.E. The A-loop, a novel conserved aromatic acid subdomain upstream of the Walker A motif in ABC transporters, is critical for ATP binding. *FEBS Lett* **580**, 1049-55 (2006).

146. Oldham, M.L. & Chen, J. Snapshots of the maltose transporter during ATP hydrolysis. *Proc Natl Acad Sci U S A* **108**, 15152-6 (2011).

147. Tombline, G., Muharemagic, A., White, L.B. & Senior, A.E. Involvement of the "occluded nucleotide conformation" of P-glycoprotein in the catalytic pathway. *Biochemistry* **44**, 12879-86 (2005).

148. Senior, A.E. Reaction chemistry ABC-style. *Proc Natl Acad Sci U S A* **108**, 15015-6 (2011).

149. Wen, P.C. & Tajkhorshid, E. Conformational coupling of the nucleotide-binding and the transmembrane domains in ABC transporters. *Biophys J* **101**, 680-90 (2011).

150. Jones, P.M., O'Mara, M.L. & George, A.M. ABC transporters: a riddle wrapped in a mystery inside an enigma. *Trends Biochem Sci* **34**, 520-31 (2009).

151. Urbatsch, I.L., Gimi, K., Wilke-Mounts, S. & Senior, A.E. Investigation of the role of glutamine-471 and glutamine-1114 in the two catalytic sites of P-glycoprotein. *Biochemistry* **39**, 11921-7 (2000).

152. Loo, T.W., Bartlett, M.C. & Clarke, D.M. The "LSGGQ" motif in each nucleotide-binding domain of human P-glycoprotein is adjacent to the opposing walker A sequence. *J Biol Chem* **277**, 41303-6 (2002).

153. Bakos, E. et al. Characterization of the human multidrug resistance protein containing mutations in the ATP-binding cassette signature region. *Biochemical Journal* **323**, 777-783 (1997).

154. Ye, J., Osborne, A.R., Groll, M. & Rapoport, T.A. RecA-like motor ATPases--lessons from structures. *Biochim Biophys Acta* **1659**, 1-18 (2004).

155. Jones, P.M. & George, A.M. Role of the D-loops in allosteric control of ATP hydrolysis in an ABC transporter. *J Phys Chem A* **116**, 3004-13 (2012).

156. Zhou, Y., Ojeda-May, P. & Pu, J. H-loop histidine catalyzes ATP hydrolysis in the E. coli ABC-transporter HlyB. *Phys Chem Chem Phys* (2013).

157. Dzagania, T. et al. The histidine-loop is essential for transport activity of human MDR3. A novel mutation of MDR3 in a patient with progressive familial intrahepatic cholestasis type 3. *Gene* **506**, 141-5 (2012).

158. Chen, J., Lu, G., Lin, J., Davidson, A.L. & Quiocho, F.A. A tweezers-like motion of the ATP-binding cassette dimer in an ABC transport cycle. *Mol Cell* **12**, 651-61 (2003).

159. Bohm, A., Diez, J., Diederichs, K., Welte, W. & Boos, W. Structural model of MalK, the ABC subunit of the maltose transporter of Escherichia coli: implications for mal gene regulation, inducer exclusion, and subunit assembly. *J Biol Chem* **277**, 3708-17 (2002).

160. Gerber, S., Comellas-Bigler, M., Goetz, B.A. & Locher, K.P. Structural basis of trans-inhibition in a molybdate/tungstate ABC transporter. *Science* **321**, 246-50 (2008).

161. Hollenstein, K., Dawson, R.J. & Locher, K.P. Structure and mechanism of ABC transporter proteins. *Curr Opin Struct Biol* **17**, 412-8 (2007).

162. Mourez, M., Hofnung, M. & Dassa, E. Subunit interactions in ABC transporters: a conserved sequence in hydrophobic membrane proteins of periplasmic permeases defines an important site of interaction with the ATPase subunits. *EMBO J* **16**, 3066-77 (1997).

163. Higgins, C.F. & Linton, K.J. The ATP switch model for ABC transporters. *Nat Struct Mol Biol* **11**, 918-26 (2004).

164. Jardetzky, O. Simple allosteric model for membrane pumps. *Nature* **211**, 969-70 (1966).

165. Smith, P.C. et al. ATP binding to the motor domain from an ABC transporter drives formation of a nucleotide sandwich dimer. *Mol Cell* **10**, 139-49 (2002).

166. Janas, E. et al. The ATP hydrolysis cycle of the nucleotide-binding domain of the mitochondrial ATP-binding cassette transporter Mdl1p. *J Biol Chem* **278**, 26862-9 (2003).

167. van der Does, C. & Tampe, R. How do ABC transporters drive transport? *Biol Chem* **385**, 927-33 (2004).

168. Senior, A.E., al-Shawi, M.K. & Urbatsch, I.L. The catalytic cycle of P-glycoprotein. *FEBS Lett* **377**, 285-9 (1995).

169. van Veen, H.W., Margolles, A., Muller, M., Higgins, C.F. & Konings, W.N. The homodimeric ATP-binding cassette transporter LmrA mediates multidrug transport by an alternating two-site (two-cylinder engine) mechanism. *EMBO J* **19**, 2503-14 (2000).

170. Urbatsch, I.L., Sankaran, B., Bhagat, S. & Senior, A.E. Both P-glycoprotein nucleotide-binding sites are catalytically active. *J Biol Chem* **270**, 26956-61 (1995).

171. Sharma, S. & Davidson, A.L. Vanadate-induced trapping of nucleotides by purified maltose transport complex requires ATP hydrolysis. *J Bacteriol* **182**, 6570-6 (2000).

172. Tombline, G., Bartholomew, L.A., Urbatsch, I.L. & Senior, A.E. Combined mutation of catalytic glutamate residues in the two nucleotide binding domains of P-glycoprotein generates a conformation that binds ATP and ADP tightly. *J Biol Chem* **279**, 31212-20 (2004).

173. Jones, P.M. & George, A.M. Mechanism of the ABC transporter ATPase domains: catalytic models and the biochemical and biophysical record. *Crit Rev Biochem Mol Biol* **48**, 39-50 (2013).

174. Oliveira, A.S., Baptista, A.M. & Soares, C.M. Inter-domain communication mechanisms in an ABC importer: a molecular dynamics study of the MalFGK2E complex. *PLoS Comput Biol* **7**, e1002128 (2011).

175. Orelle, C., Ayvaz, T., Everly, R.M., Klug, C.S. & Davidson, A.L. Both maltose-binding protein and ATP are required for nucleotide-binding domain closure in the intact maltose ABC transporter. *Proc Natl Acad Sci U S A* **105**, 12837-42 (2008).

176. Oldham, M.L., Davidson, A.L. & Chen, J. Structural insights into ABC transporter mechanism. *Curr Opin Struct Biol* **18**, 726-33 (2008).

177. Khare, D., Oldham, M.L., Orelle, C., Davidson, A.L. & Chen, J. Alternating access in maltose transporter mediated by rigid-body rotations. *Mol Cell* **33**, 528-36 (2009).

178. Oldham, M.L. & Chen, J. Crystal structure of the maltose transporter in a pretranslocation intermediate state. *Science* **332**, 1202-5 (2011).

179. Chen, J. Molecular mechanism of the Escherichia coli maltose transporter. *Curr Opin Struct Biol* **23**, 492-8 (2013).

180. Bao, H. & Duong, F. ATP alone triggers the outward facing conformation of the maltose ATP-binding cassette transporter. *J Biol Chem* **288**, 3439-48 (2013).

181. Bao, H. & Duong, F. Discovery of an auto-regulation mechanism for the maltose ABC transporter MalFGK2. *PLoS One* **7**, e34836 (2012).

182. Bohm, S., Licht, A., Wuttge, S., Schneider, E. & Bordignon, E. Conformational plasticity of the type I maltose ABC importer. *Proc Natl Acad Sci U S A* **110**, 5492-7 (2013).

183. Gould, A.D., Telmer, P.G. & Shilton, B.H. Stimulation of the maltose transporter ATPase by unliganded maltose binding protein. *Biochemistry* **48**, 8051-61 (2009).

184. Gould, A.D. & Shilton, B.H. Studies of the maltose transport system reveal a mechanism for coupling ATP hydrolysis to substrate translocation without direct recognition of substrate. *J Biol Chem* **285**, 11290-6 (2010).

185. Chu, B.C., Chan, D.I., Dewolf, T., Periole, X. & Vogel, H.J. Molecular dynamics simulations reveal that apo-HisJ can sample a closed conformation. *Proteins* (2013).

186. Dawson, R.J. & Locher, K.P. Structure of a bacterial multidrug ABC transporter. *Nature* **443**, 180-5 (2006).

187. Ward, A., Reyes, C.L., Yu, J., Roth, C.B. & Chang, G. Flexibility in the ABC transporter MsbA: Alternating access with a twist. *Proc Natl Acad Sci U S A* **104**, 19005-10 (2007).

188. Shintre, C.A. et al. Structures of ABCB10, a human ATP-binding cassette transporter in apo- and nucleotide-bound states. *Proc Natl Acad Sci U S A* **110**, 9710-5 (2013).

189. Lee, A.G. How lipids affect the activities of integral membrane proteins. *Biochim Biophys Acta* **1666**, 62-87 (2004).

190. Hunte, C. & Richers, S. Lipids and membrane protein structures. *Curr Opin Struct Biol* **18**, 406-11 (2008).

191. Luecke, H., Schobert, B., Richter, H.T., Cartailler, J.P. & Lanyi, J.K. Structure of bacteriorhodopsin at 1.55 A resolution. *J Mol Biol* **291**, 899-911 (1999).

192. Rasmussen, S.G. et al. Structure of a nanobody-stabilized active state of the beta(2) adrenoceptor. *Nature* **469**, 175-80 (2011).

193. Kato, H.E. et al. Crystal structure of the channelrhodopsin light-gated cation channel. *Nature* **482**, 369-74 (2012).

194. Haga, K. et al. Structure of the human M2 muscarinic acetylcholine receptor bound to an antagonist. *Nature* **482**, 547-51 (2012).

195. Manglik, A. et al. Crystal structure of the micro-opioid receptor bound to a morphinan antagonist. *Nature* **485**, 321-6 (2012).

196. Wu, H. et al. Structure of the human kappa-opioid receptor in complex with JDTic. *Nature* **485**, 327-32 (2012).

197. De Marcos Lousa, C. et al. The NBDs that wouldn't die: A cautionary tale of the use of isolated nucleotide binding domains of ABC transporters. *Commun Integr Biol* **2**, 97-9 (2009).

198. Fleischer, R., Wengner, A., Scheffel, F., Landmesser, H. & Schneider, E. Identification of a gene cluster encoding an arginine ATP-binding-cassette transporter in the genome of the thermophilic Gram-positive bacterium Geobacillus stearothermophilus strain DSMZ 13240. *Microbiology* **151**, 835-40 (2005).

199. Kunert, B. Freie Universität Berlin (2011).

200. Vahedi-Faridi, A. et al. Crystal structures and mutational analysis of the arginine-, lysine-, histidine-binding protein ArtJ from Geobacillus stearothermophilus. Implications for interactions of ArtJ with its cognate ATP-binding cassette transporter, Art(MP)2. *J Mol Biol* **375**, 448-59 (2008).

201. Eckey, V., Landmesser, H. & Schneider, E. Studying subunit-subunit interactions in a bacterial ABC transporterby in vitro assembly. *Biochim Biophys Acta* **1798**, 1250-3 (2010).

202. Lange, V. et al. A MAS NMR study of the bacterial ABC transporter ArtMP. *Chembiochem* **11**, 547-55 (2010).

203. Weidlich, D. et al. Residues of a proposed gate region in type I ATP-binding cassette import systems are crucial for function as revealed by mutational analysis. *Biochim Biophys Acta* **1828**, 2164-72 (2013).

204. Miller, J.H. *Experiments in molecular genetics*, (Cold Spring Harbor Laboratory, 1972).

205. Sambrook, J., Fritsch, E.F., Maniatis, T. & Nolan, C. *Molecular Cloning: A Laboratory Manual*, (Cold Spring Harbor Laboratory, 1989).

206. Studier, F.W. Protein production by auto-induction in high density shaking cultures. *Protein Expr Purif* **41**, 207-34 (2005).

207. Cohen, S.N., Chang, A.C. & Hsu, L. Nonchromosomal antibiotic resistance in bacteria: genetic transformation of Escherichia coli by R-factor DNA. *Proc Natl Acad Sci U S A* **69**, 2110-4 (1972).

208. Mao, L. et al. Production of membrane proteins for NMR studies using the condensed single protein (cSPP) production system. *J Struct Funct Genomics* **10**, 281-9 (2009).

209. Al-Qodah, Z. Production and characterization of thermostable alpha-amylase by thermophilic Geobacillus stearothermophilus. *Biotechnol J* **1**, 850-7 (2006).

210. Folch, J., Lees, M. & Sloane Stanley, G.H. A simple method for the isolation and purification of total lipides from animal tissues. *J Biol Chem* **226**, 497-509 (1957).

211. Lange, V. Freie Universität Berlin (2008).

212. Nikaido, K., Liu, P.Q. & Ames, G.F. Purification and characterization of HisP, the ATP-binding subunit of a traffic ATPase (ABC transporter), the histidine permease of Salmonella typhimurium. Solubility, dimerization, and ATPase activity. *J Biol Chem* **272**, 27745-52 (1997).

213. Schuck, P. Size-distribution analysis of macromolecules by sedimentation velocity ultracentrifugation and lamm equation modeling. *Biophys J* **78**, 1606-19 (2000).

214. Vistica, J. et al. Sedimentation equilibrium analysis of protein interactions with global implicit mass conservation constraints and systematic noise decomposition. *Anal Biochem* **326**, 234-56 (2004).

215. Hayes, D., Laue, T. & Philo, J. Program Sednterp: Sedimentation Interpretation Program (Alliance Protein Laboratories, Thousand Oaks, CA, USA, 1995).

216. Keller, S. et al. High-precision isothermal titration calorimetry with automated peak-shape analysis. *Anal Chem* **84**, 5066-73 (2012).

217. Houtman, J.C. et al. Studying multisite binary and ternary protein interactions by global analysis of isothermal titration calorimetry data in SEDPHAT: application to adaptor protein complexes in cell signaling. *Protein Sci* **16**, 30-42 (2007).

218. Brautigam, C.A. GUSSI 1.0.8d. (2013).

219. Pervushin, K., Riek, R., Wider, G. & Wuthrich, K. Attenuated T2 relaxation by mutual cancellation of dipole-dipole coupling and chemical shift anisotropy indicates an avenue to NMR structures of very large biological macromolecules in solution. *Proc Natl Acad Sci U S A* **94**, 12366-71 (1997).

220. Linser, R., Fink, U. & Reif, B. Assignment of dynamic regions in biological solids enabled by spin-state selective NMR experiments. *J Am Chem Soc* **132**, 8891-3 (2010).

221. Williamson, M.P. Using chemical shift perturbation to characterise ligand binding. *Prog Nucl Magn Reson Spectrosc* **73**, 1-16 (2013).

222. Kelley, L.A. & Sternberg, M.J. Protein structure prediction on the Web: a case study using the Phyre server. *Nat Protoc* **4**, 363-71 (2009).

223. Bennett-Lovsey, R.M., Herbert, A.D., Sternberg, M.J. & Kelley, L.A. Exploring the extremes of sequence/structure space with ensemble fold recognition in the program Phyre. *Proteins* **70**, 611-25 (2008).

224. Gouet, P., Courcelle, E., Stuart, D.I. & Metoz, F. ESPript: analysis of multiple sequence alignments in PostScript. *Bioinformatics* **15**, 305-8 (1999).
225. Hollenstein, K., Frei, D.C. & Locher, K.P. Structure of an ABC transporter in complex with its binding protein. *Nature* **446**, 213-6 (2007).
226. Zoghbi, M.E., Fuson, K.L., Sutton, R.B. & Altenberg, G.A. Kinetics of the association/dissociation cycle of an ATP-binding cassette nucleotide-binding domain. *J Biol Chem* **287**, 4157-64 (2012).
227. Zoghbi, M.E., Krishnan, S. & Altenberg, G.A. Dissociation of ATP-binding cassette nucleotide-binding domain dimers into monomers during the hydrolysis cycle. *J Biol Chem* **287**, 14994-5000 (2012).
228. Damas, J.M., Oliveira, A.S., Baptista, A.M. & Soares, C.M. Structural consequences of ATP hydrolysis on the ABC transporter NBD dimer: molecular dynamics studies of HlyB. *Protein Sci* **20**, 1220-30 (2011).
229. Akbey, U. et al. Quadruple-Resonance Magic-Angle Spinning NMR Spectroscopy of Deuterated Solid Proteins. *Angew Chem Int Ed Engl* (2014).
230. Schneider, W.M., Inouye, M., Montelione, G.T. & Roth, M.J. Independently inducible system of gene expression for condensed single protein production (cSPP) suitable for high efficiency isotope enrichment. *J Struct Funct Genomics* **10**, 219-25 (2009).
231. Grossman, T.H., Kawasaki, E.S., Punreddy, S.R. & Osburne, M.S. Spontaneous cAMP-dependent derepression of gene expression in stationary phase plays a role in recombinant expression instability. *Gene* **209**, 95-103 (1998).
232. Linser, R., Sarkar, R., Krushelnitzky, A., Mainz, A. & Reif, B. Dynamics in the solid-state: perspectives for the investigation of amyloid aggregates, membrane proteins and soluble protein complexes. *J Biomol NMR* **59**, 1-14 (2014).
233. Asami, S. & Reif, B. Proton-detected solid-state NMR spectroscopy at aliphatic sites: application to crystalline systems. *Acc Chem Res* **46**, 2089-97 (2013).
234. Gardner, K.H. & Kay, L.E. Production and Incorporation of 15N, 13C, 2H (1H-δ1 Methyl) Isoleucine into Proteins for Multidimensional NMR Studies. *Journal of the American Chemical Society* **119**, 7599-7600 (1997).
235. Nieuwkoop, A.J. & Rienstra, C.M. Supramolecular protein structure determination by site-specific long-range intermolecular solid state NMR spectroscopy. *J Am Chem Soc* **132**, 7570-1 (2010).
236. Franks, W.T. et al. Magic-angle spinning solid-state NMR spectroscopy of the beta1 immunoglobulin binding domain of protein G (GB1): 15N and 13C chemical shift assignments and conformational analysis. *J Am Chem Soc* **127**, 12291-305 (2005).
237. Gronenborn, A.M. et al. A novel, highly stable fold of the immunoglobulin binding domain of streptococcal protein G. *Science* **253**, 657-61 (1991).
238. Tang, M. et al. Solid-state NMR study of the charge-transfer complex between ubiquinone-8 and disulfide bond generating membrane protein DsbB. *J Am Chem Soc* **133**, 4359-66 (2011).
239. Tang, M., Berthold, D.A. & Rienstra, C.M. Solid-State NMR of a Large Membrane Protein by Paramagnetic Relaxation Enhancement. *J Phys Chem Lett* **2**, 1836-1841 (2011).
240. Li, Y., Berthold, D.A., Gennis, R.B. & Rienstra, C.M. Chemical shift assignment of the transmembrane helices of DsbB, a 20-kDa integral membrane enzyme, by 3D magic-angle spinning NMR spectroscopy. *Protein Sci* **17**, 199-204 (2008).
241. Inaba, K. & Ito, K. Structure and mechanisms of the DsbB-DsbA disulfide bond generation machine. *Biochim Biophys Acta* **1783**, 520-9 (2008).
242. Linser, R. Backbone assignment of perdeuterated proteins using long-range H/C-dipolar transfers. *J Biomol NMR* **52**, 151-8 (2012).

243. Tang, M. et al. Structure of the disulfide bond generating membrane protein DsbB in the lipid bilayer. *J Mol Biol* **425**, 1670-82 (2013).

244. Jacso, T. et al. Periplasmic loop P2 of the MalF subunit of the maltose ATP binding cassette transporter is sufficient to bind the maltose binding protein MalE. *Biochemistry* **48**, 2216-25 (2009).

245. Tusnady, G.E. & Simon, I. The HMMTOP transmembrane topology prediction server. *Bioinformatics* **17**, 849-50 (2001).

246. Ray, A., Lindahl, E. & Wallner, B. Improved model quality assessment using ProQ2. *BMC Bioinformatics* **13**, 224 (2012).

247. Eckey, V., Weidlich, D., Landmesser, H., Bergmann, U. & Schneider, E. The second extracellular loop of pore-forming subunits of ATP-binding cassette transporters for basic amino acids plays a crucial role in interaction with the cognate solute binding protein(s). *J Bacteriol* **192**, 2150-9 (2010).

248. Li, J. et al. Transient formation of water-conducting states in membrane transporters. *Proc Natl Acad Sci U S A* **110**, 7696-701 (2013).

249. Kwan, T. et al. Functional analysis of a tryptophan-less P-glycoprotein: a tool for tryptophan insertion and fluorescence spectroscopy. *Mol Pharmacol* **58**, 37-47 (2000).

250. Swartz, D.J., Weber, J. & Urbatsch, I.L. P-glycoprotein is fully active after multiple tryptophan substitutions. *Biochim Biophys Acta* **1828**, 1159-68 (2013).

251. Chen, Y. et al. Nucleotide binding to nucleoside diphosphate kinases: X-ray structure of human NDPK-A in complex with ADP and comparison to protein kinases. *J Mol Biol* **332**, 915-26 (2003).

252. Verdon, G. et al. Formation of the productive ATP-Mg2+-bound dimer of GlcV, an ABC-ATPase from Sulfolobus solfataricus. *J Mol Biol* **334**, 255-67 (2003).

253. Zaitseva, J. et al. Functional characterization and ATP-induced dimerization of the isolated ABC-domain of the haemolysin B transporter. *Biochemistry* **44**, 9680-90 (2005).

254. Ramaen, O. et al. Biochemical characterization and NMR studies of the nucleotide-binding domain 1 of multidrug-resistance-associated protein 1: evidence for interaction between ATP and Trp653. *Biochem J* **376**, 749-56 (2003).

255. Pretz, M.G. et al. Thermodynamics of the ATPase cycle of GlcV, the nucleotide-binding domain of the glucose ABC transporter of sulfolobus solfataricus. *Biochemistry* **45**, 15056-67 (2006).

256. Qu, Q., Russell, P.L. & Sharom, F.J. Stoichiometry and affinity of nucleotide binding to P-glycoprotein during the catalytic cycle. *Biochemistry* **42**, 1170-7 (2003).

257. Sauna, Z.E. et al. Catalytic cycle of ATP hydrolysis by P-glycoprotein: evidence for formation of the E.S reaction intermediate with ATP-gamma-S, a nonhydrolyzable analogue of ATP. *Biochemistry* **46**, 13787-99 (2007).

258. Ortiz, D., Gossack, L., Quast, U. & Bryan, J. Reinterpreting the action of ATP analogs on K(ATP) channels. *J Biol Chem* **288**, 18894-902 (2013).

259. Siarheyeva, A., Liu, R. & Sharom, F.J. Characterization of an asymmetric occluded state of P-glycoprotein with two bound nucleotides: implications for catalysis. *J Biol Chem* **285**, 7575-86 (2010).

260. Jacso, T., Schneider, E., Rupp, B. & Reif, B. Substrate transport activation is mediated through second periplasmic loop of transmembrane protein MalF in maltose transport complex of Escherichia coli. *J Biol Chem* **287**, 17040-9 (2012).

10 List of tables

11 Table of figures

Curriculum Vitae

For reasons of data protection,
the curriculum vitae is not included in the online version

Curriculum Vitae

13 Appendix

A

B
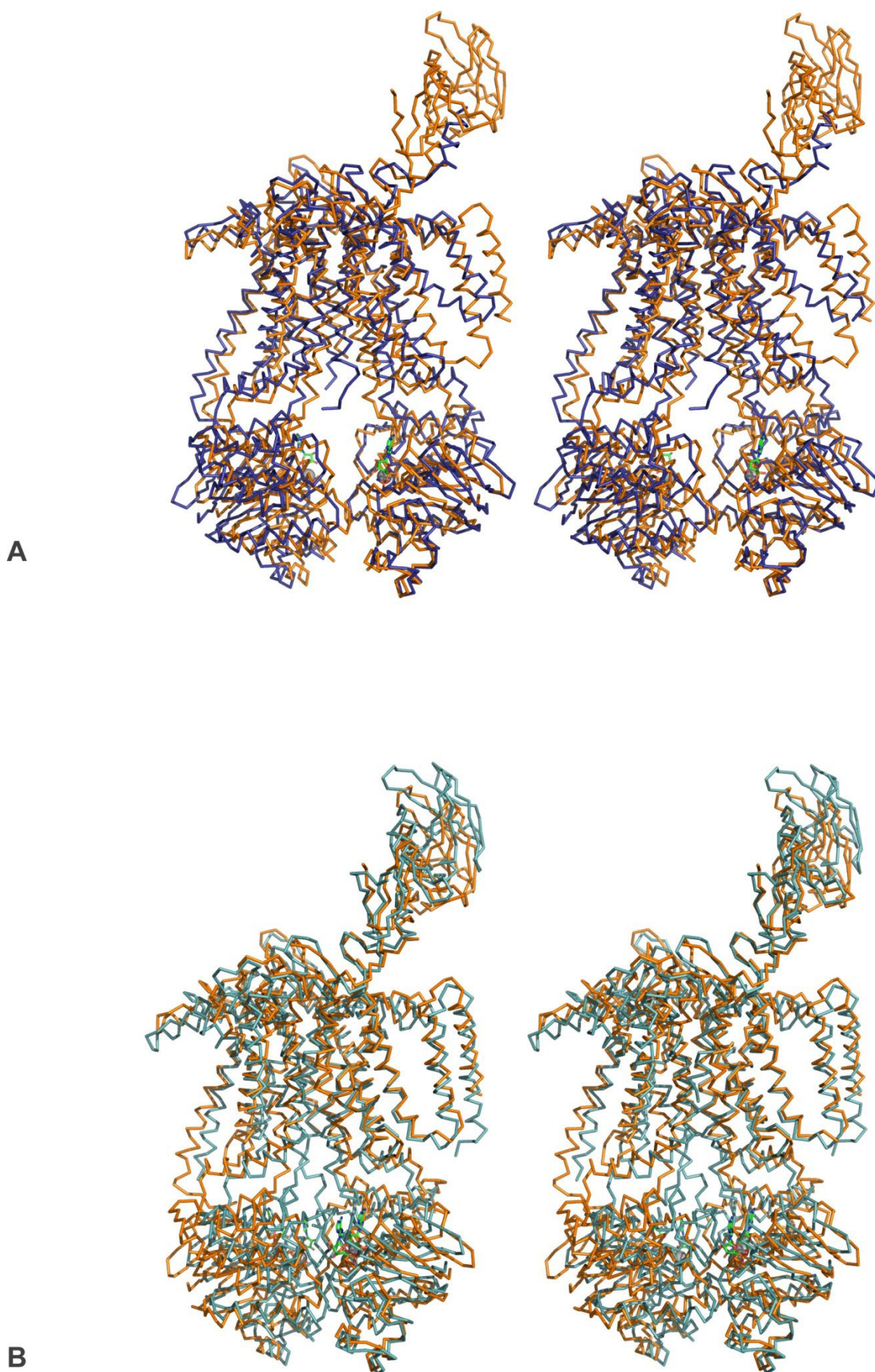
Figure 60: Stereo representation of different X-ray structures of the maltose transporter of *E. coli* The substrate binding protein was omitted for this figure. **A** Inward-facing state (3FH6) in blue and pre-translocation state (3PUZ) in orange **B** Pre-translocation state (3PUZ) in orange and transition state (3PUV) in cyan

Figure 61: Assigned HSQC spectrum of ArtP in phosphate buffer. The assignmen was accomplished by A. Chowdhury, Dr. E. Ploskon-Arthur. Dr. Britta Kunert prepared the protein and recorded the solution NMR spectra in collaboration with Dr. P. Schmieder.

Multiple sequence alignment (ESPript) of ModB_2ONK, MalF_3FH6, MalG_3FH6, ArtM_phyre and MetI_3DHW.
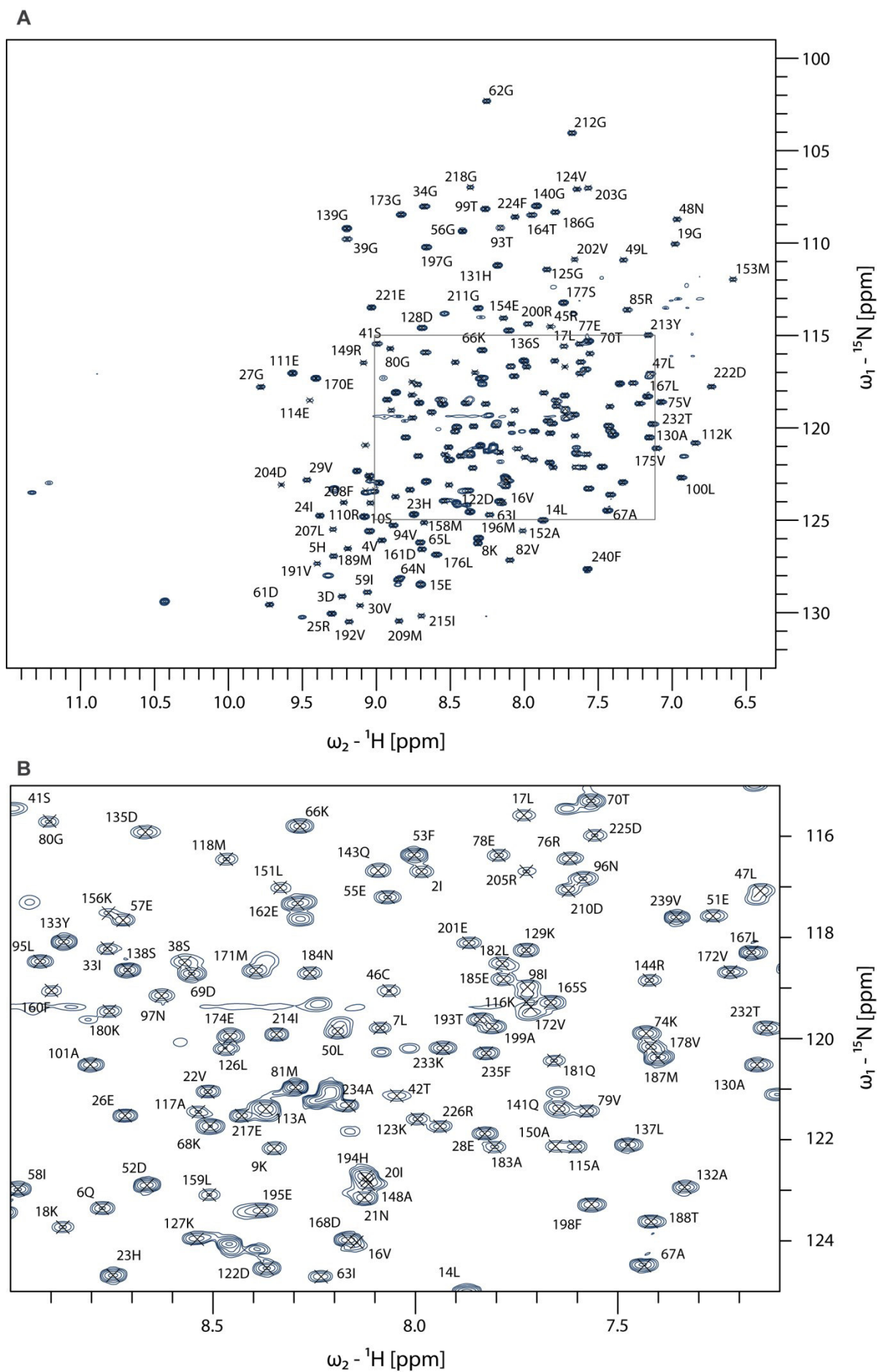
```
              1        10        20        30        40        50
ModB_2ONK    ..ITHLL..........MGHHHHHHHHHHHSSGE.NLYFQGHMRLLFSALLALLS.....SII
MalF_3FH6    MAQGEYLFAITTLILSSAGLYIFANRKAYAWRYVYVPGMAGMGLFVLFPLVCTIAIAFTNYSST
MalG_3FH6    MAQGEYLFAITTLILSSAGLYIFANRKAYAWRYVYVPGMAGMGLFVLFPLVCTIAIAFTNYSST
ArtM_phyre   ...............................................................
MetI_3DHW    ...............................................................

                    60        70        80        90       100
ModB_2ONK    .........GNF.......ALISTLIAVIFGTPLAYILARKSFPGKSVVEGIVDLPVVIPHTVAGI
MalF_3FH6    NQLTFERAQEVLLDRSWMAMVQPKS......QK......ARLF...LLFVL.......ATGSLIPE
MalG_3FH6    NQLTFERAQEVLLDRSWQAGKTYNFGLYPAGDEWQLALSDGETGKNY
ArtM_phyre   ..MDFRFDIIVEYAPYFFQGLLATIGVSLAGIIFGLILGLFIGLG...KMSTNLLVRLPFS.....
MetI_3DHW    MSEPMMLLVRGVWETLAMTFVSGFFGEVIGLPVGVLLY.VTRPGQIANAKLYRTVS.........

                  110       120       130       140
ModB_2ONK    ALLVFGSS.GLIGS......
MalF_3FH6    QISWDHWKLALG
MalG_3FH6    LSDAFKFGGEQKLQLKETTAQPEGERANLRVITQNRQALSDITAILPDGNKVMMSSLRQFSGTQP
ArtM_phyre   .WYINFFRGTPLVVQILLVHFG
MetI_3DHW    ..AIVNIFRSIPFIILLVWM.IP

                  150       160       170       180       190       200
ModB_2ONK    FSPLKFVDALPGI.......VVAMLFVSVPIYINQAKEGFASVDVRLEHVARTLGSSPLRVFFTVSLP
MalF_3FH6    ..PFIGLNTHGG...VIFAYLGGIALHVWTIKGYFETIDSSLEEAAALDGATPWQAFRLVLLPLSVP
MalG_3FH6    VKPAWFSDPTTARTMLLIVNTWLGYPYMMILCMGLLKAIPDDLYEASAMDGAGPFQNFFKITLPLLI
ArtM_phyre   VMPLFFAQPN.GIVSLAVSLSLNSAAYVAEIFRAGIQSIDKGQMEAAARSLGMTHAQAMRYIILPQA
MetI_3DHW    FTRVIVGTSI.GLQAAIVPLTVGAAPFIARMVENALLEIPTGLIEASRAMGATPMQIVRKVLLPEAL

                  210       220       230
ModB_2ONK    LSVRHIVAGAIMSWARGISEFGAVVIA...........YY
MalF_3FH6    ILAVVFILSFIAAITEVPVASLLRDVN...SYTLA..VGMQ
MalG_3FH6    KPLTPLMIASFAFNFNNFVLIQLLTNGGPDRLGTTTP..AGYT
ArtM_phyre   LKRMIPPFANEFIVLIKDSSLGMVIAAPEIMYWGKAAA.GEYY
MetI_3DHW    PGLVNAATITLLITLVGYSAMGGAVGAGGLGQIGYQYGYIGYNA

                  240       250       260       270       280
ModB_2ONK    PMIAPTLIYERYLSE.....GLSAAM..PVAAILLLSLAVFVALRIIVGREDVSEGQG
MalF_3FH6    QYINPQ.NYL.W....GDFAAAAVMSALPITIVFLLAQ..RWLVNGLTAGGVKG....
MalG_3FH6    DLLVNY.TYRIAFEGGGGQDFGLAAAI....ATLIFLLVG.ALAIVNLKATRMKFD....
ArtM_phyre   RVWEPYL........TVAFIYLLITLSLSKLSHYLE..RKYSTQ....
MetI_3DHW    TVMNTVLV........LLVILVYLI.QFAGDRIVRAVT..RK......
```

Figure 62: Amino acid sequence alignmnent for ArtM and other TMDs with published 3D structures. The alignment was made with Clustal Omega and the figure was prepared with ESPript 3.0.

Anja Voreck   Matrikelnummer: 4486126

Eidesstattliche Erklärung

Ich versichere, die Arbeit selbstständig und lediglich unter Benutzung der angegebenen Quellen und Hilfsmittel verfasst zu haben.

Ich erkläre weiterhin, dass die vorliegende Arbeit noch nicht im Rahmen eines anderen Prüfungsverfahrens eingereicht wurde.

Berlin, den 31.05.2014